UNIVERSITÀ DI PARMA

UNIVERSITA' DEGLI STUDI DI PARMA

Dottorato di ricerca in "Scienza e Tecnologie dei Materiali"

Ciclo XXXV

Synthesis of hybrid systems for biomedical applications by the functionalization of nanostructures

Coordinatore:
Chiar.mo Prof. Enrico Dalcanale

Tutor:
Chiar.ma Prof. Franca Bigi

Dottoranda: Giorgia Gullo

Anni 2019/2023

Abstract

In this work, the synthesis of water soluble hybrid nanosystems was investigated to achieve an X-Ray enhanced Photodynamic therapy (PDT) effect. According with this, Gold Nanoparticles (AuNPs) were conjugated to a photosensitizer (porphyrin) to obtain metal-enhanced phosphorescence (MEP) and an increased $^1O_2$ generation (SOG). (4-hydroxyphenyl)porphyrin (THPP) was monofunctionalized with thiol ending linkers with different length and conjugated on AuNPs' surface. Finally, the $^1O_2$ production was evaluated through the use of ADPA under a white light irradiation. Compared to the free THPP, the conjugate NS4 produced an enhancement of $^1O_2$ both under white light and X-Rays.

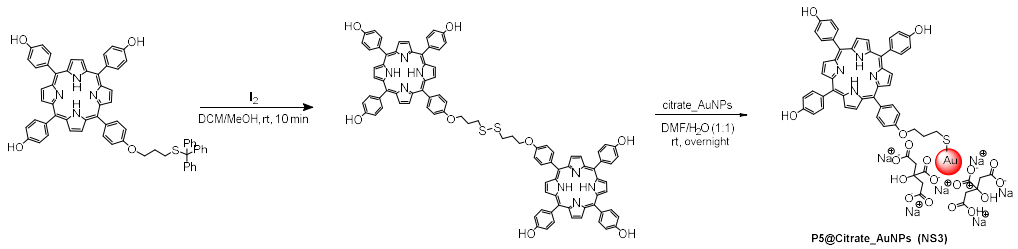

Figure 1: Conjugation reaction steps between AuNPs thiol-PEG stabilized and monoalkylated THPP with lipoic acid.

In order to improve the in vivo stability and cellular uptake of the nanosystem, the preliminar incorporation of NS1 into liposomes was investigated. Synthesis of NS2 liposomes was performed at the Technion (Israel) through the thin film layer method achieving a good encapsulation efficiency. During this abroad period, was also investigated a novel delivery system that selectively goes in lung cancer's cells to induce the silencing of KRAS mutation through the RNA interference (RNAi) technology.

Keywords: PDT, X-Ray, Singlet Oxygen production, Porphyrin, Gold nanoparticles, Liposomes, Drug delivery systems, siRNA.

Contents

Chapter 1

Introduction

1.1 Nanotechnology and Nanomedicine

The physicist Richard Feynman proposed, for the first time, the idea of nanotechnology (from nano that means "dwarf" in Greek) in his seminal lecture "*there is plenty of room at the bottom*" in 1959.[1] This concept provided researchers with new methods for examining materials between 1 nanometer to 100 nm, which is the typical scale of biologically molecules such as, for example, proteins, receptors, enzymes, antibodies and hemoglobin. The term "*nanotechnology*" was introduced only later, in 1974, from Professor N. Taniguchi to describe the manipulation and/or engineering of nano-objects on the scale of molecules. Since synthetic nanoscale objects are naturally small, they can pass through biological barriers, such as the blood-brain barrier, cell membranes and blood vessel walls. Additionally, due to altered quantum mechanical properties, nano-objects display tunable physical (such as electrical, magnetic, optical, mechanical) and chemical (such as reactivity, melting point, or biological properties) properties that are significantly different from those of the same materials in larger scale. Nano-objects can have a large variety of shapes (such as nanospheres, nanotubes, nanorods, and nanowires) and materials (such as silica, gold, semiconductors, iron oxides, lipid- or polymer-based) and can thus be solid, porous, or hollow, depending on the application. Due to their high transport capabilities, nanoobjects are advantageous tools for biosensors, imaging contrast agents and medicinal carriers.

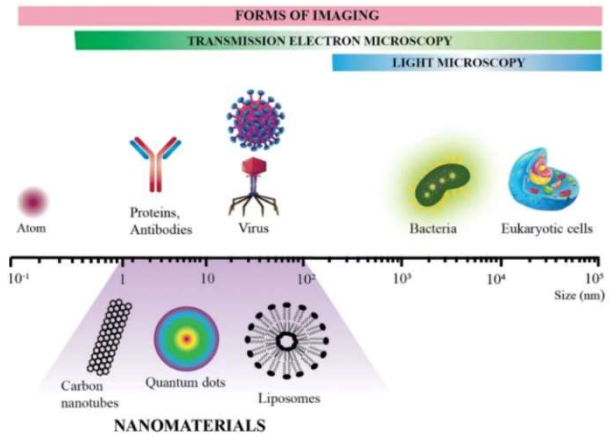

Figure 1.1: Relative size comparison of nanomaterials, microbiological and other biological entities. *Reproduced from ref.*[2] *and used under Creative Commons Attribution 4.0 International License.*

The use of nanoscale technologies in the medical field is known as nanomedicine (from biomedical imaging to drug delivery and therapeutics). Nanomedicine, defined by the European Science Foundation (ESF) as "*the science and technology of diagnostic treating and preventing disease and traumatic injury, of relieving pain, and of preserving and improving human health, using molecular tools and molecular knowledge of the human body*" is a recent example of the interdisciplinary field created by the convergence of nanotechnology and medicine. The goals of this young and rapidly developing medical area are similar to those of conventional medicine: efficient therapies with reduced side effects, fast and accurate diagnosis and non-invasive evaluation of the treatment's efficiency.

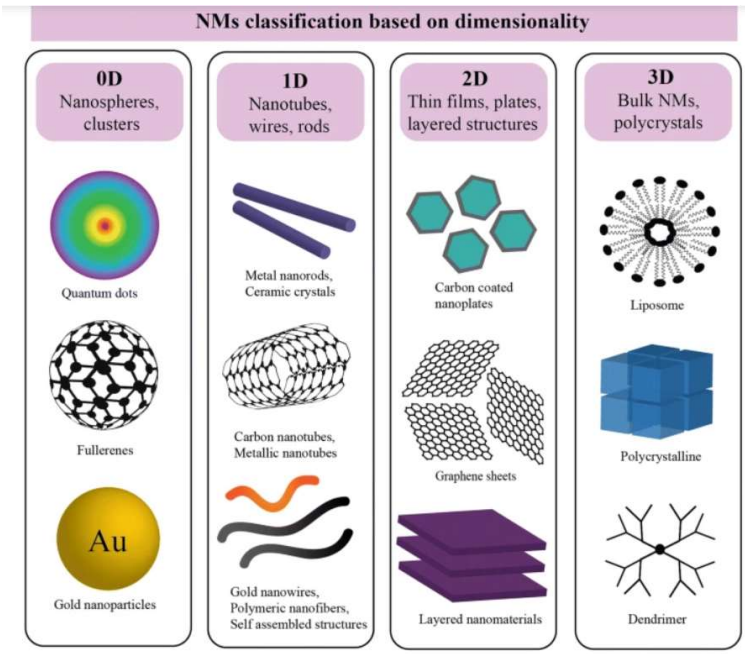

Figure 1.2: Schematic illustrating the relative dimensions of nanoparticles with examples of each category. *Reproduced from ref.*[2] *and used under Creative Commons Attribution 4.0 International License.*

In this scientific field, two approaches are pursued: the "bottom-up" approach, in which nanoscale materials and devices are built up starting from molecular compounds that self-assemble spontaneously in multi-component systems using molecular recognition. The second approach is the so-called "top-down" approach, that involves the breaking down of a large scale material through its disassembling in order to generate from it the required nanostructures . Since these systems are

assembled through weak non-covalent interactions as hydrogen bonds, electrostatic bonds and π-π interactions, the main advantage of the "top-down" approach is the reversibility of these systems.[3]

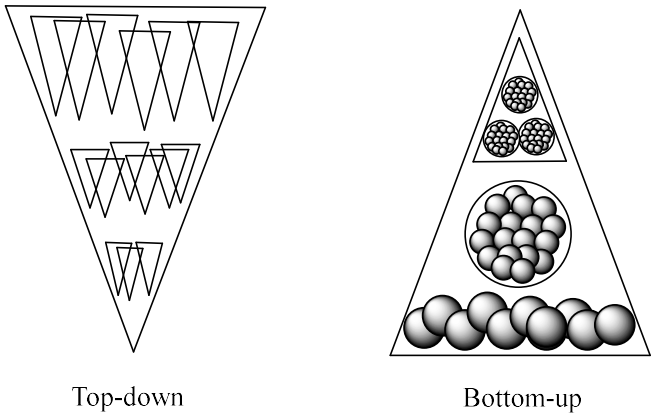

Figure 1.3: Top-down and Bottom-up approach for the construction of nanostructures.

As nature does, the self-assembly of molecules such as oligopeptides and nucleic acids may leads to nanosized structures able to perform specific functions. These assemblies are not the result of an aggregation of species formed randomly but are directed by particular intermolecular interactions. Nowadays, researchers are exploring organic, inorganic and hybrid nanorobots. As technology improved, some methods started fusing organic and inorganic components to produce a more sophisticated robot system known as a *hybrid nanosystem*. Research institutions all across the world are receiving more funding to investigate and improve in fields like nanosystems as interest in nanomedicine rises. Numerous applications have been the focus of nanomedicine, which has opened up new career opportunities with the development of new technologies and nanomaterials. The primary areas of application for nanomedicine are outlined on the following page: (1) Drug delivery: Drug delivery refers to formulations, techniques, technologies, and systems that can safely transport a pharmaceutical substance into the body to produce the wanted therapeutic effect. In order to increase the bioavailability and pharmacokinetics of therapies, drug delivery is based on nanoscale molecules or particles that have been designed to recognize a specific place in the body. Bypassing biological barriers, multi components targeted devices can deliver a

variety of therapeutic substances directly to cells as well as tissues in the microenvironment.[4] (2) Therapy methods: Several nanosystems have medical qualities that can be used in therapeutic treatments, or they may be even enhanced with bioactive substances that have therapeutic effects in biological systems.[5] (3) Imaging: Some nanostructures, nanoparticles in particular, can be employed to label biological structures, improving contrast and facilitating the biodistribution as, for example, superparamagnetic iron oxide nanoparticles used as contrast agents in magnetic resoncance imaging (MRI).[6] (4) Cell and Tissue Repair and Replacement: Nanotechnology provides fresh, biocompatible coatings that increase their adherence, toughness, and lifetime or even as a scaffold. To enhance the interface properties for tissue replacement and regeneration, new kinds of nanomaterials are being investigated. For example, nanopolymers can be used to cover devices in contact with blood to disperse clots or prevent their formation.[7]

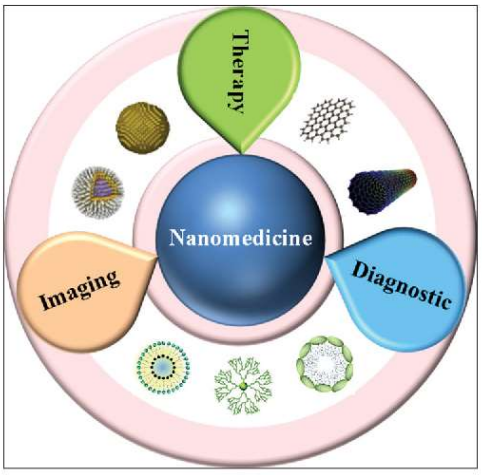

Figure 1.4: Schematic representation of major nanotechnology applications in biomedical field. *Reproduced from ref.*[8] *copyright © 2021 TheMMJ.*

1.2 Photodynamic therapy and porphyrins

It has been known for 100 years that light and chemicals can interact causing cancerous cell's death. O. Raab, a medical student from Germany, was the first to describe, in 1900, how the interaction of light and chemicals can cause cell death. Although H. von Tappeiner and A. Jodlbauer recognized that oxygen plays an important role in photosensitization reactions in 1904, only in 1907 they coined the term "*photodynamic action*" to describe this cytotoxic effect.[9] Photodynamic Therapy (PDT) is a therapeutic treatment used for several diseases, including cardiovascular, dermatological and ocular conditions.[10] However, the oncological area uses PDT most frequently to treat various types of superficial and deep solid tumors. PDT involves a PS, light of a certain wavelength and molecular oxygen to promote the destruction of the targeted tissue. A PS that selectively accumulates in tumor tissue (during a drug-light interval) is administered (topically or intravenously) and it is followed by the exposure to the specific wavelength light, which is typically in the red spectral area (600 nm; *figure 1.5*).[11]

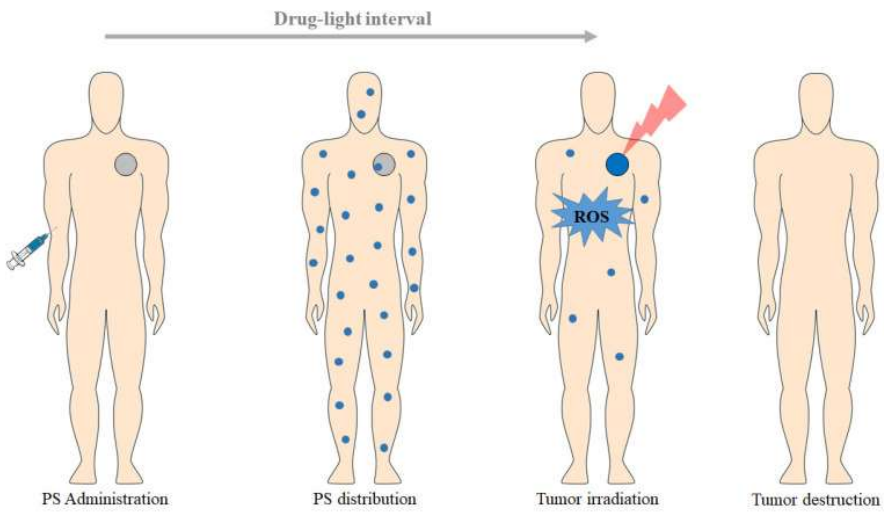

Figure 1.5: Representation of the clinical application of PDT protocol for the treatment of a solid and localized tumor. *Taken from ref.*[12] *Copyright © 2021 used under* Creative Commons Attribution (CC BY) license.

The photodynamic reaction begins with the PS in the target tissue absorbs light, which activates a sequence of photochemical processes that result in the production of Reactive Oxygen Species (ROS). PDT has the unique property of primarily acting as an antenna to activate oxygen through the absorption of light

energy, recovering at its initial state at the end of the process, ready for another round of treatment. Indeed, it can participate in thousands of therapeutic cycles until it is photobleached, metabolized or otherwise eliminated from the cell or tissue. The optical and photophysical properties that make a good PS can be summarized as: (i) high capacity to absorb light and (ii) high capacity to produce ROS and $^1O_2$. Since the light must be efficiently delivered to the PS to make PDT most effective, lasers and light-emitting diodes (LEDs) are light sources that are commonly used in PDT.[13] The mechanism of production of ROS and $^1O_2$ from a PS is described in *figure 1.6* that shows the modified Jablonski diagram of the PDT action: after light absorption, the PS is transformed from its ground state (singlet state, PS) to a short-lived, electronically excited singlet state (a few nanoseconds or less, PS_{Es} or $^1PS^*$).[14] This excited state is very unstable and can decay to the ground state, losing energy through light emission (fluorescence) or heat production (internal conversion). However, the singlet state can undergo through the non-radiative process of intersystem crossing to a more stable, long-lived, electronically excited state (triplet state, PS_{Et} or $^3PS^*$). This excited state can decay to the ground state through light emission (phosphorescence) or undergo two kinds of reactions. The triplet state has a longer lifetime (up to tens of microseconds), which allows sufficient time for direct transfer of energy to molecular oxygen (O_2). This energy transfer step brings to the formation of singlet oxygen ($^1O_2$) and the ground state of the PS, called type II reaction. The singlet oxygen is extremely reactive and can interact with a large number of biological substrates, inducing oxidative damage and ultimately cell death. The type I reaction can also occurs if the excited state of the PS reacts directly with a substrate, like cell membrane or a molecule, to yield free radicals and radical ions. These radicals react with molecular oxygen, producing ROS, such as $O2^{-\bullet}$, $HO^\bullet$, and H_2O_2, which produce oxidative damage that can lead to biological lesions.

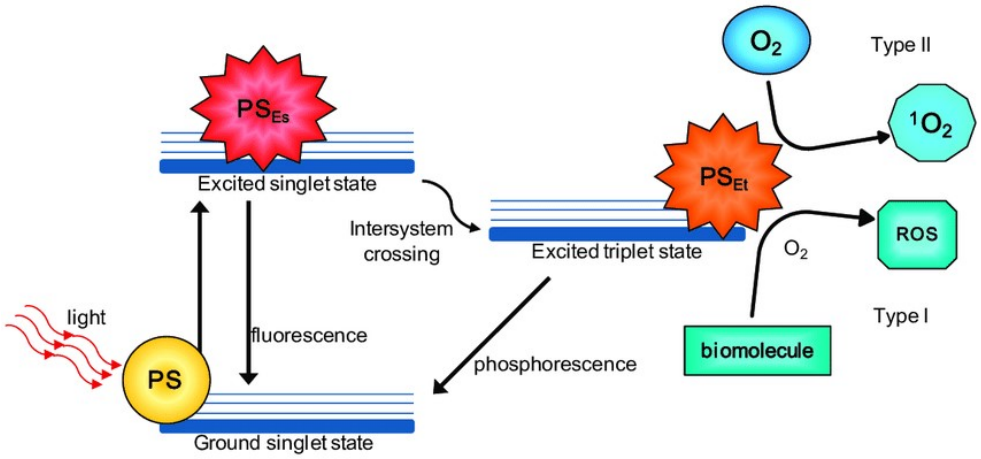

Figure 1.6: Type I and Type II reactions in PDT (photodynamic therapy). Schematic Jablonski's diagram showing PDT's mechanism of action. *Reproduced by ref.*[15] *Copyright © 2016 Creative Commons by Attribution (CC-BY) license.*

The compounds produced from type I and type II reactions are responsible for the effect of the cell death and therapeutic on PDT. Type I and type II reactions can take place simultaneously and the ratio between these processes depends on some factors as the PS, oxygen concentration, substrate and binding affinity of the sensitizer to the substrate. However, type II reaction predominates during PDT, and singlet oxygen is the main cytotoxic agent responsible for the biological effects. Only cells near to the location of the ROS production (areas where the PS is localized) are directly impacted by PDT because of the high reactivity and brief half-life of the ROS. The type of PS, its extracellular and intracellular location, the total dose administered, the dose of irradiation, the availability of oxygen, and the interval between the administration of PS and the exposure to light all play a role in the degree of damage and cytotoxicity caused by PDT.[14]

Compared to traditional approaches for cancer treatment, like chemotherapy, radiotherapy and surgery that are highly invasive often damaging the involved and nearby organs, PDT shows a huge number of advantages such as no long-term side effects and the possibility of being repeated many times at the same site if needed. Then it often costs less than other cancer treatments, it usually takes only a short time and is most often done as an outpatient procedure. Unfortunately, performing PDT on deeper and hypoxic tumors is more challenging due to the low oxygen concentration and poor light penetration (light absorption by the PS and energy transfer to the oxygen). Moreover, more superficial and thus more oxygenated tumors allow an higher production of ROS making PDT a more successful treatment.

In addition to light and oxygen, photosensitizers are one of the three essential components of PDT. As in each classification of drugs, there are a number of conditions and properties that define the ideal photosensitizer: stability at room temperature, chemical purity, high photochemical reactivity, photosensitive effect only under a specific wavelength, absorption bands that should not overlap other substances in the body like melatonin or hemoglobin, low cytotoxicity in the dark, and easy solubility in biological environment of the body. Photosensitizers are generally divided into two main categories: porphyrins or non-porphyrins. Porphyrins ("purple" from the Greek) are macromolecules composed by 16-atom rings containing four nitrogen atoms that belong to the class of tetrapyrroles in which also hemoglobin and myoglobin (two O_2-binding proteins found in blood) are comprise. These highly conjugated molecules possess an heterocyclic macrocycle and may also contain a core metallic element like iron and magnesium. They are macrocycles with a framework made of bridging meso carbon atoms with sp_2 hybridization. The structure has 18-electrons and is entirely aromatic and the presence of a 22 π electron system allows a long wavelength absorption. More complicated porphyrins can be created by replacing hydrogens in meso positions with various functional groups (shown in *figure 1.7*). The new substituents in the meso sites can be the same or different and on the type of these substituents is possible to tune and control physical and chemical properties of the porphyrin.

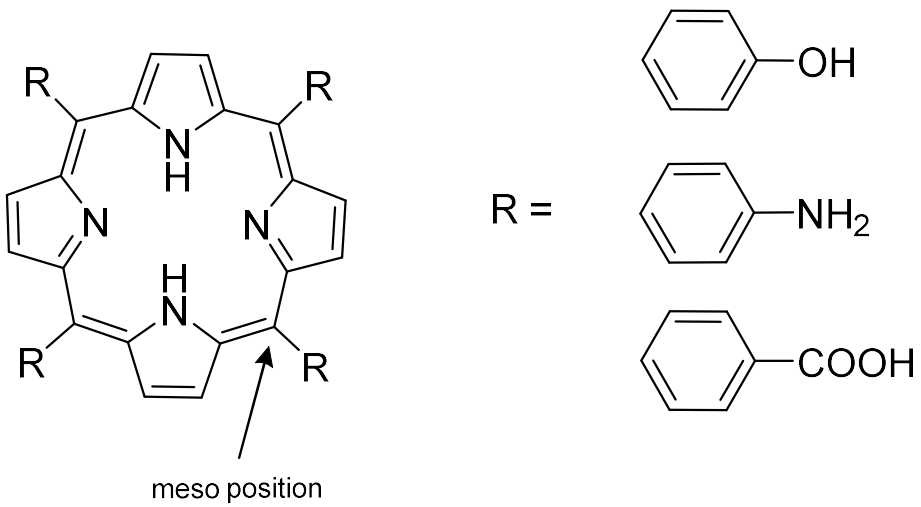

Figure 1.7: Porphyrin ring with some examples of substituents on the *meso*-positions.

As a result, porphyrins have caught the attention of researchers in all the world for their potential use as photosensitizing drugs. Porphyrin-based photosensitizers can be further classified as first, second or third generation photosensitizers (*figure 1.8*). Hematoporphyrin derivative (HpD) and Photofrin are example of first generation photosensitizers.[16] Due to their low tumor selectivity, weak absorption in the near-infrared that does not allow them to easily penetrate tissues and their strong and lasting skin photosensitization, a number of second generation photosensitizers have been developed to alleviate certain problems. Compared with first generation compounds, these second generation photosensitizers absorb light at a longer wavelength, are chemically pure and cause less photosensitization effects after treatment. Third generation photosensitizers are second generation photosensitizers coupled to vehicles such as antibodies and liposomes for selective accumulation in the tumor tissue, and they now represent an important studied topic in this field.[17] Third generation PSs offer several advantages compared to the free second-generation PS such as an high stability, high conjugation or loading efficiency, tunable size, easy functionalization, slow degradation, long cycle time, biocompatibility, and low degree of decomposition in biological applications, which enable the tumor targeting and delivery of the PS and its controllable release.

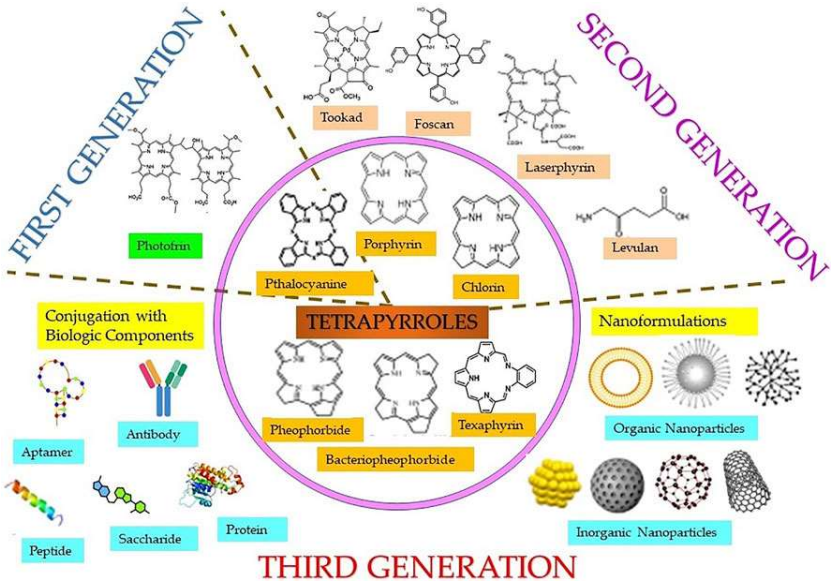

Figure 1.8: Classification of different classes (inner circle) of tetrapyrrole photosensitizers and different generations of photosensitizers including first, second, and third generation (in the form of conjugates linked with targeting biologic moieties and nanoparticles).[18]

Absorption and fluorescence spectroscopy in the UV-Vis range are excellent tools for characterizing the optical properties of porphyrins. Depending on the substituents in meso positions, these macrocycles exhibit a strong absorption band in the visible region, between 400 and 500 nm, also known as B bands or Soret band that results from a S_0 to S_2 transition, which moves an electron from its ground state to its second excited state. The 'Q bands' can be seen at longer wavelengths, between 480 and 650 nm, are less intense than then previous one and are generated from the forbidden transition. The number of the Q bands and their intensity depends on the symmetry and form of the porphyrin (i.e. salt form or with a metal in the core). Porphyrins, have some noteworthy properties such as photochemical (if used as photosensitizers in PDT or catalyst in photosynthesis), optical and supramolecular (when used in nanotechnology in self-assembly systems).

1.3 Hybrid Materials and 3D-SAM: Gold nanoparticles

Hybrid materials are composites formed by a synergistic combination of organic and inorganic components at the nanometer level and, in recent years, are gaining popularity and exhibiting novel features that are not present in their pure counterparts. The explanation of these new properties becomes more important as the size of the hybrid material decreases. Self-assembled monolayers (SAM) is a prominent class of nano-sized hybrid materials consisting of a single layer of organic molecules that spontaneously bonds and assembles in a ordered way on a solid substrate as a result of chemical or physical forces occurred during the deposition process. The organic molecules have a functional group that can bind non-covalently or covalently with the inorganic component's surface atoms. The chemisorption typically acts as the driving force for SAM's production. Because of this, a strong chemical affinity between the surface and adsorbate is necessary and can be guaranteed through the introduction, for example, of a thiol group on noble metals surface as gold or carboxylic acid groups on oxides of silver or iron. These materials are also characterized by the presence of a "tail" group at the end of the alkyl chain that guarantees certain properties to the material itself (*figure 1.9*).

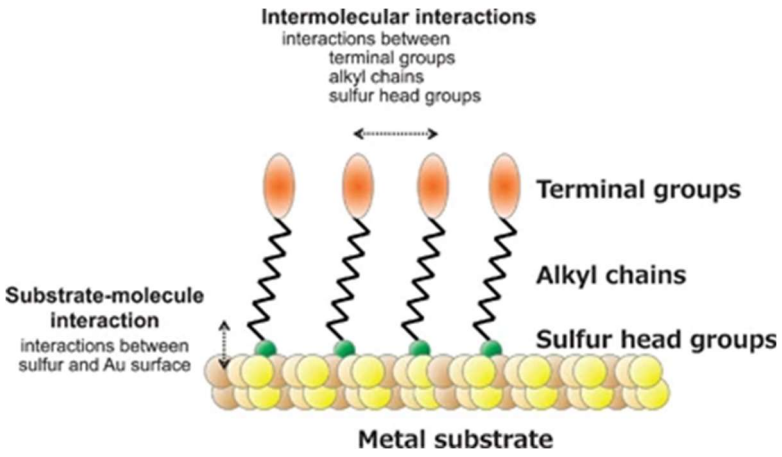

Figure 1.9: Illustration of a typical self-assembled monolayer (SAM) of an alkanthiol derivative on a metal surface.[19]

SAMs are frequently divided into 2D or 3D depending on the kind of substrate. In the first case, a flat inorganic surface of Au, Si, SiO2, GaAs, etc. is covered with an organic monolayer. In the second case, the inorganic structure, which has a three-dimensional shape (spherical, rod-like, piramids, etc.), is entirely encased by the organic parts. Those 3D-SAM with an inorganic component made of noble metals (Au, Ag, or Cu) are increasingly being used in a variety of practical domains, including nanosensory, nanoelectronic, and catalysis. These nanostructures, often referred to as monolayer protected clusters (MPCs) or noble metal nanoparticles (NPs), have been functionalized with a wide range of organic components, depending on the desired property. For example, it is possible to introduce hydrophilic or hydrophobic molecules to the entire nanostructure altering its solubility in solvents with different polarities (as will be discussed in *chapter 2*).

As described in the previous chapter, nanotechnology gave rise to a new field of medicine, called “nanomedicine”. “Therapeutic nanomedicine” tries to alleviate the problems of conventional drugs such as no selectivity, lack of effectiveness and several side effects. Metal nanoparticles, mainly gold (Au), silver (Ag), copper (Cu), platinum (Pt) and palladium (Pd), thanks to their easy synthesis and purification as well as biocompatibility, have been largely studied and used, especially in diagnostics, giving rise to “*theranostic*” systems. *Theranostics* is a term derived from a combination of the words therapeutics and diagnostics. In this emerging field of medicine, drugs and/or techniques are uniquely combined to simultaneously or sequentially diagnose and treat medical conditions. Since

ancient times, people have used gold as a medicinal agent to treat sickness.[20] Today, gold, in particular gold nanoparticles (AuNPs), have emerged as an intriguing studied topic in cancer imaging, treatment, and especially cancer detection. A relatively new area of study under nanophotonics and nano-optics is *plasmonics* (or nanoplasmonics) that investigates the electron's oscillations in metallic nanostructures and nanoparticles (NPs). One of the most remarkable characteristics of metallic nanostructures is its *surface plasmon resonance* (SPR), which is caused by the collective oscillation of metal conduction electrons excited by the electromagnetic field of light. When a NP (for example a spherical NP as shown in figure *1.10*) is hit by a light beam and interacts with it, the electromagnetic field causes a shift of the electrons of conduction in the NP, that results in the formation of an electric dipole, due by the accumulation of a negative charge in one side and of a positive charge on the other side dipole, due by the accumulation of a negative charge in one side and of a positive charge on the other side.

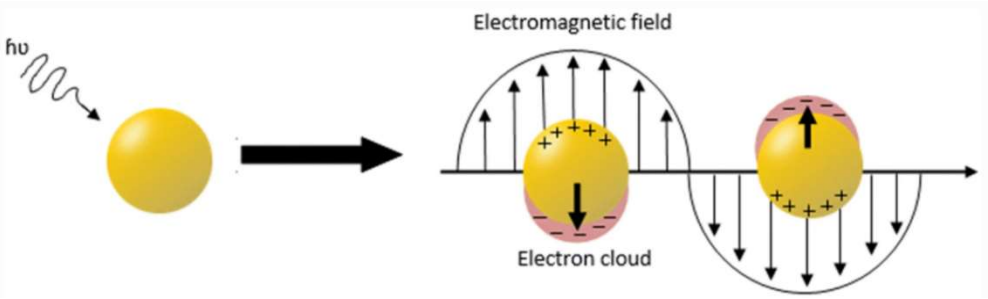

Figure 1.10: Surface Plasmon Resonance of gold nanoparticles.[21]

For metallic NP that has a smaller size than the wavelength of the photons of interaction, the plasmons, not propagating, are called *localized surface plasmons* (LSPs). By measuring the absorbance of the solution that contains NPs as a function of wavelength, SPR is typically observed. Shape, size, surface ligand, solvent, temperature, and proximity of other NPs in the solution are all factors that affect the signal that is produced. These factors can extremely influence the band's position, width and other characteristics produced by the SPR, called *surface plasmon resonance band* (SPRB or SPB).[22]

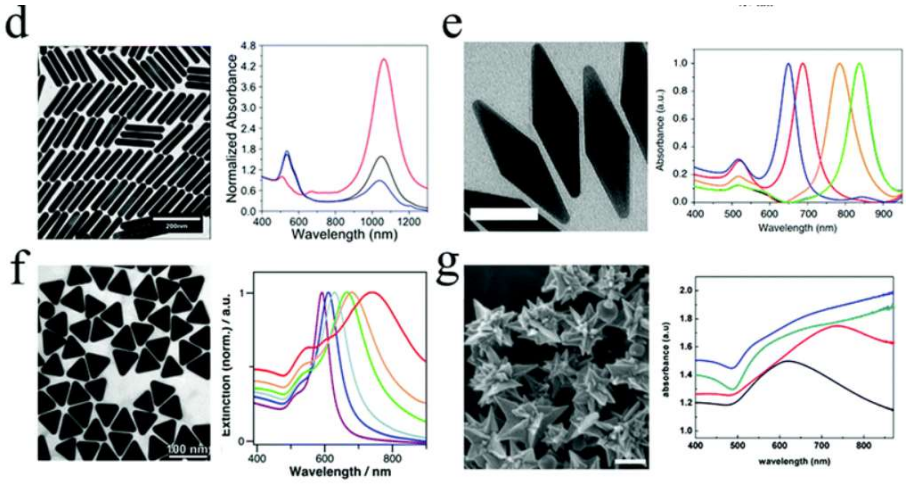

Figure 1.11: Different shapes of nanoparticles (TEM images and SPR extinction spectra of various sizes of nanoparticles): (d) nanorods (scale bar 200 nm) *reproduced from ref.*[23] *Copyright © 2015 American Chemical Society*, (e) nanobipyramids (scale bar 50 nm), (f) nanotriangles (scale bar 100 nm), (g) nanostars (scale bar 100 nm). *Reproduced from ref.*[24] *Copyright © The Royal Society of Chemistry 2019.*

Regarding spherical NPs, changing different conditions as the type of precursor of NPs, the reducing agent, the ratio between the reagents, solvent and temperature is possible to obtain NPs with a defined diameter. The formation of AuNPs is mainly performed following a "bottom up" strategy (see *chapter 1.1*) since it originates from individual molecules and involves a chemical or biological reduction. This chemical reduction is divided into two steps: nucleation and successive growth. When this two steps are completed in the same process, it is called *in situ synthesis*, while, in contrast, it is called *seed-growth method*. Concerning the *in situ synthesis*, in general, the preparation of AuNPs involves two reactions: (i) a reduction using agents like borohydrides, aminoboranes, hydrazine, citric and oxalic acids, sugars, hydrogen peroxide, sulfites, hydrogen, acetylene, exc. and (ii) a stabilization by agents like trisodium citrate dihydrate, sulfur ligands (expecially thiolates), nitrogen-based ligands (including heterocycles), surfactant (in particicular cetyltrimethylammonium bromide, CTAB). This in situ synthesized AuNPs are usually used for a further functionalization with other linkers that can create stronger interactions than the stabilizing agents.

1.4 Optical properties

Recent researches have revealed that plasmonic nanoparticles can effectively photosensitize the synthesis of $^1O_2$ by photoexciting at their LSPR wavelength. Certain nanomaterials, when they absorb light, produce excited states, which can interact with a close PS to increase the production of ROS. Three different types of nanoparticles with different composition and mechanism of production of enhanced PS activity have been identified, called *nanoparticles light antennas* (*figure 1.12*). [25]

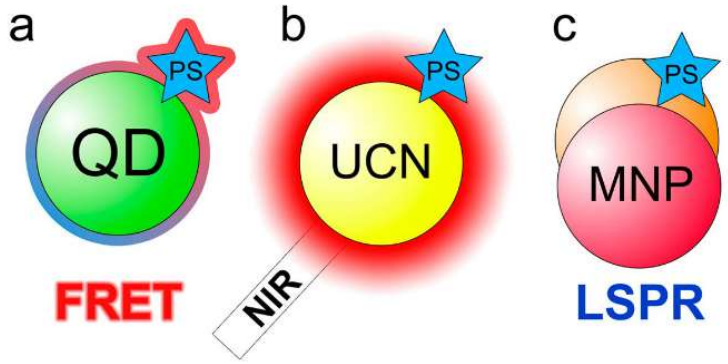

Figure 1.12: Nanoantennas for photodynamic therapy and their mechanisms of action. (a) Quantum dots (QDs), based on Förster resonance energy transfer (FRET). (b) Up-conversion nanoparticles (UCNs). (c) Metal nanoparticles (MNPs), which show a localized surface plasmon resonance (LSPR). *Reproduced by ref.*[26] *Copyright © European Society for Photobiology 2016.*

(1) Quantum dots (QDs) have been widely studied as antennas for PDT as FRET donors. In order to make them attractive for efficient photosensitization via FRET, QDs need several features such as an high photostability, a strong emission that can be tuned to overlap the absorption of the PS and a large surface that allows an high loading degree of PS molecules.

(2) Up-Conversion Nanoparticles (UCNs) are nanomaterials composed that encapsulate a lanthanide or actinide ions like Er^{3+}, Yb^{2+} or Tm^{3+}. These nanoparticles can convert low-energy light (NIR) into high-energy radiation (UV and/or visible via an anti-Stokes emission effect). Thus, UNCs has the advantage to use NIR light to excite conventional PSs, reaching deeper tissues.

(3) Plasmonic Nanoparticles (MNPs) have the incredible property to both enhance the electromagnetic radiation on their surface (called *localised*

field enhancement) and to produce energy transfer processes, increasing the efficiency of $^1O_2$ production from conventional PSs in PDT treatment. The development of plasmonic antennas of $^1O_2$, was first developed on solid supports and today many efforts have been made to develop it in solution (see *chapter 1.4.4*).

In the next pages are discussed the most relevant optical properties that can born from the combination of NPs with a PS.

1.4.1 Metal enhanced fluorescence (MEF) and Metal enhanced phosphorescence (MEP)

Metal-enhanced fluorescence (MEF) is a method that improves the photoluminescence intensity of materials, such as quantum dots, dyes, carbon dots, and so on. This effect is ascribed to the excitation of localized surface plasmon with resonances (LSPRs) of gold and has consequently the effect to enhance the electronic excitation of surface-anchored molecules, that results to an enhancement of their fluorescence. The plasmonic nanoparticle here serves as a transmitting optical antenna to transfer the near field to the far field at the fluorescence wavelength. In MEF, metals quench the fluorescence when the PSs are very close to their surface while, when the fluorophores are placed very close at an optimum distance from the metallic nanostructures, they gain the additional plasmon-enhanced optical fields. Zhang et al. described another optical properties of a nanosystem, the metal-enhanced phosphorescence (MEP). As MEF, it is also a surface plasmon coupled as shown in *figure 1.13 (bottom)*, where a non-radiative energy transfer occurs from excited distal fluorophores to the surface plasmon electrons in a metallic nanostructure which in turn radiate PS phosphorescent emission efficiently.[27]

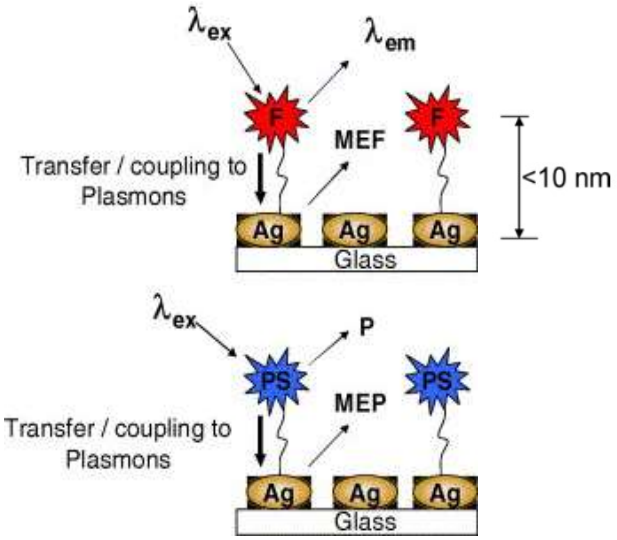

Figure 1.13: Graphical representation of metal-enhanced fluorescence (top and middle), and for metal-enhanced phosphorescence (bottom). *Reproduced from ref.*[27] *Copyright ©* 2006 Elsevier B.V. All rights reserved.

Figure 1.14 shows a modified Jablonski diagram that described the possible mechanisms for the enhanced excitation of fluorophore when is close to a plasmon resonance particle. Firstly, metal allows an enhanced absorption that excites a PS from the ground state S_0 to an excited state, S_n. S_n then relaxes to the lowest excited singlet state S_1, facilitating intersystem crossing (ISC) causing an higher generation of singlet oxygen. This observation of Metal-Enhanced $^1O_2$ generation (ME^1O_2) suggests that this approach may be important for singlet oxygen based clinical therapy, where an high supply of $^1O_2$ is required.

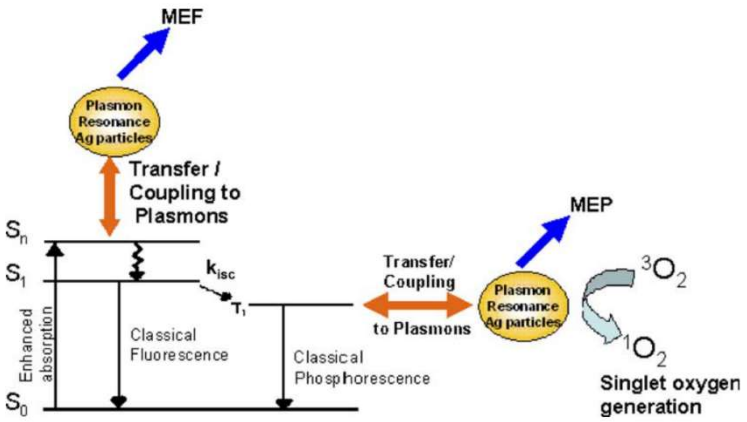

Figure 1.14: Schematic Jablonski diagram for Photosentisitizer and surface plasmon enhanced Singlet Oxygen generation. *Reproduced from ref.*[28] *Copyright ©* Springer Science + Business Media, LLC 2007

As described in the last chapter, a wide range of nanostructures are able of increase the production of $^1O_2$ in solution. Gold nanostructures/protoporphyrin IX have been widely examined in their ability to enhance $^1O_2$ in solution.[29,30] However, no single nanostructure has been reported to retain this enhancement in biological media. Modulating the particle's characteristics (like size, shape, composition), the optical properties of the nanoparticle can be determined in order to optimize this light-harvesting ability and to improve radiative processes near the photosensitizers. The most important feature to increase the PS activity is the overlap between the plasmon resonance of NPs and PS absorption, whereas plasmon overlap with PS emission will quench its activity.[31]

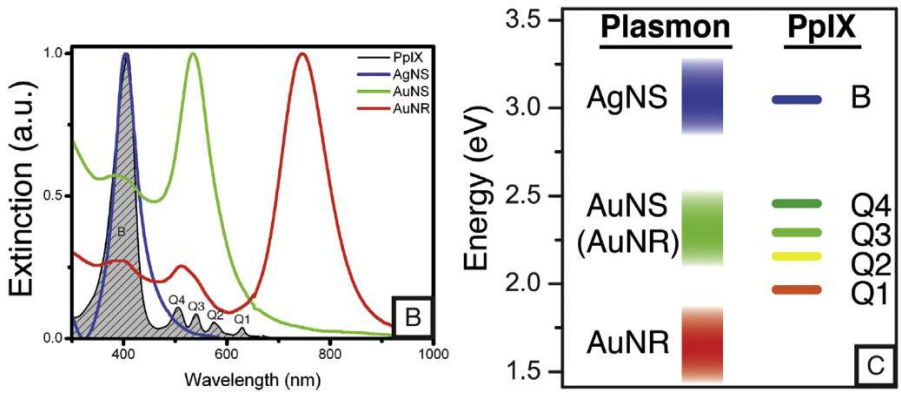

Figure 1.15: (B) Absorption spectra of PpIX (shaded gray), AgNS (blue), AuNS (green), and AuNR (red). (C) Jablonski diagram of plasmon resonances for each particle and the Q and B excitation bands of PpIX, illustrating the overlap between the various plasmon resonances and these PpIX excitation energies. *Reproduced from ref.*[30] *Copyright © 2013 Elsevier B.V. All rights reserved.*

Another important feature of a nanosystems able to give MEP effect is the distance between the components. Yaraki et al. demonstrated, in a system composed by AgNPs and AIE-PS, that the optimum distance to obtain the maximum enhancement of singlet oxygen generation (SOG) is shorter than the distance to achieve the highest MEF.[32] The intersystem crossing (ISC), since is a non-radiative process, tends to be enhanced at a short distance according to the Jablonski diagrams (*figure 1.16*), while radiative decay rates are promoted at longer distance.

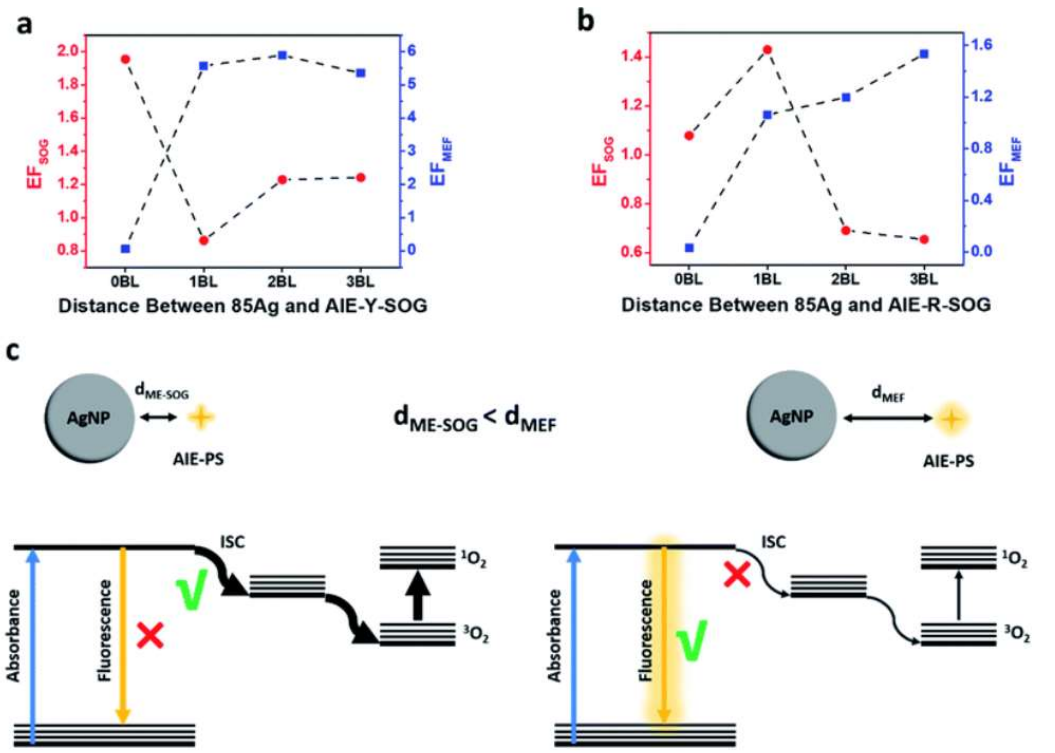

Figure 1.16: Correlation between ME-SOG (red sphere) and MEF (blue square) for (a) AIE-Y-SOG and (b) AIE-R-SOG using 85 nm AgNP with different bilayers. (c) Simplified Jablonski diagrams showing the MEF (right scheme) and ME-SOG (left scheme) mechanism of the AIE-PS nanohybrids occur at different optimum AgNPs to AIE-PS distance for maximum plasmonic enhancement. *Reproduced from ref.*[32] *Copyright © The Royal Society of Chemistry 2020.*

1.4.2 Surface enhanced Raman scattering (SERS)

Another important optical properties that can rise between PS-NPs nanosystem is Surface-enhanced Raman scattering (SERS) causes a significant enhancement in Raman signal intensity. Raman scattering, after light–molecule interactions, is originated from the energy of laser photons shifting as inelastic scattering. However, the intensity of the signal originated from the Raman scattering is very low in intensity due to the presence of few photons that show an inelastic scattering. The mechanisms of Raman scattering enhancement was firstly proposed by Fleischmann et al. on a roughened silver electrode.[33] During the last decades, how the enhancement mechanism works was widely studied and discussed, but only two theories nowadays have been accepted: electromagnetic- or chemical-based. First, when the incident light hits particles smaller than the incident wavelength, localized surface plasmons are excited, inducing an enhanced electrical

field near the particle surface and this results in an enhanced Raman scattering of adsorbates. In the chemical-enhancement mechanism, through a chemical binding, the molecule is chemisorbed on the metallic surface, generating a charge-transfer resonance, due to the electronic interaction between the conduction band of the nanostructure and the molecular orbital. If occurs a coupling between the resonance and the vibrational states of the molecule, a reallocation of electron density can be obtained consequently leading to a SERS enhancement.

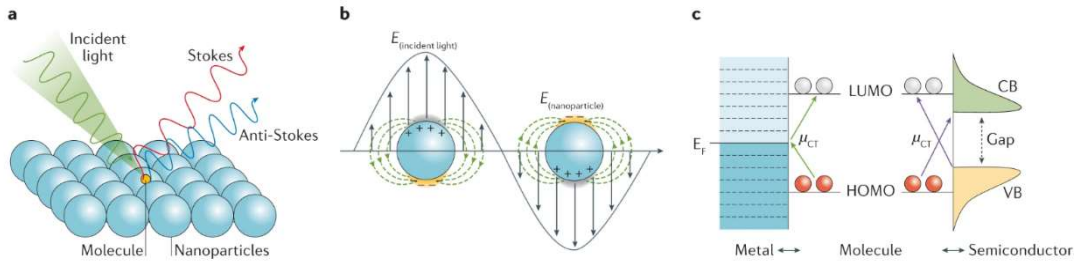

Figure 1.17: (a) Enhanced Raman scattering of a molecule adsorbed on nanoparticles resulting in emitted radiation with a lower (red) or higher (blue) frequency than the incident light, known as Stokes and anti-Stokes scattering, respectively. (b) Localized surface plasmon resonance contribution to surface-enhanced Raman spectroscopy (SERS). (c) Charge transfer (CT) contribution to SERS at a metal–molecule or semiconductor–molecule interface. *Reproduced from ref.*[34] *Copyright © 2022, Springer Nature Limited*

1.4.3 Auger effect

Over the last few years there has been a considerable increase in interest of combine metal nanoparticles (especially gold) with the radiation therapy, giving an enhanced effect called *Nanoparticle Enhanced X-ray Therapy or NEXT*. The metal NPs can selectively scatter and/or absorb the high energy gamma/X-ray radiations. Among the several emissions that occur when X-rays radiation hit a metal, the most relevant effects to cancer radiotherapy are scattered X-rays/photons, Auger electrons, photoelectrons, Compton electrons and fluorescence photons. In particular, the Auger effect was observed for the first time in 1920's years by Pierre Victor Auger that gave rise to the Auger Electron Spectroscopy that concerns on the emission of Auger electrons when a sample is hit by X-rays or energetic electrons.

It is a physical phenomenon in which, when X-rays hits a core electron it is then removed, leaving a vacancy that is filled by an electron from a higher energy level resulting in a release of energy. Although this energy is mainly released in the form of an emitted photon, it can also be transferred to another electron, which is expelled from the atom: this second electron is called *Auger electron*.

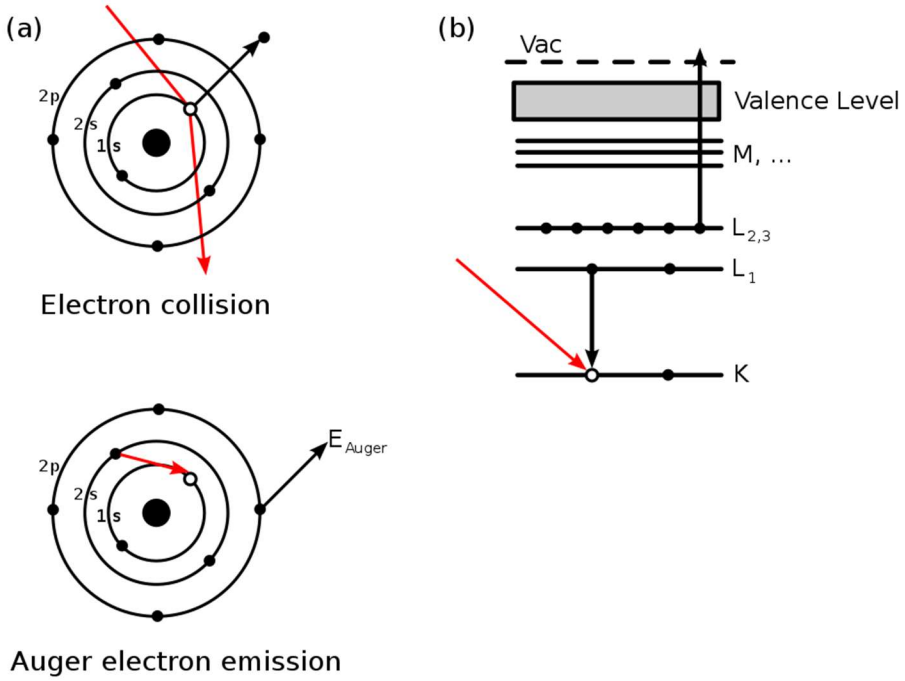

Figure 1.18: a) illustrates sequentially the steps involved in Auger deexcitation. (b) illustrates the same process using X-ray notation, $KL_1L_{2,3}$.

1.4.4 Nanotechnology on PDT and X-Ray PDT

As *US-National Cancer Institute* states, traditional Photodynamic therapy (PDT), deeply discussed in the previous *chapter 1.2*, is successfully employed to treat superficial tumors (e.g. under the skin or on the lining of internal organs or cavities) by the generation of an active form of oxygen (singlet oxygen) that destroys nearby cancer cells. One of the limitations of the standard PDT is the low PS selectivity on cancer cells: the higher is the selectivity, the higher is the accumulation of the PS in cancer cells and consequently the side effects for patients are decreased. PS

selectivity can be enhanced increasing the hydrophilicity of the photosensitizer or by imparting amphiphilic properties to the structures. Over the last decade, the development of nanotechnology and nanomedicine has been observed using nanomaterial platforms for diagnostic and therapeutic treatments, allowing the drug delivery to target tissues and improving the efficacy of anti-cancer therapy. In PDT studies has become very attractive the use of nanoparticles for the following reasons: (1) nanoparticles can increase the water solubility of the PS, thus its selectivity, reducing the side effects; (2) PSs can be used for PDT treatment in lower dose; (3) 50–100 nm particles can improve penetration and retention effect (EPR effect) thus the tumor targeting and the cellular uptake, and (4) nanoparticles can enhance also the PSs photostability, their difficult synthesis and purification and a slow body clearance.

A limitation of the traditional PDT is the laser radiation employed to excite the photosensitizer (PS) that isn't able to penetrate enough to reach inner tissues into the body. To overcome this last drawback, a variation of the classical PDT was proposed, in which X-ray, a deeper penetrating radiation, is employed reaching tissues and deep seated tumors easily. Unfortunately, the standard PSs cannot absorb an high amount of the X-ray radiation, consequently causing a low efficiency of production of cytotoxic species as $^1O_2$ or other reactive oxygen species (ROS).

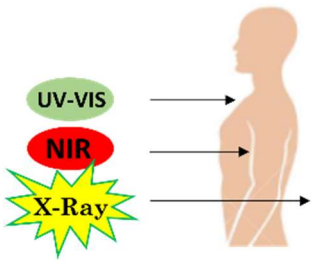

Figure 1.19: X-Ray as more penetrating radiation for PDT.

Introducing heavy metal nanoparticles (with high Z), due to their ability to excellently absorb X-rays, is possible to develop novel PS suitable for X-Ray based clinical applications. In combination with a PS, nanopartciles can be introduced as enhancers of energy leading to an improved generation of $^1O_2$ or ROS. Even if the mechanism of this enhancement is still under investigation, is well known that when X-rays hit an high Z metal, the metal is able to absorb the energy of the radiation giving rise to multiple possibilities of eventual outcome as summarized

in *figure 1.20*. Among the several emissions that occur, the most important for cancer radiotherapy are scattered X-rays/photons, photoelectrons, Compton electrons, Auger electrons and fluorescence photons.

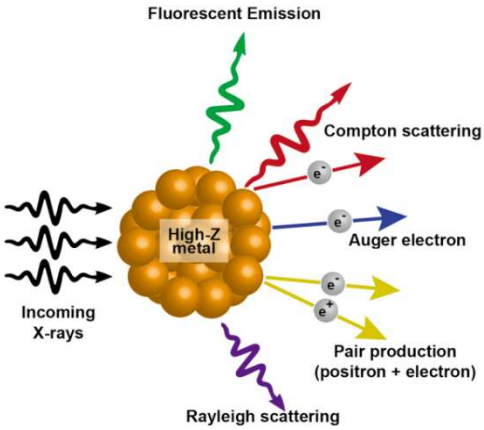

Figure 1.20: Schematic illustrating potential interactions of incident photons with a gold atom or other high-Z materials[35].
Adapted from ref.[35] *Copyright © 2013 Pioneer Bioscience Publishing Company.All rights reserved.*

One of the hypothesis for this enhancement can be ascribed to the principle of photon activation therapy (PAT), whereby direct absorption of X-rays by metalated PS generates Auger electrons (described in the previous chapter) and free radicals using the photoelectric effect. As represented schematically in *figure 1.21*, the mechanism in photon-activation of high-Z atoms leads to the emission of Auger electrons and photoelectrons, that react with nearby biomolecules or through radiolysis of water, inducing the formation of free radicals to cause direct or indirect cellular damage. Thus, the photon absorption by high-Z atoms contributes to the enhancement of energy deposition such that a good tumor damage can be achieved even with low irradiation dose[18].

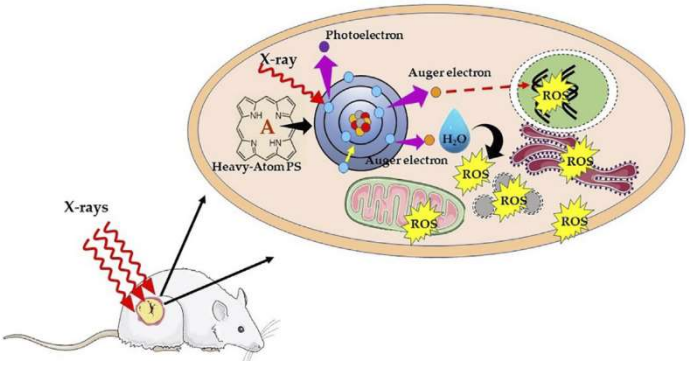

Figure 1.21: Schematic illustration of mechanism of X-ray photon activation therapy. *Adapted from ref.*[18] *Copyright © 2022 Sarbadhikary, George and Abrahamse.*

Beyond this emissions, a further possible explanation to the enhanced generation of $^1O_2$ and ROS from PS can be ascribed to the highly localized plasmonic field of the Nanoparticles (i.e. Gold nanoparticles, AuNPs) and their aggregates, as experimentally determined by Khaing et al.. In their work, they noted that in surface-enhanced Raman scattering (SERS), the enhancement is proportional to the fourth power of the electric field ($|E|^4$) confirming that localized plasmonic field of AuNPs can significantly enhance ROS generation and that the effect is increased with larger particles.[36] They tested three representative particle sizes (19, 66, and 106 nm in diameter) and since the cellular uptake of various AuNPs is size-dependent, the highest uptake and the highest enhancement of ROS formation under a laser light at 532 nm was obtained with 66 nm AuNPs that led to the lowest viability of cancer cells after PDT treatment (*figure 1.22, right).*

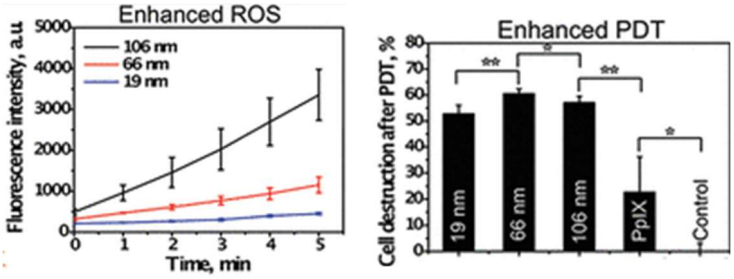

Figure 1.22: Enhancement of ROS (left) and enhancement of PDT (right) increasing AuNPs size.

Among various metallic nanoparticles, AuNPs have been widely explored for drug delivery, photothermal therapy and photodynamic therapy due to their

biocompatibility, the non-toxic nature of the gold core, its chemical stability and strong light absorption at tunable plasmon resonance wavelength. The functionalization of the AuNPs' surface with PS can be achieved via covalent bonds or weak interactions like electrostatic interactions and van der Waals interactions.

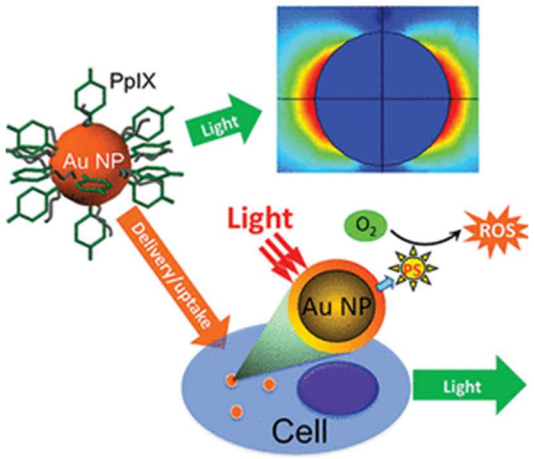

Figure 1.23: Gold Nanoparticle-Enhanced Generation of Reactive Oxygen Species from Protoporphyrin IX. *Adapted from ref.*[29] *Copyright © 2012 American Chemical Society.*

1.5 Drug Delivery systems: an overview on liposomes

Drug delivery systems (DDS) is a huge field of investigation which main gold is to improve the administration and efficacy of pharmaceutical compounds such as drugs, enzymes, peptides, antibodies, vaccines and many others. Today the most common mode of administering drugs is trough oral pills and injection: Oral pills offer controlled doses, portability and the non-invasive nature of administration but on the other hand, they have the limitation of not deliver macromolecules like proteins. Injections, instead, are able to deliver bigger therapeutic molecules, but have the disadvantage of being invasive and used inappropriate.[37] Amoabediny et al. estimated that 70% of drugs currently employed in medicine are water insoluble and that many promising drugs are discarded from therapeutic treatments due to their poor physical and chemical properties.[38] In the conventional drug delivery treatments, low water solubility is one of the hardest challenge to overcome that causes a poor biodistribution and bioavailability. These limitations gave rise to the development of novel drug delivery systems (DDS) in order to improve oral and

injectable nanosystems, but also to open other administration routes like transdermal, pulmonary, ocular and nasal routes. In nanotechnology field, one of the most used delivery system is nanovectors that have the ability to overcome several biological barriers and to localize one or more bioactive molecules into the target tissue. The nanovectors currently used and studied can be divided into three main categories or "generations" (*figure 1.24*).

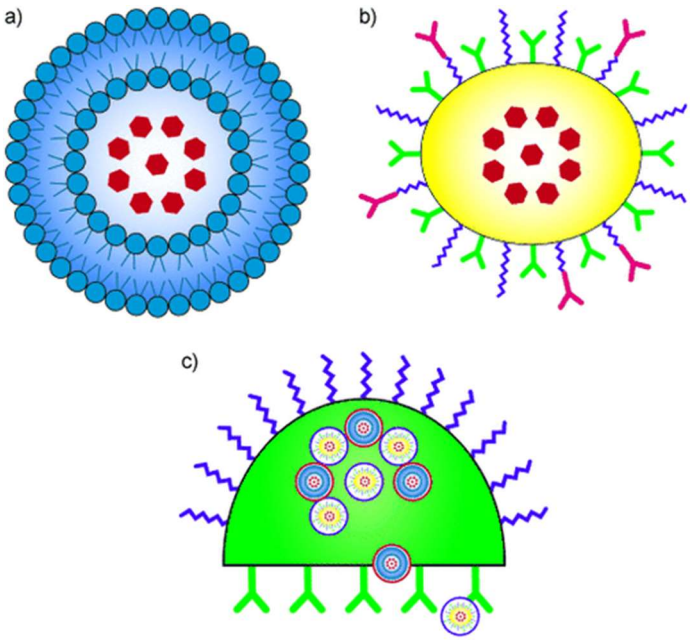

Figure 1.24: a) First-generation nanovectors composed by a container and an active principle. b) Second-generation nanovectors able to target their therapeutic action through antibodies or other biomolecules, c) Third-generation nanovectors are capable of more complex functions, such as time-controlled deployment of multiple waves of active nanoparticles across different biological barriers and different subcellular targets. *Reproduced from ref.*[39] *Copyright © 1999-2023 John Wiley & Sons, Inc. All rights reserved.*

The first generation (*figure 1.24, a*) comprises all the passive delivery systems which localization into the target site is due only to the size of the particles and not to a specific recognition of the tumor and which mechanism of action brings to an enhanced permeation and retention (EPR) effect. These systems are generally functionalized on their surface with a so-called "stealth" layer (for example, polyethylene glycol, PEG) that improve their circulation time. The most well-known system that belongs to this generation in clinical treatments are liposomes but other systems of this category are widely used like metal nanoparticles. The second generation of nanovectors (*figure 1.24, b*) are characterized by specific

functionalities on their surface which are responsible to the molecular recognition of the target tissue and/or of the triggered release of the cargo at the desired site. Antibody-functionalized liposomes and nanoparticles are the best examples of this second class of nanovectors but also pH-sensitive polymers and iron oxide nanoparticles. Another new technology belonging to this class is based on the coupling of nanoparticles to small interfering RNA (siRNA), which can cause the silencing of specific genes responsible for cancer. Through the use of targeted nanoparticles, siRNA can slow block the growth of tumors without expose the patient to the side effects often related to the traditional cancer therapies. The construction of nanosystems of the third generation has the role to successfully overcome the barriers that the drug or vector face when introduced in the body, significantly increasing the probability of reach the target tissues at a concentration needed for obtaining a therapeutic efficacy (*figure 1.24, c*).

Through delivery systems, the nanosystem is able to face several obstacles such as metabolic clearance and chemical instability of the drug, osmotic pressure and endoepithelial barriers. Liposomes are recognized as a versatile drug delivery system for several applications in medicine thanks to their ability of both targeting drugs to proper cells and tissues and of facilitating their delivery and cellular uptake. The potential use of liposomes as vehicles of several drugs to cells was recognized in the 1970s.[40] Although the huge amount of work on how liposomes can deliver drugs, the molecular mechanisms of interaction between liposome and cell has not been completely clarified.[41]

Liposomes are lipid-based spherical vesicles that have at least one lipid bilayer. The hydrophobic ends of the lipids in the bilayer face each other inwards and the hydrophilic tails of the lipid face away from each other and interact with the aqueous medium. This enables liposomes to be loaded with hydrophobic molecules between the lipid bilayer and hydrophilic molecules in the aqueous core. Generally, liposomes have three main components: a primary lipid (HSPC, DSPG, DMPC, POPC and so on), cholesterol, and DSPE-PEG_{2000} (*figure 1.25*). Cholesterol increases the stability of the liposome while reducing permeability of water-soluble substances across the membrane and the PEG is important in drug delivery application as it increases the retention time of the liposomes in the body.

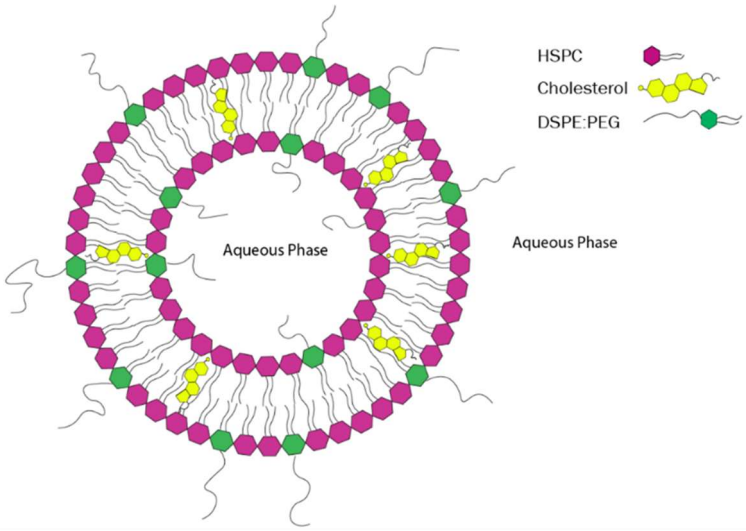

Figure 1.25: Schematic representation of the HSPC – Chol -PEG 2000:DSPE liposome.

Liposome properties can be tuned considerably changing lipid composition, size, surface charge and method of preparation. Furthermore, on the components of the bilayer depends the 'rigidity' of the system and the charge of the bilayer. For example, the formation of a more permeable and less stable bilayers is promoted using unsaturated phosphatidylcholine species (like egg or soybean phosphatidylcholine), whereas the use of saturated phospholipids with long acyl chains (like dipalmitoylphos phatidylcholine) creates a rigid and impermeable bilayer.[42] They, thanks to their biocompatibility, biodegradability and low toxicity, are widely used as carriers in cosmetic, food, farming and pharmaceutical industries. One of the most attractive properties of liposomes is their ability to encapsulate both hydrophobic and hydrophilic molecules, avoiding their decomposition, and allowing the release of the entrapped material at designated sites. On the basis of their size and number of bilayers, liposomes can be divided into one of two categories: (1) *multilamellar vesicles* (MLV) and (2) *unilamellar vesicles*. In multilamellar liposomes, vesicles have an onion structure with several bilayers while, in unilamellar liposomes, the vesicle is composed by a single phospholipid bilayer sphere. Unilamellar vesicles can be further divided into two other categories: (1) large unilamellar vesicles (LUV) and (2) small unilamellar vesicles (SUV). All the methods of preparing liposomes involve four basic stages: (1) Dry down lipids from organic solvent, (2) Disperse the lipid in aqueous media, (3) Purify the resultant liposome and (4) Analyze the final product. Molecules can be

loaded into liposomes by two major techniques: active and passive loading. In active loading, liposomes are first produced before introducing the substance into the liposome. In passive loading, the molecule is dissolved in the aqueous solution in which the liposomes are produced. Passive loading techniques include three different methods: (1) Mechanical dispersion method, (2) Solvent dispersion method and (3) Detergent removal method. The most employed method was the solvent dispersion that can be divided into two techniques: Ethanol injection and thin film layer method. Ethanol injection is a method in which a lipid solution of ethanol is quickly injected to an excess of buffer. The main drawbacks of this method are that the heterogeneity of the population (30 to 110 nm), the high dilution of liposomes, the difficult removal of ethanol and the high probability of inactivation of various biologically active macromolecules in the presence of ethanol.[42] Concerning the thin film layer method (deeply described in *chapter 3*), hydrophilic cargoes can be inserted in the hydration mediums of the film and then incapsulated (passively) into the liposome during their formation in the hydration process. Then an extruder allows the reduction of the liposomes' size and lamellarity. When lipids are first mixed to an aqueous solution, large multi-lamellar vesicles (micro-scale) are formed. An extruder is thus used to let these vesicles to pass through nanopore membranes and reduce them to vesicles of desired size (nanoscale). The main drawbacks of this method method are the difficulty of removal of the organic solvent, the low encapsulation efficiency, and the small-scale production.

1.6 References

(1) Feynman, R. P. There's Plenty of Room at the Bottom. *Eng. Sci.* **1960**, *23* (5), 22–36.

(2) Poh, T. Y.; Ali, N. A. B. M.; Mac Aogáin, M.; Kathawala, M. H.; Setyawati, M. I.; Ng, K. W.; Chotirmall, S. H. Inhaled Nanomaterials and the Respiratory Microbiome: Clinical, Immunological and Toxicological Perspectives. *Part. Fibre Toxicol.* **2018**, *15* (1), 46. https://doi.org/10.1186/s12989-018-0282-0.

(3) M. Mendes, P. Cellular Nanotechnology: Making Biological Interfaces Smarter. *Chem. Soc. Rev.* **2013**, *42* (24), 9207–9218. https://doi.org/10.1039/C3CS60198F.

(4) Evans, J. Five Big Ideas for Nanotechnology. *Nat. Med.* **2009**, *15* (4), 348–348. https://doi.org/10.1038/nm0409-348.

(5) Sanna, V.; Pala, N.; Sechi, M. Targeted Therapy Using Nanotechnology: Focus on Cancer. *Int. J. Nanomedicine* **2014**, *9*, 467–483. https://doi.org/10.2147/IJN.S36654.

(6) Bogart, L. K.; Pourroy, G.; Murphy, C. J.; Puntes, V.; Pellegrino, T.; Rosenblum, D.; Peer, D.; Lévy, R. Nanoparticles for Imaging, Sensing, and Therapeutic Intervention. *ACS Nano* **2014**, *8* (4), 3107–3122. https://doi.org/10.1021/nn500962q.

(7) Dalby, M. J.; Biggs, M. J. Special Focus on Nanoscale Regeneration. *Nanomed.* **2015**, *10* (5), 677–680. https://doi.org/10.2217/nnm.15.34.

(8) Banerjee, S. Nanomedicine - Impact and Perspectives. In *MMJ-A Journal by MIMER Medical College, Pune, India*; Banerjee, Dr. S., Ed.; 2018; Vol. 2, pp 5–8. https://doi.org/10.15713/ins.mmj.25.

(9) Noble, B. &. *Die sensibilisierende Wirkung fluoreszierender Substanzen: Gesammelte Untersuchungen über die photodynamische Erscheinung|Paperback*. Barnes & Noble. https://www.barnesandnoble.com/w/die-sensibilisierende-wirkung-fluoreszierender-substanzen-hermann-von-tappeiner/1136892041 (accessed 2023-01-11).

(10) Dougherty, T. J.; Gomer, C. J.; Henderson, B. W.; Jori, G.; Kessel, D.; Korbelik, M.; Moan, J.; Peng, Q. Photodynamic Therapy. *J. Natl. Cancer Inst.* **1998**, *90* (12), 889–905. https://doi.org/10.1093/jnci/90.12.889.

(11) *Photodynamic Therapy (PDT): Principles, Mechanisms and Applications – Nova Science Publishers*. https://novapublishers.com/shop/photodynamic-therapy-pdt-principles-mechanisms-and-applications/ (accessed 2023-01-11).

(12) Correia, J. H.; Rodrigues, J. A.; Pimenta, S.; Dong, T.; Yang, Z. Photodynamic Therapy Review: Principles, Photosensitizers, Applications, and Future Directions. *Pharmaceutics* **2021**, *13* (9), 1332. https://doi.org/10.3390/pharmaceutics13091332.

(13) Kamkaew, A.; Chen, F.; Zhan, Y.; Majewski, R. L.; Cai, W. Scintillating Nanoparticles as Energy Mediators for Enhanced Photodynamic Therapy. *ACS Nano* **2016**, *10* (4), 3918–3935. https://doi.org/10.1021/acsnano.6b01401.

(14) Dolmans, D. E. J. G. J.; Fukumura, D.; Jain, R. K. Photodynamic Therapy for Cancer. *Nat. Rev. Cancer* **2003**, *3* (5), 380–387. https://doi.org/10.1038/nrc1071.

(15) Calixto, G. M. F.; Bernegossi, J.; De Freitas, L. M.; Fontana, C. R.; Chorilli, M. Nanotechnology-Based Drug Delivery Systems for Photodynamic Therapy of Cancer: A Review. *Molecules* **2016**, *21* (3), 342. https://doi.org/10.3390/molecules21030342.

(16) Levy, J. G. Photodynamic Therapy. *Trends Biotechnol.* **1995**, *13* (1), 14–18. https://doi.org/10.1016/S0167-7799(00)88895-2.

(17) O'Connor, A. E.; Gallagher, W. M.; Byrne, A. T. Porphyrin and Nonporphyrin Photosensitizers in Oncology: Preclinical and Clinical Advances in Photodynamic Therapy. *Photochem. Photobiol.* **2009**, *85* (5), 1053–1074. https://doi.org/10.1111/j.1751-1097.2009.00585.x.

(18) Sarbadhikary, P.; George, B. P.; Abrahamse, H. Potential Application of Photosensitizers With High-Z Elements for Synergic Cancer Therapy. *Front. Pharmacol.* **2022**, *13*, 14.

(19) Tanaka, M.; Hayashi, T.; Morita, S. The Roles of Water Molecules at the Biointerface of Medical Polymers. *Polym. J.* **2013**, *45* (7), 701–710. https://doi.org/10.1038/pj.2012.229.

(20) Grodzinski, P.; Silver, M.; Molnar, L. K. Nanotechnology for Cancer Diagnostics: Promises and Challenges. *Expert Rev. Mol. Diagn.* **2006**, *6* (3), 307–318. https://doi.org/10.1586/14737159.6.3.307.

(21) Fuller, M. A.; Köper, I. Biomedical Applications of Polyelectrolyte Coated Spherical Gold Nanoparticles. *Nano Converg.* **2019**, *6* (1), 11. https://doi.org/10.1186/s40580-019-0183-4.

(22) Petryayeva, E.; Krull, U. J. Localized Surface Plasmon Resonance: Nanostructures, Bioassays and Biosensing—A Review. *Anal. Chim. Acta* **2011**, *706* (1), 8–24. https://doi.org/10.1016/j.aca.2011.08.020.

(23) Scarabelli, L.; Sánchez-Iglesias, A.; Pérez-Juste, J.; Liz-Marzán, L. M. A "Tips and Tricks" Practical Guide to the Synthesis of Gold Nanorods. *J. Phys. Chem. Lett.* **2015**, *6* (21), 4270–4279. https://doi.org/10.1021/acs.jpclett.5b02123.

(24) Olesiak-Banska, J.; Waszkielewicz, M.; Obstarczyk, P.; Samoc, M. Two-Photon Absorption and Photoluminescence of Colloidal Gold Nanoparticles and Nanoclusters. *Chem. Soc. Rev.* **2019**, *48* (15), 4087–4117. https://doi.org/10.1039/C8CS00849C.

(25) Kostron e Hasan - 2016 - Front Matter.Pdf.

(26) Front Matter. In *Comprehensive Series in Photochemical & Photobiological Sciences*; Kostron, H., Hasan, T., Eds.; Royal Society of Chemistry: Cambridge, 2016; pp P001–P006. https://doi.org/10.1039/9781782626824-FP001.

(27) Zhang, Y.; Aslan, K.; Malyn, S. N.; Geddes, C. D. Metal-Enhanced Phosphorescence (MEP). *Chem. Phys. Lett.* **2006**, *427* (4), 432–437. https://doi.org/10.1016/j.cplett.2006.06.078.

(28) Zhang, Y.; Aslan, K.; Previte, M. J. R.; Geddes, C. D. Metal-Enhanced Singlet Oxygen Generation: A Consequence of Plasmon Enhanced Triplet Yields. *J. Fluoresc.* **2007**, *17* (4), 345–349. https://doi.org/10.1007/s10895-007-0196-y.

(29) Khaing Oo, M. K.; Yang, Y.; Hu, Y.; Gomez, M.; Du, H.; Wang, H. Gold Nanoparticle-Enhanced and Size-Dependent Generation of Reactive Oxygen Species from Protoporphyrin IX. *ACS Nano* **2012**, *6* (3), 1939–1947. https://doi.org/10.1021/nn300327c.

(30) Hayden, S. C.; Austin, L. A.; Near, R. D.; Ozturk, R.; El-Sayed, M. A. Plasmonic Enhancement of Photodynamic Cancer Therapy. *J. Photochem. Photobiol. Chem.* **2013**, *269*, 34–41. https://doi.org/10.1016/j.jphotochem.2013.06.004.

(31) Sapsford, K. E.; Berti, L.; Medintz, I. L. Materials for Fluorescence Resonance Energy Transfer Analysis: Beyond Traditional Donor–Acceptor Combinations. *Angew. Chem. Int. Ed.* **2006**, *45* (28), 4562–4589. https://doi.org/10.1002/anie.200503873.

(32) Yaraki, M. T.; Hu, F.; Rezaei, S. D.; Liu, B.; Tan, Y. N. Metal-Enhancement Study of Dual Functional Photosensitizers with Aggregation-Induced Emission and Singlet Oxygen Generation. *Nanoscale Adv.* **2020**, *2* (7), 2859–2869. https://doi.org/10.1039/D0NA00182A.

(33) Fleischmann, M.; Hendra, P. J.; McQuillan, A. J. Raman Spectra of Pyridine Adsorbed at a Silver Electrode. *Chem. Phys. Lett.* **1974**, *26* (2), 163–166. https://doi.org/10.1016/0009-2614(74)85388-1.

(34) Han, X. X.; Rodriguez, R. S.; Haynes, C. L.; Ozaki, Y.; Zhao, B. Surface-Enhanced Raman Spectroscopy. *Nat. Rev. Methods Primer* **2022**, *1* (1), 1–17. https://doi.org/10.1038/s43586-021-00083-6.

(35) Kwatra, D.; Venugopal, A.; Anant, S. Nanoparticles in Radiation Therapy: A Summary of Various Approaches to Enhance Radiosensitization in Cancer. *Transl. Cancer Res.* **2013**, *2* (4), 13.

(36) Khaing Oo, M. K.; Yang, Y.; Hu, Y.; Gomez, M.; Du, H.; Wang, H. Gold Nanoparticle-Enhanced and Size-Dependent Generation of Reactive Oxygen Species from Protoporphyrin IX. *ACS Nano* **2012**, *6* (3), 1939–1947. https://doi.org/10.1021/nn300327c.

(37) Anselmo, A. C.; Mitragotri, S. An Overview of Clinical and Commercial Impact of Drug Delivery Systems. *J. Controlled Release* **2014**, *190*, 15–28. https://doi.org/10.1016/j.jconrel.2014.03.053.

(38) Amoabediny, G.; Haghiralsadat, F.; Naderinezhad, S.; Helder, M. N.; Akhoundi Kharanaghi, E.; Mohammadnejad Arough, J.; Zandieh-Doulabi, B. Overview of Preparation Methods of Polymeric and Lipid-Based (Niosome, Solid Lipid, Liposome) Nanoparticles: A Comprehensive Review. *Int. J. Polym. Mater. Polym. Biomater.* **2018**, *67* (6), 383–400. https://doi.org/10.1080/00914037.2017.1332623.

(39) Riehemann, K.; Schneider, S. W.; Luger, T. A.; Godin, B.; Ferrari, M.; Fuchs, H. Nanomedicine—Challenge and Perspectives. *Angew. Chem. Int. Ed.* **2009**, *48* (5), 872–897. https://doi.org/10.1002/anie.200802585.

(40) Gregoriadis, G. The Carrier Potential of Liposomes in Biology and Medicine: (First of Two Parts). *N. Engl. J. Med.* **1976**, *295* (13), 704–710. https://doi.org/10.1056/NEJM197609232951305.

(41) Düzgüneş, N.; Nir, S. Mechanisms and Kinetics of Liposome–Cell Interactions. *Adv. Drug Deliv. Rev.* **1999**, *40* (1–2), 3–18. https://doi.org/10.1016/S0169-409X(99)00037-X.

(42) Akbarzadeh, A.; Rezaei-Sadabady, R.; Davaran, S.; Joo, S. W.; Zarghami, N.; Hanifehpour, Y.; Samiei, M.; Kouhi, M.; Nejati-Koshki, K. Liposome: Classification, Preparation, and Applications. *Nanoscale Res. Lett.* **2013**, *8* (1), 102. https://doi.org/10.1186/1556-276X-8-102.

Chapter 2

Synthesis of hybrid systems by the functionalization of inorganic nanostructures

2.1 Introduction

Every year, increasing numbers of publications describe the design of new systems for X-Ray PDT. In order to achieve a synergistic effect able to induce an enhancement of $^1O_2$ and ROS according to the phenomenon discussed in the *chapter 1.4.4*, a nano system composed by a porphyrin and AuNPs needs to observe the following requirements: (1) a covalent interaction between the porphyrin and AuNPs using a linker of an opportune length, (2) water solubility and (3) an effective intracellular delivery. The size of AuNPs needs to be of 20/40 nm in order to be delivered and, at the same time, to better absorb the radiation (as is furtherly explained in *Chapter 2.2.2*). The first of these requirements arose from different studies that demonstrated that AuNP complexes generally quench the $^1O_2$ production of nearby chromophores. However, many papers reported that it is possible to obtain an enhanced PDT effect under laser irradiation at a fixed distance and position of the PS on AuNPs (see *chapter 2.2.3*). To allow this conjugation, was decided to use thiolated linkers due to the strong affinity between Gold and sulphur. The second point underline the importance of the water solubility of the nano system that can be achieved by using water soluble AuNPs or even improved introducing water soluble chains on the PS as reported in *figure 2.1*.

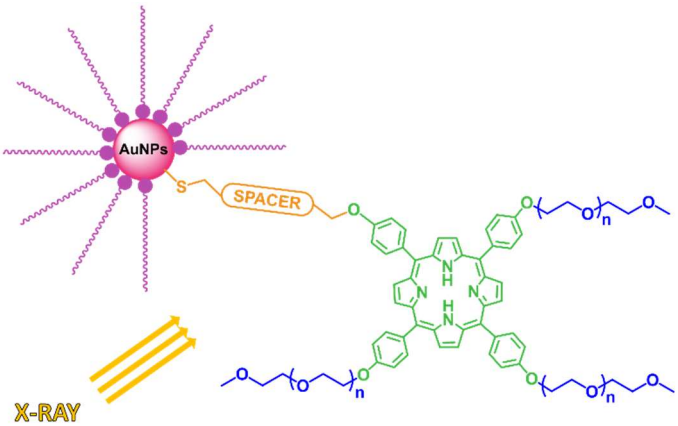

Figure 2.1: Schematic illustration of the water soluble hybrid nano system.

The last requirement involves the importance of a delivery system of PS@AuNPs that guarantee its cellular uptake. Cellular uptake is one of the most important processes regulating the biological activity of molecules, and it is determined by the

interactions between the molecule and the plasma membrane. To increase the AuNPs uptake, Chithrani et al.[1] reported that liposomes can be used as a "Trojan Horse" to overcome the energetically unfavourable endocytotic uptake of small AuNPs and to deliver large numbers of the AuNPs into cells. Based on the experimental data for smaller NPs, a 1000-fold increase in the uptake of small AuNPs can be achieved by their incorporation on and into the surface of liposomes. In order to enhance the cellular uptake of PS-Au nano system, the development and application of various nanomaterial designs for gene and drug delivery is currently one of the key focus areas in nanomedicine. Liposomes have been well established as an effective drug delivery system, due to the simplicity of their preparation and unique characteristics. Once liposomes reach the cells, in order to allow the release of their content, several strategies have been previously explored to destabilize the bilayer using physiological and external stimuli. The triggering approaches previously reported include changes in pH (typical in cancer)[2], externally delivered heat, for example *via* alternating magnetic field or infrared light[3], enzymes[4] and non-thermal effects caused by light irradiation[5]. These approaches have certain limitations, in particular triggering of light-sensitive liposomes by visible light is limited by its relatively shallow (few mm) penetration of light into biological tissues. As a result of this modest penetration depth, visible light cannot activate photosensitizers (PS) located deeply in the body and generate sufficient amount of $^1O_2$ or ROS to release the liposome cargo required for the therapeutic effects. With its excellent tissue penetration depth, X-ray radiation employed for PS-AuNPs enhanced PDT, can also be used as liposome triggering offering an alternative approach via standard radiotherapy approaches (radiation therapy). Deng et al.[6] designed an X-ray- triggerable liposomes by encapsulating a photosensitizer, Verteporfin (VP), and gold nanoparticles in a liposomal bilayer of 100/200 nm. They demonstrated that when these liposomes were exposed to X-rays, enhanced $^1O_2$ generation from VP was achieved due to the interaction between gold nanoparticles with incident X-rays (*figure 2.2*).

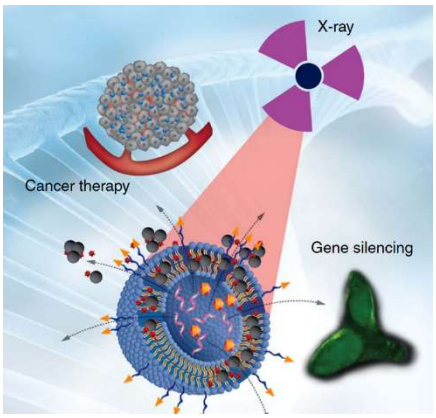

Figure 2.2: Targeted liposomes loaded with VP and gold in a lipid bilayer would release gene or drug under X-ray radiation. Reproduced from ref.[6]

2.2 Results and Discussion

On the basis of the above results reported in the literature, in this chapter of my PhD thesis is discussed the synthesis, characterization and the optical properties of water soluble hybrid nano systems composed by 20/40 nm AuNPs and porphyrins covalently bound through linkers of tuned length. As will be discussed in *chapter 2.2.3*, Kaneara et al.[7] demonstrated that the di, tri and tetra alkylated porphyrins can bring to face-to-face coordination of the porphyrin on AuNPs surface and consequently to the quenching of $^1O_2$ production. Mono alkylated porphyrin with the linkers were synthesized and their conjugation reaction on citrate AuNPs was investigated. After the synthetic steps, the ability of the nano system to produce $^1O_2$ under visible light and X-ray radiation was investigated. In *scheme 2.1* are shown two main strategies followed for the conjugation reaction between porphyrin and AuNPs: (a) synthesis of AuNPs with thiolated ligand bearing a leaving group and subsequent coupling reaction with the porphyrin and (b) functionalization of porphyrin with thiol-ending chains and subsequent binding on AuNPs surface.

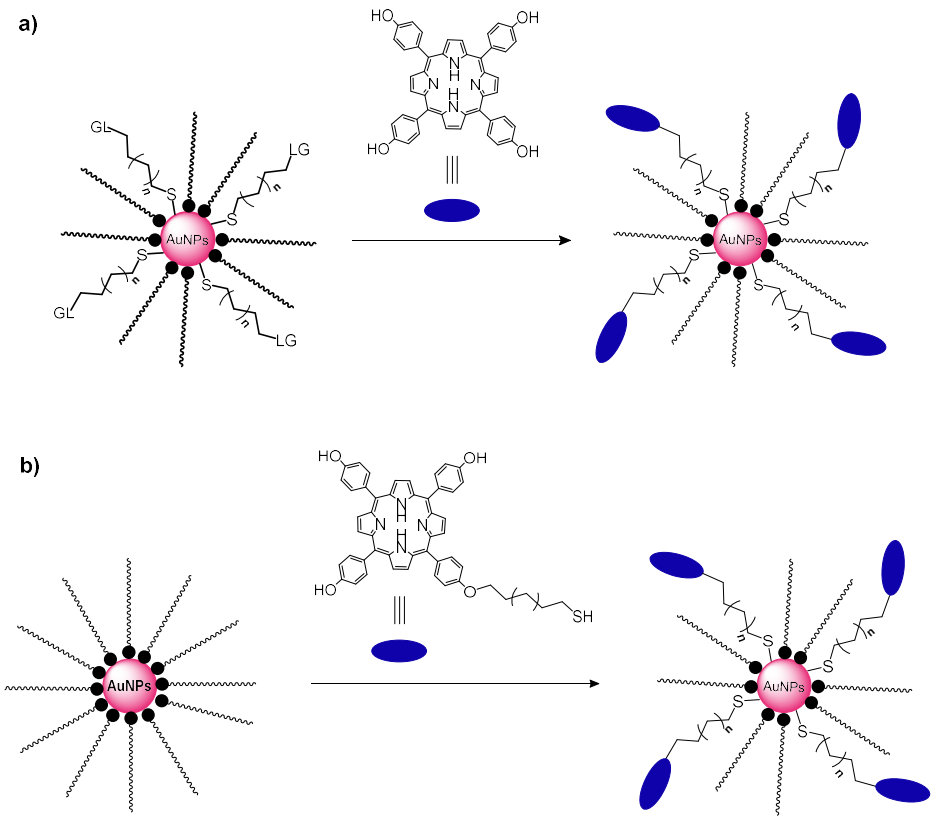

Scheme 2.1: : Strategies to conjugate porphyrins on gold nanoparticles surface. LG: leaving group.

2.2.1 Synthesis of thiol ending linkers

In this chapter the preparation of water soluble and hydrophobic thiol ending linkers with tuned length chain is presented in order to achieve a retained or even an enhancement in the production of cytotoxic species, in particular $^1O_2$ by the PS when covalently connected on gold nanoparticles surface.

To achieve an higher $^1O_2$ production of the nano system, the linkers must present some features and in their design all these features have to be taken in consideration. Linkers employed as connectors between PS and AuNPs were designed with two different functional groups: one being a leaving group (LG) to create a covalent bond with 5,10,15,20-Tetrakis(4-hydroxyphenyl)-21H,23H-porphine (THPP) that is characterized by four phenolic functionalities that can act as nucleophile.

On the other ending part of the linker, a thiol moiety (SH) is necessary to obtain a strong and covalent interaction on gold nanoparticles surface due to the strong affinity between gold and sulfur (*figure 2.3*).

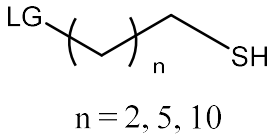

Figure 2.3: Generic structure of hydrophobic thiol ending linker.

Furthermore, another important feature is the length of the linker, i.e. the distance between THPP and AuNPs that plays an important role in the $^1O_2$ production. Indeed, if the PS is located too close to the AuNP surface, an energy transfer can take place from the PS to the AuNP leading to a quenching of the $^1O_2$ while PS placed between about 5-30 nm from the AuNP surface can instead lead to an enhancement effect. Another important point to take into account is the reaction of thiol ending group on the leaving group at the other end, that can bring to a product of polymerization. In order to avoid this side reaction, in some cases different sulfur protecting groups (acetal, trityl, *tert*-butyldimethylsilane or even the dimer of the linker as "self-protecting" group) were exploited and different sulfur protected linkers were synthesized.

In this work are presented also some hydrophilic thiol ending linkers with different lengths which generic structure is shown in *figure 2.4* in order to combine all the features described above with an improvement of the water solubility of the conjugates (PS@AuNPs) for their biological application in PDT. In particular a PEG chain with 17 repeating units was chosen following a previous work on the solubilization of THPP in water.

Figure 2.4: Generic structure of water soluble thiol ending linker. LG = leaving group

Lipoic acid, an organo-sulfide compound derived from caprylic acid (octanoic acid), is a small amphiphilic molecule composed by eight carbon atoms, a carboxylic group and two of sulfur in a disulfide bond. In nature it exists in two forms, as a cyclic disulfide (oxidized form) or as an open chain with the name of dihydrolipoic acid, showing two sulfhydryl groups in the C_6 and C_8 position. The carbon atom in C_6 is chiral and the molecule exists as two enantiomers (R)-(+)-lipoic acid (RLA) and (S)-(-)-lipoic acid (SLA).[8] In medicine it is widely used thanks to its excellent antioxidant properties and it participates in various mechanisms such as the reduction of glutathione (GSH) and ascorbic acid. There are many advantages to using lipoic acid as a linker. First of all, it has the ability to form two S-Au bonds with the surface of AuNPs and, secondly, thanks to the presence of the carboxyl group, NPs can be connected to other molecules through coupling reactions, for example with a phenolic hydroxy group of porphyrin THPP or to a primary amine to generate a more hydrophilic derivative t. In this case, a terminal PEG-NH_2 molecule was used as the primary amine, to increase the solubility of lipoic acid in water (solubility = 0.24 g / L).

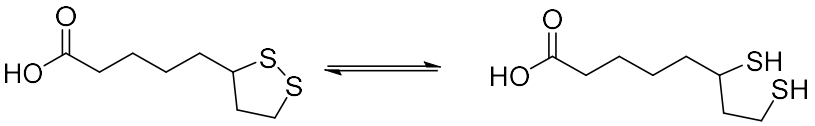

Figure 2.5: Two forms of lipoic acid, oxidized form (left), reduced form (right).

Furthermore, since the two forms of lipoic acid are easily interconvertible by redox reactions (*figure 2.5*), through the disulfide bridge, the oxidized form acts as a protecting group avoiding the reaction of sulfur atoms on the carboxylic moiety and the disulfide bond can be easily broken and the linker can act as a chelating ligand on gold nanoparticles surface. Lipoic acid can be directly bound on PS's functionalities through esterification reactions or bound to other glycolic chains to create a longer spacer as is shown in *Scheme 2.2* for the synthesis of the linker **(5)**.

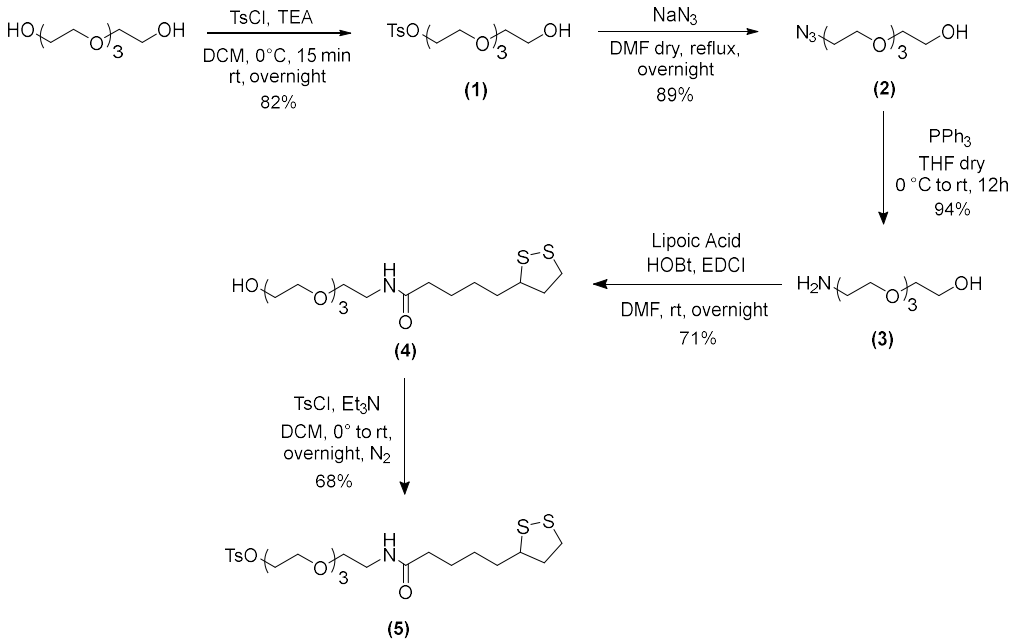

Scheme 2.2: Scheme of reaction to obtain the thiol ending linker **5**.

Scheme 2.2 shows the reaction steps to obtain compound **5**, the LA-PEG4-OTs linker, consisting of a disulfide ring, derived from lipoic acid (LA) connected through an amide bond to a PEG_4 chain ending with a tosylate group. Unfortunately, Linker **5** presented problems of instability over time. In fact, the newly product was isolated as a pale yellow oil but, once the solvent was completely removed, it changed consistency and became insoluble in any other solvents (including DCM, DMF, DMSO and water). For this reason, was very difficult use it after characterization in the following steps, unless used immediately after preparation. In order to improve the yield of the product, a different synthetic strategy was also explored (*Scheme 2.3*), but compound **4a** revealed to be even less stable than compound **5** and it was not possible to isolate the final compound.

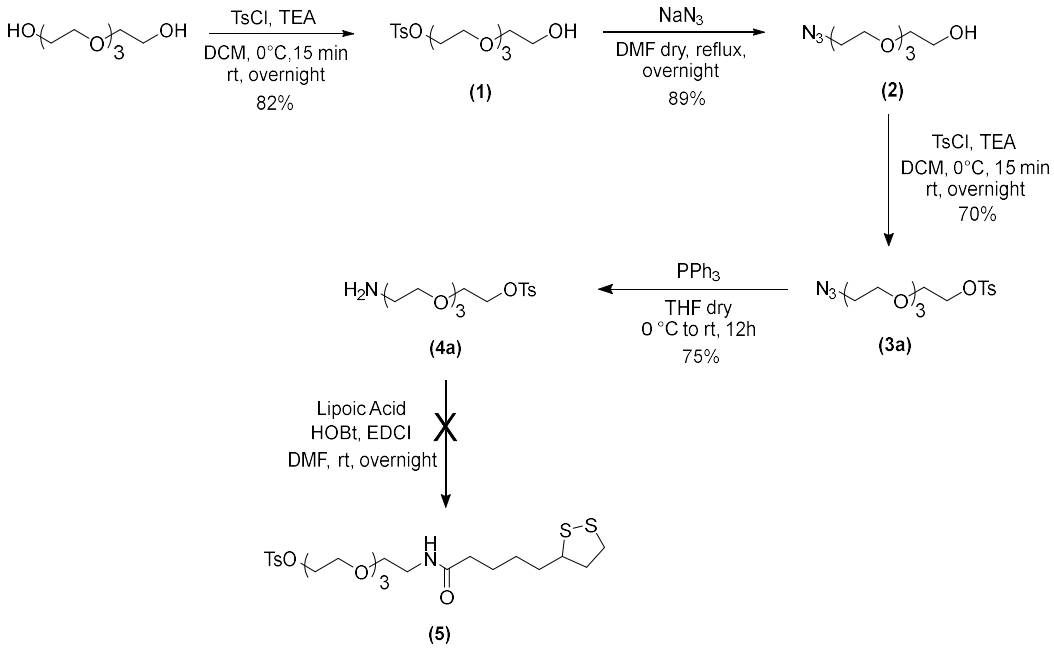

Scheme 2.3: Alternative synthetic strategy to obtain the thiol ending linker **5**.

Following the first synthetic approach (*scheme 2.2*), compound **4** was obtained in 71% yield, using 1-ethyl-3- (3-dimethylaminopropyl) carbodiimide (EDC) as coupling reagent and 4-Dimethylaminopyridine (DMAP) as catalyst in dichloromethane (DCM). In order to obtain the best reaction conditions, different molar ratios, solvents and coupling reagents were tested (*table 2.1*).

Entry	*Coupling reagents*	*Base*	*Solvent*	LA/HO-PEG$_4$-NH$_2$	*Yield*
1	EDC, HOBt	Et_3N	DCM	1:1.5	55%
2	DCC	DMAP	DCM	1:1	31%
3	EDC	DMAP	DCM	1:1	54%
4	EDC	DMAP	DMF	1.5:1	16%
5	EDC, HOBt	Et_3N	DMF	1.5:1	38%
6	EDC	DMAP	DCM	1:1	71%

Table 2.1: optimization of the conditions for the synthesis of linker **4**: EDC = 1-ethyl-3- (3-dimethylaminopropyl) carbodiimide; HOBt = hydroxybenzotriazole; Et_3N = triethylamine; DCC = dicyclohexylcarbodiimide; DMAP = 4-dimethylaminopyridine; DCM = dichloromethane; DMF = N, N-dimethylformamide.

In *table 2.1* are shown all the conditions in which the reaction was performed to optimize the yield. The reactions carried out in DCM gave the best results, however, as regards the coupling reagents, EDC demonstrated to be the most advantageous. The use of DCC has led to a lower yield, probably due to the partial loss of product during filtration with celite in ethyl acetate, used to remove the reaction by-product (DCU). The addition of HOBt, on the other hand, did not lead to any improvement in the yield. In *entry 6* the yield was improved to 71% modifying the product purification procedure. Indeed, the modest yields were probably due to the fact that the product, being partially soluble in water, was partly lost in the aqueous phase during the extraction. Therefore, the reaction mixture was directly loaded on the chromatographic column and the product obtained by separation was analyzed by ^{1}H NMR spectroscopy.

In the ^{1}H NMR spectrum of lipoic acid in $CDCl_3$ (*figure 2.6, a*), being 5- membered ring and containing the S-S bond, originates a series of diagnostic multiplets at δ = 3.6-3.5 ppm, integrating for one proton, two overlapped signals integrating for two protons at δ = 3.1-3.08 ppm, and other two multiplets at δ = 2.5-2.4 ppm and at δ = 2.0-1.8 ppm, integrating for one proton, respectively. These four multiplets are due to the four diasterotopic protons of the dithiolane ring. In the ^{1}H NMR spectrum of **4** in $CDCl_3$ (*figure 2.6, b*), are presents the diagnostic multiplets of lipoic acid described above and at δ = 2.19 ppm a small up-field shifted (~ 0.2 ppm) triplet signal, integrating for two protons, which is ascribed to the protons in α position to the carboxyl group of the amide and this signal is diagnostic for the success of the coupling reaction. At δ = 3.86 – 3.38 ppm is also present a large multiplet, integrating for 17 H, ascribed to the 16 aliphatic protons of the tetra polyethylene glycol chain and to the proton of the five-members ring of the lipoic acid.

Then, the final compound **5** was obtained with a 68% yield through a tosylation reaction of **4** with tosylchloride in presence of Et_3N. It was characterized through NMR spectroscopy. ^{1}H NMR spectrum of linker **5** (*figure 2.6, c)* presents, at δ = 7.81 ppm and 7.36 ppm, two duplets integrating for two protons, respectively, and a singlet at δ = 2.45 ppm, integrating for three protons, due to aromatic and aliphatic hydrogen of the OTs group. In the spectrum is found also a down-shifted triplet at δ = 4.15 ppm, integrating for two protons, that is related to the methylene protons in α to the -OTs group.

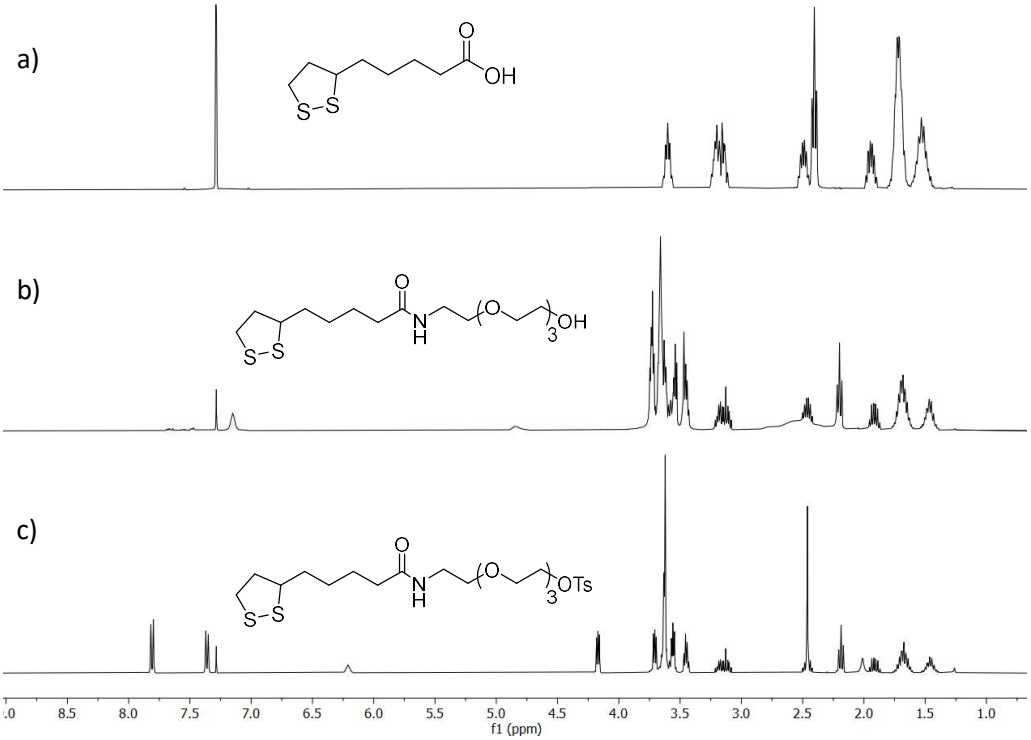

Figure 2.6: ^{1}H NMR spectrum (400 MHz, $CDCl_3$) of lipoic acid (top), thiol ending linker **4** (middle) and thiol ending linker **5** (bottom).

The synthesis of linker **7** was designed as quicker alternative to compound **5** to improve the stability and the solubility in organic solvents of the linker. Linker **7** presents an alkyl chain with 6 carbon atoms instead of a PEG chain.

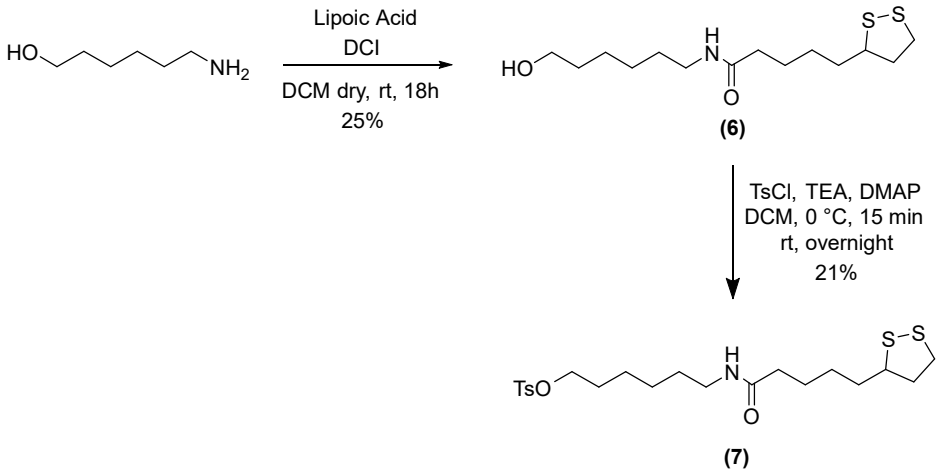

Scheme 2.4: Synthetic strategy to obtain the thiol ending linker **7**.

Compound **6** was obtained with a yield of 25% and the final product **7** was obtained from the reaction of **6** with tosyl chloride (TsCl) in the presence of Et_3N and DMAP. After a chromatographic purification step, the linker **7** was obtained in a yield of 21% as reported in the *Scheme 2.4* and it was characterized by NMR spectroscopy and ESI-MS spectrometry. The ^1H NMR spectrum of the isolated compound, recorded in DMSO-d_6 (*figure 2.6*), shows two doublets at δ = 7.84 ppm and 7.37 ppm, integrating for two protons, respectively, and a singlet at δ = 2.50 ppm, integrating for three protons, related to the OTs group. The triplet at δ = 4.04 ppm, integrating for two protons, is related to the methylene protons in α to the -OTs group, whereas the methylene protons in α to amide nitrogen gave rise to a multiplet at δ = 2.80-2.78 ppm. As in the ^1H NMR spectrum of linker **5** are present the diagnostic signals of lipoic acid and an up-shifter triplet at δ = 2.18 ppm. The ESI(+)-MS analysis with flow injection detected a peak with retention time of 1.23 min, having in the related mass spectrum an isotopic distribution of m/z = 459.9 $[M+H]^+$ that is in agreement with the structure.

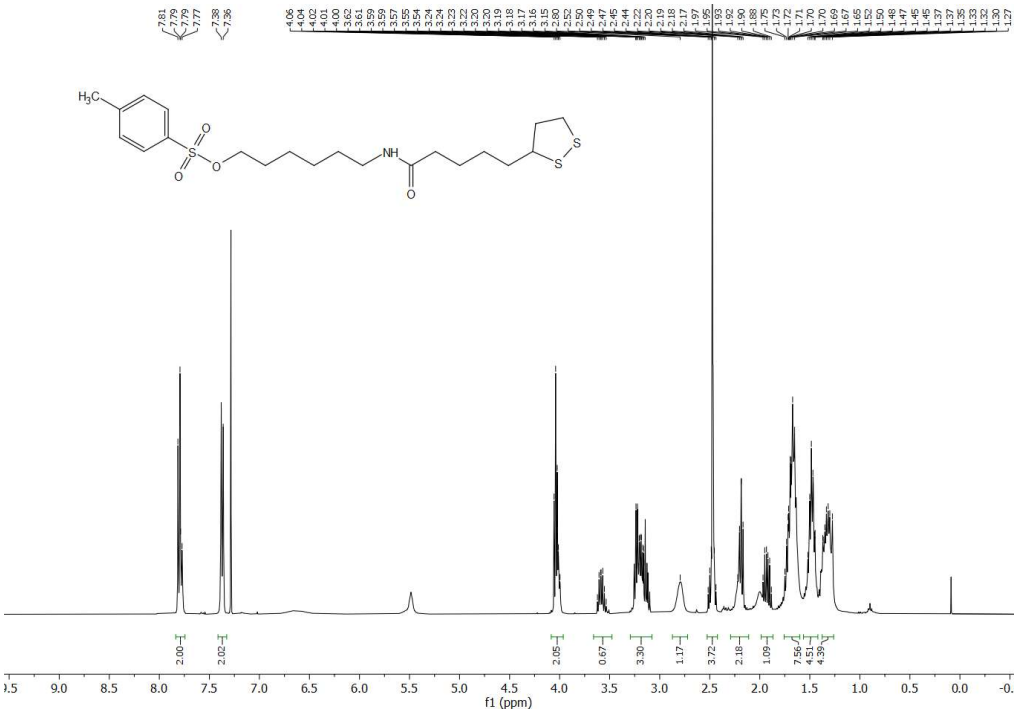

Figure 2.6: ^{1}H NMR spectrum (400 MHz, $CDCl_3$) of linker **7**.

Due to the high instability of linkers **5** and **7**, another long chain linker having protected thiol group (with a 11 carbon chain) was designed and synthesized. As primary reaction (*scheme 2.5*) the functional thiol-anchoring group was protected as a thioester group (-$SCOCH_3$) to avoid oxidation and to prevent unwanted side-reactions. Bromo-undecen-1-ene was treated with thioacetic acid and AIBN (radical initiator) in toluene at 90°C for 2 hours and after a column chromatography, linker **8** was obtain in a yield of 78% and confirmed by NMR.

Scheme 2.5: Synthetic approach for linker **8**.

^{1}H NMR in $CDCl_3$ (*figure 2.7*) presents a singlet signal at δ = 2.33 ppm, integrating for three, ascribed to the methyl protons of the thioester and a triplet at δ = 3.42 ppm relative to the protons of methylene in α-position respect to the thioester

functional group. Although the spectrum reveals the presence in low percentage of the starting where the diagnostic signals of the protons of the alkene are present in the zone between δ = 4.00 and 6.00 ppm, the linker was used for the next step of reaction without any further purification.

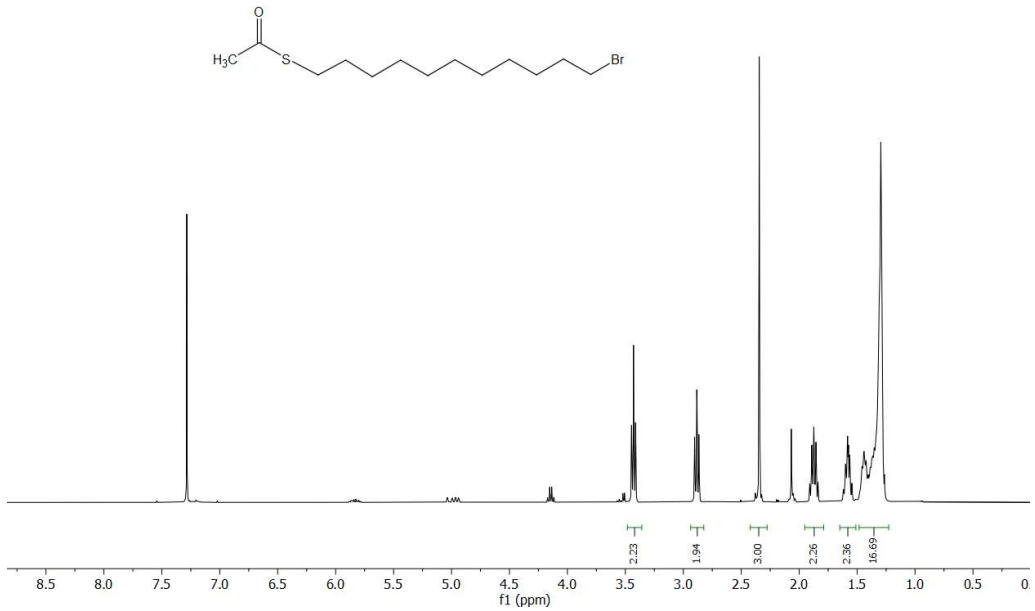

Figure 2.

Figure 2.7: ^{1}H NMR spectrum (400 MHz, $CDCl_3$) of thiol protected linker **8**.

As described previously, since the length of the linker is one of the most important factor to evaluate that can regulate the amount of singlet oxygen produced, shorter linkers have been synthesized to figure out how the spacing between the surface of NPs and the PS can affect the emission properties of the PS itself. Linkers with three carbon atoms were chosen because in the literature they appear to be the most promising linkers to give a positive effect on the ability of the photosensitizer to produce an enhanced singlet oxygen when exposed under a laser light irradiation. Unfortunately, linkers with short chains (and consequently with low molecular weights) present several difficulties in the synthesis, purification and handling steps since they are extremely volatile. In the *Scheme 2.6* is shown the retrosynthetic analysis starting from low cost alkenes to obtain a C_3 thiol ending linkers with different leaving groups on the other extremity of the chain. In details, since the synthesis of linker **12** showed several problems in the isolation due to the

easily volatilization of the final product and of the intermediate **11**, an alternative synthetic approach was designed to obtain linker **12a** that presents a tosyl group instead of the chloride in order to increase the molecular weight of the whole linker and to allow its isolation.

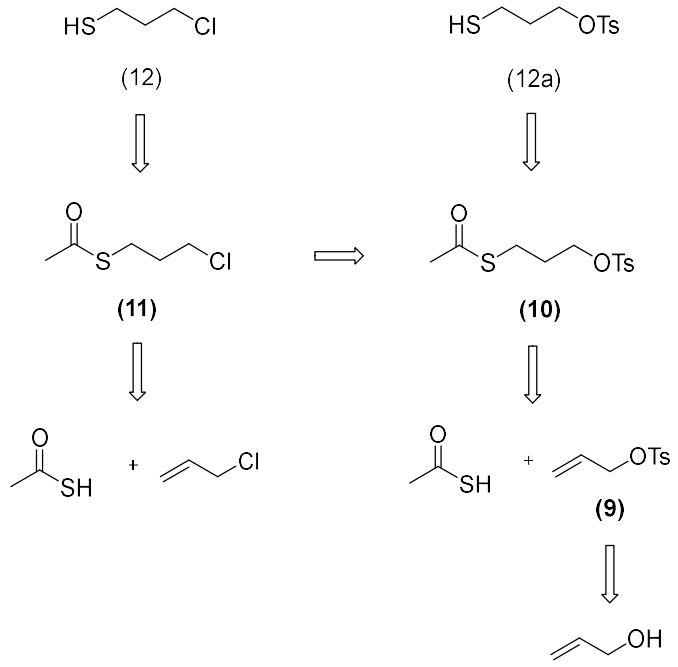

Scheme 2.6: retrosynthetic approaches for linker **12** and **12a**.

In the *Scheme 2.7* are reported all the synthetic steps with relatives conditions to obtain linkers **12** and **12a**.

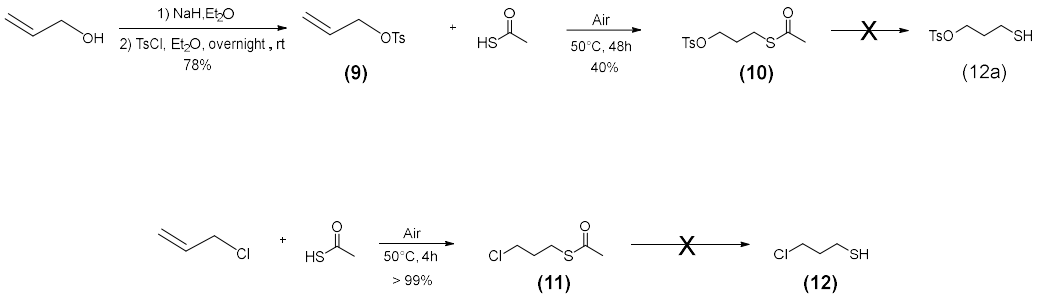

Scheme 2.7: Synthetic approaches for linker **12** and **12a**.

Intermediate **10** was synthesized as a precursor of the linker **12a**. Starting from allyl alcohol, it was first reacted with NaH and then with tosyl chloride. To check the progress of the reaction, a portion of the crude was withdrawn and analyzed by GC-MS and TLC thin layer chromatography (TLC) and after a chromatographic purification step, the product was obtained as a colorless oil in a yield of 85% and characterized by NMR in $CDCl_3$ and GC-MS.

The derivatives **10** and **11** were obtained through the same radical reaction with thioacetic acid of compound **9** and allyl chloride, respectively. In general, air was blown into a vial containing thioacetic acid by heating to 45 °C. This step serves to form the radical on the sulfur by thermal initiation. Then, **9** and allyl chloride were added inside the respective vial and the reactions were left for four hours under heating between 40 and 60 ° C. Product **10** and **11** were obtained as a red oils in 40% and quantitative yield respectively and both characterized by NMR in $CDCl_3$. In *figure 2.8* are showed the ^1H NMR of intermediate **10** (bottom) **11** (top) and the successful of the reaction is ascribed to the signals at δ = 2.32 and 2.35 ppm respectively, where a singlet, which integrates for three protons, indicates the presence of the methyl group of the thioacetate moiety. Only **11**, due to its easy volatilization, was characterized also with GC-MS (with DB-5 column and a flow at 1 mL/min) that revealed a relative peak at m / z of 152.05 (100). The peak at M + 2 that is one third of the peak M is proof of obtaining the desired product because it is due to the isotopic abundance of ^{37}Cl compared to ^{35}Cl (25:75%).

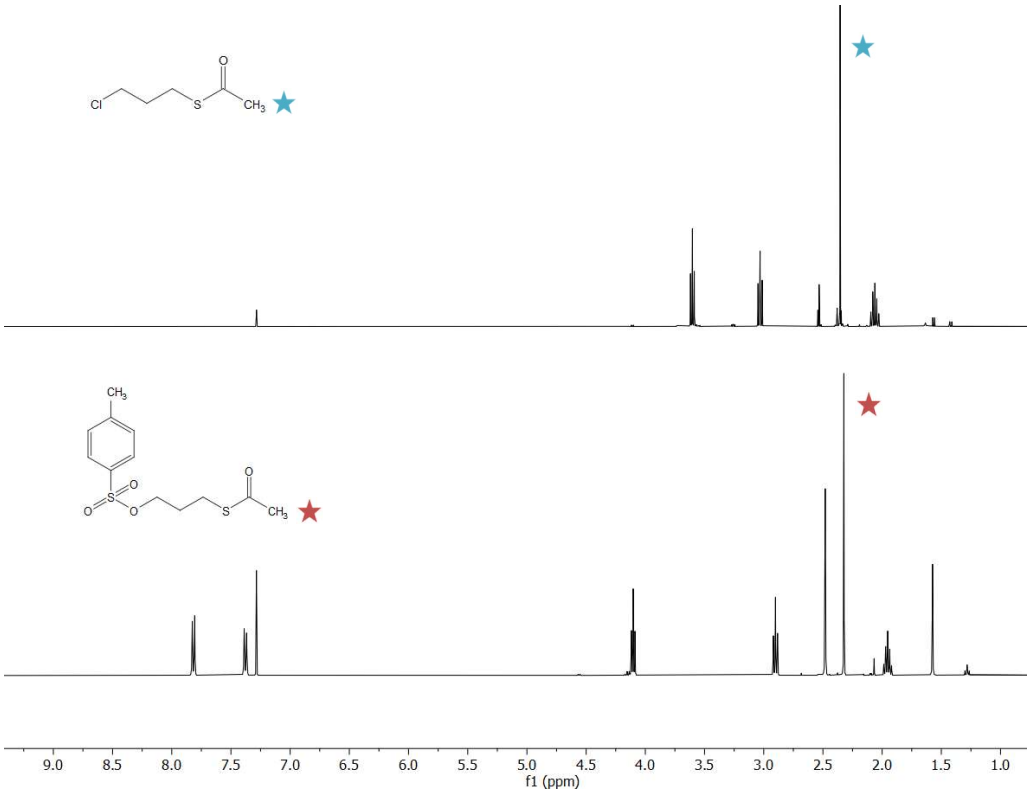

Figure 2.8: ^{1}H NMR spectrum (400 MHz, $CDCl_3$) of intermediate **10** and **11**.

Unfortunately, the deprotection steps of thioacetate moiety of linkers **10** and **11** to give the linkers **12a** and **12** respectively through a reaction of hydrolysis, did not work. Deprotection steps of linkers **10** and **11** was unexpectedly complex since both in a basic and acidic environment, were obtained oligomerization products due to the fact that the compounds **12** and **12a** have a nucleophile at one end and a good leaving group at the other end. Since this result was predictable in the basic environment, it was decided to study the reaction in an acid environment. In particular, for linker **11** were carried out some tests by varying the temperature and the reaction time to minimize the formation of oligomers. It has been observed that, even if in low yield, the desired product was obtained selectively in the first 30 minutes of reaction by heating at 65 ° C. It was also observed that the reaction did not take place at room temperature. Product **12** was obtained starting from a solution of the compound **11** in methanol, to which was added a solution of concentrated hydrochloric acid in catalytic amount. The reaction mixture was then heated at 65 ° C for 30 minutes, then neutralized with a 1M NaOH solution,

providing the product with a low yield (12%). The presence of product **12** was determined only by GC-MS without any isolation since in the meantime the commercially available compound was bought. The spectrum (GC-MS) of the product revealed a relative peak at m/z of 110 (100) $[MH]^+$ (100). To avoid the problem of oligomerization of the linker, thiol functionality of linker **12** was protected with different protecting groups and some preliminary reactions with phenol (a substrate similar to the phenolic group of porphyrin) were conducted to test their feasibility and orthogonality (*Scheme 2.8*). Exploiting the acetyl group as a protecting group, also linker **11** can be used in the reaction with phenol.

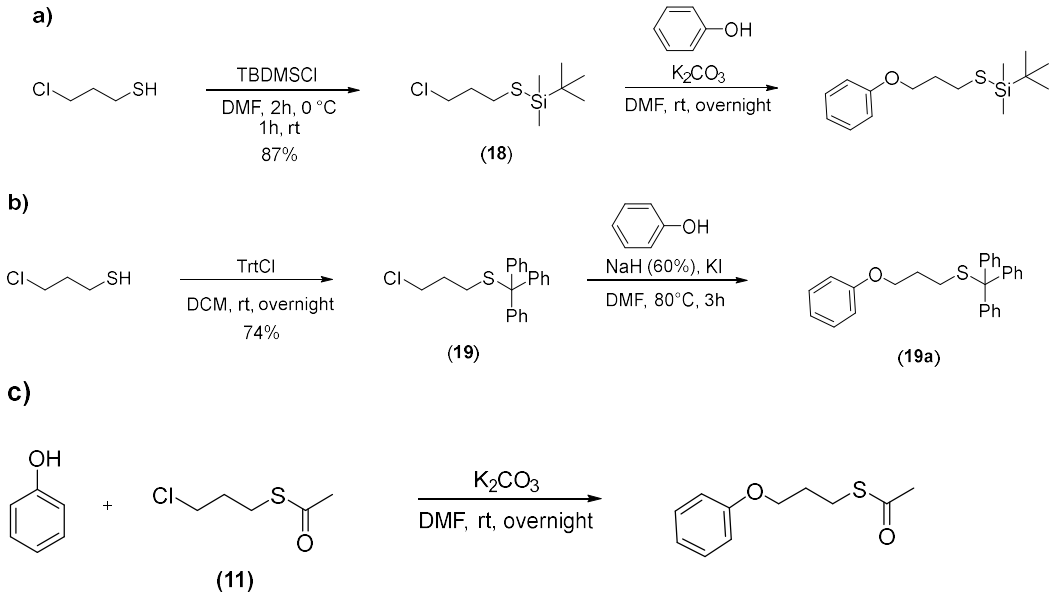

Scheme 2.8: Synthetic approaches for linker **18** and **19.** Reaction of **11**, **18** and **19** with phenol model reaction.

1-Chloropropanethiol was treated with tert-Butyldimethylsilyl chloride and with Trityl chloride to obtain protected thiol linkers **18** in a yield of 87% and **19** in a yield of 74% respectively and both the linkers were characterized by NMR. Linker **18** was characterized also by GC-MS and the chromatogram presents a peak with a m/z = 168 that corresponds to the fragments of the linker without the tert-butyl functional group $[C_5H_{12}ClSSi]^+$. Then, all the thiol protected linkers were tested in the reaction with phenol as model as showed in the *scheme 2.8*: the second step of reactions a), b) and c) was performed using one equivalent of potassium carbonate in dimethylformamide at room temperature overnight and monitored

by TLC and GC-MS. In this conditions, in c) was observed a collateral reaction in which occurred preferably the attack of phenol on the carboxylic group of thioester, confirmed by GC-MS that revealed a peak m/z of 136 (100). In a), GC-MS revealed a peak with m/z of 152 (100), 208 (9), that correspond to the mass of a by-product given by the attack of phenol directly on the silicon atom. In b), the reaction was performed with one equivalent of sodium hydride (60% in paraffin oil) as base in dimethylformamide at room temperature overnight. Since this reaction gave a low conversion of the reagents into the product at room temperature, potassium iodide was added in a catalytic amount and the reaction mixture was heated at 80 °C. After 3h hours, the conversion of the reagents was completed, as evidenced examining the crude by TLC and ^{1}H NMR. The trityl removal step was performed in two different conditions: firstly, **19a** was treated with triethylsilane followed by trifluoroacetic acid in DCM for 3h at room temperature but the reaction did not work. Then, **19a** was dissolved in a mixture of chloroform and methanol (65:35) in presence of $AgNO_3$ and pyridine. After 1h at room temperature, the precipitate was filtrated, washed with methanol and then redispersed into chloroform and 38% (v/v) of concentrated HCl. The reaction was stirred for 2h and, after the filtration of AgCl formed, the solvent was evaporated under reduced pressure and the product was obtain in a yield of 91%. In *figure 2.9* is reported the ^{1}H NMR of the linker **19** (*top*), the crude of the explorative reaction between **19** and phenol (*middle*) and the final deprotection step of sulphur from trityl (*bottom*). The successful of the reaction between phenol and linker **19** is confirmed by the triplet signal at δ = 3.94 ppm, integrating for two protons, that is down-shifted compared to the triplet of the reagent at δ = 3.48 ppm. The presence of phenolic moiety is confirmed by the multiples at δ = 7.01-6.81 ppm and δ = 7.53-7.19 ppm, integrating for 15 protons, ascribed to the four aromatic protons. In the bottom spectrum, the successful of the deprotection step is confirmed by the lack of the 15 aromatics protons of the trityl group in the zone between δ = 7.60-7.10 ppm and by the presence of a triplet signal at δ = 1.42 ppm, integrating for one proton, ascribed to the proton of free sulphur atom.

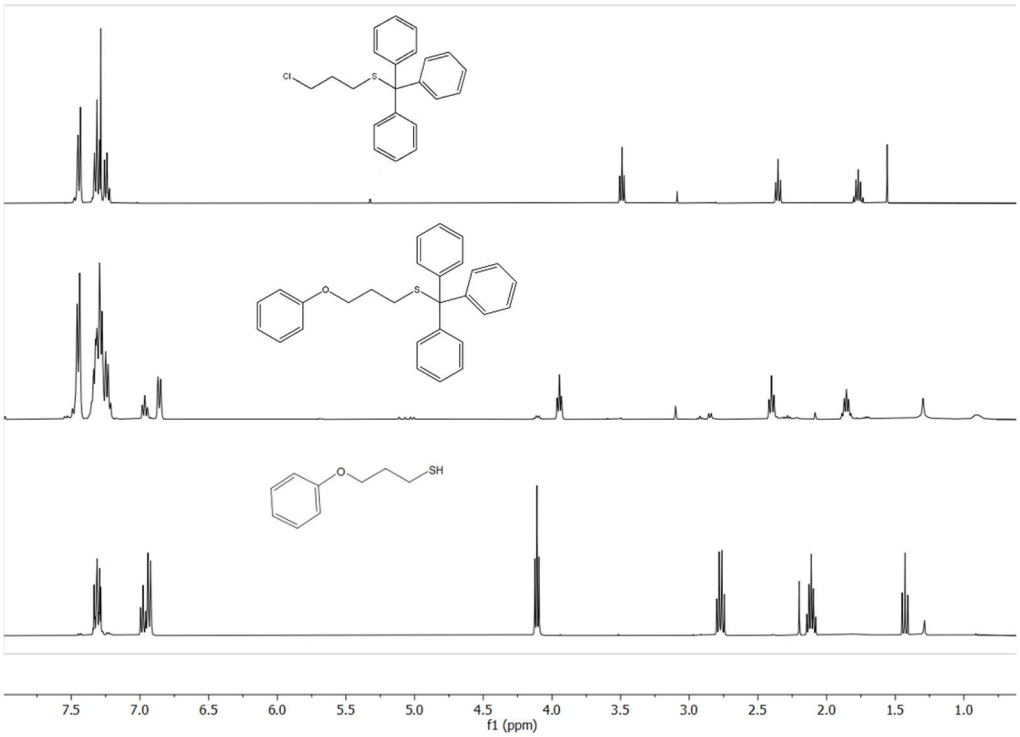

Figure 2.9: ^{1}H NMR spectrum (400 MHz, $CDCl_3$) of linker **19** (*top*) compared with the product spectra of its reaction with phenol (*middle*) and of the final deprotection step of trityl group (*bottom*) .

As different short linker, Cysteine, an amino acid that presents a thiol functional group, was employed and opportunely functionalized. Like other amino acids, cysteine exists as a zwitterion at neutral pH as shown in *figure 2.10* and, since it has two nucleophilic sites and an electrophilic one, it can bring to products of self-reaction. Due to this reactivity problem, in some cases a derivative of cysteine was used, L-cysteine methyl ester that is a compound salified with HCl and consequently more soluble in polar solvents than L-cysteine. For this reasons its use should prevent some collateral reactions of oligomerization and improve the water solubility of PS@AuNPs conjugates.

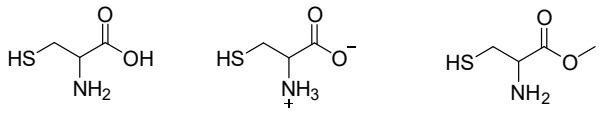

L-cysteine Zwiterrionic form L- cysteine methyl ester

Figure 2.10: Chemical structure of L-cysteine, its zwitterionic form and L- cysteine methyl ester.

L-cysteine methyl ester, having a primary amine group, was used to conjugate the tetra-(4-carboxypheny)porphyrin (TCPP), bearing four carboxylic acid functionalities in the para position of the phenyl rings on gold nanoparticles.
Also in this case the reactivity of L-cysteine was previously tested in a model reaction, i.e. with benzoic acid that is a substrate similar to the functionalities of the porphyrin, to optimize the attack of the amine group rather than of the thiol group. In *Scheme 2.9*, is reported the general reaction between L-cysteine methyl ester and benzoic acid with the different conditions tested.

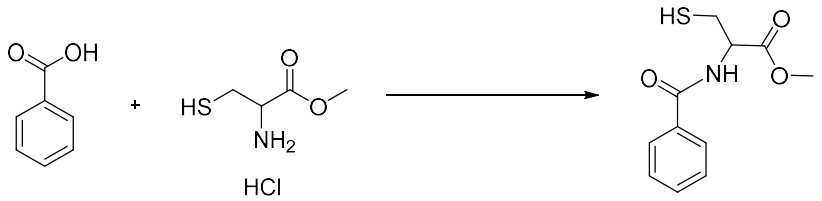

Entry	Conditions	Yield
1	DIPEA, EDC, DMAP DCM, 0 °C, 1h	Low conversion
2	EDC, Et_3N H_2O	No conversion
3	DIPEA, EDC, DMAP DCM, rt, overnight	60%

Scheme 2.9: Generic synthesis of L-cysteine methyl ester with benzoic acid with all the conditions tested.

In *entry 2* water was use to improve the solubility of cysteine in DCM but the reaction did not show any conversion of the reagents. In *entry 3*, the reaction was performed with DIPEA, EDC as coupling agents and DMAP in catalytic amount in dry dichloromethane at room temperature overnight to promote the attack of the amine group over the thiol group. After one hour, the reaction was quenched with a saturated aqueous solution of $NaHCO_3$ and the crude was purified on chromatographic column to obtain the product in a yield of 60%. The confirmation of the presence of free thiol functional group is given in the NMR spectrum (*figure 2.11*) where a triplet at δ = 1.43 ppm that integrates for one proton is ascribed to the proton of the thiol.

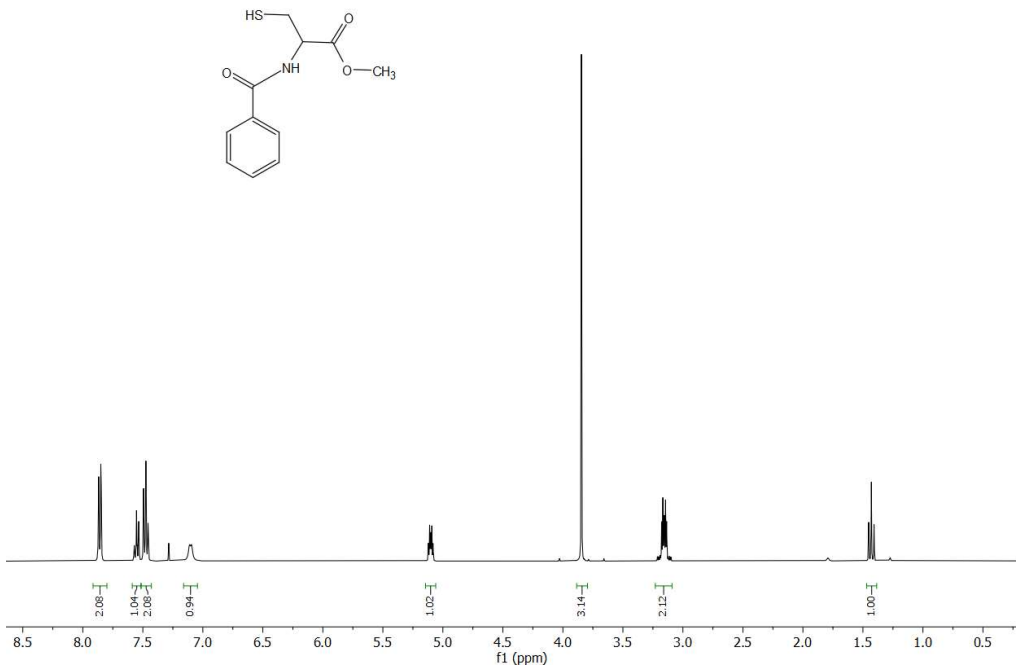

Figure 2.11: ^{1}H NMR spectrum (400 MHz, $CDCl_3$) of preliminary reaction of L-cysteine methyl ester with benzoic acid.

As described previously, another simple synthetic method to avoid the self-reaction of thiol moiety with the other end of the linker itself, is to exploit a dimerization reaction to create a sulfur-sulfur bridge as a self-protecting group and then an esterification reaction of the carboxylic group to prevent a collateral nucleophilic attack during the formation of the amidic bond with TCPP (*Scheme 2.10, b*). In order to avoid the second step of methylation, the same reaction was firstly performed on L-cysteine methyl ester (*scheme 2.10, a*) but it never brought to the dimerized product 16a.

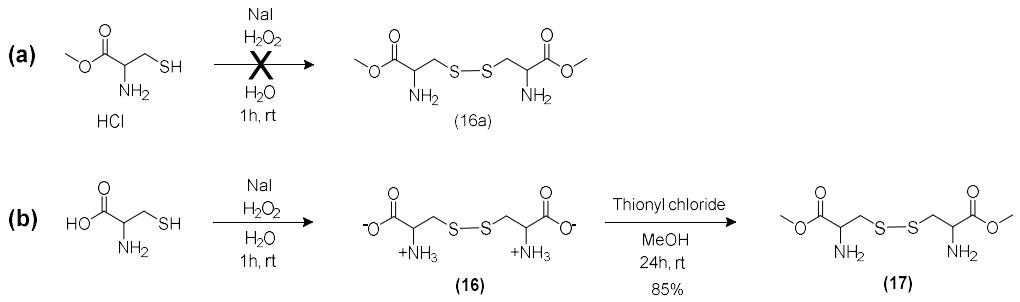

Scheme 2.10: Synthetic approach to protect the thiol group of cysteine.

For this reason, L-cysteine was treated with sodium iodide and hydrogen peroxide in water and stirred at room temperature for one hour to obtain, after filtration and washings with cold water, a solid white chuck (**16**) that since was insoluble in any solvent it was used without any characterization for the next step. **16** was then mixed with an excess of thionyl chloride and methanol for 24 hours at room temperature and the product **17** was obtained as a white solid in a yield of 85%.[9] The successful of the reaction was confirmed by NMR in methanol-d_4 and LC-MS (ESI). In *figure 2.12* ^{1}H NMR spectrum shows the lack of the triplet in the aliphatic zone between δ = 1.5 ppm and δ = 1.3 ppm usually ascribed at the proton of free thiol group while in the mass spectrum is present a relative peak at m/z = 269 (100) $[MH+1]^+$.

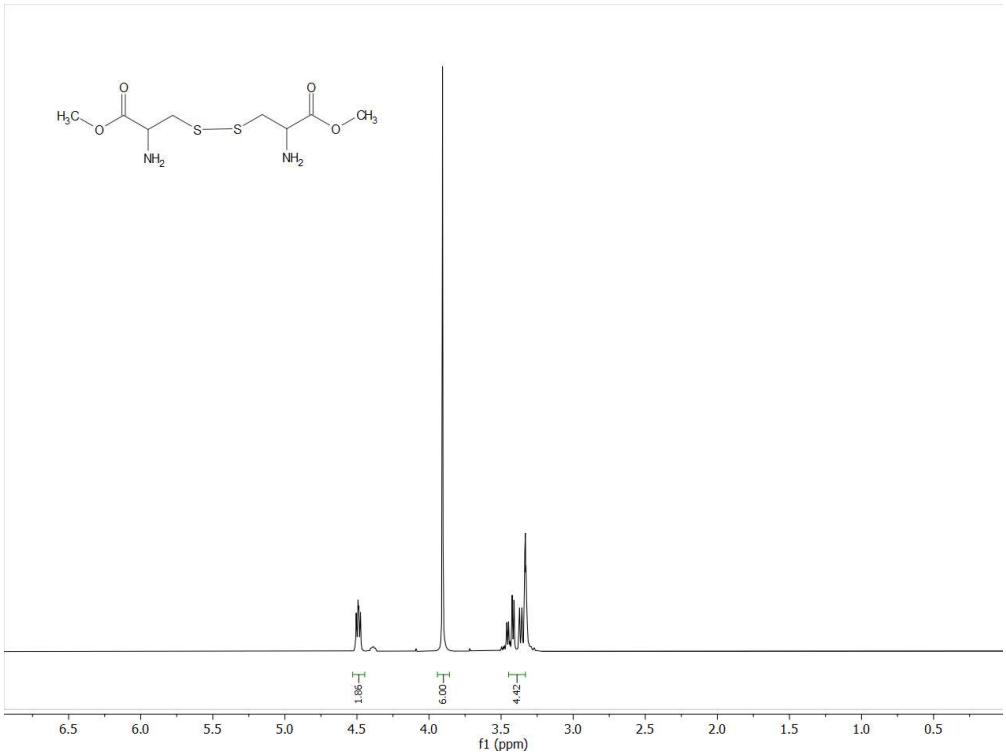

Figure 2.12: ^{1}H NMR spectrum (400 MHz, MeOD) of thiol protected linker **17**.

As briefly described in the introduction, in order to improve the water solubility of the conjugates, water soluble polymers like polyethylene glycol (PEG) and polyethylene imine (PEI) with low or high molecular weight could be exploited. These polymers are biologically inert, non-immunogenic, and hydrophilic molecules

and can be used in the conjugation reactions directly bound on the PS's functionalities or as stabilizing and capping agents onto gold nanoparticle surfaces. In details, in *figure 2.13* are shown the structures of the commercial available PEGs and PEI used and subsequently their functionalization. Tetra ethylene glycol has four repeating units with a hydroxyl group for each end. Since can be difficult to promote the functionalization of only one hydroxyl group, generally, poly ethylene glycol with higher molecular weights have a better water solubility on one hand but, on other hand, their purification and characterization is more complicated. Tetra ethylene glycol was opportunely functionalized (as shown in *scheme 2.2* on the synthesis of linker **5**) to alkylate THPP. Since this molecule wasn't enough hydrophilic to make the porphyrin water soluble, a longer poly ethylene glycol chain was chosen (HO-PEG_{750}-OMe). In particular, this molecule has only hydroxyl functional group on one end and a methoxy group on the other end in order to avoid the double attack of the porphyrin on the same chain.

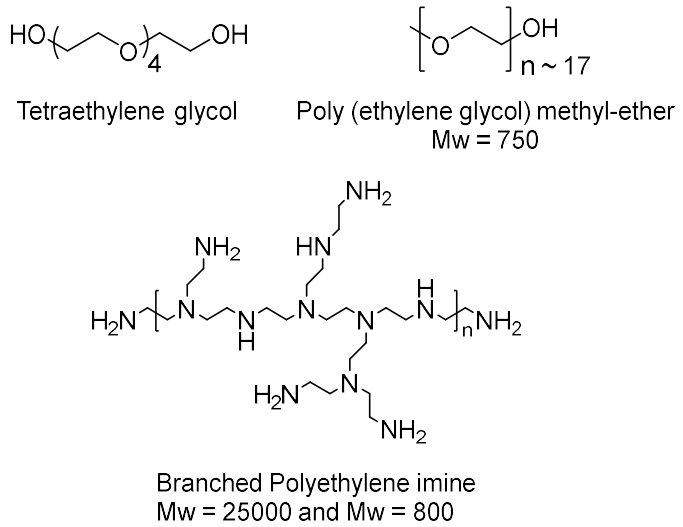

Figure 2.13: Water soluble polymers employed as linkers, capping and stabilizing agents.

Tosylation reaction of tetra ethylene glycol was already shown for the synthesis of linker **5**. The same reaction conditions were employed for the tosylation of the hydroxyl group of HO-PEG_{750}-OMe; it was reacted with tosyl chloride at room temperature overnight. After a chromatographic separation, the product **14** was obtain in a 85% yield and confirmed by NMR spectroscopy. Compounds **1** and **13**

(*scheme 2.11*) were used directly in the reaction with THPP to improve its water solubility or further functionalized to convert the tosyl group in a thiol group and bound it on gold nanoparticle's surface. In the *Schemes 2.11* the steps and the supposed intermediate of both the reactions are reported. **1** or **13** were mixed with two equivalent of thiourea in ethanol and after 24 hours at reflux a solution of sodium hydroxide in ethanol and water was added. After 3 hours at reflux the reaction was monitored by TLC and after a chromatographic separation, product **14** and **15** are obtained in a yield of 45% and 68% respectively and confirmed by NMR spectroscopy.

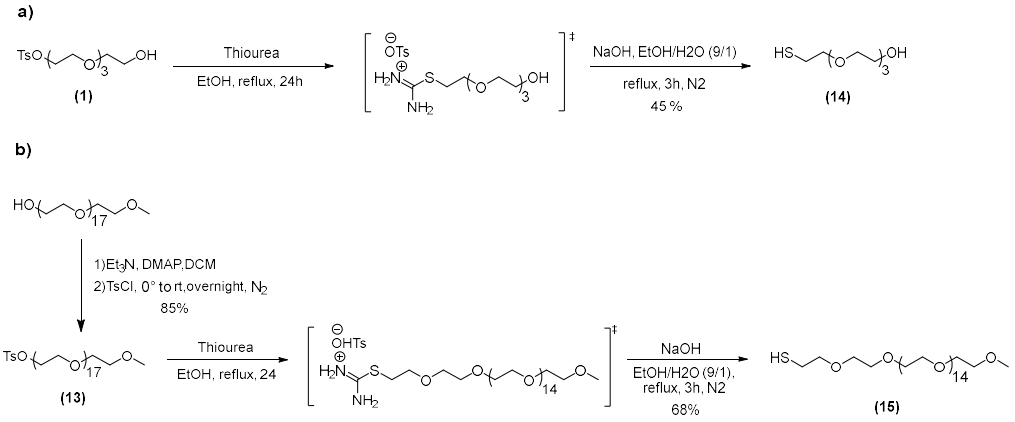

Scheme 2.11: Synthetic approach to create a thiol ending group on water soluble PEG chains.

^{1}H NMR spectra in $CDCl_3$ of **14** and **15** (*figure 2.14*) reveals for both the products a triplet signals at δ = 1.63 ppm each integrating for one proton that is ascribed to -SH group. Moreover, the lack of signals in the aromatic zone (~ 6 – 7 ppm) indicates the successful of the reaction with the complete removal of tosylate groups.

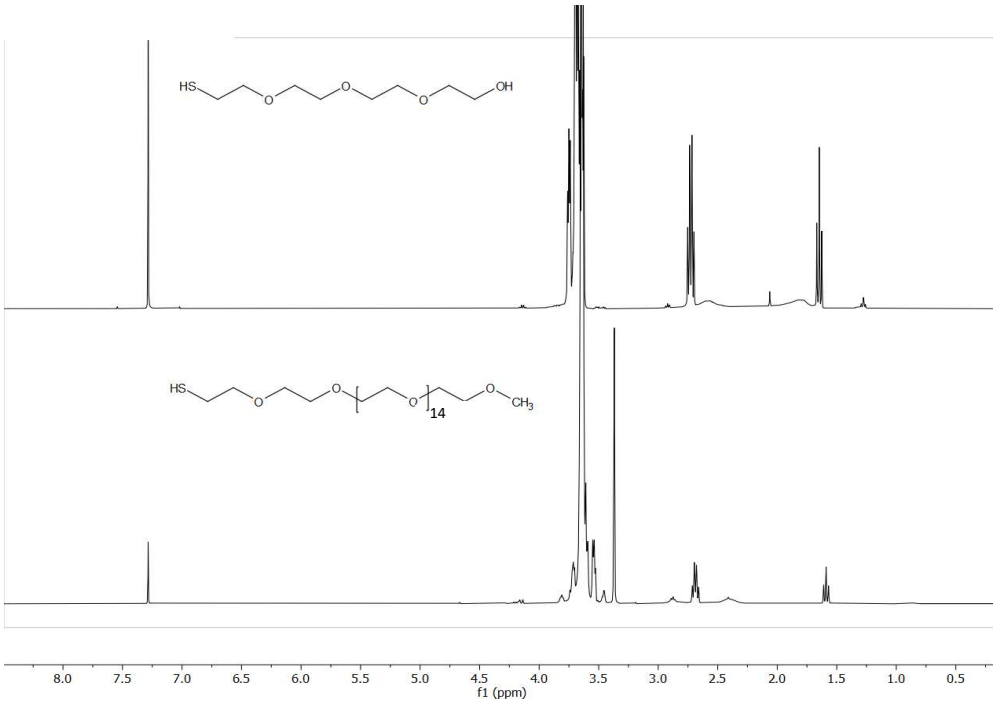

Figure 2.14: ^{1}H NMR spectrum (400 MHz, $CDCl_3$) of thiol PEG chains **14** and **15**.

2.2.2 Synthesis of functionalized AuNPs

Au nanoparticles are employed in this work in order to adsorb X-ray energy and to promote the formation of $^1O_2$ and ROS in the presence of a photosensitizer for the PDT treatment of deep seated cancer. Thus, it was selected to synthesize AuNPs with the following requirements: (1) water solubility, (2) stability in the application media without aggregation or agglomeration, (3) size between 20 and 40 manometers in order to guarantee an efficient absorption of radiation but also to be encapsulated into 100-200 nm liposomes and (4) be able to provide a function or specific interaction with the photosensitizer.[10] Gold nanoparticles is one of the most extensively studied engineered nanomaterials (ENMs). In general, the preparation of AuNPs involves a chemical reduction that is characterised by two steps[11]: (i) reduction of the gold precursor (usually tetrachloroauric(III) acid in its hydrate form) using reducing agents such us borohydrides, aminoboranes, formaldehyde, hydroxylamine, saturated and unsaturated alcohols, citric and oxalic acids, sugars, sulfites, carbon monoxide, hydrogen, acetylene and (ii) stabilization of the growing nanostructures by agents such as *trisodium citrate dihydrate*, *sulfur-based ligands* (in particular thiolates), phosphorus ligands, nitrogen-based ligands (including heterocycles), polymers and surfactant (in particular CTAB , cetyltrimethylammonium bromide). Being these two processes competitive in solution, the size and shape of the resulting AuNPs largely depend on the balance between several factors such as the strength of the reducing agent, the concentration of the precursor in solution, and the ability of the stabilising agent to passivate the gold surface of the growing structures.

To study the functionalization of AuNPs two different conjugation strategies were followed: (1) one step conjugation in which the thiol ending ligand is bound directly on the surface of AuNPs during the step of reduction with $NaBH_4$ and (2) two step conjugation in which sodium citrate is used as reducing and capping agent and then is exchanged with a thiol ending ligand. Regarding the first strategy, was used linker **5** synthesized previously where $HAuCl_4$ and compound **5** were first mixed in water to promote the formation of Au-LA-PEG_4-OTs precursors as shown in *scheme 2.12* (**5**@AuNPs).

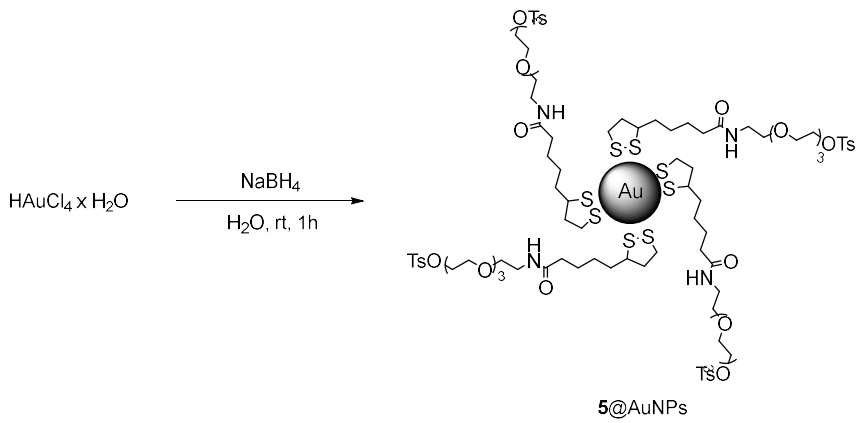

Scheme 2.12: Synthesis of AuNPs capped with linker **5**.

The addition of $NaBH_4$ initiates the reduction of Au ions and the rapid growth of Au-LA-PEG_4-OTs NPs and the formation of AuNPs is manifested by a rapid color change of the solution from yellow to red. By varying the mole ratio of Gold to linker it is possible to control the size of the resulting metal core. In a preliminary study the $HAuCl_4$/linker ratio of 4000:1 (AuNPs@**5**_ratio 1) and 600:1 (AuNPs@**5**_ratio 2) were tested and the AuNPs conjugated to compound **5** were subsequently characterized by UV-vis and dynamic light scattering (DLS) spectroscopy. In general, the stability of colloidal dispersions is mainly due to the effect of the high surface/volume ratio, steric or charge repulsions and attractive van der Waals interactions that can cause their aggregation. In our case, the linker used for the synthesis of NPs should be able to protect them from aggregation. In the case of 600:1 ratio, the presence of a precipitate occurred and the solution turned in a dark color over time, a signal of nanoparticles aggregation, while in the case of 4000:1 ratio the solution retained its red colour. Both the samples were characterized by UV-vis spectroscopy (*figure 2.15*) that shows the LSPR bands of the AuNPs conjugated to linker **5**. Sample with 4000:1 ratio showed a sharper band (black line) than 600:1 sample (red line) that presents a broad band confirming the aggregation of the nanoparticles.

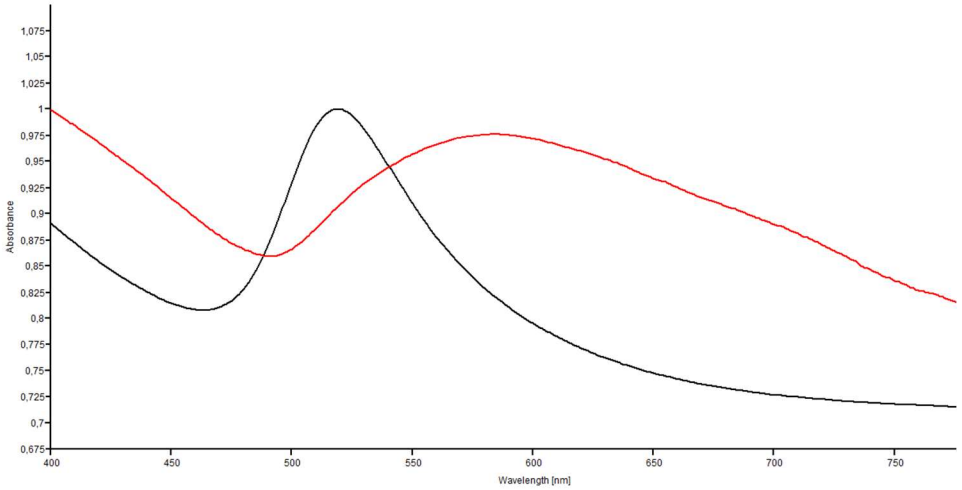

Figure 2.15: UV-Vis spectra of the samples with a ratio ligand:Au of 4000:1 (black line) and 600:1 (red line).

Only **5**@AuNPs (ratio 1) were then reacted with THPP for the further functionalization of **5**@AuNPs. This reaction was performed in DMF and H_2O with K_2CO_3 as base, stirred overnight at room temperature and centrifuged at 9000 rpm for 20 minutes. The precipitate, after washing with DMF, was examined by UV-VIS spectroscopy. The absence of the porphyrin Soret band showed that the S_N2 reaction did not occur.

A different synthetic strategy was shown by Wang and his colleagues[12] who prepared Au (or Ag) nanoparticles in a single process that required only heating an aqueous solution of the metal precursor and polyamine. The reducing capability of amines has been known for a long time, but the detailed mechanism of how Au and Ag nanoparticles are formed by amines has not yet been clarified. Although the amine-based synthesis of Au nanoparticles are usually accomplished at 60−100 °C, Kim et al.[13] demonstrated that PEI-capped Au nanoparticles can be formed at room temperature. The formation of metal nanoparticles occurs in a single process which involves heating an aqueous solution of metal precursor and polyamine without the addition of a reducing agent and a protective agent. Furthermore, the size and optical properties of PEI-stabilized Au nanoparticles can be controlled by changing the molar ratio of the reactants. Polyethyleneimine (PEI), a cationic polymer with abundant amino-group, displays attractive properties including fine robustness, excellent film-forming ability, good biocompatibility and high water solubility. As first attempt, the reaction between bPEI (Mw = 25 kDa) and $HAuCl_4$ was performed

at room temperature overnight as reported in *scheme 2.13*. Since the reaction was conducted with a strong excess of $HAuCl_4$, was decided to represent several AuNPs bound by one molecule of PEI. The reacted mixture was then centrifuged at 9000 rpm for 20 minutes and washed with copious amounts of deionized water. The PEI-capped Au nanoparticles thus obtained were redispersed in ethanol and characterized by UV-vis, DLS and Fourier transform infrared (FTIR) spectroscopy.

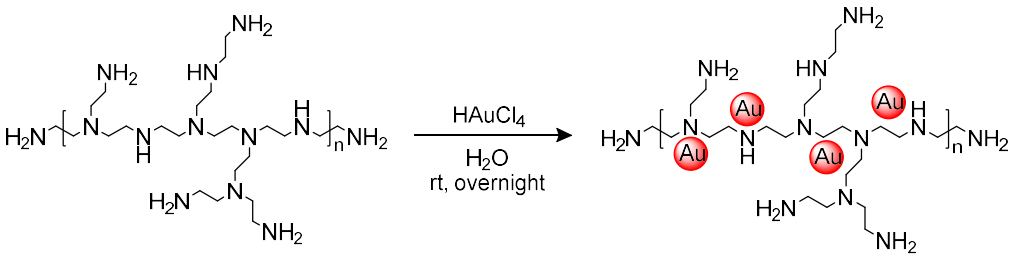

Scheme 2.13: Synthesis of AuNPs capped with branched PEI.

UV-vis spectra, recorded in water, shows a peak at 522 nm that confirms the formation of AuNPs by the presence of the characteristic LSPR band while the presence of bPEI is confirmed by the FTIR spectrum (*figure 2.16*) of the film obtained by evaporation of ethanol solution on the sample carrier of the instrument. The diameter of AuNPs was calculated to be 20 nm according to Haiss's theory.[14]

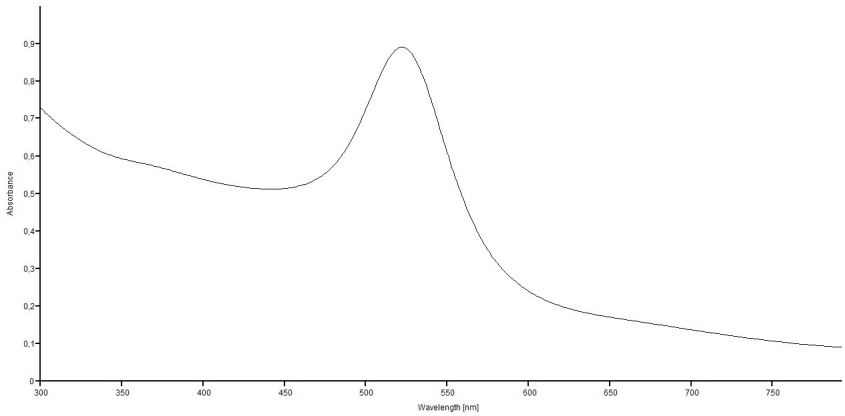

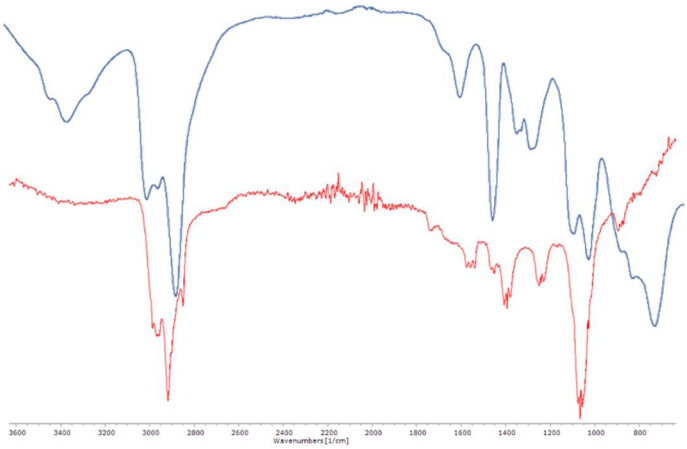

Figure 2.16: UV-vis (H_2O, *top*) and FTIR (*bottom*) of bPEI@AuNPs in ethanol (*blue line*) and bPEI (*red line*).

In the stacked IR spectra showed in *figure 2.16* is reported the IR pattern of bPEI@AuNPs (*blue line*) and bPEI (*red line*) where is clearly visible the stretching signal of C-H, N-H and NH_2 abundantly repeated in the scaffold of the polymer in the zone between 3100-2800 cm^{-1}. Then, the sample was centrifuged and redispersed in water to perform DLS and study the stability over time in this medium. DLS surprisingly showed an aggregation of the nanoparticles in water, presenting a peak at 407 nm and a polydispersity index (PDI) of 0.39. For this reason the protocol of reaction was changed mixing $HAuCl_4$ and bPEI in water at 80°C for 35 minutes in a ratio of 1:3.4 as shown in the *Scheme 2.14* in order to increase the stabilization of AuNPs by the polymer. In this case bPEI with different molecular weight were use: 25 kDa and 800 Da. The last one bPEI, smaller and easier to characterize, is supposed to be better encapsulated into liposomes. Following this procedure, only the solution with bPEI of 25 kDa turned to red after 35 minutes that is indicative for the reduction of gold and the formation of the nanoparticles while the solution with bPEI of 800 Da became blue with a precipitate, indicative for aggregation. The first mixture was thus centrifuged at 15,000 rpm for 20 minutes and after removal of the supernatant the resulting precipitate was washed with water twice, then redispersed into water and characterized by UV-vis, IR and DLS.

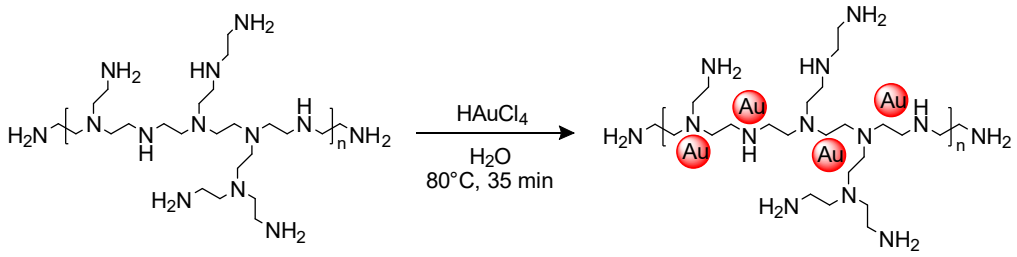

Scheme 2.14: Synthesis of AuNPs capped with branched PEI.

Although the UV-vis showed a peak at 528 nm that corresponds to 40 nm AuNPs without any band that indicates aggregations, the DLS showed an Z-average of 241 (d.nm) as showed in *figure 2.17*. This behavior is probably due to the presence of the polymer that creates aggregates in solution, shielding AuNPs and avoiding their agglomeration. Although the use of an high molecular weight polymer allowed an easy synthesis of the AuNPs, since it forms large aggregates, it is not suitable to be included into liposomes and thus into cells. In further developments will be explored the study on 800 Da bPEI as capping agents for AuNPs, maybe in combination with a reducing agent.

			Size (d.n...	% Intensity:	St Dev (d.n...
Z-Average (d.nm):	241,4	Peak 1:	157,9	89,6	30,29
PdI:	0,335	Peak 2:	23,84	10,4	3,764
Intercept:	0,930	Peak 3:	0,000	0,0	0,000

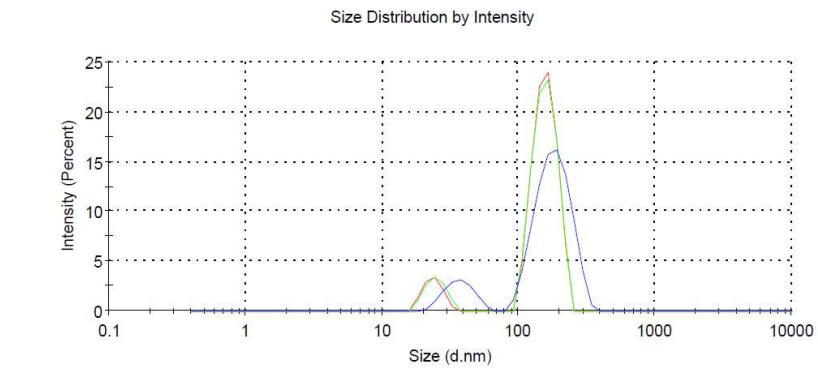

Figure 2.17: DLS of bPEI@AuNPs.

In order to create a water soluble nanosystem, preformed water soluble AuNPs were then conjugated to water soluble slightly lipophilic porphyrins. In the next pages is shown a method of gold nanoparticles functionalization that exploits the preformation of AuNPs stabilized by sodium citrate (NaCt) used both as reducing and capping agent. Then the exchange of -citrate with other ligands bearing thiol-group, whose synthesis is discussed in the *chapter 2.2.1*, is performed mixing the linker with the citrate@AuNPs. The exchange of the citrate with the ligands is due to the higher affinity of sulfur for gold than citrate creating covalently interaction rather than an electrostatic one. This methodology was published for the first time by Turkevich and his coworkers[15] and has become one of the mile-stones of AuNPs synthesis. Since then, the synthetic method has been modified and improved by Frens et al.[16] for a diverse area of interests including surface-induced catalytic activities, drug delivery in biological systems and nano-toxicology studies. Hydrophilic nanoparticles of gold used in these studies and reported in this chapter were prepared using Turkevich method.

In the last decades, many improvements have been accomplished regarding the synthetic methodologies used for the preparation of noble metal nanoparticles. These improvements were mainly aimed to have better control of crucial parameters responsible for the dimensionality of the nanoparticles (size and monodispersity). Among the various methods of synthesis available, the most common one involves the chemical reduction, in solution, of a metal salt precursor with a reducing agent. A stabilizing agent is then used to passivate the surface of the growing nanostructures and to prevent their aggregation once they have been formed. The nature of this stabilizing agent also determines the solubility properties of the resulting NPs. Turkevich method allows the synthesis of Gold nanoparticles stabilized by sodium citrate (NaCt) and their size can be tuned changing Gold/NaCt ratio (*figure 2.18*).

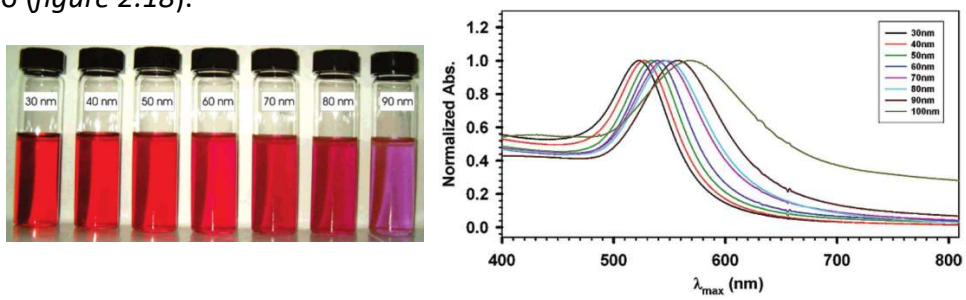

Figure 2.18: Colors of gold nanoparticles at different particle sizes. The size increases with the decreasing of Au/NaCt ratio. *Reproduced from ref.*[17] *Copyright © 2007 American Society.*

As Frens had already pointed out, the variation of the citrate concentration modifies the gold particle size within a large range. Kimling et al.[18] stated that the thermal citrate reduction shifts the SPR maximum from 517 to higher wavelengths and that this is indicative of larger particles while the citrate concentration is reduced. The explanation of this effect is the role that citrate plays in the passivation of formed gold particles. A high citrate concentration allows the stabilization of smaller particles, while for smaller concentrations, the coverage is incomplete and a coarsening process leads to the aggregation of larger entities while, in contrast, increasing the gold concentration above 0.8 mM leads to a destabilization of the smaller particles and results in a size increase. In order to obtain AuNPs with a size of 25-30 nm, a solution of the metal precursor ($HAuCl_4$) was dissolved in water and refluxed with sodium citrate (37 mM) in a ratio of 1:4 for 15 minutes (*scheme 2.15*). Sodium citrate causes the reduction of gold (III) to gold (0) and the mixture turned into deeply red solution.

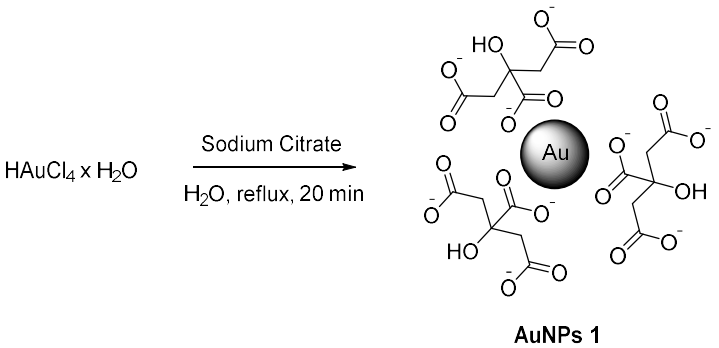

Scheme 2.15: Synthesis of citrate@AuNPs.

After cooling, an aliquot of this solution was characterized by UV-vis and dynamic light scattering (DLS) without any purification and directly used for exchange reactions. In *figure 2.19* was reported the UV-Vis spectra (*top*) in water with the SPR centered at 523 nm that confirm the obtainment of AuNPs of 25 nm, while the DLS (*middle*) characterization shows three peaks. The peaks reveal the presence of nanoparticles with an average size of 68 nm (80%) and a small peak of 3.7 nm (20%). This result shows that the Z-average is of 23 (d.nm) and that some nanoparticles form aggregates in solution. In *figure 2.19 (bottom)* was reported also the *TEM* image of AuNPs that revealed a size of 21 nm.

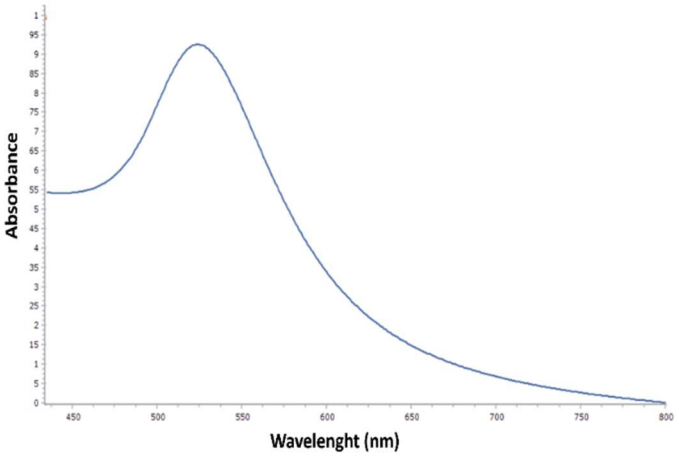

			Size (d.n...	% Intensity:	St Dev (d.n...
Z-Average (d.nm):	23,28	**Peak 1:**	68,19	80,0	44,83
PdI:	0,666	**Peak 2:**	3,702	20,0	1,543
Intercept:	0,827	**Peak 3:**	0,000	0,0	0,000

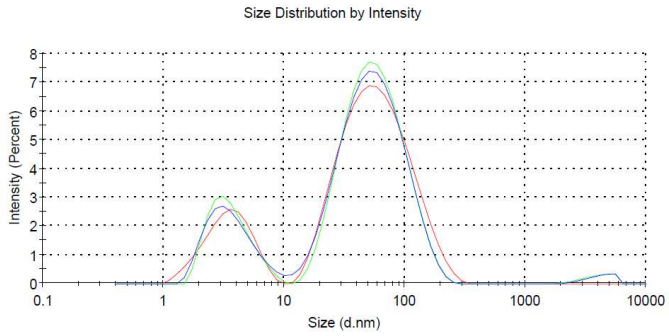

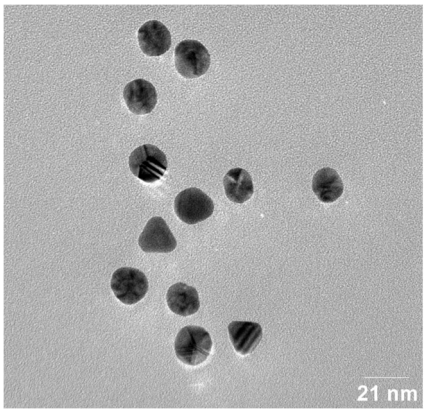

Figure 2.19: UV-Vis spectra (*top*), DLS spectra (*middle*) and TEM (*bottom*) of citrate@AuNPs.

2.2.2.1 Exchange of sodium citrate on AuNPs with thiolated linkers

After synthesis, usually, AuNPs present on their surface stabilizing (binding) or templating molecules which, often, do not have the necessary requisites to be used in biomedical applications. Consequently, modifications are often necessary because give rise to thermodynamically stable colloidal solutions and ensure high hydrophilicity. By exploiting the Au-S bond, it is possible to cover the metal surface with molecules soluble in an aqueous environment containing thiol functional groups which replace the original capping agent (NaCt). In numerous examples reported in the literature, the surface of the AuNPs is functionalized with polyethylene glycol thiolate (PEG-SH), which allows an increase of solubility in water and in biological systems.

Firstly, was tested the ability of some linkers to exchange sodium citrate on AuNPs surface and then their conjugation to porphyrins. As preliminary study was tested the efficiency of exchange with cysteine, 3-chloropropane thiol, lipoic acid and PEG_{750}-SH (linker **15**) and the stability of the obtained AuNPs over time was tested. As already mentioned above, cysteine is considered a suitable agent in the functionalization of gold nanoparticles, thanks to the presence of the functional group -SH. Furthermore, the presence of the -NH2 or -COOH groups could allow to conjugate the AuNPs-Cys(-NH_2) system with the PpIX (-COOH) through coupling reactions. After the preparation of the AuNPs-citrate, the L-cysteine molecules can be bound to the surface of the AuNP through a ligand exchange reaction. To study the effect of the different ratios between gold concentration/cysteine (C_{Au}/C_{Cys}) on the interparticle interactions observing the evolution of the surface plasmon

resonance band (SPR) of gold nanoparticles, 5 solutions at different concentrations of L-cysteine were prepared, mixed to five different aliquot of a gold nanoparticles solution (0.06 mM; 0.1 mM; 0.3 mM; 0.45 mM; 0.6 mM) and 5 UV-vis absorption measurements were performed (*figure 2.20, left*) which correspond to the C_{Au}/C_{cys} ratio of 5:1, 3:1, 1:1, 1:1.5, 1:2. As can be seen from the spectra, as the concentration of cysteine increases, there is a broadening of the absorption peak, which moves towards longer wavelengths and the color of the solution changes from reddish to blue. A possible model illustrating both the binding of cysteine to gold nanoparticles and the formation of particle aggregates is schematized in *figure 2.20 (right)*. After the adsorption of cysteine onto the gold nanoparticles, the cysteine molecule still have two functional groups free to form hydrogen bonds between particles. It was then confirmed by Mocanu et al.[19] that the addition of cysteine reduces the (negative) surface charge of the gold nanoparticles, thus increasing their tendency to aggregate.

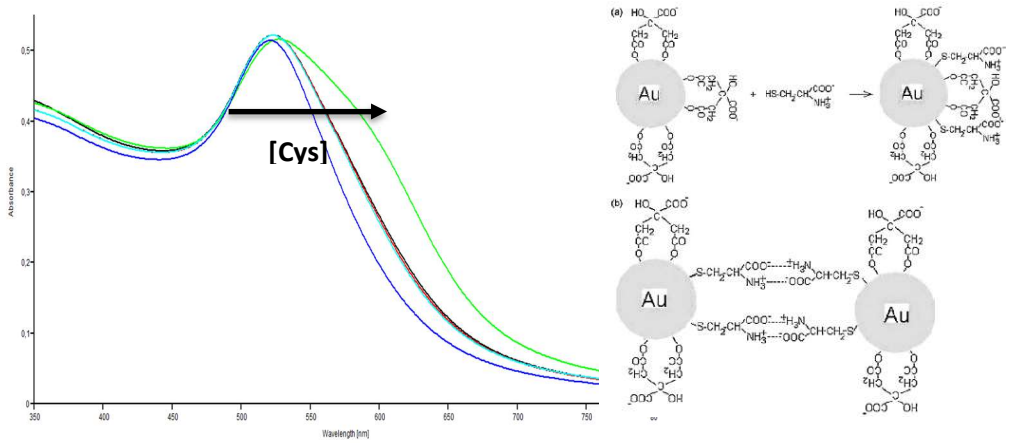

Figure 2.20: UV-vis spectra of cysteine@AuNPs that shows the aggregation and precipitation of AuNPs with the increase of cysteine (*left*). Mechanism of aggregation due to the formation of hydrogen bond of cysteine (*right*).[19]

In order to avoid the formation of hydrogen bonds between the COO^- of the cysteine with the NH_3^+ of a nearby cysteine, thus limiting the aggregation between particles, an attempt has been made to replace L-cysteine with L-cysteine methyl ester. Contrary to our expectations, we obtained greater aggregation with the formation of a precipitate.

We hypothesized that the lack of COO^- leads to the further decrease of the negative charge on the surface of the nanoparticles and this can lead to an increased tendency to aggregation. A further reason of this behavior was ascribed to the low

solubility in water of L-cysteine methyl ester that can cause the precipitation. As last attempt, was furtherly tested the conjugation of 5,10,15,20-Tetrakis-(4-carboxyphenyl)-porphyrin (TCPP) to cysteine@AuNPs previously synthesized using a C_{Au}/C_{cys} ratio of 1:1.5 (*scheme 2.16*). To conjugate the PS to the amino group of cysteine on the surface of the gold nanoparticles, the activation of the carboxylic group of the TCPP is required and EDC and N-hydroxysuccinimide (NHS) were used as coupling reagents.

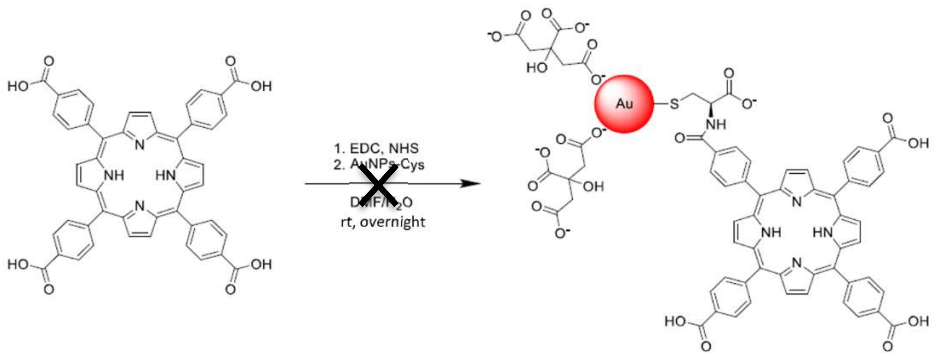

Scheme 2.16: Attempt to react TCPP and Cysteine@AuNPs.

The reaction mixture was then centrifuged at 9000 rpm for 20 minutes, the precipitated was washed with DMF twice, redispersed into DMSO and characterized by UV-vis spectroscopy. Unfortunately, the spectra of the precipitate didn't show the LSPR of AuNPs but only the pattern of TCPP and on the bottom of the flask was observed a gold film that can be ascribed to metallic gold that precipitates after the decomposition of AuNPs. Regarding the other linkers, it was easier to find the right amount of ligand avoiding aggregation. Briefly, an excess of the ligand is introduced in 3 mL of citrate@AuNPs (2.2 nM) (*scheme 2.17*), the reaction was stirred overnight at room temperature and then centrifuged twice through washings with water or methanol.

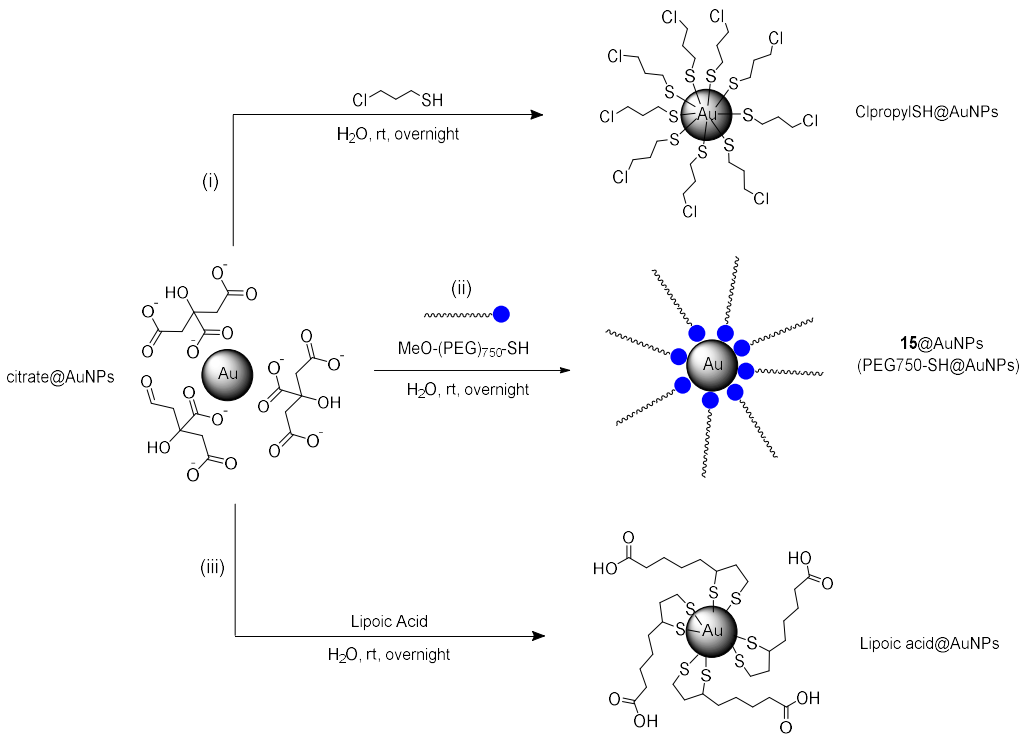

Scheme 2.17: Exchange of sodium citrate with (i) 3-chloro propane thiol, (ii) MeO-PEG_{750}-SH and (iii) lipoic acid.

All the AuNPs were characterized by UV-vis (*figure 2.21*) and presented a band at 527 nm that slight shifted to the red of ~ 4-5 nm compared with the band of citrate@AuNPs (blue dashed line). UV-vis spectra of PEG_{750}SH@AuNPs (green line) and Lipoicacid@AuNPs (red line) retained the shape of the band before exchange reaction while ClpropylSH@AuNPs band (black line) showed a decrease in absorbance and shoulder after 600 nm that indicates aggregation. In Scheme 2.17 the citrate ligands, still present after exchange, are omitted for clarity.

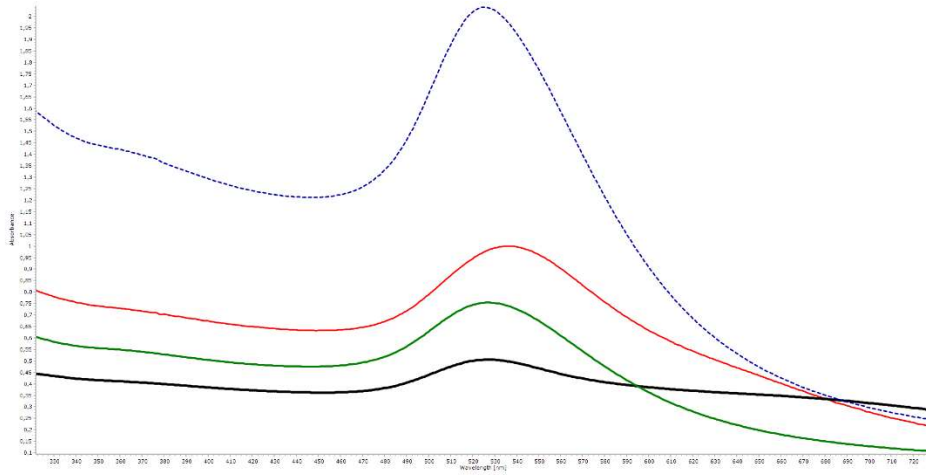

Figure 2.21: UV-vis spectra of ClpropylSH@AuNPs (**black line**), $PEG_{750}SH$@AuNPs (**green line**), Lipoicacid@AuNPs (**red line**) and citrate_AuNPs (**blue dashed line**).

ClpropylSH@AuNPs and LA@AuNPs were then reacted with a solution of THPP and several attempts were made to bind porphyrin on functionalized AuNPs by substitution reactions with the linkers (S_N2 and S_NAc respectively) but, in any case, the amount of bound porphyrin was negligible.

Then, $PEG_{750}SH$@AuNPs was prepared to be employed in a different approach, that is the conjugation of suitable functionalized porphyrins to AuNPs in which $PEG_{750}SH$ is able to increase the hydrophilicity of the entire conjugate. For this reason, in the next chapter is discussed the functionalization of THPP and PPIX with thiol ending linker (which synthesis is presented in *chapter 2.1*) to increase the amount of porphyrin on AuNPs surface. In the next chapter is also discussed the functionalization of porphyrins with water soluble molecules to allows their use in biological medium.

2.2.3 Synthesis of functionalized porphyrins

In both the strategies shown in *scheme 2.12*, the surface modification of AuNPs is performed via self-assembly of thiolated species on the surface of the gold core, that is possible due to the strong interaction between gold and sulfur. In literature is reported that the amount of porphyrin loaded on gold nanoparticles is higher following the strategy showed in *scheme 2.18* that involves the functionalization of the porphyrin with a thiol ending linker and a thiol water soluble chain (PEG) following the procedure of sodium citrate exchange.

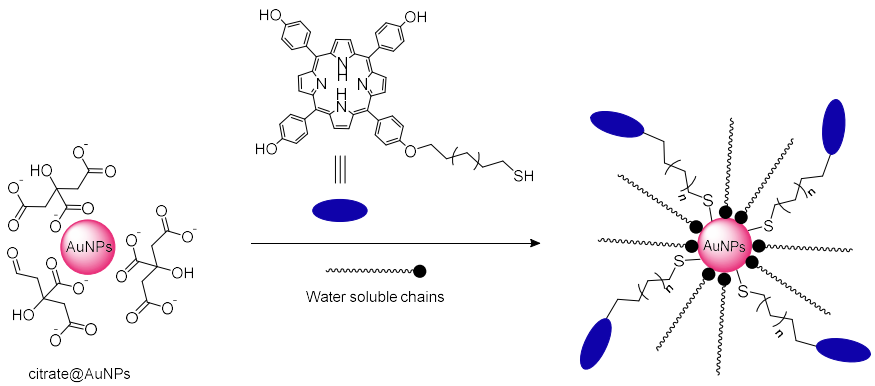

Scheme 2.18: Exchange of sodium citrate with THPP-SH and PEGSH.

The synthetical design of porphyrin was based on some literature studies: Calavia et al.[20] showed that a PS with short anchor chain (C3) was found to be more efficient in the production of $^1O_2$ than a PS with a longer chain (C11) when attached to the surface of the AuNPs. Moreover, Imahori et al.[21] showed that on Au surface the degree of the PS quenching may be affected by the orientation of the porphyrin planes depending on the number of the methylenes including the even-and-odd effect. Their study exhibited an even-and-odd dependence on the number of the methylene groups in the chain. The quantum yield of the nanosystem became saturated at around n = 6, and then decreased gradually (n = 7, 10, 11). The spectroscopic and electrochemical origin of this even-odd progression was explained as shown in *figure 2.22*. Assuming that the spacer with even number of the methylenes is oriented at an angle of 30° from the surface normal, the porphyrin plane is tilted heavily to the gold surface. On the other hand, the porphyrin is almost perpendicular to the gold surface when the spacer has the odd

number of the methylene. Based on these models, the structures of the monolayers can be understood on the chain's length of the linker but in the eventuality of long methylene spacers (n = 7, 10, 11), both odd and even, a folding of the chain can be observed forcing the porphyrin to stay perpendicularly close to Au surface.

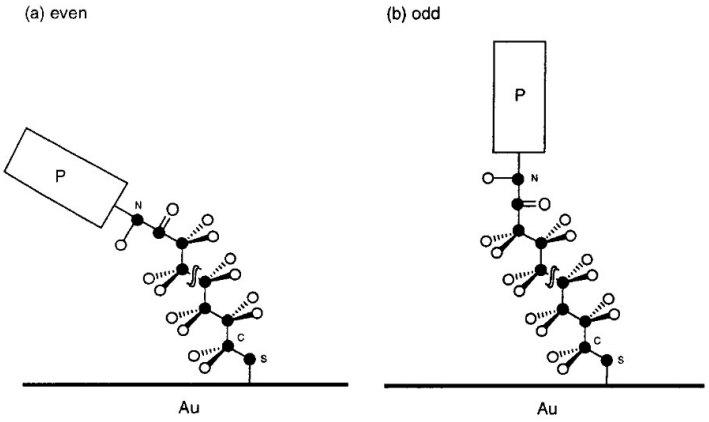

Figure 2.22: Proposed structures of porphyrin monolayer on Au for chains with (a) an even and (b) odd number of methylene groups.

Although the article did not consider the possible folding of the chain, it was decided to synthesize a mono-thiol ending functionalized porphyrins with chains of tuned odd length (C3, C7, C11) aiming to obtain an enhancement of $^1O_2$ when bound onto gold nanoparticles surface. Porphyrin mainly used was 5,10,15,20-Tetrakis(4-hydroxyphenyl)-21H,23H-porphine (THPP) due to its highly stability at light and air and ease of treatment rather than other porphyrins used like Protoporphyrin (PPIX), well known in literature as one of best porphyrin for the singlet oxygen production in PDT. In this chapter, is presented the functionalization of porphyrin with the linkers previously reported, its subsequent conjugation to gold nanoparticles (AuNPs) and the effect of the different conjugates on photophysical properties and $^1O_2$ production. Generally, porphyrins can be synthesized following mainly two methodologies: pre-functionalization and post-functionalization as shown in *figure 2.23.*

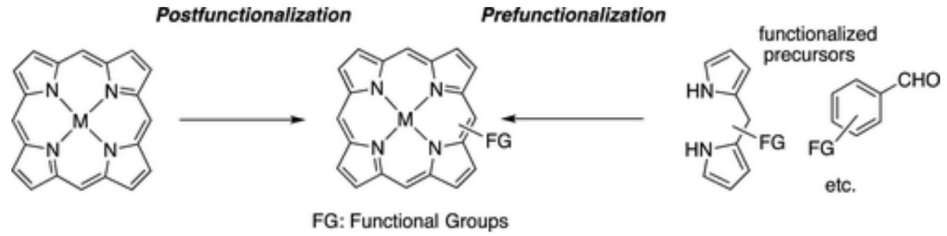

Figure 2.23 : Post- and pre-functionalization of porphyrins. *Reproduced from ref.[22] Copyright © 2016 American Chemical Society.*

Post-functionalization of porphyrins can be further classified into two categories (*figure 2.24*): one is core-functionalization and the other is peripheral-functionalization.

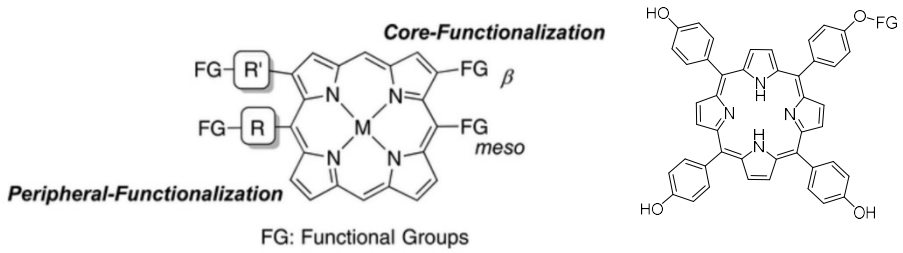

Figure 2.24: (left) Classification of porphyrin functionalization by position, (right) THPP mono functionalized.

In this chapter the synthetic approach is focused on the selective functionalization of only one of the functionalities of the commercially available THPP with thiolated linkers in order (1) to avoid the formation of networks as that one published by Canitez et al.[23] who employed a tetradentate porphyrin (p-TPP-SAc) containing four thiolacetate ending groups (*figure 2.25*, *a*) and (2) to bind the other functionalities with hydrophilic chains to increase the water solubility of the system and also to reduce, by steric hindrance, the possibility of stacking interactions with the AuNP surface (*figure 2.25,* b) or with other porphyrins (*figure 2.25,* c) quenching the singlet oxygen production.

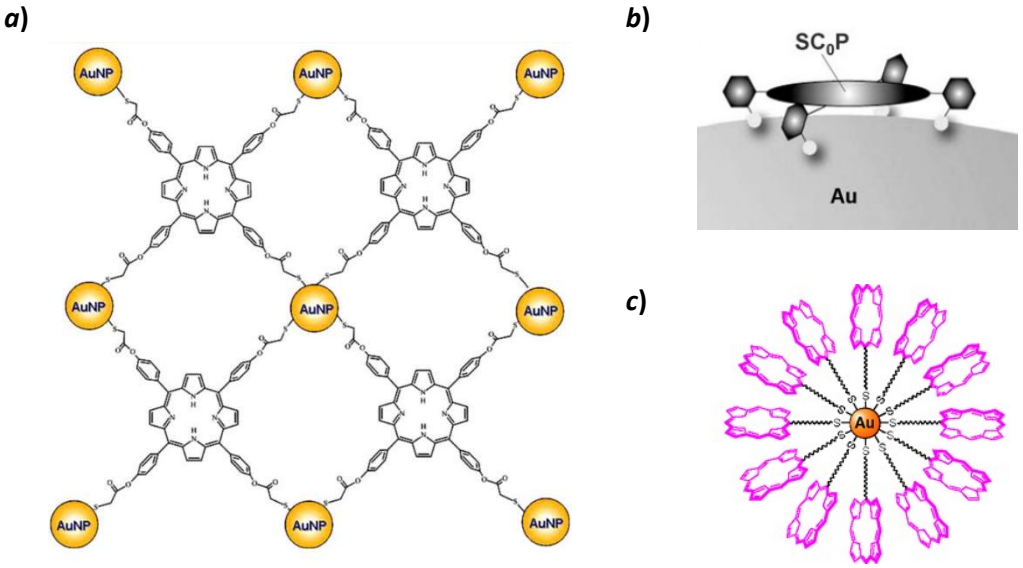

Figure 2.25 : (*a*) The plausible network structure of AuNP@p-TPP-SAc supposed in a previous work. *Reproduced from ref.*[23] *© Springer Science+Business Media B.V. 2011.*

Before reacting the porphyrin (THPP) with lipoic acid, the model reaction of phenol and lipoic acid was studied to optimize the reaction conditions.

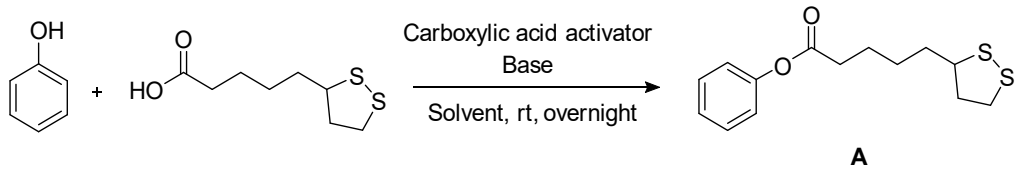

Scheme 2.19: General reaction scheme of phenol and lipoic acid to optimize the reaction's conditions.

The conversion of the reagents into the product was controlled by TLC. In *entry 1*, the product was isolated with a chromatography column and obtained in a yield of 44%, while for the other conditions (table 2.2, *entries 2-9*) the yield estimation was calculated by ^{1}H NMR using an internal standard (trimethoxy benzene) in the crude, comparing the singlet signal at δ = 6.11 ppm that integrates for three protons with the multiplet signal of the phenol at δ = 2.42-7.39 ppm that should integrates for two protons.

Entry	Base	Carboxylic acid activators	Solvent	Yield of **A**[a]
1	-	EDC, DMAP	DCM	44% [b]
2	K_2CO_3	EDC, DMAP	DMF	42%
3	NaH	EDC, DMAP	DMF	8%
4	t-BuOK	EDC, DMAP	DMF	25%
5	DIPEA	EDC, DMAP	DCM	50%
6	DIPEA	EDC, DMAP	DMF	40%
7	DIPEA	$SOCl_2$	DMF	x
8	DIPEA	EDC, DMAP	THF/DMF	4%
9	NaOH	EDC, DMAP	DMF	3%

Table 2.2: optimization of the conditions for the synthesis between phenol and lipoic acid (see scheme 2.1). (a) the reported yields were calculated through NMR of the crude with trimethoxy benzene as internal standard. (b) isolated yield by chromatography column.

Due to the extremely low solubility of porphyrin in DCM, the reaction needs to be performed into DMF, although the higher yield was obtained in DCM (*entry 5*). Since in the other conditions the crude still presents the reagents, can be concluded that, at room temperature, the conversion of the reagents into product **A** is quite low but at same time in the reaction with porphyrin is not worth it to increase the temperature in order to promote the mono alkylated product avoiding the attack of lipoic acid on the other phenolic functionalities of the porphyrin. For both reasons in the reaction between THPP and lipoic acid was decided to use K_2CO_3 as base, EDC and DMAP as acid activators and DMF as solvent. Since THPP has four functionalities that can react, we faced the problem of monofunctionalization. Usually, mono alkylation of THPP could be planned by activating only one phenolic oxygen as nucleophile when the base is used in defect respect to the porphyrin. Only in the case of lipoic acid, the best yield was obtained with a slight excess (if compared to the stoichiometric ration to obtain the monoalkylation) of K_2CO_3 and linker and in the presence of EDC, DMAP as coupling reagents following the best conditions found out during the optimization process of the model reaction between phenol and lipoic acid. In this reaction the ratio between THPP/lipoic acid/K_2CO_3 was 1:1.1:1.1.

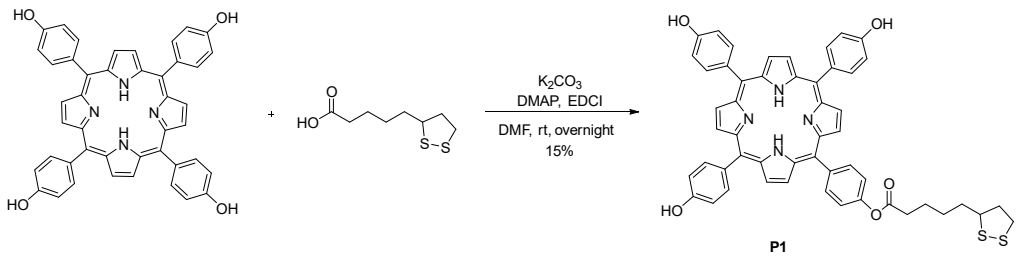

P1

Scheme 2.20 : Scheme of reaction of mono alkylated porphyrin **P1**.

Lipoic acid was dissolved into DMF and stirred with EDC and DMAP, while THPP was dissolved in a solution of DMF and mixed with K_2CO_3. After 30 minutes, the activated lipoic acid solution was added to THPP solution and the reaction was stirred at room temperature overnight to reduce as much as possible the percentage of dialkylated, tri-alkylated and tetra-alkylated by-products. After purification, **P1** was obtained in a yield of 45% as shown in *scheme 2.20* and characterized by ^{1}H and ^{13}C NMR and UV-Vis spectroscopy.

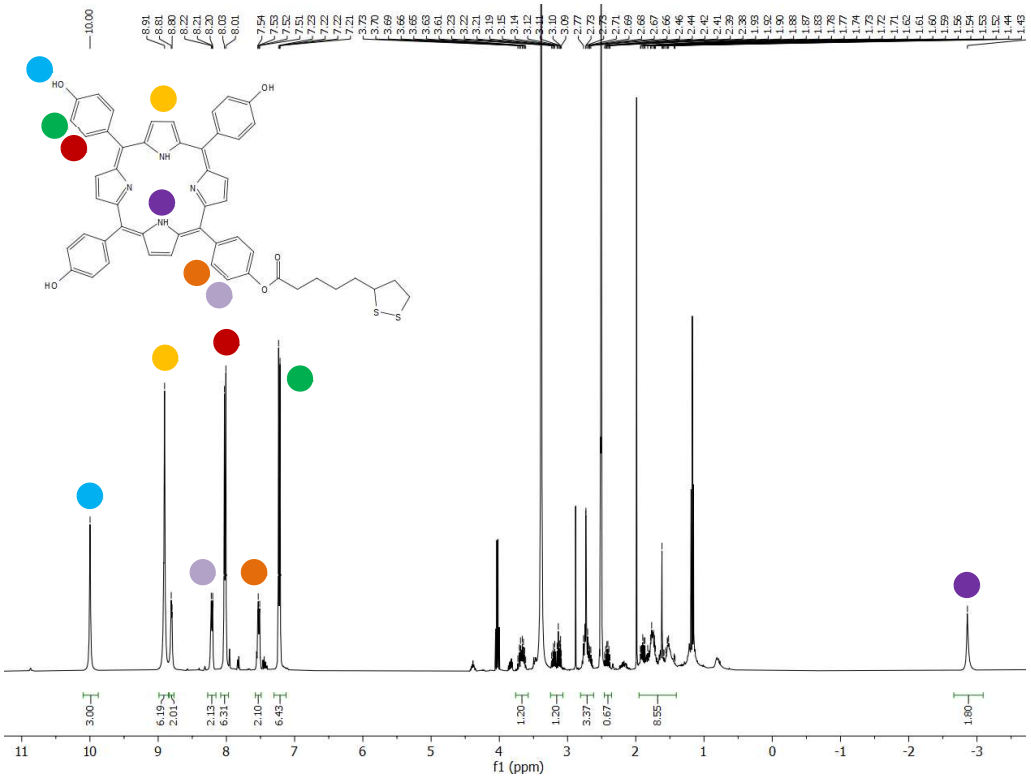

Figure 2.26 : ^{1}H NMR (400 mHz, DMSO-d_6) of **P1**.

In the *figure 2.26* is reported the ^{1}H NMR (400 MHz, DMSO-d_6) of product **P1**. The successful of the reaction is confirmed by the aromatic protons of phenolic moiety alkylated by lipoic acid that present two doublet signals, each integrating for two protons, that are down shifted at δ = 8.20 ppm and δ = 7.53 ppm. Furthermore, the three free phenolic functionalities gave also two doublet signals, each integrating for six protons, at δ = 8.01 ppm and δ = 7.23 ppm and the singlet at δ = 9.98 ppm, integrating for three protons, is ascribed to the three protons of the free hydroxyl groups of phenol. Finally, protons on the pyrrolic rings present a multiplet signal centered at δ = 8.85-8.75 ppm and integrating for eight protons. A further presence of lipoic acid on THPP is given by the diagnostic signals of lipoic acid which ^{1}H NMR spectra has been already described in *chapter 2.2.1*.
To better understand the interpretation of ^{1}H NMR of alkylated porphyrins, in *figure 2.27* is reported the zoom of the aromatic zone of THPP (reagent, *top*) and THPP_mono alkylated (product, *bottom*) where is more clear the down shifting of alkylated aromatic protons of acylated phenol.

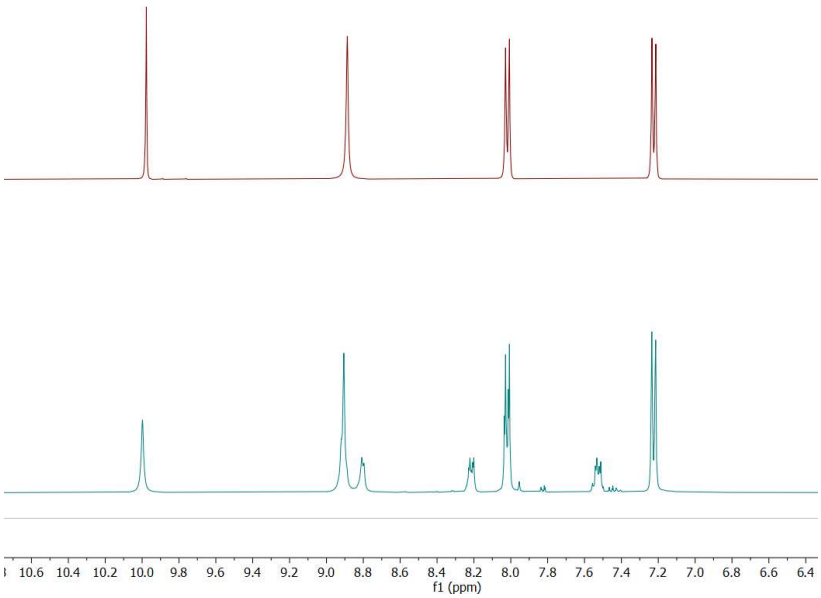

Figure 2.27 : ^{1}H NMR (400 mHz, DMSO-d_6) of THPP (*top*) and **P1 (***bottom*).

Uv-Vis spectra of **P1** (*figure 2.28*) was performed dissolving it into DMSO (black line) and water (pH= 11, to allow its deprotonation thus it solubility, red line) to obtain a 1 µM solution.

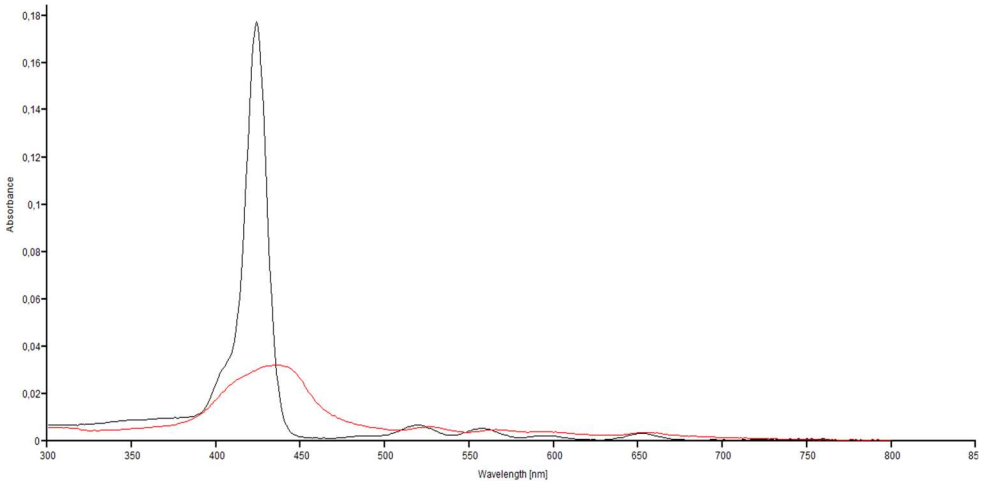

Figure 2.28 : UV-vis spectra of **P1** (1 µM) in DMSO (black line) and in water at pH=11 (red line).

As can be deducted from *figure 2.28*, in water the absorbance of the Soret Band of P1 is highly reduced, probably due to the low solubility in water even at pH of 11. In order to employ PS@AuNPs in biological systems, that are aqueous media, arose the necessity to synthesize thiol monoalkylated porphyrins soluble in water. To make the system hydrophilic, three PEG chains were bound to the phenolic hydroxy groups of THPP to obtain triPEG-THPP-$(CH_2)_n$-SH. This can be pursued thought two different strategies as shown in the *scheme 2.21*: (a) pre functionalization with PEG chains followed by the monoalkylation with the linker and (b) post functionalization with PEG chains of pre synthesized mono alkylated PS.

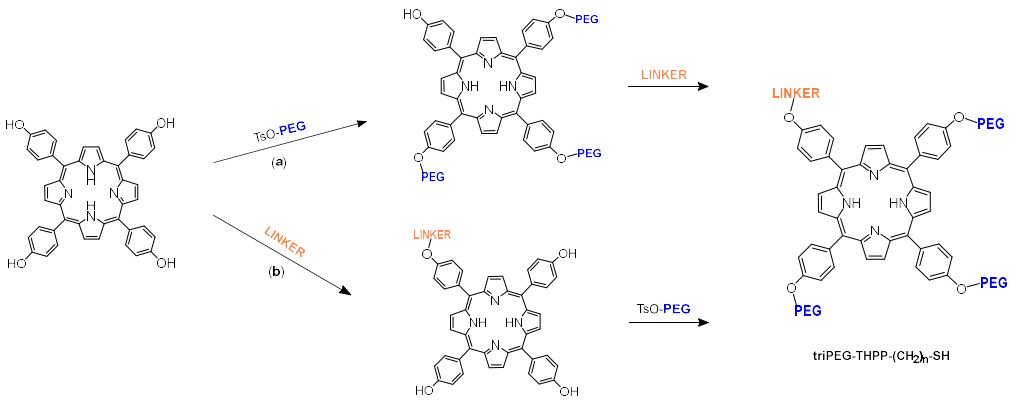

Scheme 2.21 : Two strategies of synthesis of triPEG-THPP-$(CH_2)_n$-SH.

Firstly, following strategy (a), 1 eq of THPP was stirred in a solution of DMF with 3 eq. of K_2CO_3 for 30 minutes, then linker **13** was added and the solution was stirred at room temperature for 48h as design in *Scheme 2.22*. Then, after purification, **P2** was obtained in yield of 80% and it was characterized by ^1H and ^{13}C NMR spectroscopy in DMSO-d_6 and UV-Vis spectroscopy in DMSO and water. The tetra-alkylated co-product was isolated in a yield of 12%.

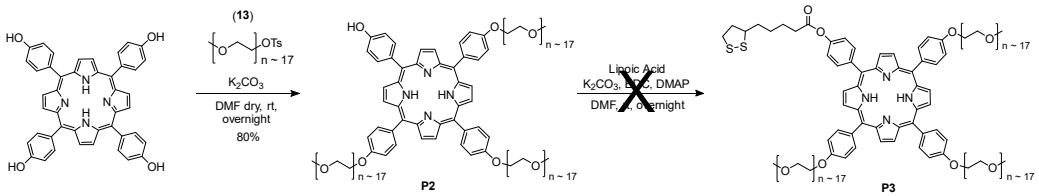

Scheme 2.22 : Scheme of synthesis of **P2** and **P3** starting from THPP and linker **13**.

Figure 2.29 shows the ^1H NMR spectra in DMSO-d_6 of the product recorded at 353 Kelvin. The spectra shows, in the aromatic zone, six signals: a broad signal at δ=9.72 ppm ascribed to the proton of the free hydroxyl group of phenol, a multiplet at δ= 8.89-8.82 ppm ascribed to the eight protons of the four pyrrole rings and two doublets at δ=8.09 ppm and δ=7.39 ppm each integrating for six protons, ascribed respectively to the phenyl protons in the meta and in the ortho position of the ether bond with the PEG chains. These signals confirm the successful of the reaction. Further diagnostic signals are two doublets, each integrating for two protons, at δ= 7.99 ppm and δ= 7.22 ppm, ascribed to the protons of the unreacted aromatic ring respectively in meta and ortho to the free hydroxyl group. In the aliphatic zone two triplets are observed at δ= 4.43 ppm and δ= 3.97 ppm, each integrating for six

protons, which correspond to the methylene of PEG chains in α and β to the oxygen bound to the porphyrin. Then is present an huge multiplet between δ= 3.78 and 3.43 ppm integrating for 196 protons, which corresponds to all the other methylene of the PEG chains, and a singlet at δ= 3.24 ppm, integrating for nine protons, which is ascribed to the three methyl groups at the end of the PEG chains. Finally, the singlet at δ= -2.77 ppm is ascribed to the two N-H protons of the pyrrole rings of porphyrin.

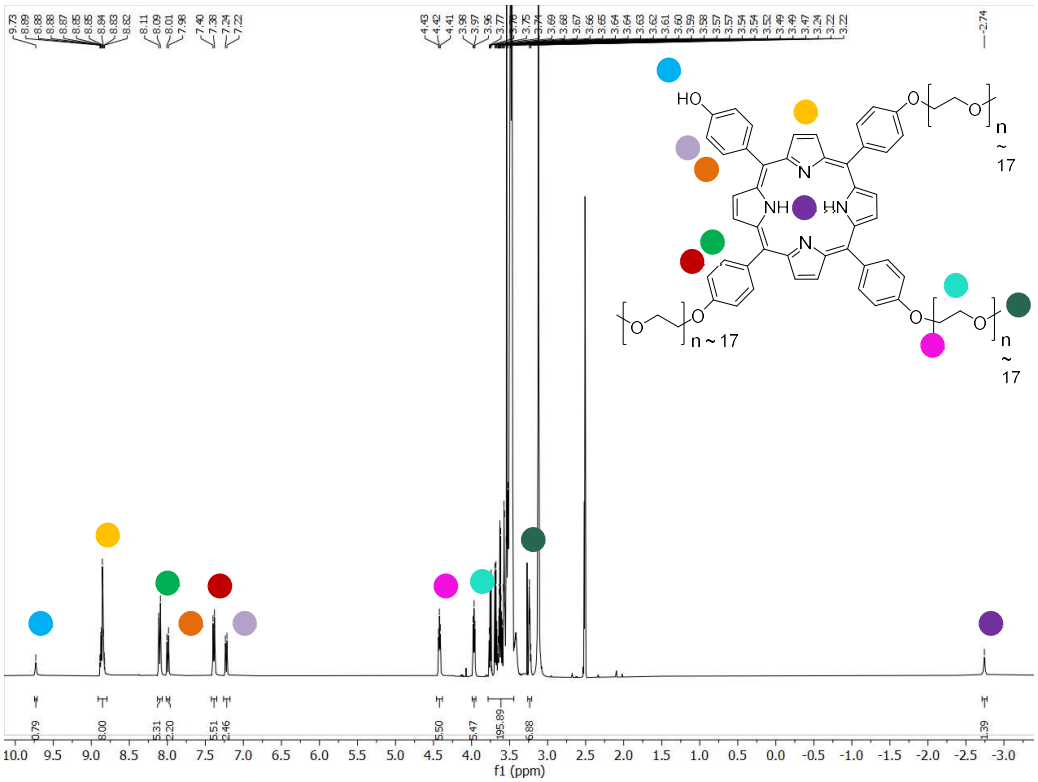

Figure 2.29 : ^{1}H NMR (400 mHz, DMSO-d_6) of **P2**.

As was previously described in *scheme 2.22*, **P3** can be obtained by reacting **P2** with K_2CO_3 and lipoic acid (as usual activated with EDC and DMAP) in DMF. Since after 16 hours at room temperature **P2** didn't convert into **P3**, the temperature was increased to reflux but also in this case the product was not observed. This was ascribed to the steric hindrance of the PEG chains that could prevent this reaction. For this reason, strategy (b) described in *scheme 2.21* was followed as an alternative approach: 1 eq of *mono-lipoic_acid-THPP* (**P1**, whose synthesis is described in *Scheme 2.20* and ^{1}H NMR characterization in *figure 2.26*) was reacted with 4 eq of

K_2CO_3, 3.5 eq of PEG chain **13** and the reaction mixture was stirred at room temperature overnight. The crude, after the evaporation of the solvent under reduced pressure, was dissolved in a low amount of THF and the product was precipitated with diethyl ether obtaining a red oil in a yield of 49% that was characterized by ^{1}H NMR.

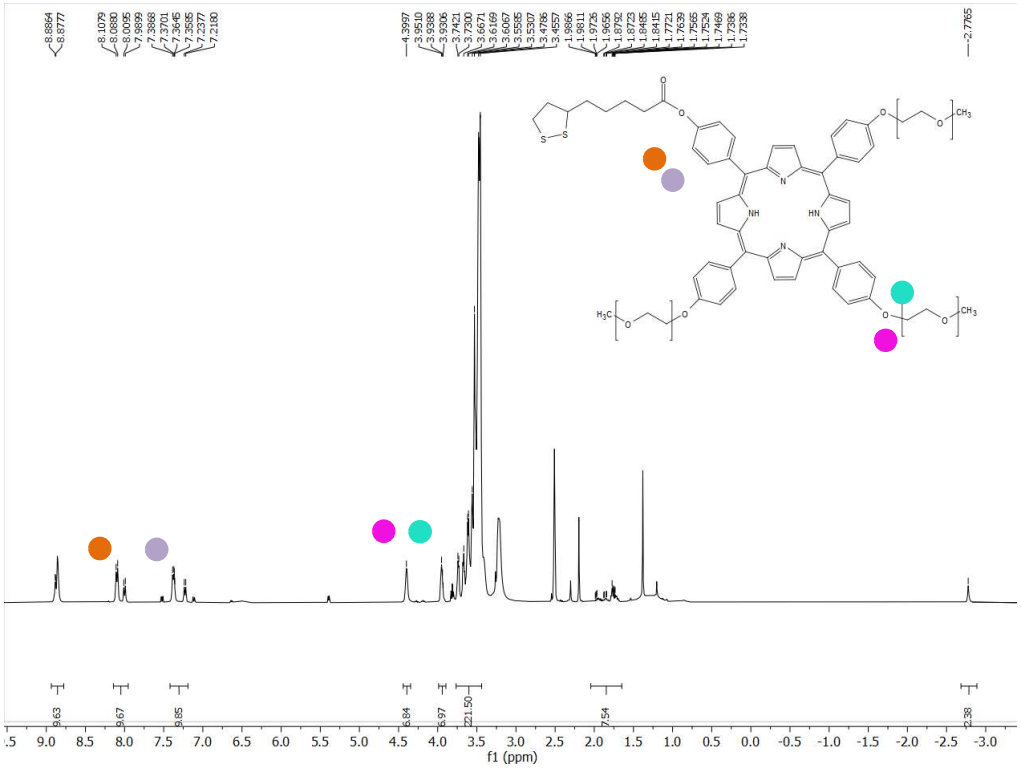

Figure 2.30 : ^{1}H NMR (400 mHz, DMSO-d_6) of **P3**.

In *figure 2.30* is reported ^{1}H NMR spectrum in DMSO-d_6 of **P3** in which the presence of PEG chains is confirmed by the huge multiplet at δ= 3.77-3.32 ppm integrating for 225 protons and the multiplets at δ= 4-41-4.38 and δ= 3.95-3.93 ppm each integrating for six protons ascribed to the protons of aliphatic chains of PEG near the phenolic functionalities. In the aromatic zone, the successful of the reaction is confirmed also by the up-shifted of the two douplets at δ= 8.00 ppm and 7.23 ppm, each integrating for two protons, ascribed to the protons of phenolic functionality bound to lipoic acid. Since the porphyrins can be easily alkylated with PEG chains,

THPP was monoalkylated with other linkers having protected thiol ending and different length's chain (*scheme 2.23*).

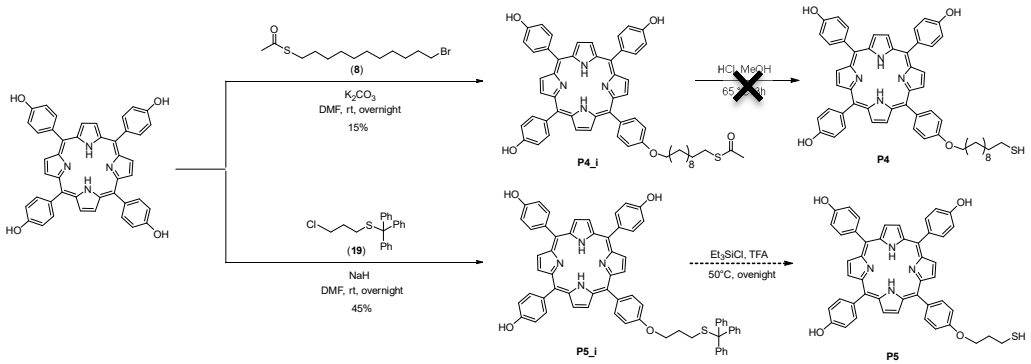

Scheme 2.23 : Scheme of synthesis of **P4** and **P5** starting from THPP and linker **8** and **19** respectively.

Differently from the synthesis of **P1**, in these cases the functionalization of THPP were performed using a defect of base to promote the monoalkylated product. Intermediate **P4_i** and **P5_i** were synthesized starting from THPP using K_2CO_3 and linker **8** (for **P4_i**) and NaH and linker **19** (for **P5_i**) to obtain the products in a yield of 15% and 48% respectively after purification on silica plates. Both the intermediates were characterized by ^{1}H NMR spectroscopy and underwent the next step of deprotection. *Figure 2.31* shows the ^{1}H NMR in DMSO-d_6 of **P4_i**; also in this case there are, in the aromatic zone, the diagnostic signals relatives to the monoalkylated product: a broad signal at δ=9.80 ppm ascribed to the proton of the free phenolic hydroxyl groups, a multiplet at δ=8.87-8.80 ppm ascribed to the eight protons of the four pyrrole rings and two doublets at δ=8.08 ppm and δ=7.32 ppm each integrating for two protons, due respectively to the phenyl protons in the meta and in the ortho position of the ether bond with the linker **8**. These signals confirm the successful of the reaction. Further diagnostic signals are two doublets, each integrating for six protons, at δ= 7.98 ppm and δ= 7.22 ppm, ascribed to the protons of the unreacted aromatic ring respectively in meta and ortho to the free hydroxy groups. In the aliphatic zone there are the signals of the alkylic chain and a singlet at δ= 2.30 ppm that integrates for three protons relative to the methyl group of the acetyl. Finally, the singlet at δ= -2.77 ppm is ascribed to the two protons of the pyrrole rings of porphyrin.

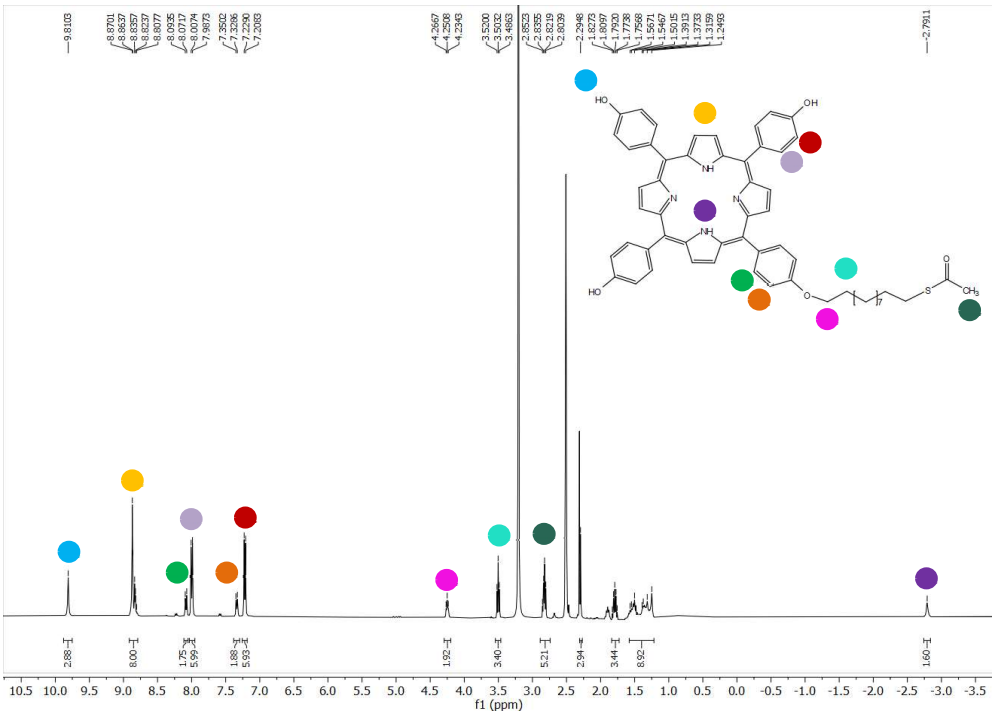

Figure 2.31 : ^{1}H NMR (400 mHz, DMSO-d_6) of **P4_i**.

The cleavage of the thioacetate group to obtain free thiol group was attempted by an acidic hydrolysis with methanol and HCl (37%) for 3 hours at 65 °C. Unfortunately, this reaction didn't work and the attention was focused to the product **P5**.

Also **P5_i** was characterized by ^{1}H NMR, which spectra (*figure 2.33*, top) shows the diagnostic signals of monoalkylated product and the presence of a multiplet at δ= 7.44-7.23 ppm in the aromatic zone that integrates for 25 protons relatives to the 15 protons of the three phenyl groups on the sulfur and the eight protons in orto position of the four phenolic groups. To find the best reaction conditions, a model reaction was performed using simple phenol. In this case, the removal of trityl protecting group was accomplished using $AgNO_3$, pyridine and HCl at room temperature for 2 hours. These conditions, when applied to the porphyrin **P5_i,** failed to give **P5**. Thus different removal conditions were found out.

Thus, **P5_i** was reacted with triethylsilyl chloride (Et_3SiCl) and an excess of trifluoroacetic acid (TFA) in DCM at 50 °C for 24 hours. After purification, the product was isolated in a 58% yield and characterized by ^{1}H NMR and ESI-MS. Surprisingly, in the ^{1}H NMR spectra, the aromatic signals of **P5** were different from

the expected signals of a mono alkylated porphyrin. Thus, the ESI(+)-MS analysis with flow injection detected a peak having in the related mass spectrum a distribution of m/z 752 $[M+2H]^{2+}$, 1504 $[M+H]^{+}$. From this pattern, the peak with m/z: 1504 can be ascribed to the formation of the dimer of **P5** which structure is reported in *figure 2.32*.

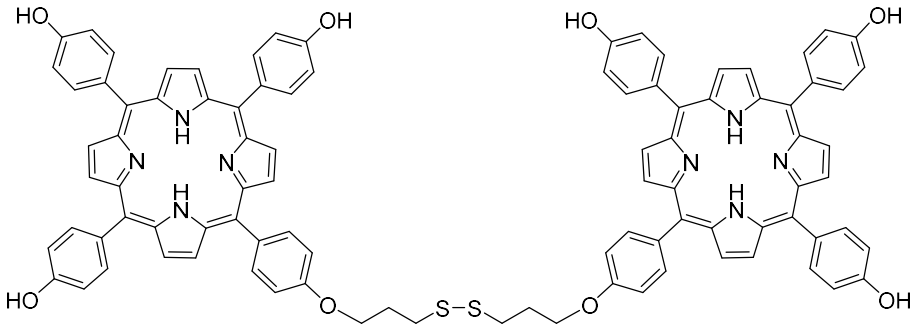

Figure 2.32 : Hypothetical structure of dimer of **P5_b** obtained from the deprotection of **P5_i**.

To further confirm the obtainment of a dimerization product, **P5_i** was reacted with I_2 in methanol at room temperature for 10 minutes as described in *scheme 2.24*. This conditions are reported in literature in order to obtain the deprotection of trityl and the formation of S-S bond using I_2 as oxidant in one step on synthesis.[24]

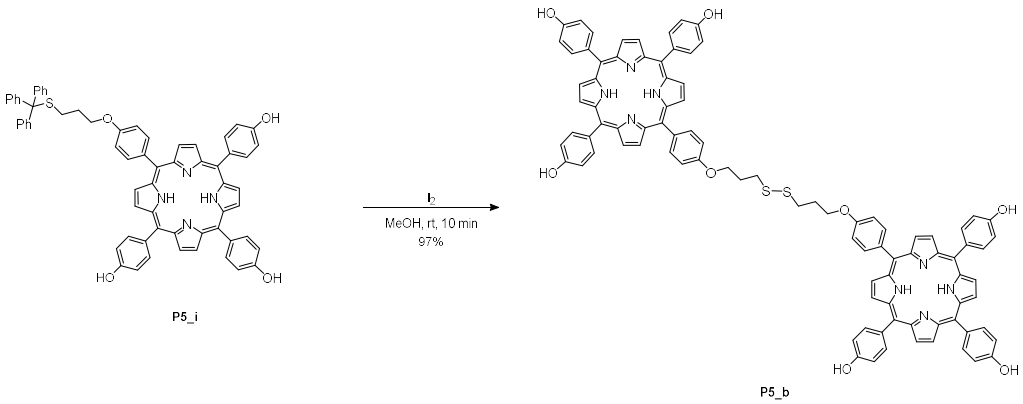

Scheme 2.24 : Synthesis of **P5_b** through a dimerization reaction.

The product was characterized by ^{1}H NMR spectroscopy that revealed the same peaks of the ^{1}H NMR spectra of the initially desired product **P5** and this confirmed

the obtainment of **P5_bis** also with the initial conditions (reported in the *scheme 2.23*). For this reason, the product of dimerization is indicated as **P5_b**. In *figure 2.33* are reported ^{1}H stacked NMR of **P5_i** (top) and **P5_b** (bottom) that show the disappearance of the multiplet related to the phenyl groups of trityl. In addition, the signals ascribed to the aliphatic chain are down shifted and the signals related to the aromatic protons of phenolic group attached to the propylic chain are down shifted at δ= 8.19 and δ= 7.23.

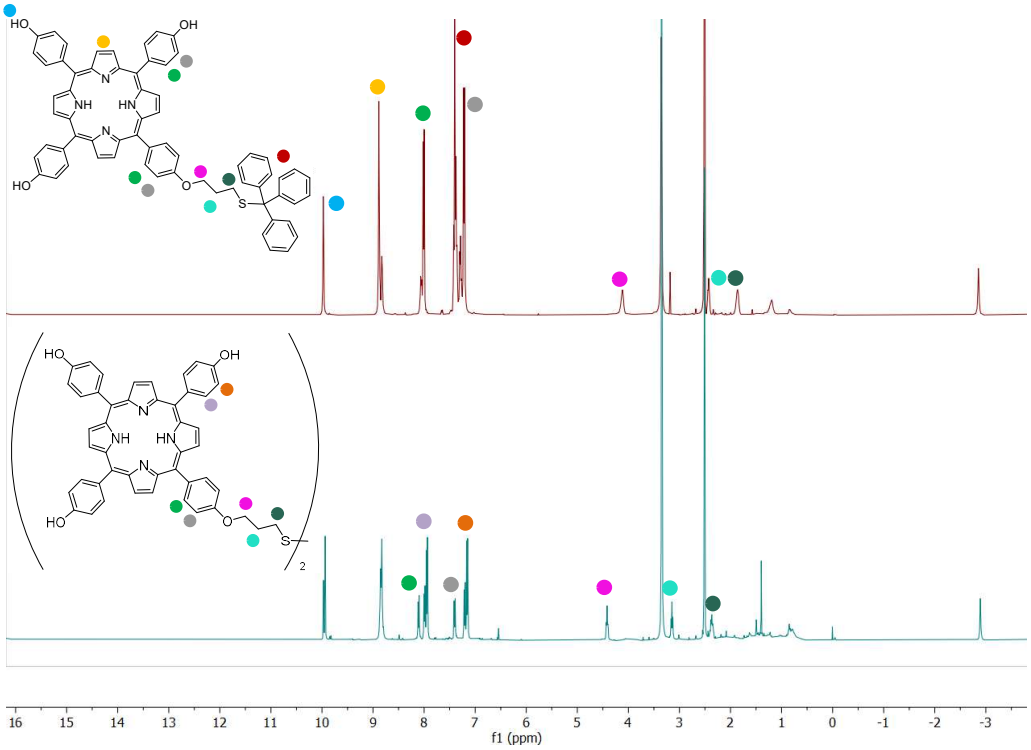

Figure 2.33 : ^{1}H NMR (400 MHz, DMSO-d_6) of **P5_i** (top) and **P5_b** (bottom).

In order to increase the water solubility of **P5_b**, **P5_i** was reacted with 3.3 equivalent of NaH (60%) and 3.3 equivalent of PEG chains (linker **13**) and refluxed overnight. The crude of the reaction was examined by ^{1}H NMR that surprisingly showed the disappearance of the signals of the propylic chain due to the loss of the linker and the achievement of the triPEGylation of THPP. Thus, the crude was treated with 2.6 equivalents of linker **19** in presence of K_2CO_3 and refluxed for 48 hours as shown in *scheme 2.25*.

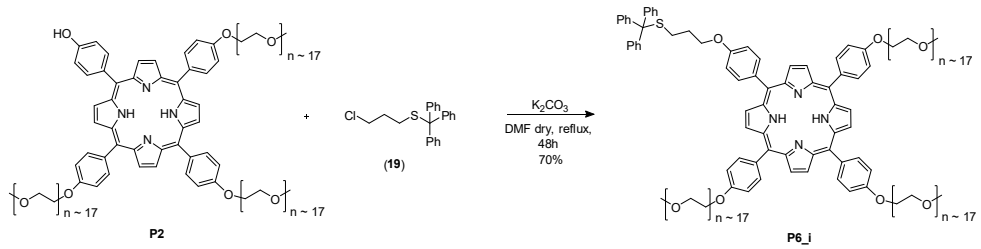

Scheme 2.25 : Scheme of synthesis of **P6_i**.

The intermediate **P6_i** was obtained in a yield of 70% and characterized by ^{1}H NMR. ^{1}H NMR spectra recorded in DMSO-d_6 at 333 Kelvin (*figure 2.34*) shows the diagnostic signals of full-alkylated porphyrin in the aromatic zone at δ= 8.84 ppm and at δ= 8.06 ppm and the aromatic protons of the trityl group at δ= 7.35 ppm with the lack of the protons of the free phenolic functionality. In the spectra are also present, in the aliphatic zone, the signals of the protons of the propylic chain: a multiplet at δ= 4.38-4.36 ppm, a multiplet at δ= 2.48-2.45 ppm and another at δ= 1.90 ppm each of them integrating for two protons. Finally, are present also the signals of the protons of the three PEG chains.

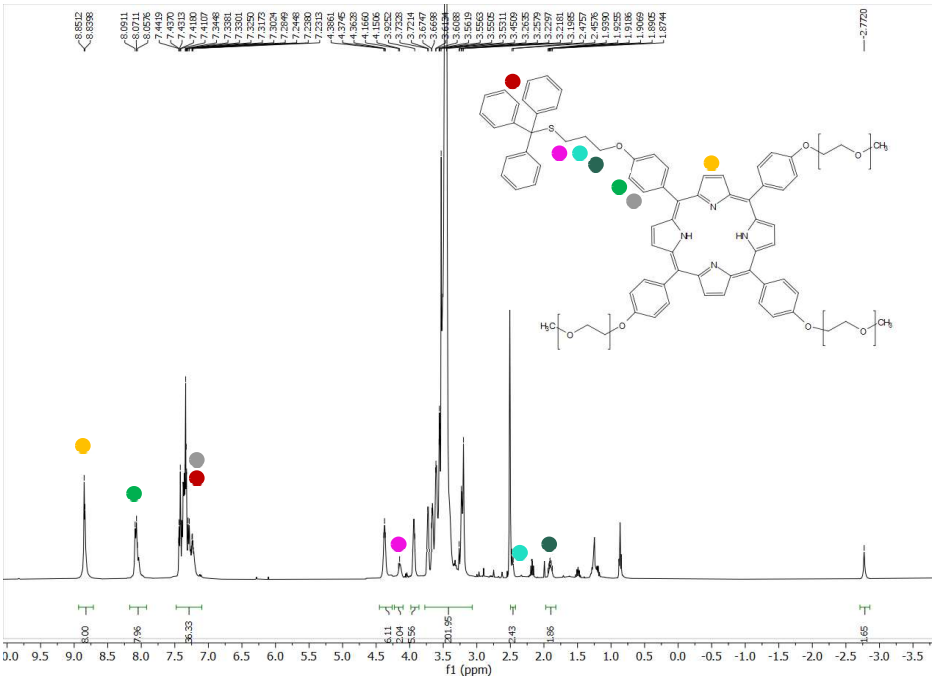

Figure 2.34 : ^{1}H NMR (400 mHz, DMSO-d_6, 333 Kelvin) of **P6_i**.

At the moment, the deprotection step of the trityl group of **P6_i** to obtain the final product **P6** (see *scheme 2.26*) is still under study. Different conditions were tested as summarized in *table 2.3*.

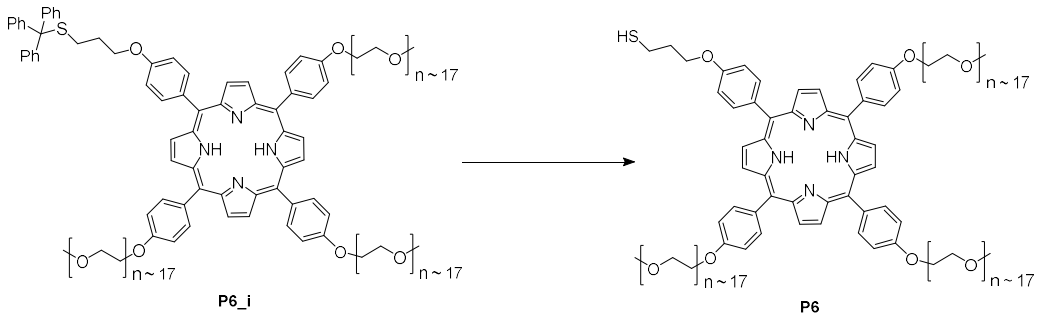

Scheme 2.26 : Scheme of synthesis of **P6**.

Entry	Conditions
1	TFA, phenol, 73°C, 1h
2	TFA, Et_3SiCl, DCM, 50°C, overnight

Table 2.3: Deprotection conditions of **P6_i** to obtain **P6**.

In both the conditions, the monitoring and purification of the reaction mixture was very complicated probably due to the formation of **P6** and of the product of dimerization (as observed during the synthesis of **P5**). For this reason was decided to push the reaction directly towards the dimerization product of **P6_i** as described into *scheme 2.27*. Using Iodide in methanol at room temperature for 10 minutes as previously described, is possible to remove the protecting group (trityl) and to create an S-S bond in one synthetic step.

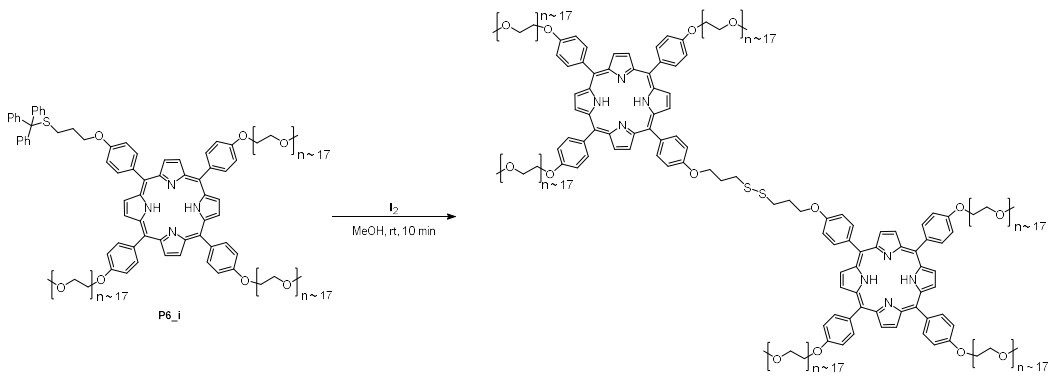

Scheme 2.27 : Scheme of synthesis of **dimerization of P6_i**.

After the removal of I_2, the obtained solid was characterized by ^{1}H NMR. Unfortunately, the ^{1}H NMR was very complicated to interpretate probably due by the presence of different products and the low molar amount used for characterization. For this reason, was decided to introduce PEG chains in the last step of the synthetic pathway after the obtainment of **P5_b** as shown in *scheme 2.28*. **P5_b** was treated with an excess of linker **(13)**, K_2CO_3, a catalytic amount of KI and after three days at 60°C was extracted with dichloromethane and washed with diethyl ether to remove the excess of linker (13). **P9** was isolated with a yield of 30% and characterized with mono and bidimensional NMR.

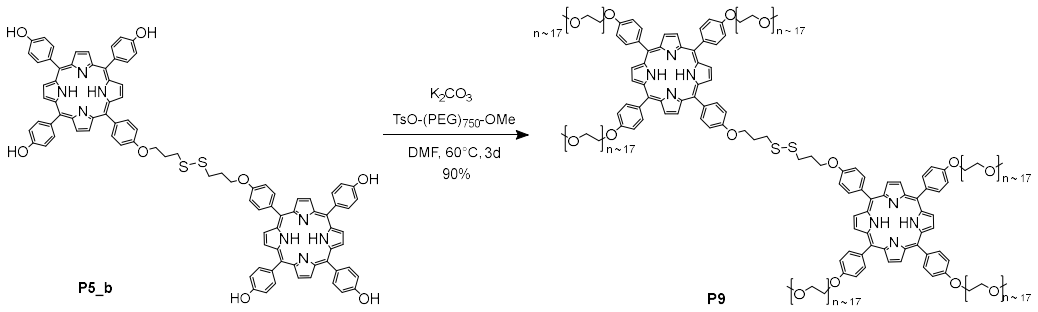

Scheme 2.28: Scheme of synthesis of **P9**.

In order to solubilize porphyrins in water, other polar molecule can be used as an alternative to long PEG chains that can prevent, by their steric hindrance, the further functionalization of the porphyrin or even their conjugation on AuNPs. Indeed, sodium sulfonate groups are quite soluble in water. Thus, tri-alkylation of THPP was performed in DMF using 3.3 eq of sodium 3-bromopropane-1-sulfonate in the presence of 3.5 eq of K_2CO_3 as shown in *scheme 2.29*.

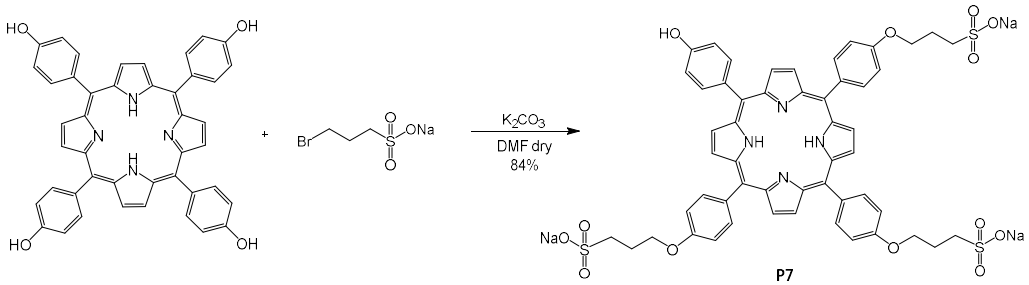

Scheme 2.29: Scheme of synthesis of **P7**.

The product **P7** was obtained by precipitation in a 84% yield and characterized by ^{1}H NMR. ^{1}H NMR spectrum in DMSO-d_6 (*figure 2.35*) shows the diagnostic signals of trialkylation in the aromatic zone at δ= 7.99 ppm and δ= 7.21 ppm where are

present two up-shifted douplets each integrating for two protons relative to the protons of the aromatic ring of the free phenolic functionality. In the spectra are also present, in the aliphatic zone, the signals of the three propylic chains: a multiplet at δ= 4.40-4.37 ppm, a multiplet at δ= 2.79-274 ppm and another at δ= 2.27-2.20 ppm each of them integrates for six protons.

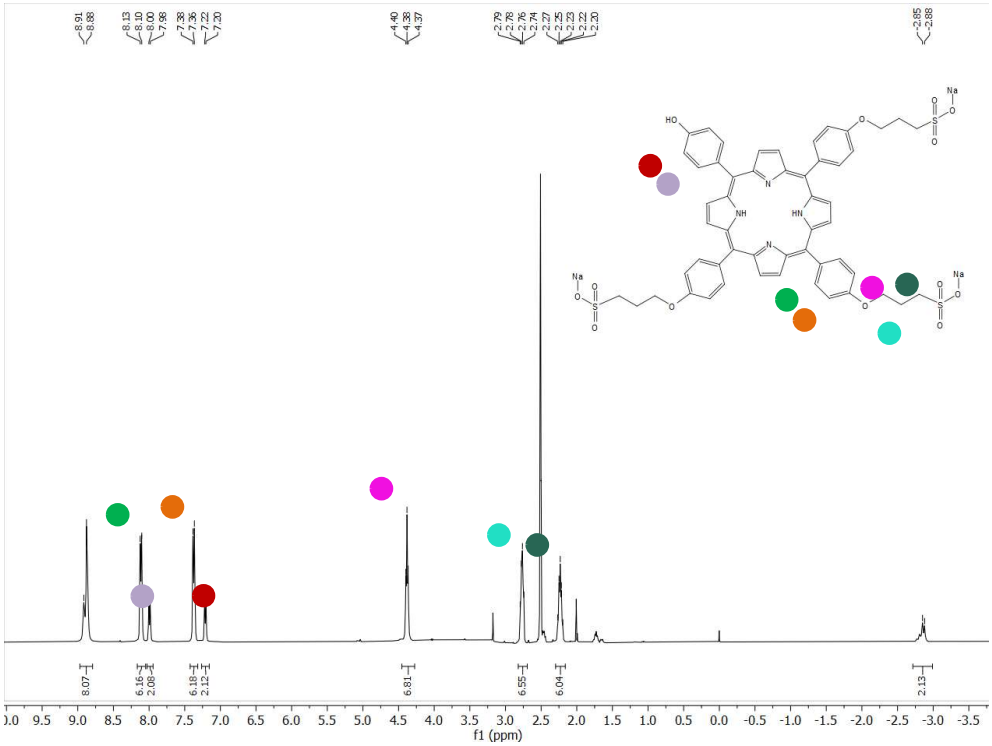

Figure 2.35: ^{1}H NMR (400 mHz, DMSO-d_6) of **P7**.

As expected, **P7** resulted to be water soluble. The next step should be the functionalization of the porphyrin free position with a thiolated linker for conjugation to AuNP offering a good alternative to **P3** or **P9**. But, considering that sulfonate groups are able to coordinate to AuNPs, it could be observed the formation of aggregates where some nanoparticles are involved. Another porphyrin, PpIX, was taken in consideration, due to its high activity in PDT. The attempts to functionalize PpIX with thiol ending linkers was not successful . Indeed, some of the synthesis reported in the literature[25] resulted to be non-reproducible mainly regarding the isolation and purification steps, and in addition, characterization of the product was not well described. To overcome this drawback,

it was evaluated that one of the most efficient approach could be the binding of PpIX on the amine groups of a polymer that can be easily purified by precipitation. As already discussed in chapter 2.1.1, PEI 25 kDa polymer was previously reacted with $HAuCl_4$ to form AuNPs, then, without any purification, it was reacted directly with PpIX previously dissolved into DMF (0.1 mM solution) as reported in *scheme 2.25*. After 6 hours at room temperature, the solution was centrifuged at 15000 rpm for 20 minutes and the precipitate was washed twice with DMSO to remove the unreacted PpIX.

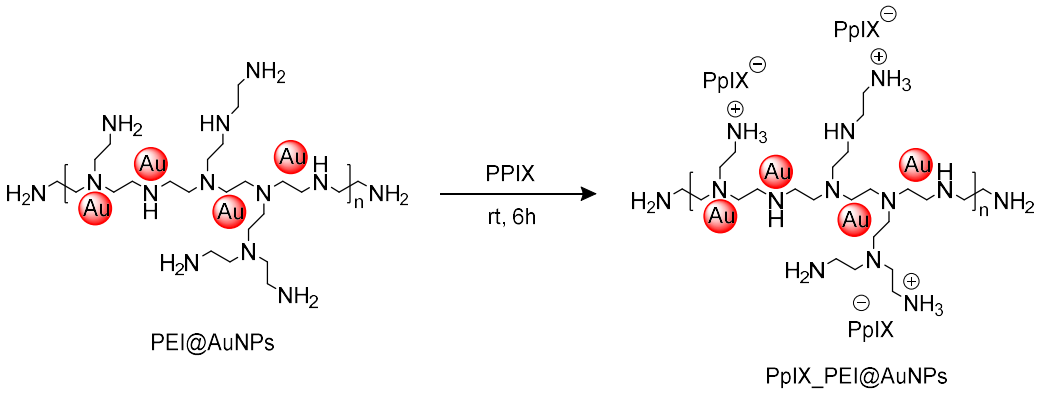

Scheme 2.30: Scheme of synthesis of PpIX_PEI@AuNPs.

Unfortunately, the ^1H NMR did not reveal the peaks of porphyrin probably due to the high molecular weight of PEI and to the low amount of porphyrin. However, the exam of the product by UV-Vis revealed the porphyrin's presence. In *figure 2.36* the product UV-Vis spectrum is reported (black line) along with the absorbance pattern of PpIX in DMSO, with the characteristic Soret band at 407 nm (red line), and the absorption of PEI@AuNPs centered at 526 nm (green line). From the black spectra, can be deducted that PpIX is successfully conjugated to AuNPs giving the conjugate PpIX_PEI@AuNPs since both the components are present, i.e. the Soret band at 407 nm and the plasmonic band, red shifted of ~ 30 nm and broader probably due to a slight aggregation of PEI@AuNPs. It was supposed that the conjugation occurred by ionic interaction between the porphyrin carboxylic groups and the primary amino groups of PEI.

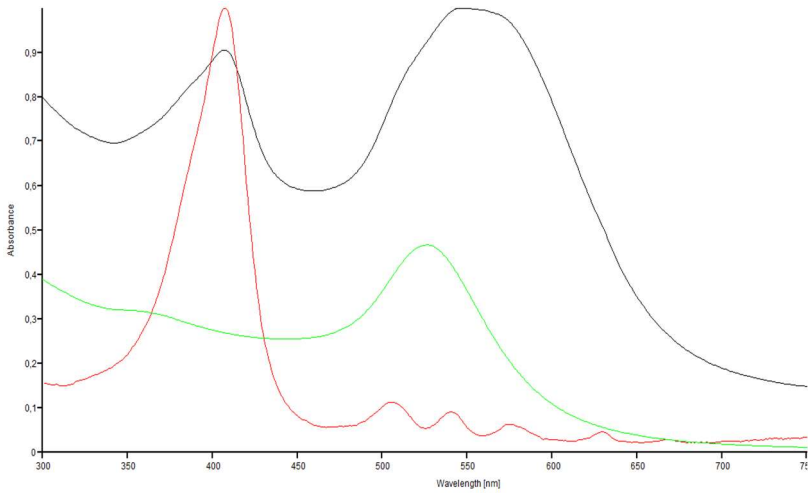

Figure 2.36: UV-vis of PPIX (red line), PEI@AuNPs (green line) and PpIX_PEI@AuNPs (black line).

To increase the amount of porphyrin on PEI@AuNPs by covalent bonds, the synthesis of PpIX chloride was attempted, but unsuccessfully. This conjugate system is not interesting as such, since the high molecular weight polymer cannot be internalized by cellular lines, but it was prepared to explore different conjugation strategy.

In addition, several synthetic approaches were examined to covalently bind PPIX thiol ending linkers (cysteine, cysteine-methyl ester and linker **17**) (cysteine, cysteine-methyl ester and linker **17**) to PpIX in order to link it to AuNPs surface. Unfortunately, during the synthetic and purification processes, some problems occurred. The problems related to the PpIX use and derivatization is due to a high photoreactivity with oxygen, which results in the oxidation of the vinyl groups by simple exposure to ultraviolet/visible in the presence of air, when the molecule is in solution. Studies reported in the literature showed that the photo-induced degradation products of the PpIX can occurred as reported in the following *figure2.37*.

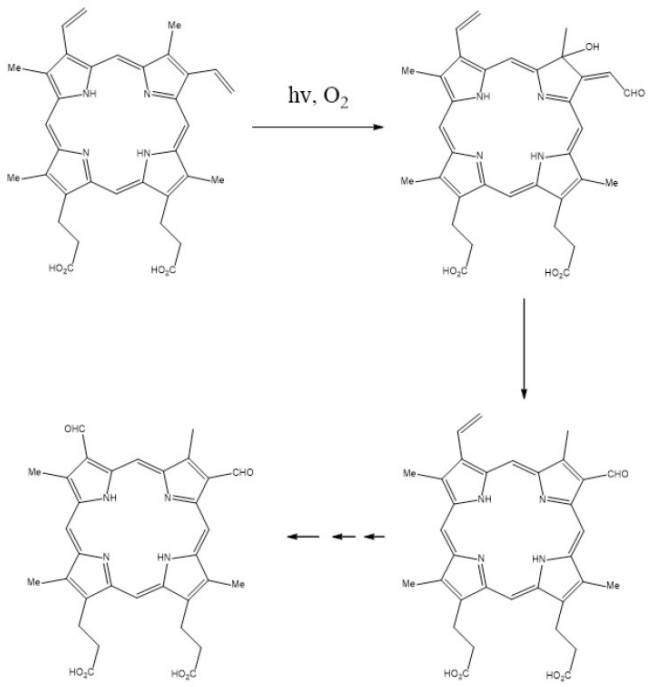

Figure 2.37: Mechanism of photodegradation of PpIX.

Successively, porphyrin **P1**, **P3** and **P5** were conjugated to AuNPs obtained and stabilized by sodium citrate and preliminary studies on the production of singlet oxygen were performed on the corresponding **P1**@AuNPs, **P3**@AuNPs, **P5**@AuNPs and PpIX_PEI@AuNPs (*Chapter 2.2.6*).

2.2.4 Conjugation of porphyrins to gold nanoparticles

In general, the conjugation reaction between porphyrin and citrate_AuNPs is conducted on 3 mL of citrate_AuNPs mixed with a solution of porphyrin in DMF or DMSO in the opportune concentration and then stirred overnight at room temperature. Firstly, the reaction of THPP with citrate_AuNPs was tested (*scheme 2.31*) in order to confirm the importance of thiol ending linkers in the loading on AuNPs.

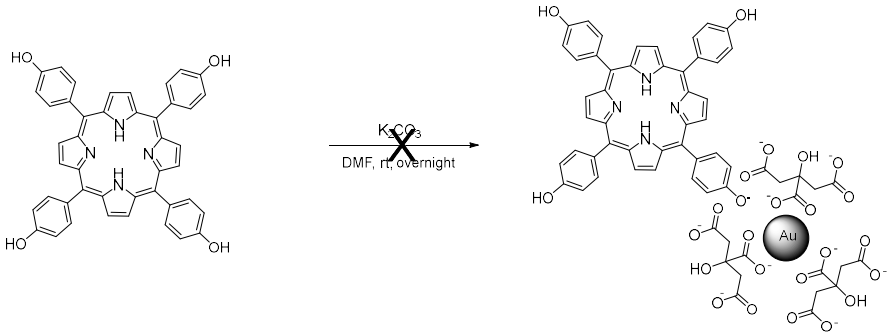

Scheme 2.31: conjugation reaction of THPP with citrate@AuNPs.

After centrifuge at 9000 rpm for 20 minutes and several washings with DMSO to remove unreacted porphyrin, the solid was redispersed into DMSO and examined at UV-Vis. The spectra didn't show any Soret band of the porphyrin confirming that the THPP porphyrin as such does not interact with AuNPs and that a convenient linker is required to conjugate the porphyrin to AuNPs. The first conjugation with a thiol functionalized porphyrin was performed with THPP monoalkylated with lipoic acid (THPP_LA, **P1**) dissolved in DMF and stirred with citrate_AuNPs (stable in water) at room temperature overnight as shown in the *scheme 2.32*.

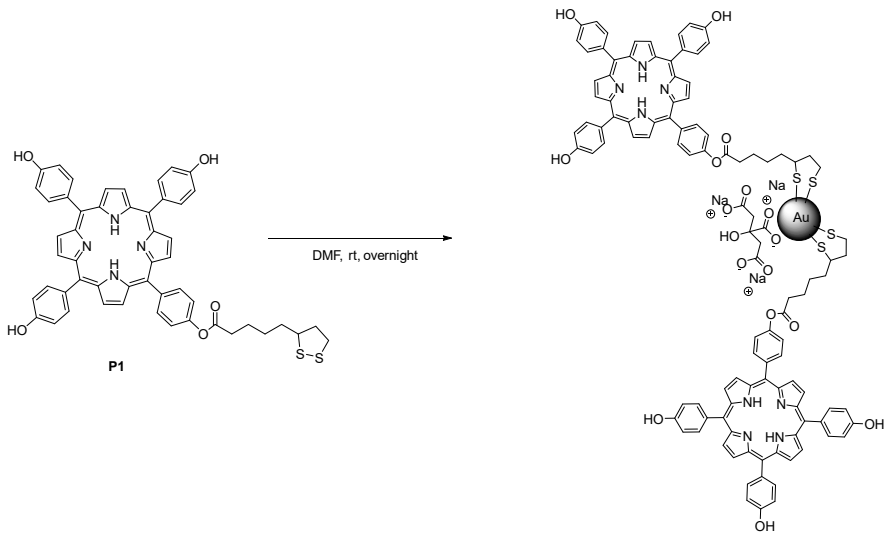

Scheme 2.32: Scheme of conjugation reaction between THPP_LA acid and citrate_AuNPs.

Since some factors can influence the conjugation process, different dilutions of THPP_LA and different volumes of citrate_AuNPs were employed to obtain the best percentage of porphyrin conjugated on AuNPs. The conditions are summarized in *table 2.4*. All the solutions were centrifuged at 9000 rpm for 20 minutes, the precipitates were washed three times with DMSO, redispersed into 3 mL of DMSO and characterized by UV-Vis in a concentration of 100 µl diluted in 900 µl using a cuvette with an optical path of 0.5 cm. In order to use an amount of porphyrin that is in excess compared to the concentration of citrate_AuNPs, concentration of citrate_AuNPs was estimated from some theoretical calculations. The first step is estimate the average size of AuNPs from the absorption in the UV-vis spectra following the method postulated by Haiss et al.:[14]

$$d = \frac{\ln \frac{(\lambda_{spr} - \lambda_0)}{L_1}}{L_2} \qquad (1)$$

where the theoretical values for d > 25 nm are $\lambda_0 = 512$, $L_1 = 6.53$ and $L_2 = 0.0216$. Obtained the average size of AuNPs from equation (1), it is possible to calculate the molar concentration of nanoparticles from the average number of gold atoms per nanoparticle. In the specific case of gold, Liu et al.[26] determined the following relationship between the average number of gold atoms (N) per nanoparticle, the particle diameter (*D*) and Avogadro number (N_A):

$$N = \frac{\pi \left(1{,}93 \frac{g}{cm^3}\right) D^3}{6 \left(197 \frac{g}{mol}\right)} \; x \; N_A = \text{atoms/nanoparticles} \qquad (2)$$

$$\text{Concentration (mol/L)} = \frac{mol\ of\ Au\ in\ the\ reaction}{N\ x\ V\ (L)} \qquad (3)$$

Combining this three equations, the concentration of citrate_AuNPs was approximately 0,2 nM. According to this, since the porphyrin is used always in an huge excess, its dilution factor, combined with the volume of citrate_AuNPs, was very important to avoid the formation of aggregates.

Entry	Conc. (mM) of THPP_LA	Vol. (mL) citrate_AuNPs	mL (THPP_LA)/ mL (citrate_AuNPs)
1	0.12	25	25/25 (1:1)
2	0.46	10	10/10 (1:1)
3	0.46	1.5	4.5/1 (3:1)
4	0.97	0.5	1:0.5 (2:1)
5	0.97	6	3:6 (1:2)

Table 2.4: Optimization conditions of THPP_LA on citrate_AuNPs.

In the UV-vis spectra (*figure 2.38*), are reported all the absorptions of the conjugates after purification process. The presence of THPP_lipoic is confirmed by the Soret band centered at 420 nm. In the UV-vis spectra of entry 2 (black line) and 3 (blue line) the band of AuNPs became broad and shifted. In the case of *entry 2*, the Soret band is present – even if in low percentage – in the case of *entry 3*, any loading of porphyrin was observed. In the other cases, entry 1 (red line) and entry 4 (light blue line) the loading of THPP_lipoic increased and the best result was obtained in the conditions reported in entry 5 (green line), where the Soret band increased its absorption due probably to the volume of gold higher than the volume of THPP_lipoic acid.

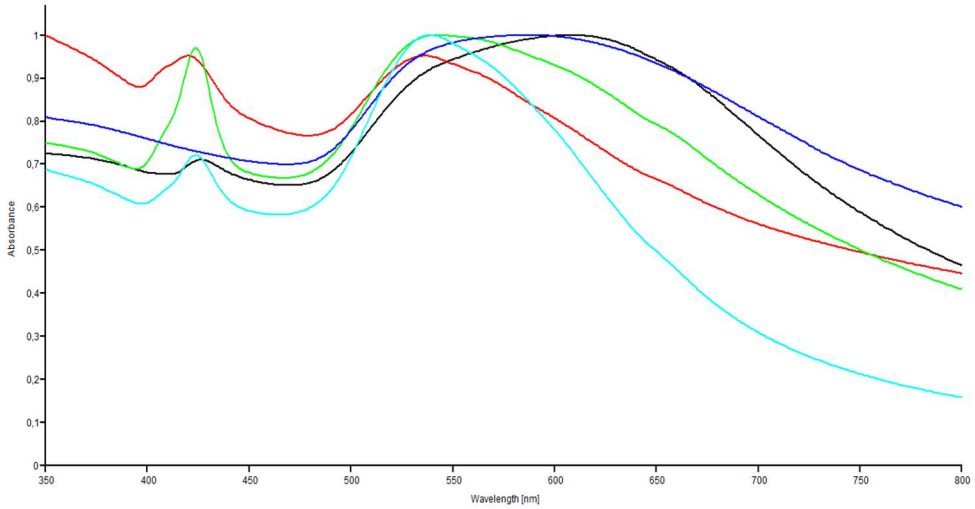

Figure 2.38: UV-vis spectra of THPP_LA on citrate@AuNPs in different conditions. UV-vis spectra of THPP_lipoic on citrate@AuNPs in different conditions. entry 1 (red line) and Entry 2 (**black line**) and 3 (blue line) entry 4 (light blue line) and entry 5 (green line).

In *figure 2.39* are overlapped the UV-vis spectra of citrate_AuNPs and THPP_LA@AuNPs (**NS1**). Besides the presence of the Soret band that confirms the conjugation of the porphyrin, a further confirm of the successful conjugation derives from the presence of LSPR of the AuNPs that is slightly red-shifted of ~ 10 nm. It was observed that the LSPR became broader after the conjugation probably due to the partial aggregation of THPP_LA@AuNPs (**NS1**) after centrifugation.

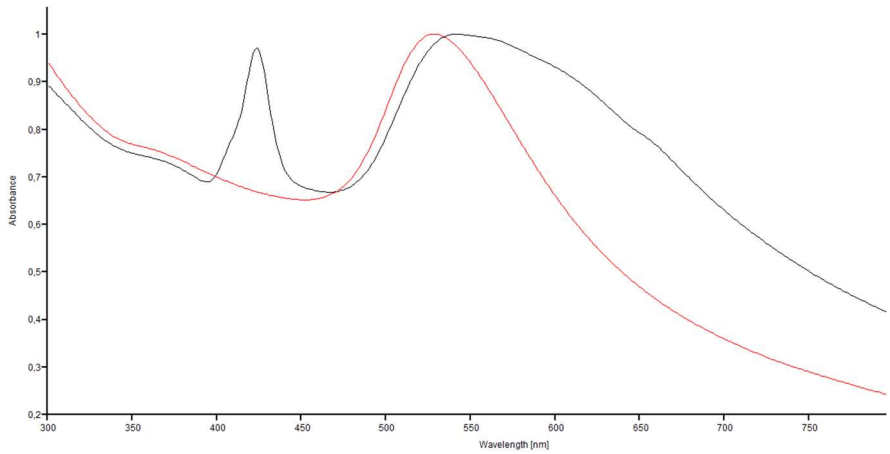

Figure 2.39: UV-vis of citrate_AuNPs (red line) and THPP_LA@AuNPs (**NS1**) (black line).

Moreover, although the presence of citrate on AuNPs surface, the conjugates weren't highly water soluble. Adding 2% of DMSO to the solution, the solubility slightly increased but the stability over the time was very low (~ 2 hours).
To improve this factor, linker **15** previously synthesized was introduced in the conjugation reaction with THPP_LA through two different strategies differing in the addition order of the two thiolated compounds, PEG_{750}-SH and THPP_LA, as shown in *Scheme 2.33*: in the first case (a) PEG_{750}-SH@AuNPs (**15**@AuNPs) were previously synthesized (see *chapter 2.2.2*) and then THPP_lipoic in a solution of DMF was added and the mixture was stirred overnight and in the second case (b) THPP_LA and PEG_{750}-SH (linker **15**) were mixed together in DMF/H_2O (1:1) and then added to a citrate@AuNPs and stirred overnight at room temperature. In both the strategies, the mixture are then centrifuged at 9000 rpm for 20 minutes, washed several times with DMSO, redispersed in DMSO or H_2O (with 2% of DMSO) and characterized by UV-Vis spectroscopy.

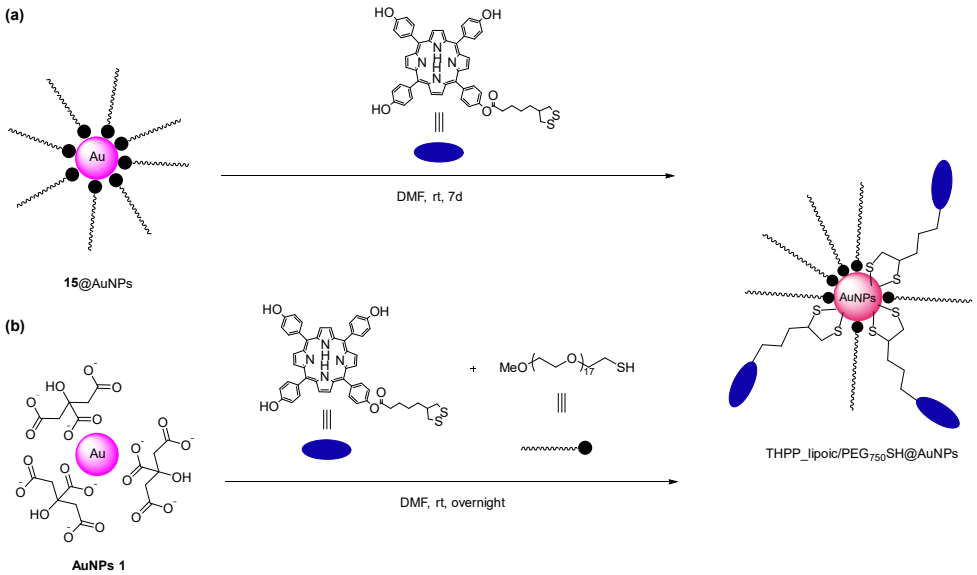

Scheme 2.33: Synthetic approaches to obtain THPP_LA/PEG_{750}SH@AuNPs (**NS2**) conjugate.

In the UV-vis spectra (*figure 2.40*) absorption of the nanosystem THPP_LA/PEG_{750}SH@AuNPs (**NS2**) obtained from both the strategies are overlapped. From the UV-vis spectra can be concluded that the conjugate from approach (b) (orange line) presented an higher loading of THPP_lipoic on AuNPs than the conjugate from synthesis (a) (blue line). Moreover, last one presented a

better solubility and stability in water rather than the conjugates without PEG chains.

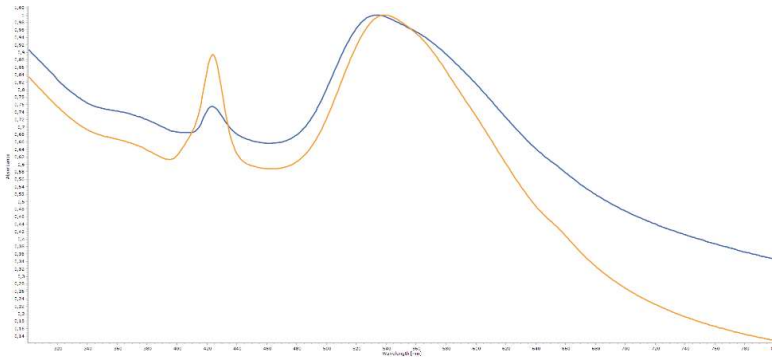

Figure 2.40 : UV-vis of THPP_LA/PEG_{750}SH@AuNPs (**NS2**) conjugate from strategy (a, blue line) and strategy (b, orange line).

As an alternative to the strategies, PEG chains can be introduced directly on the porphyrin as previously described in the *chapter 2.2.3*.

The tetrafunctionalized porphyrin **P3** was dissolved in 3 mL of DMF (1.4 mM) and added to 3 mL of citrate@AuNPs solution. After stirring at room temperature overnight, the nanosystem **NS3** were purified by centrifugation and characterized by UV-vis.

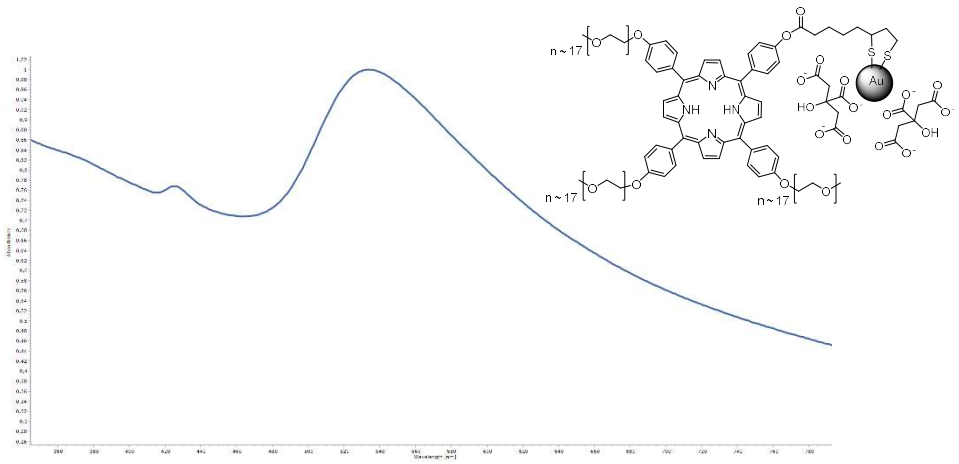

Figure 2.41: UV-vis spectra (DMSO) of tri-PEG_{750}-THPP_lipoic@citrate_AuNPs (**P3**@AuNPs, **NS3**).

In *figure 2.41*, is reported the UV-vis spectra that confirms the low loading of **P3** observing the Soret band centered at 403 nm on gold nanoparticles, probably due to the steric hindrance of PEG chains. A temperature increase did not give better results.

Also **P5_b** was conjugated to AuNPs and the conjugation reaction was performed at room temperature overnight. After centrifugation at 9000 rpm for 10 minutes and several washings with DMSO, **NS4** was characterized by UV-vis. From the UV-vis spectra (*figure 2.42*, blue line), the loading of **P5_b** revealed to be very low and in order to increase it, the reaction of conjugation was repeated increasing the temperature at 40°C. The increase of temperature allowed to obtain a higher loading of **P5_b** on AuNPs surface, as can be easily deduced from the UV-vis spectrum (*figure 2.42*, orange line) also decreasing the aggregation of AuNPs.

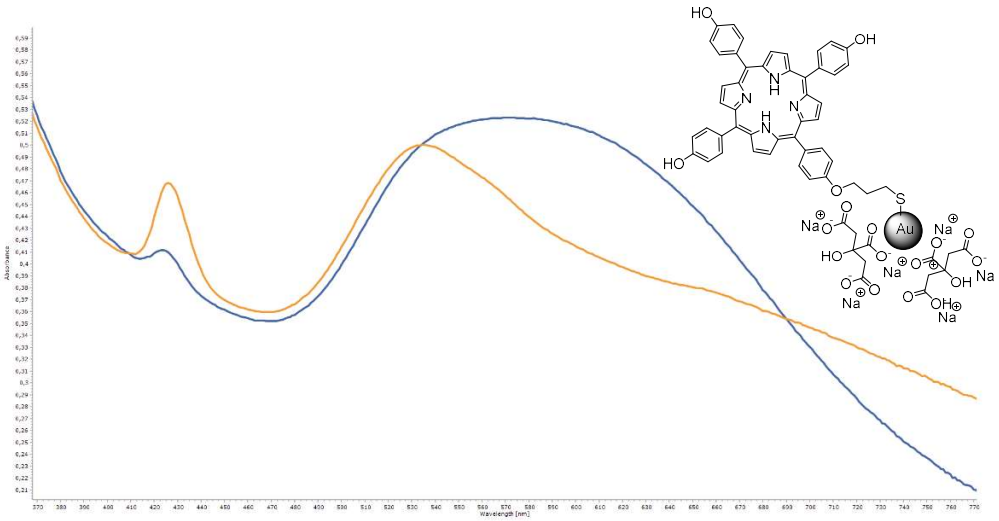

Figure 2.42: UV-vis spectra (DMSO) of THPPC3SH@citrateAuNPs (**P5_b**@AuNPs, **NS4**) at rt (blue line) and at 40°C (orange line).

Since **P5_b** is probably the dimer of THPPpropylSH, the low percentage of loading can be due to the low percentage of reduction of S-S bond. Thus, the same reaction was performed with a low amount of a reducing agent in order to improve the conjugation of **P5_b** but the percentage of loading remained almost the same.
Regarding the preparation of a nanosystem involving the porphyrin PpIX, a completely different strategy of conjugation was followed. Citrate_AuNPs were firstly mixed with 25kDa bPEI as described in *chapter 2.2.2*, then PpIX was added in a solution of DMF and stirred overnight. After centrifugation, the precipitate was redispersed into DMSO and the resulting **NS5** was characterized by UV-vis and DLS. Unfortunately, this methodology brought to highly aggregated and highly polydisperse nanoparticles. For this reason, was followed the protocol already described in *chapter 2.3* where PEI was used both as capping and reducing agent

then it is reacted with PpIX at room temperature for 6 hours (*scheme 2.34*). Its conjugation and drawbacks in biological application were previously discussed in the *Chapter 2.2.3*.

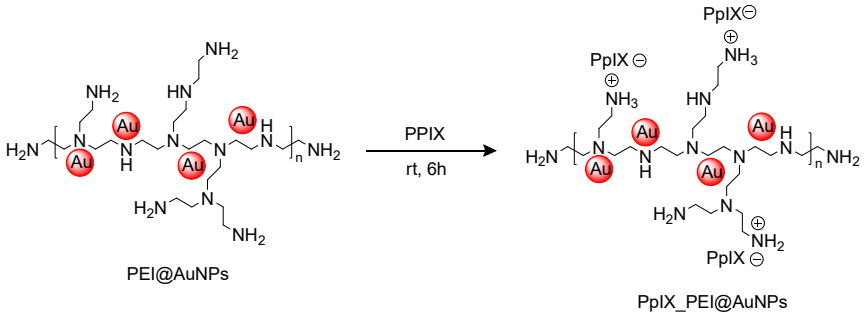

Figure 2.34: Synthesis of PpIX_PEI@AuNPs **NS5**.

2.2.5 Synthesis of Liposomes and encapsulation of nanosystem NS1 (during a period spent at Technion – Haifa).

As already presented, future development of this thesis work is to include porphyrin@AuNP nanosystems into convenient liposomes to facilitate the cellular up-take and to reach deep-seated cancer in order to deliver PDT promoted by X-Ray irradiation. An overview of different uses, structures and methods of synthesis of liposomes for biological applications have been discussed in the introduction. This chapter explains in detail the features needed by liposomes to be applied in X-ray induced PDT. Conventional liposomes are unsuitable for the on-demand content release, which limits their therapeutic utility, although they possess high efficiency of delivery. By contrast, triggerable liposomes are able to release genes/drugs in a more controlled manner, usually much faster and, depending on triggering modality, also to a specific area, and these properties contribute to their potentially greater clinical success. Several strategies have been previously employed to design responsive liposomes whose bilayer could be destabilized by using physiological and external stimuli. The triggering approaches previously reported include changes in pH (typical in cancer)[2], externally delivered heat, for example via alternating magnetic field or infrared light[3], enzymes and non-thermal effects caused by light irradiation[5]. These approaches have certain limitations, in particular triggering of light-sensitive liposomes by visible light is limited by its relatively shallow (few mm) penetration of light into biological tissues. As a result of this modest penetration depth, visible light cannot activate photosensitizers (PS)

located deeply in the body and generate sufficient amount of singlet oxygen ($^1O_2$) or other reactive oxygen species (ROS) to release the liposome cargo required for the therapeutic effects[27].

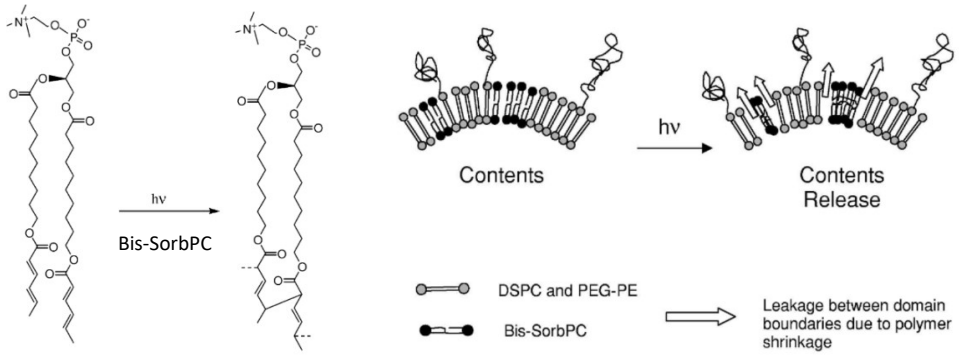

Figure 2.43 : (left) photoinduced crosslinking reaction of bis-SorbPC and (right) proposed photopolymerization-induced reduction in the surface area of bis-SorbPC domains.

Compared with light, X-rays with the suitable energy can easily penetrate the human body, activating gene/drug release in deep tissues once the X-ray triggered liposomes reach their target. This feature will open many opportunities for biomedical research and clinical medicine, from triggered gene therapies and chemotherapy, to enhanced PDT which currently suffers from limited penetration depth of illumination light (usually in the UV and visible region). With its excellent tissue penetration depth, X-ray radiation explored for liposome triggering offers an alternative approach to yield both spatial targeting (such as to a tumour site) via standard radiotherapy approaches such as the Gamma-knife and triggered release of encapsulated contents from the liposomes once they are located at the target site. Importantly, the X-ray liposome triggering can be used concurrently with radiation therapy, a common treatment modality in cancer.

Synthesis of liposomes was performed in the laboratory for Targeted Drug Delivery & Personalized Medicine Technologies at the Israel Institute of Technology – Technion (Haifa) in Israel under the supervision of Professor Avi Schroeder and Dr. Jeny Shklover. Generally, in this laboratory, liposomes are prepared by three components: primary lipid, cholesterol, and PEG 2000:DSPE in the ratio 55:40:5. The PEG helps to increase the retention time of the liposomes in the body, while the amount of cholesterol mimics the concentration of cholesterol in the cell

membrane, which plays a role in stabilizing of the bilayer and making the membrane less permeable to water soluble substances. Molecules can be loaded into liposomes by two major techniques: active and passive loading. In active loading, liposomes are first produced before introducing the substance into the liposome. In passive loading, the molecule is dissolved in the aqueous solution where the liposomes are produced in.

For the synthesis of liposomes with a concentration of 50 mM, POPC and DOPC were both employed using thin layer film method whose steps are described in *figure 2.44*. All the component were mixed, dissolved into chloroform and the solvent is slowly evaporated under reduced pressure and left under pressure of 2mbar for 30 minutes. The film formed at the bottom of the flask is conserved under vacuum overnight and hydrated with the solution to be incapsulated for one hour.

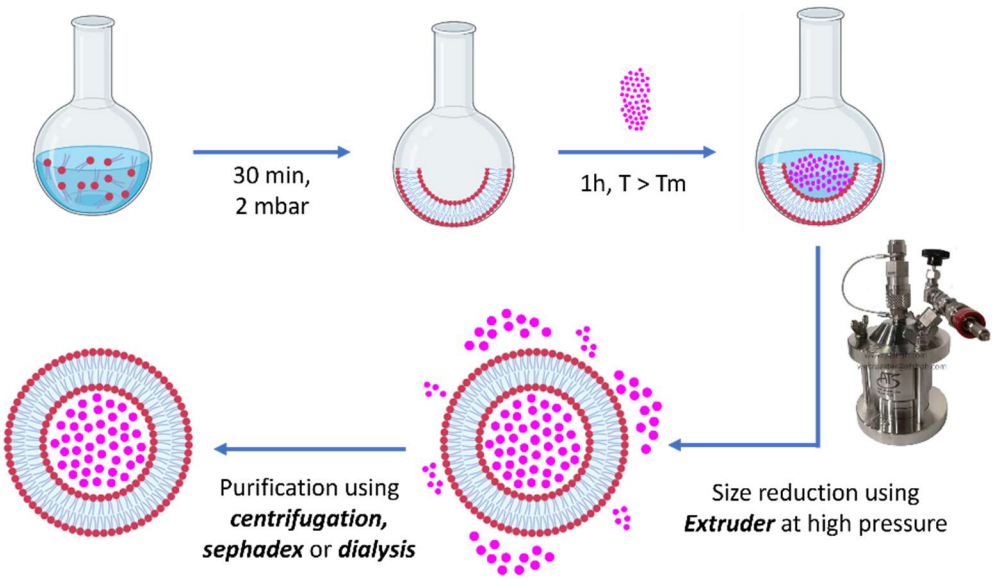

Figure 2.44: Steps of synthesis of liposomes with thin film layer method.

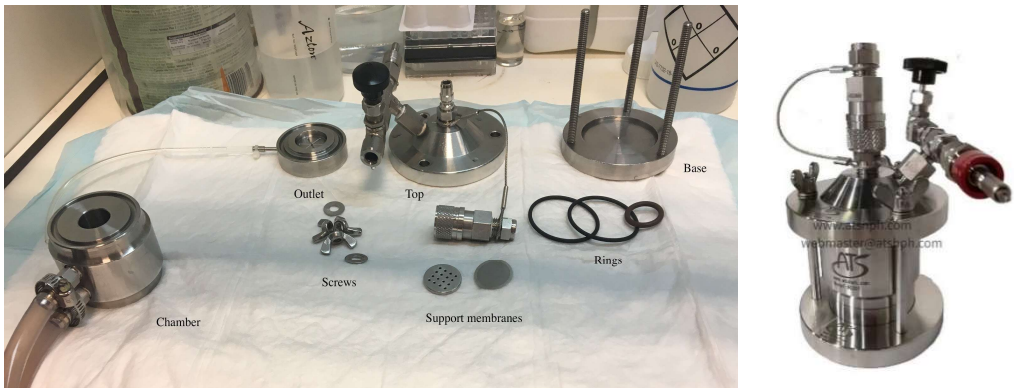

Figure 2.45: Components of extruder (left) and their assembly (right).

To prepare the extruder, the extruder water bath was turned on and set to 65°C. In *figure 2.45* are shown all the components of extruder that were assembled through the following procedure: firstly, the outlet was placed on base and the two metallic support membranes in the center of the outlet. Then, a PE drain disc, 0.2 µm and 0.4 µm membranes were carefully placed in this order, one of the larger black rings was placed in the indentation of the chamber and the small brown ring on top of the membranes, then the chamber was rested on top of the outlet and the last ring was placed on the indentation of the chamber. At the end, the top piece was placed through the nails of the base and screwed it into place, the gas (usually nitrogen) was attached to the sideways nozzle on the top piece.

Extrusion process allows to obtain, according to the dimension of the pore of the membranes, monodisperse liposomes of one dimension. Generally, for biological application, liposomes have a dimension of 100-200 nm in order to be internalized from the cells. The hydrated solution was extruded between 10 and 15 times and characterized using a Dynamic Light Scattering Method (DLS) that can provide information on the average diameter and polydispersity of the particles. It uses a photon counter that measures the fluctuations in light intensity that occur due to Doppler shift to make inferences on the size distribution of particles. Firstly, to include citrate_AuNPs into liposomes the protocol proposed by Contini et al.[28]. They investigated the size dependence of the physical chemical interaction of citrate_AuNPs with a diameter ranging from 5 to 60 nm (i.e., 5, 10, 25, 35, 50 and 60 nm) with unilamellar liposomes (diameter of ~180 nm) using two type of formulations: POPC (1-palmitoyl-2-oleoyl-glycero-3-phosphocholine) and DOPC (1,2-dileoyl-sn-glycero-3-phosphocholine). Both POPC and DOPC (lipid structure in

figure 2.46) are phosphocholine (PC) based lipids with a zwitterionic head group and consequently a neutral net charge; however, they differ in the structure of their lipid tails.

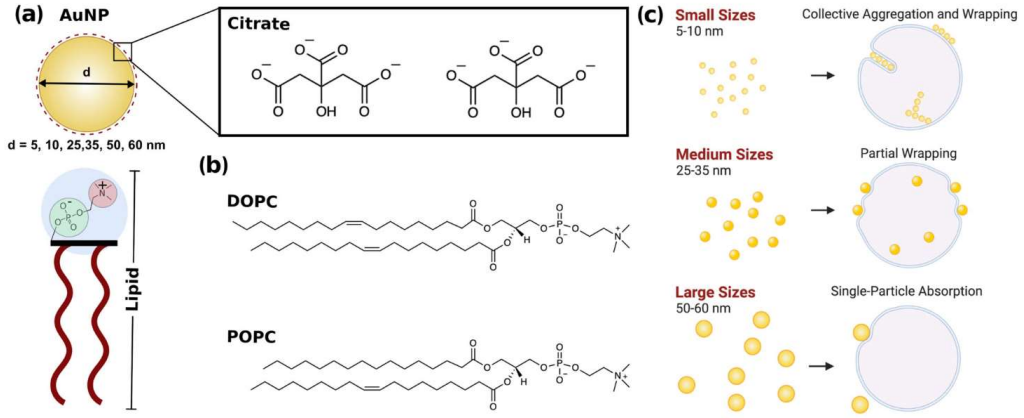

Figure 2.46: Schematic representation of the AuNP and lipid interactants and diverse outcomes arising from AuNPs–lipid membrane interactions at different size ranges. **(a)** Schematic of the citrate-stabilised AuNP and PC lipid interaction due to a combination of electrostatic and van der Waals interactions. Chemical structure of **(b)** DOPC and POPC phospholipids. **(c)** Summarising representation of the diverse AuNP–lipids interaction outcomes at different nanoparticles size range.

Lipid membranes are highly flexible, and the bilayer can be deformed due to AuNP adhesion on its surface. In *figure 2.46* it is shown that smaller AuNPs (5–10 nm) tend to form aggregates on the bilayer surface or are engulfed by the formation of wrapped linear aggregates within a tubular membrane. Conversely, larger AuNPs (25–35 nm) adsorb on the outer surface with an observable bending of membrane and characteristic penetration depth while, for diameters between 50 and 60 nm, the AuNP-membrane absorption events are affected by the increase of the membrane tension due to the decrease of the liposome/AuNP's surface area ratio. As preliminary experiment, POPC and DOPC lipids, together with Cholesterol and DSPE-2000PEG, were used to create two thin film layers that were then hydrated with 3 mL of 3.7 mM of sodium citrate. Since POPC allowed the formation of 200 nm liposomes with a better polydispersity index (~ 0.076), other liposomes were synthesized only using POPC, and several experiments were performed to encapsulate 25-35 nm citrate_AuNPs. Since citrate_AuNPs were larger than expectation and highly polydisperse, they were firstly filtered with a filter with a cut-off of 0.22 µm and then extruded (at 10 bar) two times with 0.4 and 0.2 µm membranes. After this, citrate_AuNPs were characterized with DLS.

			Size (d.nm):	% Intensity:	St Dev (d.n...
Z-Average (d.nm):	14.36	Peak 1:	33.43	76.6	11.79
PdI:	0.565	Peak 2:	1.456	23.4	0.4045
Intercept:	0.771	Peak 3:	0.000	0.0	0.000

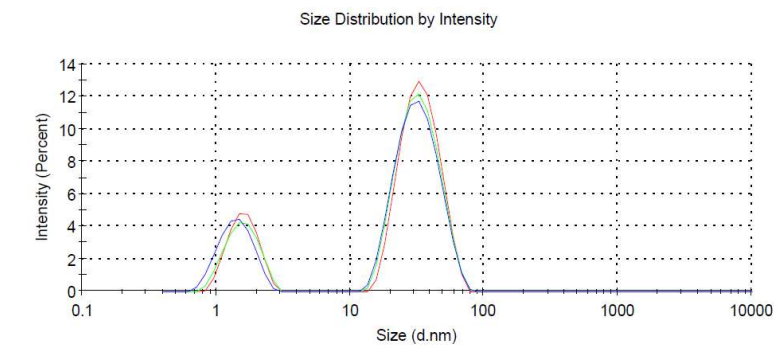

Figure 2.47: DLS of citrate AuNPs after filtration (cut-off of 0.22 µm) and extrusion for two times with 0.4 µm and 0.2 µm membranes.

After filtration and extrusion, two sizes of AuNPs were determined by DLS, 33 nm (77%) and 1.5 nm (23%) with an average size of 14 nm (*figure 2.47*). First, it was studied the encapsulation of citrate_AuNPs (pink dots) and THPP (green dots) separately, as shown in *figure 2.48*. AuNPs solution was used directly in the hydration process while THPP was firstly dissolved in water at pH 11 and 0.1% of DMSO with a final THPP concentration of 0.92 mM. Both the solution were used to hydrate the film previously synthesized, extruded 10 times at a pressure of 10-20 bar. The resulting liposomes were characterized by DLS and were purified as briefly schematized in *figure 2.48*.

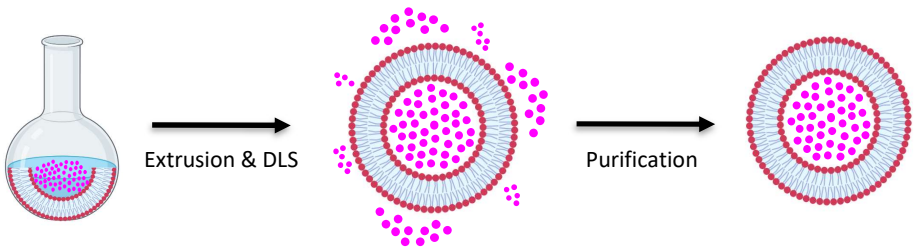

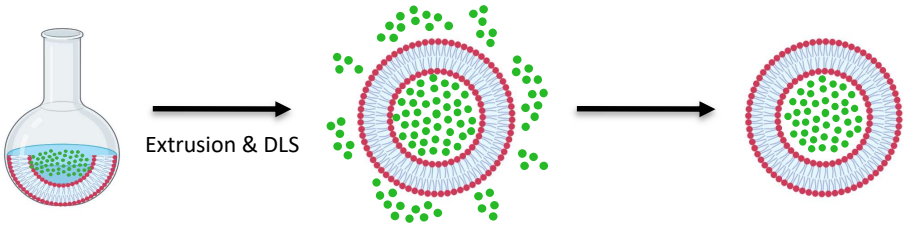

Figure 2.48: Scheme of encapsulation of citrate_AuNPs (pink dots) and THPP (green dots).

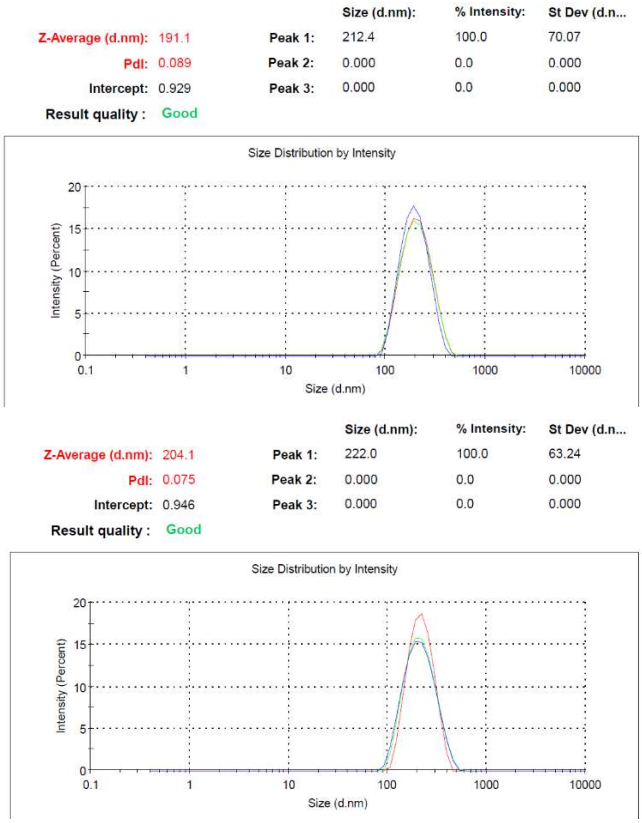

Figure 2.49: DLS of citrate_AuNPs liposomes (top) and THPP_liposomes (bottom) after 10 extrusions.

In *figure 2.49* are reported the DLS of citrate_AuNPs liposomes (*top*) and THPP liposomes (*bottom*) after extrusion repeated 10 times. The first sample showed an average size of 191 nm and a polydispersity index of 0.089 while the second sample showed an average size of 204 nm and a polydispersity index of 0.075. The second sample (THPP liposomes) revealed an average size of 174 nm and a polydispersity index of 0.1. After characterisation, each sample was purified in order to remove

the not encapsulated nanomaterial and determine the encapsulation efficiency (EE%). To remove gold nanoparticles that haven't been encapsulated in liposomes, the sample was centrifuged at 10000 rpm for 5 minutes, the supernatant was removed and characterized by UV-vis. In this case a reduced absorption ascribed to AuNPs can be seen at 524 nm evidencing that encapsulation worked. First of all, in order to quantify the amount of AuNPs encapsulated into liposomes, a calibration curve of citrate gold nanoparticles was built up measuring the absorbance of gold nanoparticles solutions with different concentrations and calculating the concentration from the equation (1), (2) and (3) discussed in the previous pages: a) 200 µl of gold nanoparticles (final concentration: 0.2 nM, A=0.734), b) 150 µl of gold nanoparticles + 50 µl of citrate water solution (final concentration: 0.15 nM, A=0.569), c) 100 µl of gold nanoparticles + 100 µl of citrate water solution (final concentration: 0.1 nM, A=0.392) and 50 µl of gold nanoparticles + 150 µl of citrate water solution (final concentration: 0.05 nM, A=0.229). From this solutions, plotting the absorbances (y) and the concentrations (x), the calibration curve resulted y = 3.4054x + 0,053 as shown in *figure 2.50*.

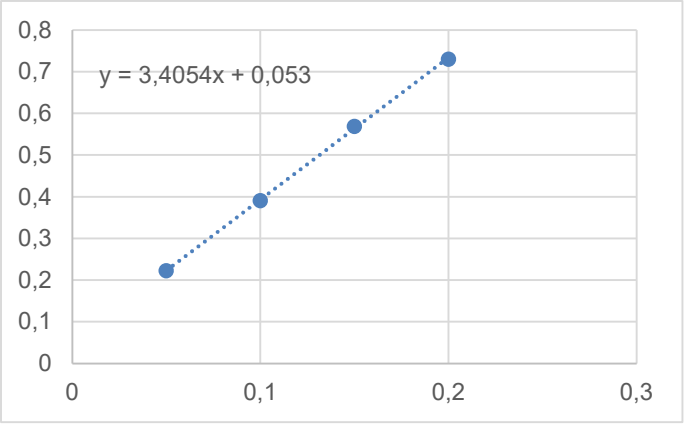

Figure 2.50: Calibration curve of citrate_AuNPs.

After centrifugation, the precipitate (free AuNPs) was redispersed in the same volume of water of the starting sample and characterized by UV-Vis spectroscopy. Since the UV-vis spectra of the sample shows a peak at 524 nm with an absorbance of 0.44, from the equation of the calibration curve was possible to calculate the concentration of free gold nanoparticles (0.11 nM). From this result, the encapsulation efficiency of AuNPs into liposomes can be calculated using this

formula: [(total drug - free drug)/ total drug] x 100 = [(0.2 – 0.1)/ 0.2] x 100 = 45%. As double test, the supernatant was treated with 1% of TRITON, a surfactant that burst liposomes so that they can release encapsulated nanoparticles. The solution was incubated for 1h at 58°C, then was centrifugated at 10000 rpm for 5 minute in order to promote the precipitation of the released AuNPs. In the end, the pellets were redispersed in the same starting volume (1.5 mL of 3.7 mM citrate solution) and characterized by UV-vis. The solution showed a peak at 510 nm with an absorbance of 0.4137. Following the same method described above, from the calibration curve, the amount of AuNPs Encapsulated was calculated through the following formula: (encapsulated drug / total drug) x 100 = (0.106/0.2) x 100 = 53%. This result was reliable with the first calculation of encapsulated AuNPs and can be concluded that the first method to calculate EE% of a nanomaterial can be followed for the next experiments. Regarding the case of porphyrin, in order to remove the unencapsulated THPP, the sample was neutralized with a solution of HCl 0.1 M. Since free porphyrin was not water soluble, the pH variation to neutrality caused its precipitation. But, the centrifugation at 10000 rpm for 5 minutes was inefficient to remove it. Other methods of purification were evaluated such as dialysis. Dialysis works on the principles of the diffusion of solutes and ultrafiltration of fluids across a semipermeable membrane or dialysis bag. This sealed dialysis bag is placed in a container of a different solution (generally pure water or phosphate buffer saline, PBS). Molecules small enough to pass through the tubing (often water, salts, and other small molecules) tend to move into or out of the dialysis bag, in the direction of decreasing concentration as shown in *figure 2.51.* Larger molecules that have dimensions significantly greater than the pore diameter are retained inside the dialysis bag.

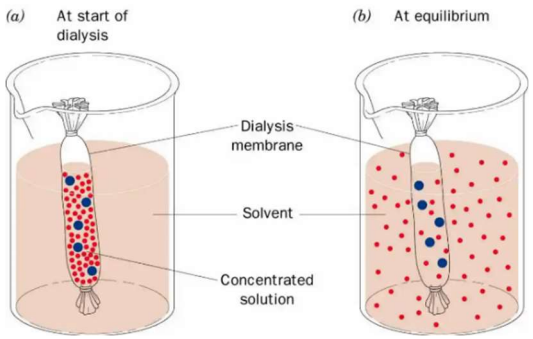

Figure 2.51: Dialysis bag as purification process.

In practice, sealed dialysis bag was put in a 3 litres beaker filled with PBS buffer or basic water (pH = 11) with 0.1% of DMSO. The buffer was changed after 1h, 3h and 24h but with both the buffer solutions the unencapsulated porphyrin didn't diffuse in the medium. As other method of purification it was used Sephadex G-50c that is a well-established gel filtration resin for desalting and buffer exchange of peptides and small biomolecules. Sephadex G-50c columns allow to separate macromolecules with molecular weight between 1.5 and 30 kDa (like liposomes) from molecules with molecular weight < 1.5 kDa (in this case THPP) as showed in *figure 2.52*.

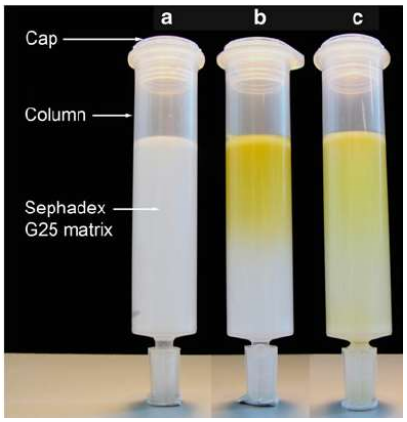

Figure 2.52: Sephadex as purification process.

Sephadex revealed to be an efficient method of purification of free THPP inside liposomes. Briefly, is reported how to use sephadex and how to calculate the final concentration of liposomes: firstly, 4 grams of Sephadex were swelled in 20 mL of double distilled water (DDW) and left it overnight, then the column (that is usually kept in a 70% ethanol solution) was cleaned to remove ethanol residues by a centrifuge of 400 g (rcf) and 4 °C for a minute and sephadex loaded on the column. The sample was then loaded and left for 4-minute incubation to allow diffusion and separation and centrifuged at 400 g and 4 degrees for 5 minutes to receive the dead volume (AKA V_0). After this, was possible to quantify the concentration of liposomes by estimating the concentration according to the $C_i*V_i=C_f*V_f$ formula (where C_i = concentration sample loaded, V_i = volume loaded, C_f = x, V_f = volume after centrifuge). Unfortunately, since free THPP remained on the Sephadex column, Since when the porphyrin is inside liposomes its absorption and consequently its

concentration can change, it wasn't possible to calculate the EE% into liposomes following the methods described above for the AuNPs. After finding the method of purification of liposomes from free AuNPs and THPP, other film were hydrated with (a) a mixed solution of THPP and citrate_AuNPs in solution (1:1) and (b) a solution of the conjugate THPPlipoic@citrate_AuNPs (NS1) as shown in *figure 2.53*. In this preliminary study, only this conjugated was tested in the experiments of encapsulation into liposomes.

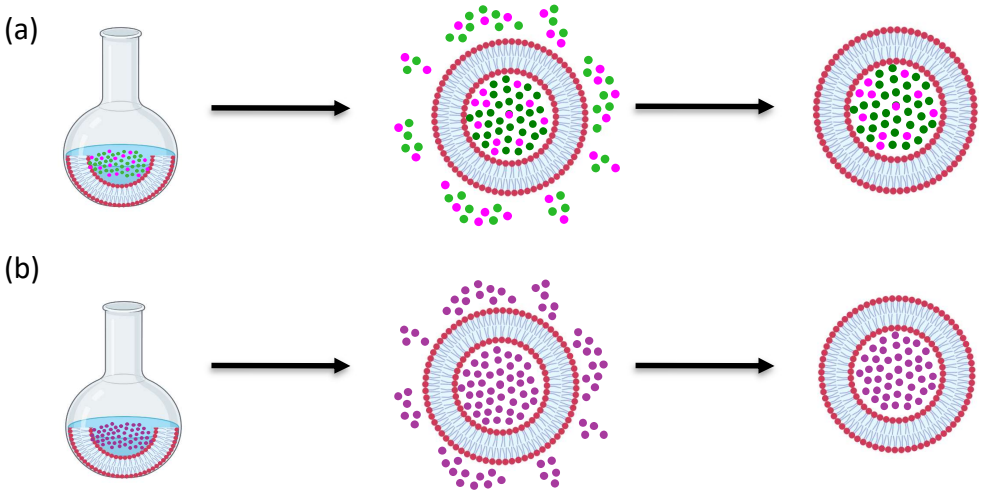

Figure 2.53: Scheme of encapsulation of mixture of THPP and citrate_AuNPs in solution (1:1) (pink and green dots) and conjugate NS1 (purple dots).

Liposomes including the mixture THPP/citrate_AuNPs in solution (1:1) and THPP@citrate_AuNPs (NS1) were extruded 5 times and characterized by DLS that revealed a peak of 160 nm (polydispersity index of 0.122) and a peak of 177 nm (polydispersity index of 0.117) respectively. The first sample was then purified by centrifugation at 10000 rpm for 5 minutes (to remove the unencapsulated AuNPs) and Sephadex G50-c (to remove the unencapsulated THPP) while the second sample was purified only with centrifuge since THPP is conjugated to AuNPs. All the samples were characterized also by UV-vis and fluorescence spectroscopy in water (pH = 11) and 0.1% DMSO.

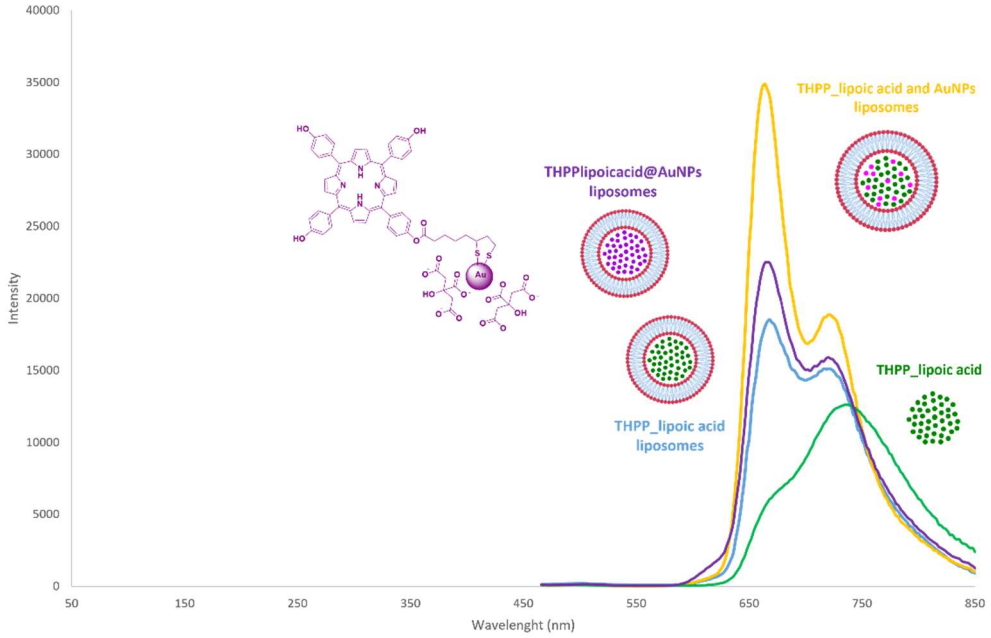

Figure 2.54: Fluorescence spectra of THPP (green line), THPP liposomes (blue line), THPP and citrate_AuNPs in solution liposomes (1:1) (yellow line) and THPPlipoic@AuNPs liposomes (purple line).

From the fluorescence spectra (*figure 2.54*) it can be stated that fluorescence of the porphyrin is retained inside liposomes in water medium (blue line) compared to the fluorescence of free porphyrin (green line), probably due by its low solubility in water. Since THPP_LA has the same concentration in the various hydration processes of the thin film layer and assuming that its encapsulation efficiency is almost the same, it was observed an huge enhancement of fluorescence when THPP and AuNPs mixed in solution were encapsulated into liposomes. When THPP_LA@citrate_AuNPs conjugate (NS1) was inserted into liposomes, this enhancement of fluorescence was highly reduced probably due to the lower encapsulation efficiency (45%) of THPP_LA when bound to AuNPs. A notably result is the possibility of simultaneously introducing free PS and AuNPs inside liposomes, allowing their conjugation directly into their inner phase in order to introduce more porphyrin into the liposomes and consequently into the cancer cells in future *in-vitro* experiments. It is important to notice that fluorescence is not an optical property that is proportional to the production of single oxygen, which is produced by PS when intersystem crossing (ISC) occurs as an alternative pathway to fluorescence (K_f) as shown in *figure 2.55*. For this reason, the decrease of

fluorescence could be due not only to lower inclusion but it could be hypothetically ascribed to the increased production of singlet oxygen.

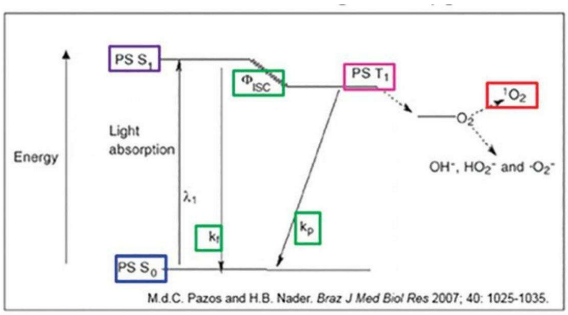

PS S_0 = singlet ground state photosensitizer
PS S_1 = short-lived singlet excited state photosensitizer (ns)
PS T_1 = long-lived triplet state photosensitizer (us)
k_f = fluorescence; k_p = phosphorescence; Φ_{isc} = intersystem crossing;
$^1O_2$ = singlet oxygen.

Figure 2.55: Mechanism of production of singlet oxygen by intersystem crossing.

For this reason, it is important to evaluate the effective singlet oxygen production of the nanosystems prepared, starting from THPP_LA@AuNPs. Some results are reported in the next chapter.

2.2.6 Singlet Oxygen production

Tada et al. presented two method to quantify the generation of $^1O_2$: directly and indirectly.[29] In our study, $^1O_2$ generation was confirmed by using anthracene-9,10-dipropionic acid disodium salt (ADPA), monitoring the photobleaching of its absorbance intensity at 380 nm by UV-vis spectroscopy. $^1O_2$ reacts with ADPA, a salt with a strong absorption in the UV region, to produce an endoperoxide, $ADPAO_2$, which has no absorption at that wavelength (*figure 2.56)*. The decrease of the ADPA absorption is directly correlated to the production of $^1O_2$.

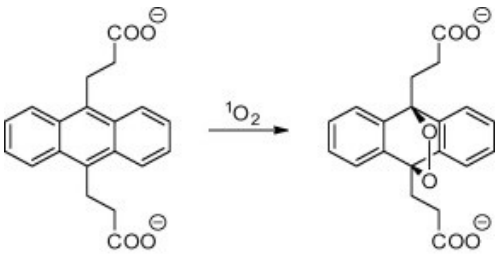

Figure 2.56: ADPA photobleaching mechanism in presence of singlet oxygen ($^1O_2$).

Even if the nano-system was originally created to produce $^1O_2$ under X-Ray radiation, as preliminary study, the $^1O_2$ production was quantified under different sources of visible light. In order to verify this phenomena, light sources employed were the following: blue (λ= 400–500 nm), green (λ= 500–600 nm), red (λ= 600–700 nm) and white light (that is given by the combination of blue, green and red light).
The main goal of irradiating the samples with LED lights instead of X-ray radiation is to conduct a preliminary study UV-vis to determine the possible enhancement/quenching of $^1O_2$ production by PS depending depending on the distance between the porphyrin and AuNPs. Penon et al.[30] demonstrated that: (1) when the porphyrin is immobilized onto the surface of the gold nanoparticles, singlet oxygen is produced, (2) the % rate of ADPA photobleaching achieved is proportional to the amount of porphyrin on the nanoparticles, (3) the solvent has a pronounced influence on the singlet oxygen quantification, probably due to the reduced lifetime of singlet oxygen in aqueous solutions as compared to that found in organic solvents. The number of Porphyrin-SH (PR-SH) molecules immobilized on the surface of AuNPs can be estimated by UV–Vis absorption spectroscopy using the absorption intensity of its Soret band. First, a calibration curve using known

concentrations of THPP_lipoic (**P1**) in DMSO solution (from 0.5 to 2.5 µM) was obtained (*figure 2.57*).

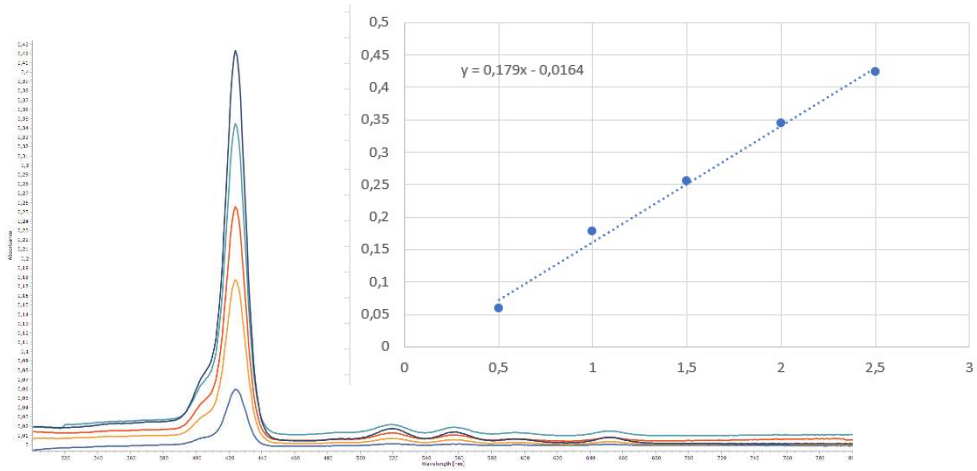

Figure 2.57: Calibration curve of THPP_lipoic in DMSO (0.5 µM, 1 µM, 1.5 µM, 2 µM, 2.5 µM).

From the calibration curve obtained and applying the Beer-Lambert law, the concentration of the THPP_lipoic immobilized on the gold nanoparticles can be estimated. To eliminate the contribution of the gold nanoparticles to the UV-Vis extinction spectrum of the functionalized nanoparticles, the extinction at 460 nm (contribution of the AuNPs) was subtracted from the corresponding Soret band of the porphyrin as indicated in *figure 2.58*, according to a method reported in the literature.[30]

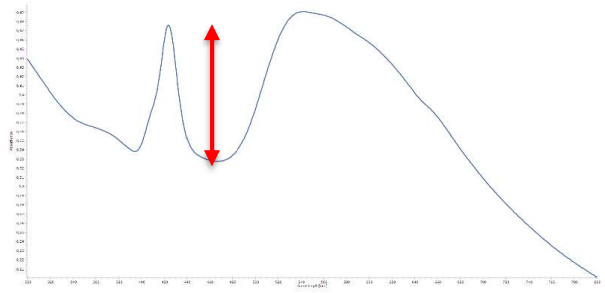

Figure 2.58: UV-Visible extinction spectra used to calculate the contribution of **THPP_LA** to the extinction intensity of **THPP_LA-AuNPs**.

With the calibration curve obtained, the concentration of THPP_LA on AuNPs can be calculated from the absorption peak at ~ 420 nm. The concentration of THPP_LA

in the conjugates THPP_LA@AuNPs and THPP_LA/PEG_{750}SH@AuNPs is 0,37 µM and 1,22 µM respectively. Then, the ability of the free porphyrin THPP_LA, THPP_LA@AuNPs and THPP_LA/PEG_{750}SH@AuNPs to produce singlet oxygen was investigated. The different samples were irradiated during 4 h in the presence of 9,10-anthracenedipropionic acid (ADPA) (270 µl of a 1.1 mM solution in methanol). The formation of the endoperoxide can be followed by measuring the UV–Vis absorption decay of the ADPA upon irradiation after every hour. The photobleaching of the ADPA upon irradiation of THPP_LA and with a blue light source is shown in *figure 2.59,* where the decrease of ADPA absorption band at λ = 378 nm indicates the percentage of the ADPA that had been converted to the endoperoxide. To be able to compare the singlet oxygen production of the different samples, the rate of ADPA photobleaching was normalized using the corresponding concentration of the photosensitizer and following equation (4):

$$Rate\ of\ ADPA\ photobleaching = \frac{Abs_{378}(t=0) - Abs_{378}\,(t=1h)}{[PR-SH](mM) * 60\ min}$$

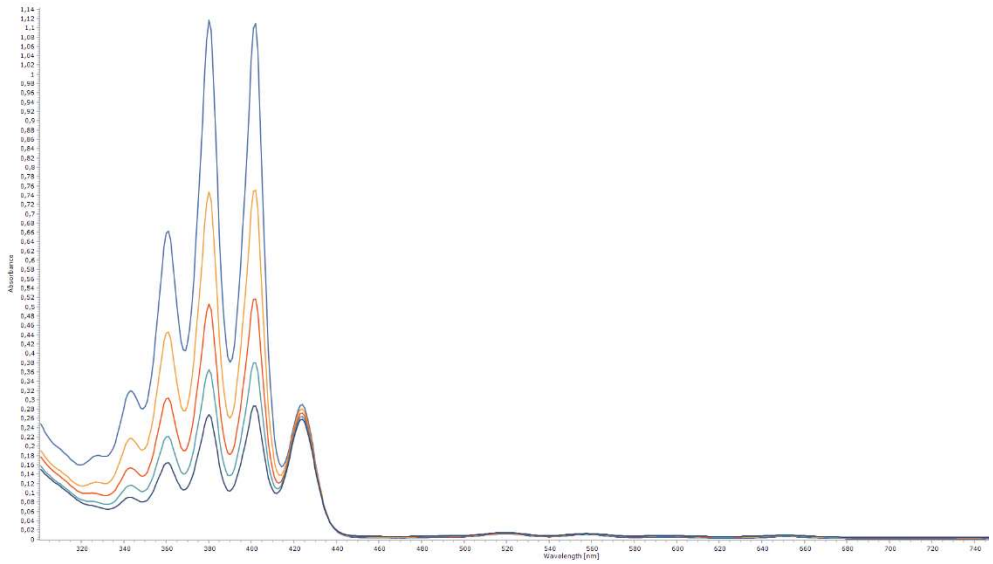

Figure 2.59: Photobleaching of ADPA in 4h upon irradiation with white light with a solution ~1 µM of THPP_LA and 1.1 mM of ADPA.

These experiments were firstly performed in DMSO since THPP_LA, THPP_LA@AuNPs and THPP_LA/PEG_{750}SH@AuNPs are not water soluble. THPP_LA

was firstly dissolved in DMSO (3 mL) and its concentration was estimated to be 1,08 µM through the calibration curve. The absorption band at 423 nm corresponds to the Soret band of the porphyrin derivative whereas the bands at ca. 340, 360, 378 and 400 nm correspond to the characteristic absorbance profile of the ADPA molecule. The rate of ADPA photobleaching obtained through the equation (4) testing red, blue, green and white light was 1,30, 2,25, 5,28 and 5,69 Abs/[mM]*min respectively after 1 h. From this result can be easily concluded that the highest $^1O_2$ production in DMSO was achieved irradiating with white light. In *figure 2.64* the time-dependent decay of the ADPA absorption is reported during irradiation of THPP_lipoic with white light while no significant changes were observed of the Soret band of the porphyrin. Compared to the free THPP_LA (5,64 Abs/[mM]*min) and using the equation (4), the photobleaching of ADPA given by the conjugates THPP_LA@AuNPs and THPP_LA/PEG_{750}SH@AuNPs was lower, being 3,81 and 2,00 Abs/[mM]*min respectively. In order to see if the $^1O_2$ production is retained in biological medium, the singlet oxygen production by the conjugate **P3**@AuNPs in water with a 5% of DMSO was tested. Firstly, the concentration of **P3** on AuNPs calculated using the calibration curve built up for **P3** was 0,75 µM. Through equation (4), the $^1O_2$ production in water was 2,80 Abs/[mM]*min that demonstrated that, also in this case, the $^1O_2$ was quenched in comparison with free porphyrin. The results obtained in the production of $^1O_2$ with lipoic acid (C6) as linker between THPP and AuNPs are summarized in *table 2.5*.

	P1 (DMSO)	**P1**@AuNPs (DMSO)	**P1**/PEGSH@AuNPs (DMSO)	**P3**@AuNPs (H_2O/5% DMSO)
Rate of ADPA photobleaching (Abs/[mM]*min)	5,64	3,81	2,00	2,80

Table 2.5: Photobleaching of ADPA of P1, P1@AuNPs, P1/PEGSH@AuNPs and P3@AuNPs.

This results demonstrated that, at this distance, the $^1O_2$ production of THPP_LA@AuNPs is quenched both in DMSO and in water. Prompted by to these results to investigate the dependence of $^1O_2$ production on the distance between AuNPs and porphyrin, the production of $^1O_2$ using a shorter linker (THPPC_3SH and THPPC_3SH@AuNPs) was tested using ADPA. Firstly, a calibration curve of THPPC_3SH

was built up from different solution in DMSO with known concentrations: 0.25 µM, 0.5 µM, 1 µM, 1.5 µM, 2 µM, 3 µM. Measuring the absorption peak of the Soret band of each solution, the calibration curve resulted to be y=0,2163x + 0,0047. Then, both THPPC$_3$SH (**P5**) and THPPC$_3$SH@AuNPs (**P5**@AuNPs) were dissolved into 3 mL of DMSO and the concentrations of the porphyrin calculated through the calibration curve were 0,95 µM and 0,22 µM respectively. As previously described, for both the solutions the production of $^1O_2$ was then investigated and in *figure 2.60* is reported the photobleaching of ADPA in presence THPPC$_3$SH (top) THPPC$_3$SH@AuNPs (bottom) for 3 hours under the irradiation of white light.

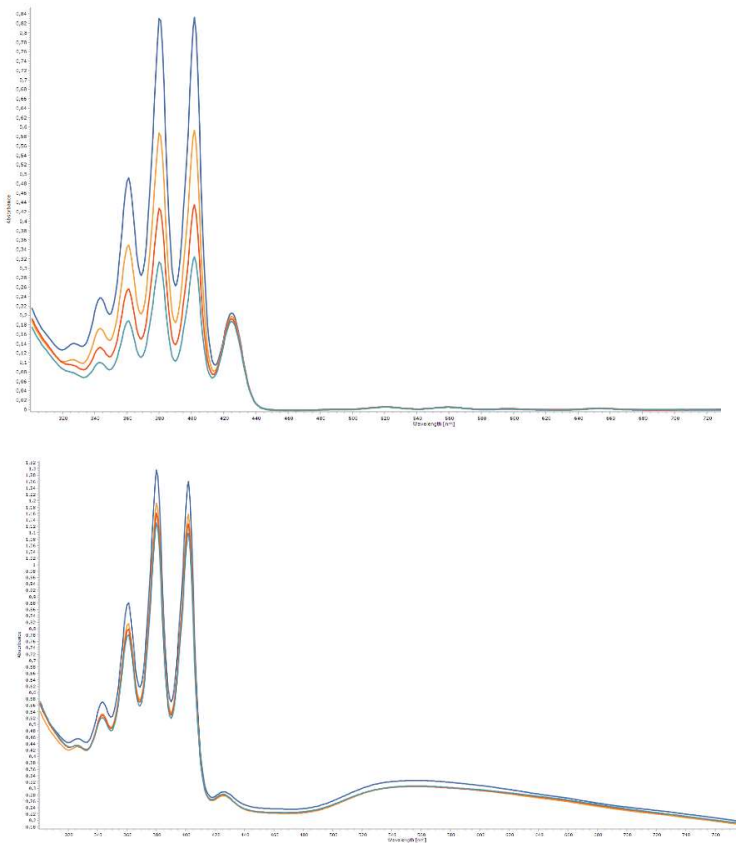

Figure 2.60: Photobleaching of ADPA during 4h upon irradiation with white light with a solution ~ 1µM of THPPpropylSH (top) and THPPpropylSH@AuNPs (bottom) in DMSO.

Using equation (4), % of photobleaching of ADPA in the first hour was 4,38 Abs/[mM]*min and 7,88 Abs/[mM]*min respectively. This was an excellent result that evidenced that, at this distance between PS and AuNP, the production of $^1O_2$

is enhanced almost twice when the porphyrin is conjugated to AuNPs. In *figure 2.61* is plotted the photobleaching of ADPA after each hour for THPPpropylSH (red line) and for THPPpropylSH@AuNPs (blu line) that easly demonstrates the enhancement of $^1O_2$ formation when the porphyrin is covalently bound on AuNPs through a linker of three carbon atoms. In this case, the rate of photobleaching of ADPA after 1 hour (y) is expressed through this formula: $(Abs_{t=0} - Abs_{t=1h})/Abs_{t=0}$ and plotted over time (x).

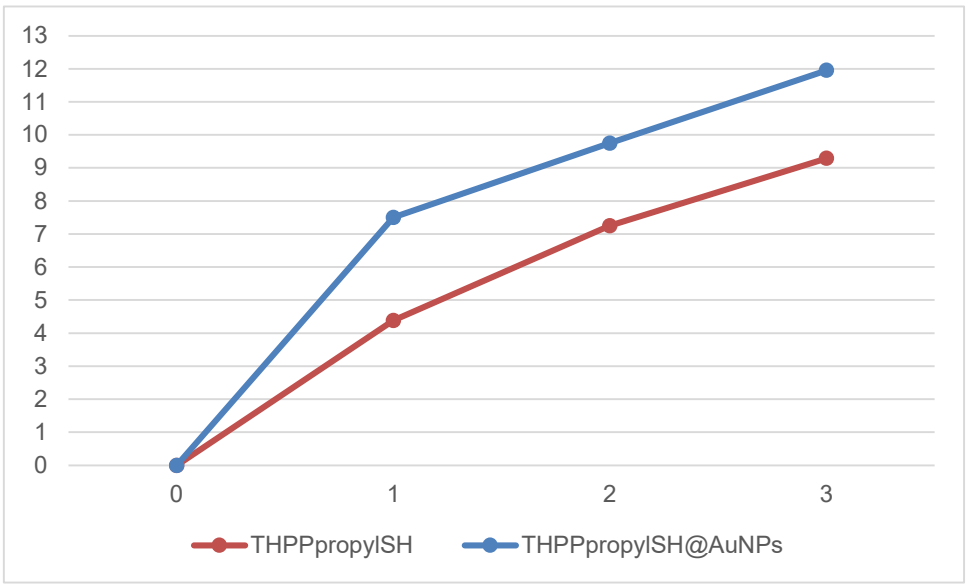

Figure 2.61: Photobleaching of ADPA in DMSO for $THPPC_3SH$ (red line) and $THPPC_3SH$@AuNPs (blue line) during 3 hours.

Last, preliminary measurements were performed using X-Ray irradiation. Thus, the $^1O_2$ production by **P5** and **P5**@AuNPs (see scheme 2.23) was examined under an X-Ray radiation with a beam working at 40 KeV and 20 mA. To distinguish the the production of $^1O_2$ generated from PS or AuNPs, thADPA, free AuNPs, free **P5** and **P5**@AuNPs were tested under X-Ray irradiation. Each sample was irradiated for 1 hour and monitored by Uv-vis every 30 minutes. Since in the first two samples there is no PS and the rate of photobleaching of ADPA cannot be normalized dividing for the concentration of the porphyrin, in *figure 2.62* (*top*) is reported the rate of consuming of ADPA by subtracting the absorbance at t=30 (or t=60) to the absorbance at t=0, then dividing the value for the absorbance at t=0. Each obtained value was then plotted in *figure 2.62* (*bottom*) as a function of time and confirms that the production of $^1O_2$ is higher for the **P5**@AuNPs sample than for the others.

t	ADPA	free AuNPs	free **P5**	**P5**@AuNPs
0	0	0	0	0
30	1,75	1,87	0	4,85
60	2,68	4,40	0,95	8,60

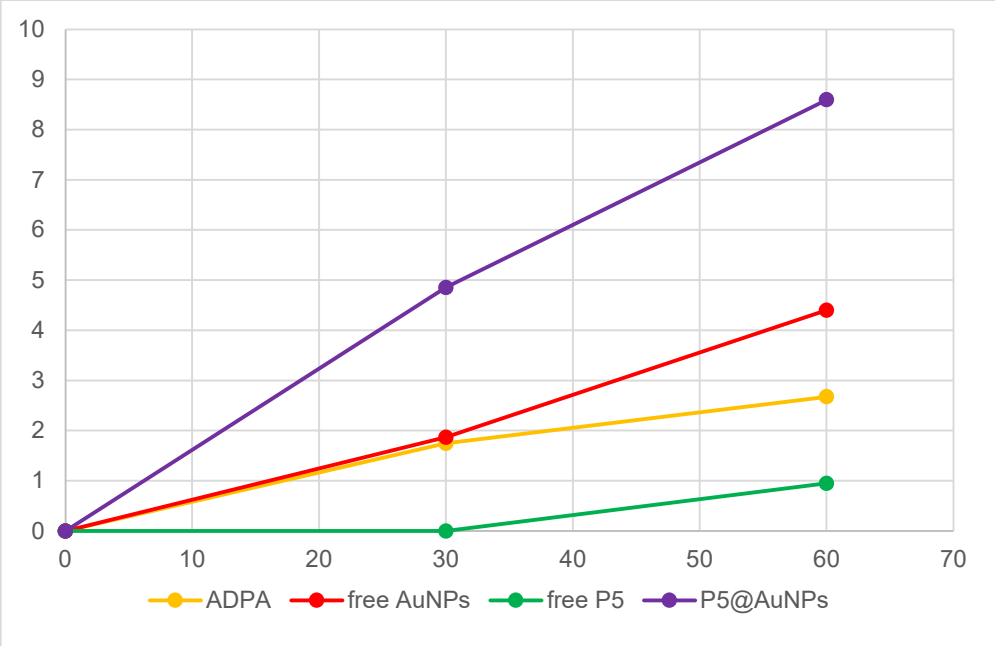

Figure 2.62: Photobleaching of ADPA in DMSO as a function of time during 1 hour of **P5**, **P5**@AuNPs, ADPA and AuNPs. Rate of photobleaching (y) over time (minutes, x).

The $^1O_2$ production under white light was studied also for PpIX_PEI@AuNPs for 3 hours, although this nanosystem is too large for cellular uptake. Firstly, as for **P1** and **P5**, a calibration curve was built up in DMSO with the concentration of 1, 2.5, 5 and 10 µM (y=0,0613x+0,0264). Since from this equation, the concentration of PPIX on PEI@AuNPs was 0.85 µM. An aliquot (500 µl) was diluted in order to obtain a final volume of 3 mL (with a final concentration of 0,14 µM) and 270 µl of ADPA 1.1 mM were added.

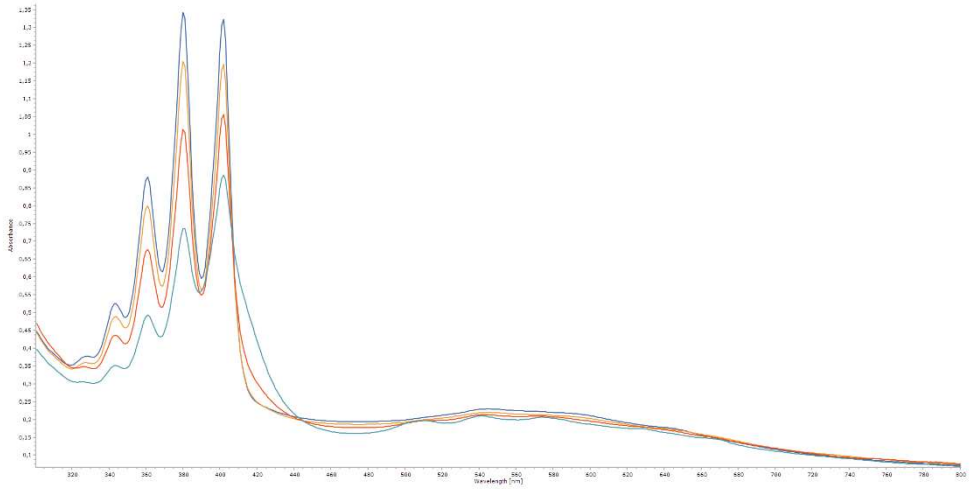

Figure 2.63: Photobleaching of ADPA of a PpIX_PEI@AuNPs solution in DMSO upon irradiation with white light during 4 h.

Figure 2.63 showed the photobleaching of ADPA of PpIX_PEI@AuNPs solution under the exposure of white light during 4 hours. The % of photobleaching of ADPA in 1 hour caused by free PpIX and PpIX_PEI@AuNPs and calculated with equation (4) was of 12.1 and 16.3 Abs/[mM]*min respectively. This result confirmed the enhancement of $^1O_2$ production given by conjugate PpIX_PEI@AuNPs and since PEI guarantees a water solubility of the conjugate, $^1O_2$ production was also tested in water. In water (with a 5% of DMSO) the % of photobleaching of ADPA in 1 hour caused by PpIX_PEI@AuNPs was 14.4 Abs/[mM]*min, as expected lower than in DMSO. This result is promising since usually in water the singlet oxygen production is quenched by the medium. In this case, although the photobleaching is slightly reduced if compared with that one in DMSO it is still enhanced respect to the free counterpart (PS).

In *table 2.6* all the results of photobleaching observed under irradiation with white light in DMSO and in H_2O (5% of DMSO) are reassumed.

		Rate of ADPA photobleaching (Abs/[mM]*min)
THPP_lipoic acid (C7, P1 & P3)	**P1 (DMSO)**	5,64
	P1@AuNPs (DMSO)	3,81
	P1/PEGSH@AuNPs (DMSO)	2,00
	P3@AuNPs (H2O/5% DMSO)	2,80
THPP_propylSH (C3, P5)	**P5 (DMSO)**	4,38
	P5@AuNPs (DMSO)	7,88
PpIX	**PpIX (DMSO)**	12,1
	PpIX_PEI@AuNPs (DMSO)	16,3
	PpIX_PEI@AuNPs (H_2O/5% DMSO)	14,4

Table 2.6: Rate of photobleaching of ADPA optimized with the concentration of the porphyrin.

In conclusion, it can stated that AuNP doesn't always quench the PS fluorescence, as often thought, since it depends on the distance between the nanoparticle and the photosensitizer.

In addition, the interesting phenomena of metal-enhanced fluorescence and, most importantly, metal-enhanced singlet oxygen production were observed, as reported also by other authors in the literature.[31]

2.3 Experimental session

Methods and Materials

All solvents were dried using standard procedures. All other reagents were of reagent-grade quality, obtained from commercial suppliers and were used without further purification. “Brine” refers to a saturated aqueous solution of NaCl. Unless otherwise specified, solutions of common inorganic salts used in workups are aqueous solutions. Reactions were monitored by TLC using 0.25 mm Merck silica gel plates (60 F254). NMR spectra were recorded at 400 MHz for ^{1}H and for ^{13}C on a Bruker Avance 400 spectrometers. Chemical shifts (δ) are expressed in ppm using the residual solvent signal as an internal reference (7.26 ppm for $CDCl_3$ and 2.5 ppm for DMSO-d_6). Coupling constants J are given in hertz (Hz) and multiplicities are reported using the following abbreviation (s = singlet, d = doublet, t = triplet, q = quartet, m = multiplet, br. s = broad singlet). Mass spectra were recorded in ESI mode. GC/MS spectra were recorded on a Agilent 5977B GC/MSD with 7820A GC System with a DB-5 column and a flow at 1 mL/min. All gold nanoparticles were purified using the centrifuge Universal 320R from Hettich. The preparation of functionalized AuNPs was performed according to the method of ligand exchange (sodium citrate exchange), that obviously gives a not complete substitution.

TEA or Et3N = Triethylamine
DCM = Dichloromethane
MeOH = Methanol
DMF = Dimethylformamide
THF = Tetrahydrofuran
AcOEt = Ethyl acetate
DMAP = 4-Dimethylaminopyridine
CDI = Carbonyldiimidazole
AIBN = 2-2'-azobisisobutyrronitrile
EDC = 1-Ethyl-3-(3-dimethylaminopropyl)carbodiimide
NHS = N-Hydroxysuccinimide
$HAuCl_4 \times 3H_2O$ = Tetrachloroauric acid trihydrate
TFA = trifluoroacetic acid

2.3.1 Synthesis of thiol ending linkers

Synthesis of Tetraethylene glycol p-toluenesulfonic acid ester (1)

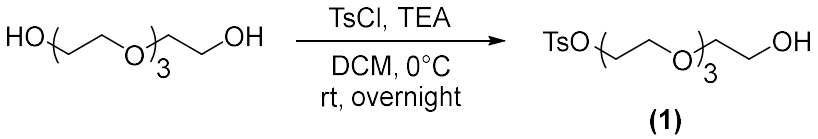

(1)

To a solution of tetraethylene glycol (10.19 g, 0.052 mol, 10 equiv) in CH_2Cl_2 (15 mL) tosyl chloride (1 g, 0.0052 mol) was added followed by TEA (1.08 mL, 0.79 g, 0.0078 mol, 1.5 equiv) addition at 0 °C. The mixture was stirred at room temperature overnight, then poured into a separatory funnel and washed (3 x 10 mL) with water. The combined organic layers were dried over Na_2SO_4, filtered and concentrated under reduced pressure to afford the product as a colorless oil in a yield of 82% (1.48 g). Rf = 0.47 (DCM/MeOH 95:5).

^{1}H NMR (400 MHz, $CDCl_3$): δ(ppm): 7.60 (d, *J* = 8.0 Hz, 2H), 7.18 (d, *J* = 8.0 Hz, 2H), 4.01 – 3.93 (m, 2H), 3.65 – 3.32 (m, 14H), 3.29 (s, 1H), 2.26 (s, 3H).

Synthesis of Tetraethylene glycol monoazide (2)

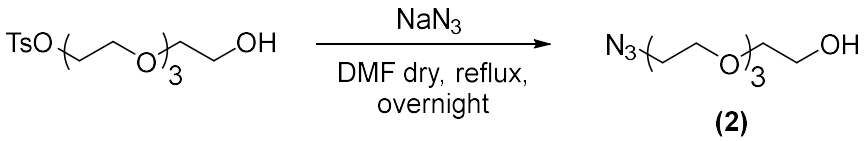

(2)

Tetraethylene glycol para-toluenesulfonate (1.8 g, 5.11 mmol), dissolved in dry DMF (15 mL), was introduced in a Schlenk tube under nitrogen. Sodium azide (764 mg, 11.75 mmol) was added under nitrogen and the reaction was refluxed overnight. At completion, the solvent was removed under vacuum. Ethyl acetate was then added and the crude was centrifuged three times to remove the salt. The product was obtained pure, without chromatographic purification, as pale yellow oil in a yield of 89% (999 mg). Rf = 0.47 (Hexane/Ethyl acetate 5:5).

^{1}H NMR (400 MHz, $CDCl_3$): δ(ppm) 3.73 – 3.54 (m, 14H), 3.40-3-32 (m, 2H).

Synthesis of 2 Tetraethylene glycol monoamine (3)

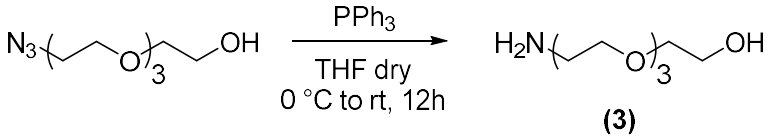

(3)

The tetrethylene glycol monoazide previously prepared (300 mg, 1.37 mmol, 1 eq.) was dissolved in dry THF and cooled to 0 °C. Triphenylphosphine (1.08 mg, 4.1 mmol, 3 eq.) was added and the solution was allowed to warm to room temperature. After stirring for 24 h water was added and the aqueous phase was extracted with toluene. The aqueous phase was concentrated under reduced pressure to obtain the product as an orange oil in a yield of 94% (250 mg). Rf = 0.35 (hexane/ethyl acetate 4:6).

^{1}H NMR (400 MHz, $CDCl_3$): δ(ppm): 3.66 – 3.40 (m, 14H), 2.96 (br. s, 3H), 2.81-2.71 (m, 2H).

Synthesis of difunctionalized tetraethylene glycol (3a)

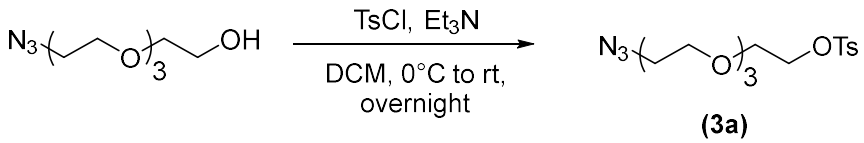

(3a)

Tetraethylene glycol monoazide (0.907 g, 4.13 mmol), dissolved in dry DCM (15 mL), was introduced into a 50 mL two necked round bottom flask, previously dried with three vacuum/nitrogen cycles. TEA (0.585 g, 5.78 mmol) was added, then the system was cooled to 0°C in an ice bath. 4-toluene sulfonyl chloride (1.10 g, 5.78 mmol) was finally added and the mixture was stirred overnight at room temperature, under nitrogen atmosphere. The reaction was monitored via TLC (AcOEt/Hexane 6:4), then, at completion, was quenched by addition of 10 mL of distilled water. The organic phase was washed three times with water and dried over anhydrous Na_2SO_4. The crude was purified by flash chromatography (Silica gel, AcOEt/Hexane 6:4 as eluent) to yield pure product as a light yellow oil in a yield of 70% (1.08 g). Rf = 0.33 (AcOEt/Hexane 6:4).

^{1}H NMR (400 MHz, $CDCl_3$): δ(ppm)= 7.77 (d, J = 8.0 Hz, 2H), 7.32 (d, J = 8.0 Hz, 2H), 4.16 – 4.08 (m, 2H), 3.71 – 3.52 (m, 12H), 3.36 (t, J = 5.0 Hz, 2H), 2.42 (s, 3H).

Synthesis of 5-(1,2-dithiolan-3-yl)-N-(2-(2-(2-(2 hydroxyethoxy)ethoxy)ethoxy) ethyl) pentanamide (4)

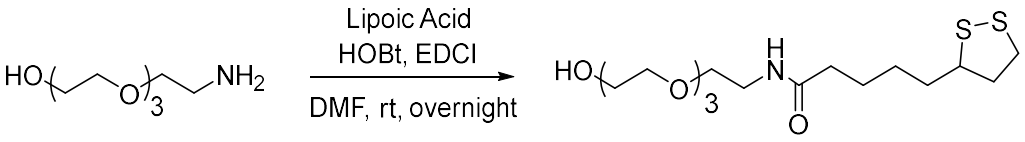

(4)

Lipoic acid (516 mg, 2.50 mmol), EDCxHCl (479 mg, 2.50 mmol) and CH_2Cl_2 (15 mL) were placed in a 50-mL round-bottom flask, cooled to 0 °C. After 10 min HO-PEG_4-NH2 (483 mg, 2.50 mmol) was slowly added under N_2 with stirring. The reaction mixture was stirred at 0 °C for 10 min, warmed to room temperature, and further stirred overnight. Then the solvent was removed under vacuum. The crude product was purified by column chromatography (Silica gel, Ethyl acetate and DCM/MeOH 95:5 as eluent) giving the product as a yellow oil in a yield of 71% (674 mg). Rf = 0.34 (DCM/MeOH 9:1).

^{1}H NMR (400 MHz, $CDCl_3$): δ(ppm): 7.15 (br. s, 1H), 4.97 (br. s, 1H), 3.81 – 3.39 (m, 17H), 3.25– 3.03 (m, 2H), 2.50-2.41 (m, 1H), 2.20 (t, J = 7.5 Hz, 2H), 1.98-1.85 (m, 1H), 1.80 – 1.36 (m, 6H).

Synthesis of 2-(2-(2-(2-aminoethoxy)ethoxy)ethoxy)ethyl 4-methylbenzenesulfonate (4a)

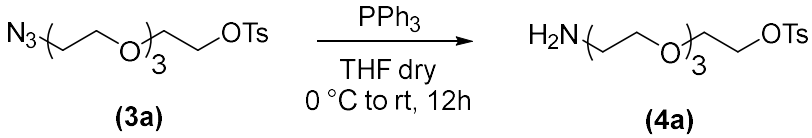

(3a) **(4a)**

Compound **3a** (205 mg, 0.55 mmol, 1 eq.) was dissolved in dry THF and cooled to 0 °C. Triphenylphosphine (433 mg, 1.65 mmol, 3 eq.) was added and the solution was allowed to warm to room temperature. After stirring for 24 h, water was added and the aqueous phase was extracted with toluene. The aqueous phase was concentrated under reduced pressure to obtained the product as a light yellow oil in a yield of 75% (138 mg). Rf = pale (hexane/ethyl acetate 4:6).

^{1}H NMR (400 MHz, $CDCl_3$): δ(ppm): 7.68 (d, J = 7.8 Hz, 2H), 7.08 (d, J = 7.8 Hz, 2H) 6.23 (br. s, 2H), 4.09 – 2.92 (m, 16H), 2.27 (s, 3H).

Synthesis of 17-(1,2-dithiolan-3-yl)-13-oxo-3,6,9-trioxa-12 azaheptadecyl4-methylbenzenesulfonate (5)

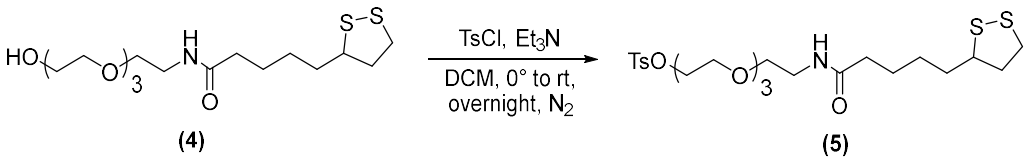

(4) (5)

Compound **4** (385 mg, 1 mmol) and para-toluene sulfonyl chloride (572 mg, 3 mmol) dissolved in dry DCM (15 mL), were introduced into a 50 mL two necked round bottom flask, previously dried with three vacuum/nitrogen cycles. TEA (303 mg, 3 mmol) and DMAP was added, then the system was cooled to 0°C in an ice bath. The mixture was stirred overnight at room temperature, under nitrogen atmosphere. The residue was quenched with aqueous HCl (pH = 3-4) end extracted with DCM. The organic phase was washed with brine and dried over anhydrous Na_2SO_4. The crude was purified through two chromatographic separations: a first flash chromatography to remove the excess of TsCl (Silica gel, Hexane/Ethyl acetate 7:3 as eluent) and a second flash chromatography (Silica gel, DCM/MeOH 94:6 as eluent) gave the product as a yellow oil in a yield of 68% (366 mg). Rf = 0.40 (DCM/MeOH 94:6).

^{1}H NMR (400 MHz, $CDCl_3$): δ(ppm): 7.81 (d, J = 8.4 Hz, 2H), 7.36 (d, J = 8.1 Hz, 2H), 6.21 (s, 1H), 4.22 – 4.11 (m, 2H), 3.76 – 3.42 (m, 16H), 3.24 – 3.04 (m, 2H), 2.53 – 2.39 (m, 4H), 2.19 (t, J = 7.4 Hz, 2H), 1.93 – 1.83 (m, 1H), 1.78 – 1.57 (m, 4H), 1.56 – 1.37 (m, 1H).

Synthesis of 5-(1,2-dithiolan-3-yl)-N-(6-ydroxyhexyl)pentanamide (6)

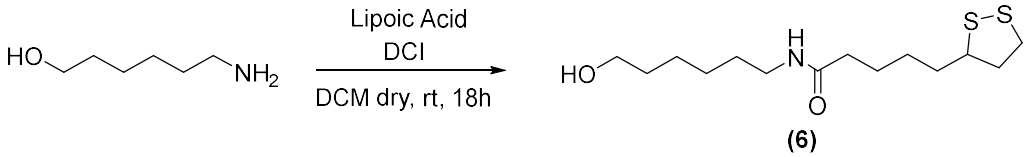

(6)

Lipoic acid (441 mg, 2.14 mmol, 1.55 eq) was dissolved in DCM (anhydrous, 30 mL) under N_2. Then, CDI (381 mg, 1.7 mmol, 1.7 eq) and the mixture was stirred for 1 h at room temperature (~ 20 °C) under N_2. 6-Aminohexan-1-ol (162 mg, 1.38 mmol, 1 eq) was added to the activated acid and the resulting reaction mixture was stirred for 18 h at room temperature. The crude was quenched with a HCl solution (pH = 3-4) and then extracted in CH_2Cl_2 , that was then washed with a saturated $NaHCO_3$ aqueous solution. The organic layers were combined, dried over anhydrous Na_2SO_4, filtered and concentrated under vacuum. The sample was purified by dissolving in the minimum amount of DCM and precipitating using an excess of hexane (~ 30 mL) under vigorously stirring. After centrifugation compound **6** was obtained in a yield of 25% (106 mg). Rf = 0.42 (DCM/MeOH 9:1).

^{1}H NMR (400 MHz, DMSO-d_6): δ(ppm): 7.74 (t, J = 5.7 Hz, 1H), 4.34 (t, J = 5.2 Hz, 1H), 3.66 – 3.53 (m, 1H), 3.42 – 3.33 (m, 2H), 3.27 – 3.07 (m, 2H), 3.06 – 2.95 (m, 2H), 2.48 – 2.35 (m, 1H), 2.05 (t, *J* = 7.3 Hz, 2H), 1.93 – 1.80 (m, 1H), 1.72 – 1.62 (m, 1H), 1.57 – 1.48 (m, 3H), 1.44 – 1.17 (m, 10H).

Synthesis of 6-(5-(1,2-dithiolan-3-yl)pentanamido)hexyl 4-methylbenzenesulfonate (7)

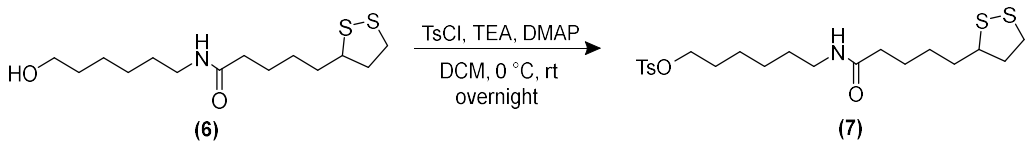

In a 50 mL two necked round bottom flask compound 6 (105 mg, 0.34 mmol), paratoluenesulfonylchloride (194.5 mg, 1.02 mmol) and DMAP were dissolved in dry DCM (15 mL), previously dried with three vacuum/nitrogen cycles. TEA (19 mg, 0.19 mmol) was added, then the system was cooled to 0°C in an ice bath. The mixture was stirred overnight at room temperature, under nitrogen atmosphere. The residue was extracted in CH_2Cl_2 with a HCl solution (pH = 3-4) and a saturated $NaHCO_3$ aqueous solution. The organic phase was dried over anhydrous Na_2SO_4 and the crude was purified through flash chromatography (Silica gel, Hexane/AcOEt 2:8 as eluent) to obtain the compound **7** as a light yellow oil in a yield of 21% (32.5 mg). Rf = 0.23 (Hexane/AcOEt 2:8).

^{1}H NMR (400 MHz, $CDCl_3$) δ(ppm): 7.84 – 7.75 (m, 2H), 7.37 (d, J = 8.0 Hz, 2H), 4.09 – 3.97 (m, 2H), 3.65 – 3.48 (m, 1H), 3.29 – 3.08 (m, 3H), 2.54 – 2.42 (m, 4H), 2.27 – 2.11 (m, 2H), 1.99 – 1.86 (m, 1H), 1.81 – 1.58 (m, 7H), 1.58 – 1.40 (m, 4H), 1.39 – 1.24 (m, 4H).

LC-MS (ESI): m/z (%) = 459.9 (100) $[MH]^+$, 460.8 (35) $[MH+1]^+$, 462 (21) $[MH+2]^+$

Synthesis of S-(11-bromoundecyl) ethanethioate (8)

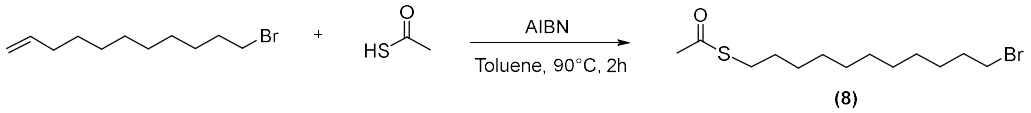

(8)

11-bromoundec-1-ene (263 µl; 279.8 mg; 1.2 mmol) was dissolved in 3 mL of toluene and mixed with 1.2 mL of a toluene solution of AIBN (c = 0.2 M, 39 mg, 0.24 mmol). The mixture was degassed and thioacetic acid (33.4 µl; 0.48 mmol) was introduced under a nitrogen atmosphere. The solution was heated at 90 °C and the reaction was completed within 2 h. Subsequently, the solution was cooled to room temperature and poured into a mixture of toluene (10 mL) and a saturated solution of $NaHCO_3$ in water (30 mL). The organic phase was collected, washed with water (2 × 15 mL), dried over Na_2SO_4 and filtered. The crude product was purified through flash chromatography (Silica gel, hexane/ethyl acetate 95:5 as eluent) to obtain the product in a yield of 78% (2.8 g). Rf = 0.28 (hexane/ethyl acetate 8:2).

^{1}H NMR (400 MHz, $CDCl_3$): δ(ppm) = 3.43 (t, J = 6.9 Hz, 2H), 2.88 (t, J = 7.3 Hz, 2H), 2.35 (s, 3H), 1.96–1.79 (m, 2H), 1.64–1.52 (m, 2H), 1.50–1.23 (m, 14H).

GC-MS: Rt = 12.84 min, m/z = 265 $[C11H23BrS]^+$.

Synthesis of allyl 4-methylbenzenesulfonate (9)

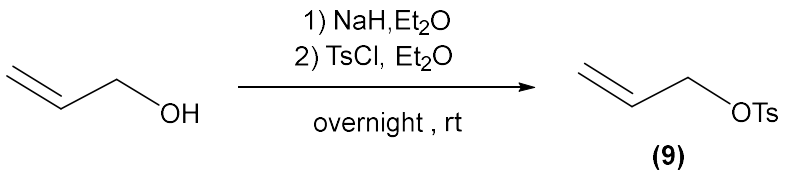

(9)

Sodium hydride (60% in mineral oil, 1.03 g, 25.8 mmol) was added under an atmosphere of N2 to allyl alcohol (1.2 mL, 17.2 mmol) solution in ether (25 mL) at 0 °C. After gas evolution, *p*- toluenesulfonyl chloride (3.3 g, 17.2 mmol) was dissolved in ether (10 mL) and was added dropwise to the reaction mixture. After the addition was complete the reaction mixture was warmed to ambient temperature and stirred for 1 hour. The reaction mixture was added to an aqueous solution of ammonium chloride (20 mL), the resulting mixture was extracted with ether, dried over Na_2SO_4, and concentrated under reduced pressure. The crude was purified by flash chromatography (Silica gel, gradient from hexane to hexane/ethyl acetate 8:2 as eluent) to obtain the product **9** in a yield of 78% (2.8 g). Rf = 0.28 (hexane/ethyl acetate 8:2).

^{1}H NMR (400 MHz, $CDCl_3$): δ(ppm): 7.82 (d, J = 8.3 Hz, 2H), 7.37 (d, J = 7.7 Hz, 2H), 5. 92 – 5.77 (m, 1H), 5.41 – 5.18 (m, 2H), 4.55 (dt, J = 6.0, 1.3 Hz, 2H), 2.47 (s, 3H).

GC/MS: Rt = 10.74 min, m/z = 212 [C10H12O3S]+, 155, 91.

Synthesis of S-(3-(tosyloxy)propyl) ethanethioate (10)

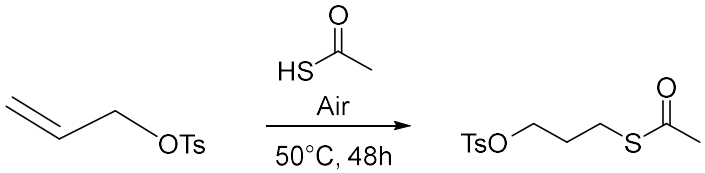

(10)

Thioacetic acid (1.88 g, 24.75 mmol) was introduced into a vial and it was heated to 45°C while introducing air for 30 minutes. After heating, allyl 4-methylbenzenesulfonate (1.05 g, 4.95 mmol) was added and the mixture was heated to a temperature of 50°C and stirred for 4 hours. Then, the solvent was removed under reduced pressure and **10** was obtained as a red oil in a 40% yield.

^{1}H NMR (400 MHz, $CDCl_3$): δ(ppm): 7.82 (d, *J* = 8.3 Hz, 2H), 7.38 (d, *J* = 7.8 Hz, 2H), 4.10 (t, *J* = 6.1 Hz, 2H), 2.90 (t, *J* = 7.1 Hz, 2H), 2.48 (s, 3H), 2.32 (s, 3H), 2.01 – 1.90 (m, 2H).

Synthesis of S(3-chloropropyl) ethanethioate (11)

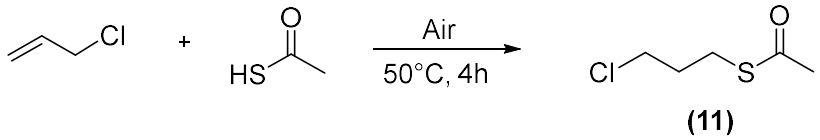

(11)

Thioacetic acid (84.72 g, 64.9 mmol) was introduced into a vial and it was heated to 45°C while introducing air for 30 minutes. After heating, allyl chloride (3.32 g, 43.3 mmol) was added and the mixture was heated to a temperature of 50°C and stirred for 4 hours. Then, the solvent was removed under reduced pressure and the product was obtained in a quantitative yield (6.2 g, 41 mmol).

^{1}H NMR (400 MHz, $CDCl_3$): δ(ppm) = 3.60 (t, J = 6.4 Hz, 2H), 3.03 (t, J = 7.0 Hz, 2H), 2.36 (s, 3H), 2.07 (m, 2H).

GC-MS: Rt = 6.95 min, m/z: 152 $[C5H9ClOS]^+$, 110 $[C3H7ClS]^+$.

Synthesis of Tosyl-poly(ethylene glycol)methyl-ether (13)

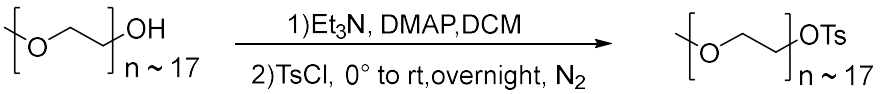

(13)

Poly (ethylene glycol) methyl-ether PEG_{17}(1 g, 1.3 mmol), triethylamine (197 mg, 271 µL, 1.95 mmol) and DMAP (some crystals) were dissolved in dry DCM (30 mL) at 0°C. Then paratoluenesulfonylchloride (595 mg, 3.12 mmol) was added. The reaction mixture was then warmed to room temperature and was stirred overnight at room temperature, under N_2 atmosphere. Then, the mixture was treated with an acidic solution of HCl (pH = 3-4) and extracted with CH_2Cl_2. The organic phase was dried over anhydrous Na_2SO_4 and the crude was purified by flash chromatography (DCM and DCM/MeOH gradient up to 9:1) to obtain the product as a colourless oil in 85% yield.

^{1}H NMR (400 MHz, $CDCl_3$): δ(ppm)= 7.80 (d, *J* = 8.0 Hz, 2H), 7.35 (d, *J* = 8.0 Hz, 2H), 4.16 (t, *J* = 4.8 Hz, 2H), 3.65 (s, 68H), 3.38 (s, 3H), 2.46 (s, 3H).

Synthesis of Thiol-tetra-ethylene glycol (14)

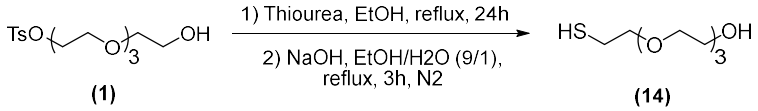

(1) (14)

Absolute ethanol (3 mL) and thiourea (41 mg, 0.54 mmol) were added to **1** (244 mg, 0.27 mmol) and allowed to reflux under argon for 24 h. After 24 h, the reaction was cooled to room temperature and sodium hydroxide (32.4 mg, 0.81 mmol) in absolute ethanol/water (9:1 v/v, 0.4 mL) was added. The reaction was heated to reflux under N_2 for 3h. The reaction was then cooled to room temperature, acidified with concentrated hydrochloric acid to pH= 2, filtered to remove the salts, and concentrated under reduced pressure. The crude oil was purified via column chromatography (EtOAc/absolute ethanol 10:1 and DCM/MeOH 95:5) to obtain the product **14** as a pale yellow oil in 45% a yield.

^{1}H NMR (400 MHz, $CDCl_3$): δ(ppm)= 3.78 – 3.60 (m, 14H), 2.78 – 2.67 (m, 2H), 1.65 (t, J = 8.2 Hz, 1H).

Synthesis of Thiol-poly(ethylene glycol)methyl-ether (15)

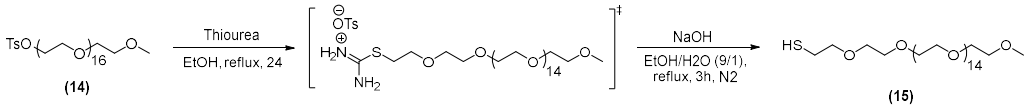

Absolute ethanol (3 mL) and thiourea (41 mg, 0.54 mmol) were added to dried **14** (244 mg, 0.27 mmol) and refluxed under argon for 24 h. After 24 h, the reaction was allowed to cool to room temperature and sodium hydroxide (32.4 mg, 0.81 mmol) in absolute ethanol/water (9:1 v/v, 0.4 mL) was added. The reaction was heated to reflux under N2 for 3h. The reaction was then cooled to room temperature, acidified with concentrated hydrochloric acid to pH= 2, filtered to remove the salts, and concentrated under reduced pressure. The crude oil was purified via column chromatography (EtOAc/absolute ethanol 10:1 and DCM/MeOH 95:5) to obtain the product as a pale yellow oil in a yield of 68%.

^{1}H NMR (400 MHz, $CDCl_3$): δ(ppm)= 3.61 (m, 66 H), 3.35 (s, 3H), 2.85 (t, J = 6.7 Hz, 2H) 1.59 (t, J = 8.2 Hz, 1H).

Synthesis of 3,3'-disulfanediyl-bis(2-aminopropanoic acid) (16)

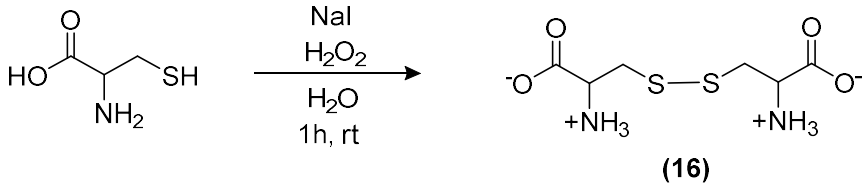

(16)

L-cysteine (242.5 mg, 2 mmol) and NaI (15 mg, 0.1 mmol) were dispersed in ice-cold water (1.94 mL) then aqueous hydrogen peroxide 30% (204 µL, 2 mmol) was added slowly into the central vortex of the reaction apparatus during 15 minutes. The reaction mixture was allowed to vigorously stir for 1 hour as it approached room temperature. The yellow slurry suspension was then filtered via Buchner funnel and washed with ice-cold water (20 mL). The solid was dried leaving it on the vacuum funnel overnight, obtaining a solid white chunk that was used without any further purification for the next reaction.

Synthesis of dimethyl 3,3'-disulfanediylbis(2-aminopropanoate) x 2HCl (17)

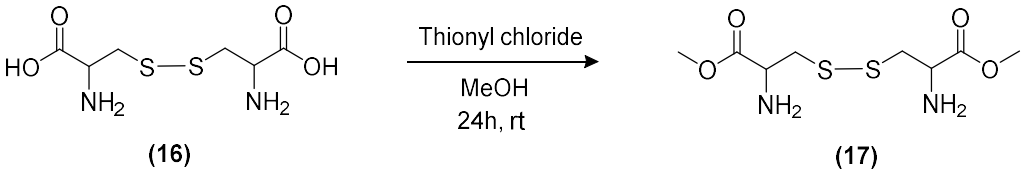

(16) (17)

Compound **16** (431 mg, 1.79 mmol) was dispersed in MeOH (6 mL) then thionyl chloride (500 µl, 6.88 mmol, 3.8 eq) was added over 15 minutes. The mixture was vigorously stirred at room temperature for 24 hours then concentrated under reduced pressure to provide a white solid in a yield of 85%.

^{1}H NMR (400 MHz, MeOD): δ(ppm)= 4.53-4-45 (m, 2H), 3.91 (s, 6H), 3.48-3.30 (m, 4H).

^{13}C NMR (400 MHz, MeOD): 168.0, 52.5, 51.4, 36.4.

LC-MS (ESI): m/z (%) = R_t: 0.22 min, 269 $[MH+1]^+$ (100), 270 $[MH+2]^+$ (18), 271 $[MH+3]^+$ (15), 272 $[MH+4]^+$ (2).

Synthesis of tert-butyl((3-chloropropyl)thio)dimethylsilane (18)

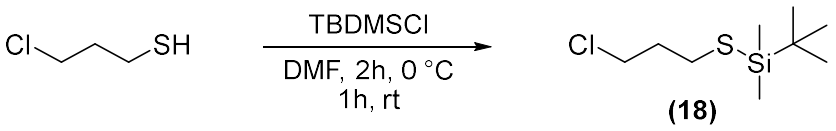

(18)

1.53 g (22.5 mmol) of imidazole were dissolved in 3.75 mL of DMF. After the addition of 1.78 mL (18 mmol) of 3-chloropropyl thiol the mixture was cooled to 0 °C and flushed with argon. 2.89 g (19 mmol) of tert-butyl((3-chloropropyl)thio)dimethylsilane (TBDMSCl) dissolved in 12.5 mL of DMF were added dropwise over a period of 40 minutes. The reaction was then allowed to stir for 2 h at 0 °C and subsequently 1 h at room temperature. The mixture was poured into an aqueous NaOH solution (2.5 g dissolved into 4.31 mL of water, 1.25 M) and extracted with DCM. The organic layers were collected and washed with water to remove most of the DMF. Then the product was distilled isolated by distillation under reduced pressure in a yield of 87%.

^{1}H NMR (400 MHz, $CDCl_3$): δ(ppm)= 3.70 (t, J = 6.2 Hz, 2H), 2.69 (t, J = 6.9 Hz, 2 H), 2.13-1.97 (m, 2H), 0.99 (s, 9H), 0.30 (s, 6H).

GC-MS: Rt = 9.27 min, m/z = 168 $[C_5H_{12}ClSSi]^+$.

Synthesis of 3-chlororopropyl triphenylmethyl sulfide (19)

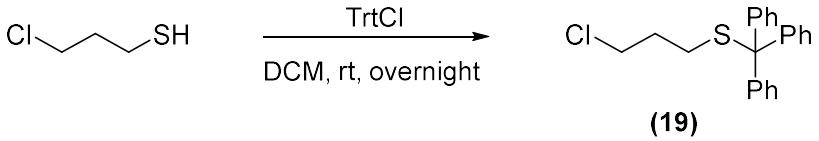

(19)

In an air-dried flask, triphenylmethylcloruro (TrtCl, 557.6 mg, 2 mmol) was added to a stirring solution of 3-chloropropyl thiol (195 µl, 2 mmol) in 40 mL (0.05 M) of DCM at room temperature. The reaction mixture was stirred at room temperature for 14 h and then the solvent was removed. The solid was purified upon recrystallization from MeOH/H_2O and the product **19** was obtained in a yield of 74% as a white solid.

^{1}H NMR (400 MHz, $CDCl_3$): δ(ppm)= 7.51-7.40 (m, J = 7.1 Hz, 6H), 7.37-7.20 (m, 6H), 7.26-7.21 (m, 3H), 3.49 (t, J = 6.5 Hz, 2H), 2.35 (t, J = 7.1 Hz, 2H), 1.77 (p, J = 6.8 Hz, 2H).

2.3.2 Synthesis of stabilized AuNPs

Synthesis of sodium citrate stabilized Gold Nanoparticles

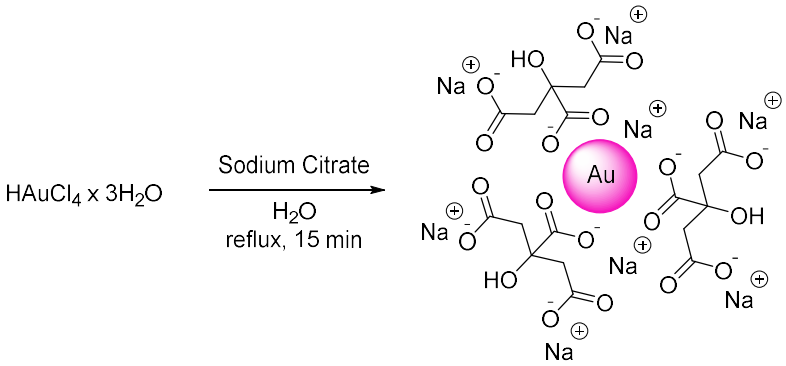

Prior to synthesis, all glassware was cleaned with aqua regia. Citrate-stabilized gold nanoparticles of 20 nm diameter were prepared following the classical Turkevich Frens procedure.[15] Briefly, $HAuCl_4 \times 3H_2O$ (18 mg, 0,0253 mmol) were dissolved in water (45 mL) and heated to reflux under stirring using a reflux condenser.
Trisodium citrate trihydrate (56 mg, 0,104 mmol) was dissolved in water (4.5 mL) and added to the boiling solution. Initially, the solution turned very dark violet and quickly changed to red. The solution was refluxed for an additional 15−20 min.

UV-Vis (H_2O): λ_{max} = 525 nm.

Synthesis of branched polyethyleneimine/citrate Gold Nanoparticles (bPEI_AuNPs)

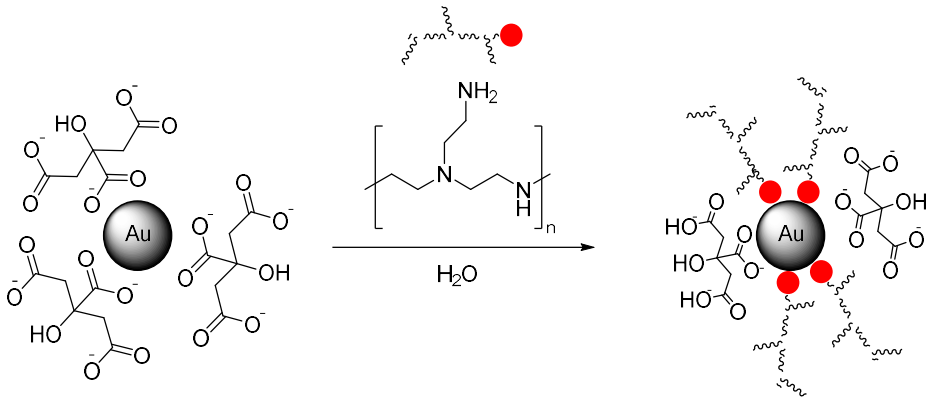

An aqueous solution of $HAuCl_4$ (13.8 mg, 0.035 mmol, dissolved into 25 mL giving a 1.4 mM solution) was mixed with branched polyethyleneamine (MW = 25000, 100 mg) and then the solution was stirred vigorously at room temperature for 16 h. The reaction mixture was then ultracentrifuged and filtered. The precipitate was washed many times with copious amounts of deionized water (3 x 15 mL). The PEI-capped Au nanoparticles thus obtained were redispersed in water (or ethanol) and gently sonicated before their characterization by FT-IR and UV-Vis spectroscopies.

UV-Vis (H_2O): λ_{max} = 522 nm.
IR (neat, cm^{-1}): 3000-2800 (C-H stretching), 1250-1020 (C-N, C-C stretching).

Synthesis of thiol-polyethylene glycol/citrate Gold Nanoparticles (PEGSH_AuNPs)

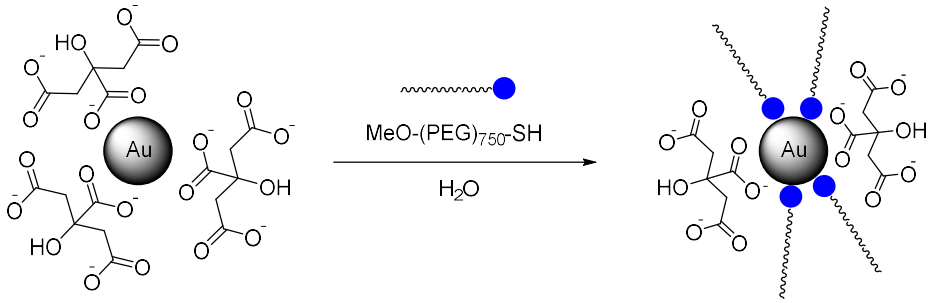

10 mL of the citrate stabilized gold nanoparticle dispersion (citrate_AuNPs) were added to a 50 mL round bottom flask containing the thiol-poly(ethylene glycol)methyl-ether ligand (2 mg, 0,003 mmol) and vigorously stirred with magnetic stirring at room temperature overnight. Then, the nanoparticle dispersion was transferred into a 1.5 mL Eppendorf tube and centrifuged at 15 000 rpm for 30 min, until a pellet was formed. The supernatant was removed, and 1 mL of 18 MΩ water was added. This washing process was repeated three times to remove any unreacted PEG ligand.

UV-Vis (H_2O): λ_{max} = 527 nm.
IR (neat, cm^{-1}): 3000-2800 (C-H stretching), 1250-1020 (C-O, C-C stretching).

Synthesis of lipoic acid/citrate Gold nanoparticles (LA_AuNPs)

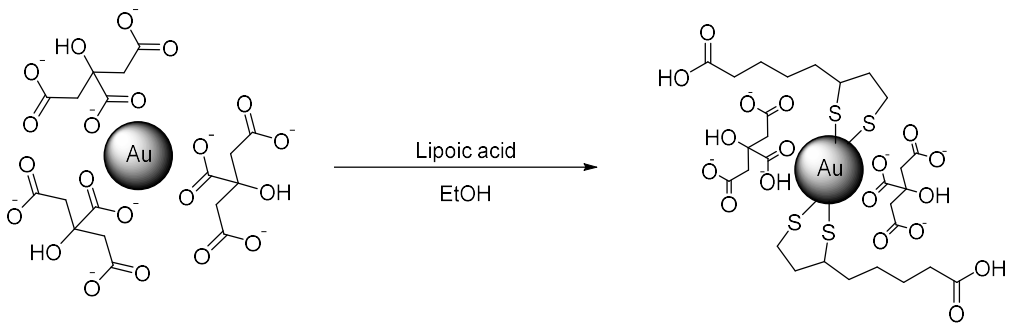

To 12 mL of citrate gold nanoparticles, 0.5 mL of a 10 mM lipoic acid stock solution was added. The stock solution was prepare d dissolving 10 mg in 4.85 mL ethanol. The mixture was stirred overnight at room temperature then centrifuged at 15 000 rpm for 20 min, the supernatant was discarded and washed 2 times with ethanol (10 mL).

UV-Vis (H_2O): λ_{max} = 526 nm.

Synthesis of Citrate/Cysteine stabilized Gold Nanoparticles

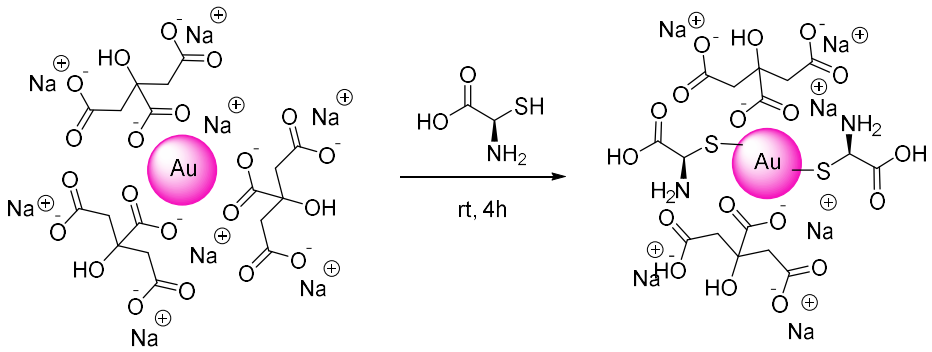

To find the better ligand exchange conditions, five solutions with different concentration of cysteine (0.06 mM; 0.1 mM; 0.3 mM; 0.45 mM; 0.6 mM) were prepared. 1 mL of cysteine solution was added to 1 mL of the citrate-stabilized gold nanoparticles solution previously prepared. The mixture was stirred for 4 h without any change in color. Finally gold nanoparticles functionalized with cysteine (AuNPs-Cys) were kept in the dark at room temperature for further conjugation (Uv-Vis characterization). In each case the nanoparticles started to aggregates probably due to the mechanism shown in *Chapter 2.2.2*.

UV-Vis (H2O): λmax(0.06 mM) = 523 nm; λ_{max}(0.1 mM) = 521 nm; λmax(0.3 mM) = 523 nm; λmax(0.45 mM) = 523 nm; λmax(0.6 mM) = 528 nm.

TEM: see results and discussion page 81 (*figure 2.19*)

2.3.3 Synthesis of functionalized porphyrins

Synthesis of THPP_Lipoic acid (THPP_LA, P1)

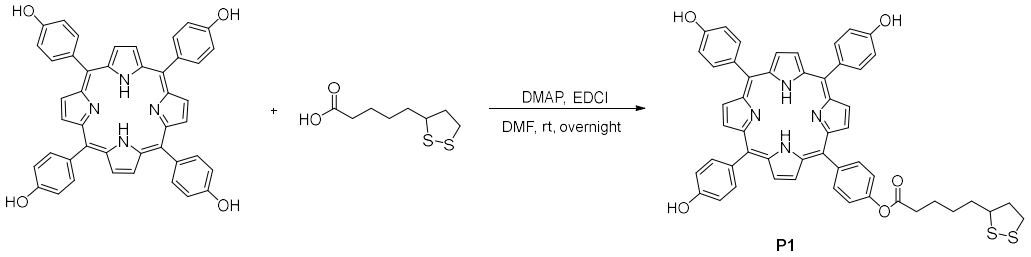

To a solution of lipoic acid (66.9 mg, 0.32 mmol) in DMF (5 mL), DMAP (cat) and EDCl (66.7, 0.35 mmol 1.2 eq) were added and the mixture was stirred for 30 min at room temperature. Then, the solution was added to a solution containing THPP (200 mg, 0.29 mmol) and K_2CO_3 (57 mg, 0.41 mmol) in DMF (10 mL).The mixture was stirred at room temperature overnight. The reaction was quenched with a aqueous saturated solution of lithium chloride and extracted with ethyl acetate (3 x 10 mL). The combined organic phases were collected, dried over anhydrous Na_2SO_4, filtered and concentrated under reduced pressure. The residual solution was chromatographed using preparative silica-gel plates and eluted with DCM/MeOH (9:1) to give the product in a yield of 15%.

^{1}H NMR (400 MHz, DMSO-d_6): δ(ppm)= 9.98 (s, 3H), 9.03 – 8.73 (m, 8H), 8.21 (d, 2H), 8.02 (d, J = 1.6 Hz, 6H), 7.53 (d, 2H), 7.21 (d, 6H), 3.77 – 3.58 (m, 1H), 3.22 – 3.06 (m, 1H), 2.81 – 2.61 (m, 2H), 2.46 – 2.32 (m, 1H), 1.94 – 1.43 (m, 8H), -2.85 (s, 2H).

^{13}C NMR (100 MHz, $CDCl_3$): δ (ppm) = 24.7, 28.6, 34.02, 34.45, 38.50, 56.59, 114.47, 118.80, 120.69, 120.78, 120.96, 132.29, 135.56, 136.01, 139.26.

UV-vis (DMSO, 1 µM): λ (nm) = 424 (Soret band), 519, 557, 595, 650 (Q bands).

Synthesis of tri-polyethylenglycolmethylether-THPP (triPEG_THPP, P2)

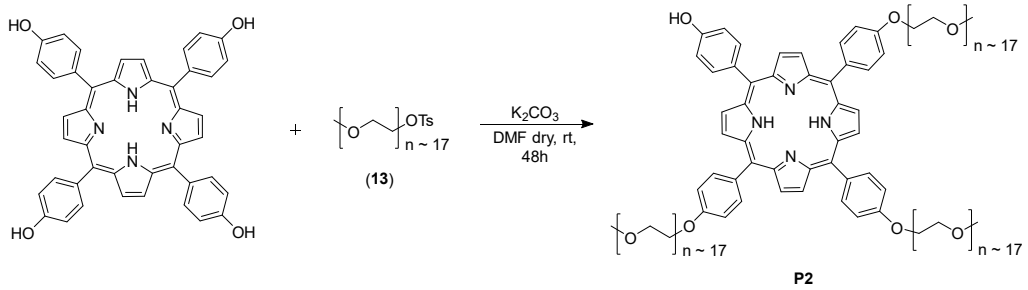

THPP (50 mg, 0.074 mmol) and K_2CO_3 (30.5 mg, 0.22 mmol) were dissolved in DMF (15 mL). The resulting solution was stirred at room temperature under an inert atmosphere for 30 min. Then *para*-methylbenzenesulfonate-PEG_{17} methylether (200 mg, 0.22 mmol) was added and the resulting solution was stirred at room temperature under an inert atmosphere for 48 h. The resulting mixture was concentrated under reduced pressure and purified by flash chromatography (DCM/Methanol/Et_3N (9:1:0.1)). The product was obtained as a red oil with a yield of 80%.

^{1}H NMR (400 MHz, DMSO-d_6, 353 Kelvin): δ(ppm) = 9.73 (s ,1H), 8.91 – 8.80 (m, 8H), 8.10 (d, J = 8.7 Hz, 6H), 8.00 (d, J = 8.4 Hz, 2H), 7.39 (d, J = 7.8 Hz, 6H), 7.23 (d, J = 8.4 Hz, 2H), 4.46 – 4.39 (m, 6H), 4.00 – 3.93 (m, 6H), 3.79 – 3.44 (m, 196 H), 3.27 – 3.18 (m, 9H), -2.74 (s,2H).

^{13}C NMR (400 MHz, DMSO-d_6): δ (ppm) = 158.8, 157.7, 135.7, 133.9, 131.7, 120.03, 114.2, 113.2, 72.7, 71.6, 70.1, 69.5, 67.8, 58.4.

Synthesis of lipoic acid-tri-polyethylenglycolmethylether-THPP (LA_triPEG_THPP, P3)

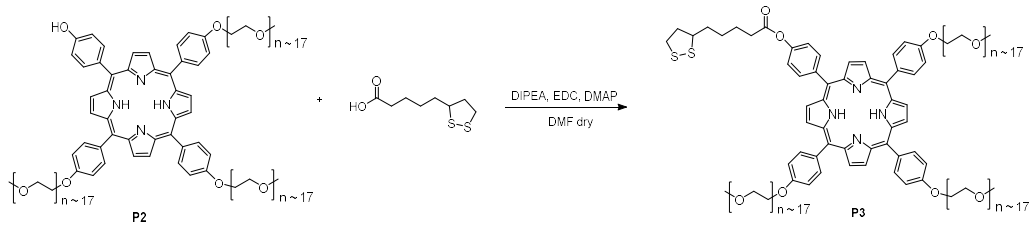

TriPEG_THPP (500 mg, 0.17 mmol) was added to a solution of DMF (15 mL) with K_2CO_3 (48 mg, 0.35 mmol) and was stirred for 30 minutes. Lipoic acid (72 mg, 0.35 mmol) was dissolved in dry DMF with EDC (67 mg, 0.35 mmol) and DMAP (cat) and after 20 minutes under stirring was added to the solution of the porphyrin. The reaction was stirred at room temperature overnight. Then DMF was removed under reduced pressure and the residual solution was diluted in THF (0.5 mL). Then diethyl ether (30 mL) was added to washed the product from the unreacted lipoic acid. The product was obtain in a yield of 49% as a red oil and characterized by ^{1}H NMR and use without any further purification in the conjugation reaction with AuNPs.

^{1}H NMR (400 MHz, DMSO-d$_6$, 333 K): δ(ppm)= 8.94 – 8.76 (m, 8H), 8.16-7.93 (m, 8H), 7.40 – 7.18 (m, 8H), 4.43 – 4.35 (m, 6H), 4.04 – 3.89 (m, 6H), 3.77 – 3.42 (m, 220H), 2.06 – 1.61 (m, 5H), -2.78 (s, 2H).

Synthesis of Undecyl ethanethioate_THPP (P4_i)

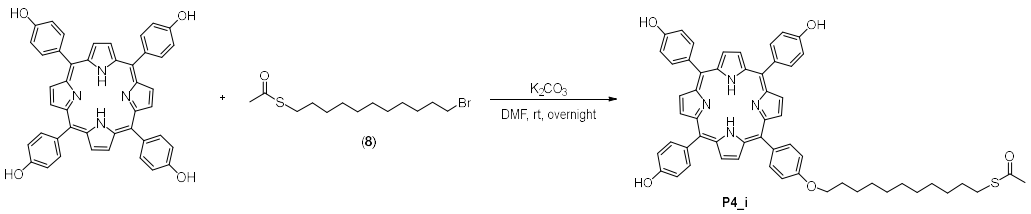

To a solution of THPP (50 mg, 0.074 mmol) and K_2CO_3 (7.2 mg, 0.052 mmol) in dry DMF (5 mL), S-(11-bromoundecyl) ethanethioate (25 mg, 0.081 mmol) was added and the solution was stirred at room temperature overnight. The mixture was quenched with a saturated aqueous solution of lithium chloride and extracted with ethyl acetate (3 x 10 mL). The combined organic phases were collected, dried over anhydrous Na_2SO_4, filtered and concentrated under reduced pressure. The residual solution was chromatographed over a silica-gel plates and eluted with DCM/MeOH (9:1) to give the product **P4_i** in a yield of 15%.

^{1}H NMR (400 MHz, DMSO-d_6): δ(ppm)= 9.81 (s, 3H), 8.90 – 8.80 (m, 8H), 8.08 (d, *J* = 8.7 Hz,, 2H), 8.00 (d, J = 8.0 Hz, 6H), 7.34 (d, *J* = 8.6 Hz, 2H), 7.22 (d, J = 8.3 Hz, 6H), 4.25 (t, J = 6.5 Hz, 2H), 3.50 (t, J = 6.7 Hz, 3H), 2.88 – 2.74 (m, 4H), 2.30 (br. s, 3H), 1.78 (q, *J* = 7.0 Hz, 2H), 1.59 – 1.20 (m, 10H), -2.79 (s, 2H).

Synthesis of $TrySC_3$-THPP (P5_i)

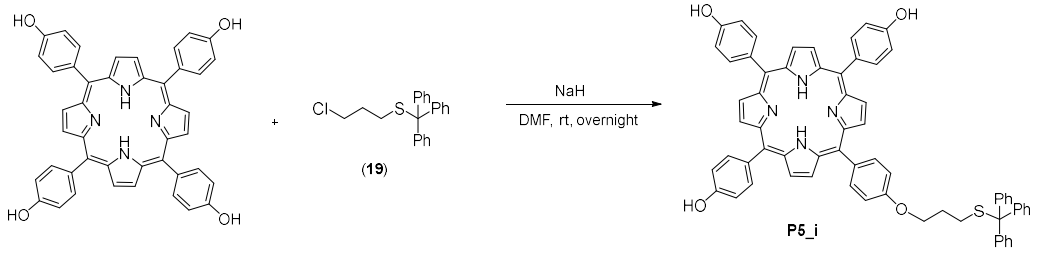

To a solution of THPP (150 mg, 0.22 mmol) and NaH (60%) (6 mg, 0.15 mmol) in dry DMF (10 mL), (3-chloropropyl)(trityl)sulfide (54.6 mg, 0.15 mmol) was added and the solution was stirred at room temperature overnight. The mixture was quenched with a saturated aqueous solution of lithium chloride and extracted with ethyl acetate (3 x 10 mL). The combined organic phases were collected, dried over anhydrous Na_2SO_4, filtered and concentrated under reduced pressure. The residual solution was chromatographed over a silica-gel plates and eluted with DCM/MeOH (9:1) to give the product in a yield of 45%.

^{1}H NMR (400 MHz, DMSO-d_6): δ(ppm)= 9.97 (s, 3H), 8.94 – 8.76 (m, 8H), 8.11 – 7.93 (m, 8H), 7.45 – 7.19 (m, 24H), 4.20 – 4.03 (m, 2H), 2.47 – 2.37 (m, 2H), 1.94 – 1.79 (m, 2H), -2.86 (s, 2H).

Synthesis of dimer (THPP_$C_3S)_2$ (P5_b)

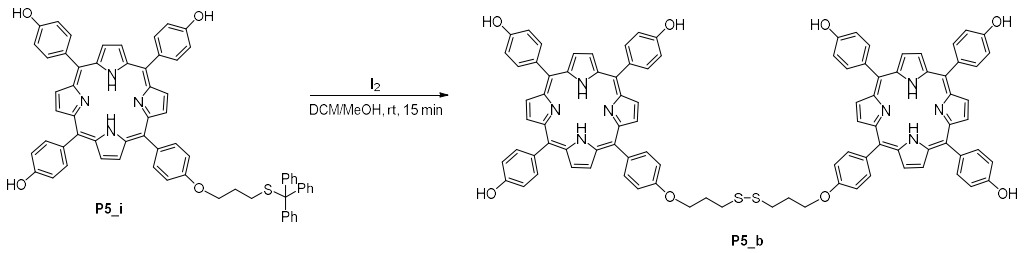

To a solution of **P5_i** (8.5 mg, 0.0085 mmol) in dry DCM (1 mL) and methanol (600 µl), iodide (2.7 mg, 0.02 mmol) previously dissolved into methanol (1 mL) was added and the solution was stirred at room temperature for 15 minutes. The reaction was quenched with a sodium thiosulfate solution (0,5 N), extracted with ethyl acetate (3 x 10 mL) and the combined organic phases were collected, dried over anhydrous Na_2SO_4, filtered and concentrated under reduced pressure. The product was then precipitated from a mixture of ethyl acetate/hexane (1:5) and centrifugated at 9000 rpm for 15 minutes. The product was obtained as a purple solid in a yield of 97%.

^{1}H NMR (400 MHz, DMSO-d_6): δ(ppm) = 9.95 (m, 3H), 8.84 (m, 8H), 8.11 (d, *J* = 8.5 Hz, 2H), 7.97 (m, 6H), 7.40 (d, *J* = 8.6 Hz, 2H), 7.18 (m, 6H), 4.42 (t, *J* = 6.0 Hz, 2H), 3.15 (t, *J* = 7.2 Hz, 2H), 2.37 (p, *J* = 6.9 Hz, 2H), -2.89 (s, 1H). **^{13}C NMR (101 MHz, DMSO-d_6):** δ (ppm) = 158.8, 157.90, 157.86, 136.01, 136.00, 135.9, 134.1, 132.40, 132.35, 120.6, 120.5, 119.8, 114.41, 114.37, 113.4, 66.4, 34.9, 29.0.

LC-MS (ESI, MeOH, 2% TFA): m/z (%) = R_t: 0.069 min, 1504 $[M+H]^+$ (23%) 752 $[M+2H]^2$ (100%).

Synthesis of sodium tetrasubstituted porphyrin triPEG_C_3S_THPP (P6_i)

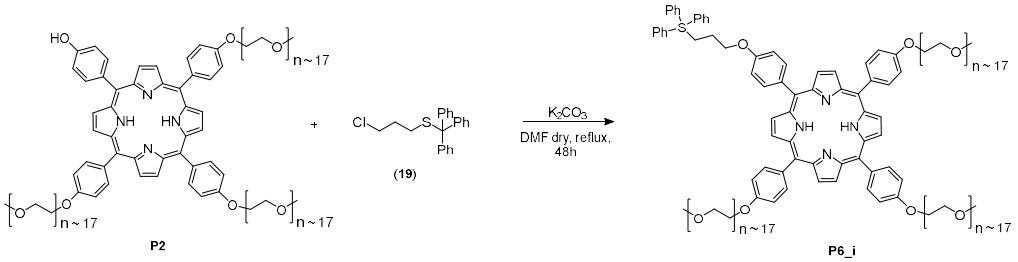

To a solution of porphyrin P2 (49 mg, 0.0165 mmol) and K_2CO_3 (3.42 mg, 0.0248 mmol) in dry DMF (15 mL), the linker **19** (15 mg, 0.043 mmol) and KI in a catalytic amount were added and the solution was stirred at reflux overnight. The mixture was redispersed in aqueous HCl solution (1 M), neutralized with $NaHCO_3$ and extracted with DCM. The organic phase was dried over Na_2SO_4 and after evaporation of DCM under reduced pressure, the residue was washed with hexane to remove the unreacted linker to give the product P6 in a yield of 70%.

^{1}H NMR (400 MHz, DMSO-d_6, 333 Kelvin): δ(ppm)= δ 9.06 – 8.51 (m, 8H), 8.18 – 7.93 (m, 8H), 7.53 – 7.05 (m, 36H), 4.47 – 4.26 (m, 6H), 4.24 – 4.07 (m, 2H), 3.98 – 3.87 (m, 6H), 3.78 – 3.11 (m, 204H), 2.50 – 2.41 (m, 2H), 1.98 – 1.81 (m, 2H), -2.77 (s, 1H).

Synthesis of sodium THPP_Sodium tripropylsulfonate (P7)

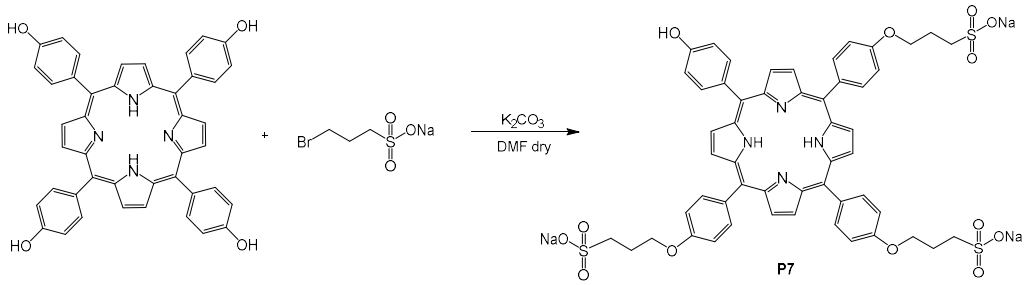

To a solution of THPP (150 mg, 0.22 mmol) and K_2CO_3 (103 mg, 0.75 mmol) in dry DMF (15 mL), sodium 3-bromopropane-1-sulfonate (164.11 mg, 0.73 mmol) was added and the solution was stirred at room temperature overnight. The mixture was concentrated under reduced pressure and redispersed in ethyl acetate. The suspension was filtered on Buchner and washed with ethyl acetate to give the water soluble product **P7** in a yield of 84%.

^{1}H NMR (400 MHz, DMSO-d_6): δ(ppm)= 8.96 – 8.80 (m, 8H), 8.15 – 8.05 (m, 6H), 8.03 – 7.96 (m, 2H), 7.43 – 7.32 (m, 6H), 7.25 – 7.16 (m, 2H), 4.38 (t, J = 6.5 Hz, 6H), 2.81 – 2.69 (m, 6H), 2.31 – 2.14 (m, 6H), -2.72 – -2.98 (m, 2H).

Synthesis of (TriPEG$_{750}$-C$_3$S-THPP)$_2$ (P9)

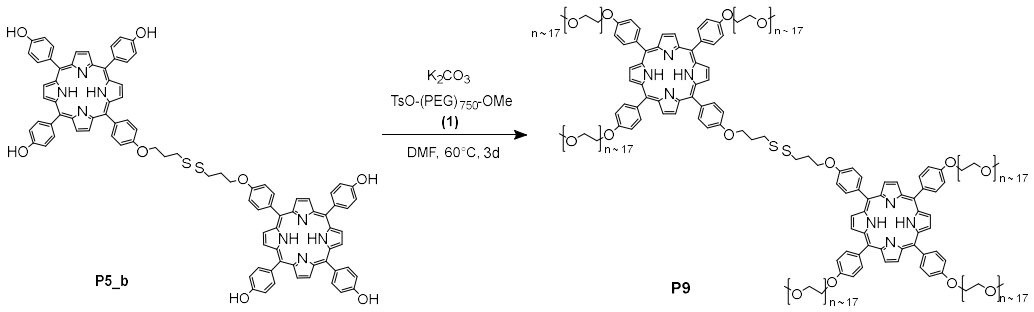

To a solution of **P5_b** (8.8 mg, 0.0059 mmol) in dry DMF (1 mL), KI (cat, ~ 0.02 mmol), K_2CO_3 (7.38 mg, 0.053 mmol) and **(13)** (38.3 mg, 0.042 mmol) were added and the solution was stirred at 25°C overnight. Then the temperature was increased to 60°C and the reaction was stirred for 3 days. The reaction mixture was quenched with water and a saturated solution of NaCl, extracted with DCM (3 x 10 mL) and the combined organic phases were collected, dried over anhydrous Na_2SO_4, filtered and concentrated under reduced pressure. The crude was then triturated with diethyl ether (3 x 5mL) and the product was obtained as a purple solid soluble in water in a yield of 30%.

^{1}H NMR (400 MHz, DMSO-d$_6$): δ(ppm)= 8.90 – 8.62 (m, 16H), 8.15 – 7.74 (m, 16H), 7.47 – 7.04 (m, 16H), 4.49 – 4.34 (m, 10H), 4.27 – 4.10 (m, 6H), 4.06 – 3.93 (m, 6H), 3.90 – 3.80 (m, 6H), 3.78 – 3.32 (m, 396H), 3.25 – 3.20 (m, 18H), 2.45 – 2.33 (m, 4H), -2.80 (s, 4H).

^{13}C NMR (400 MHz, DMSO-d6): δ (ppm) = 159.0, 158.8, 135.7, 135.5, 134.1, 131.4, 120.1, 113.6, 113.4, 72.8, 71.7, 70.6, 70.5, 70.2, 70.0, 69.6, 69.5, 68.1, 67.9, 65.3, 65.2, 64.4, 63.2, 60.7, 58.5, 35.3, 29.3, 16.6, 15.5, 9.0.

2.3.4 Synthesis of nanosystem conjugation

Conjugation of THPP_LA to citrate_AuNPs (NS1)

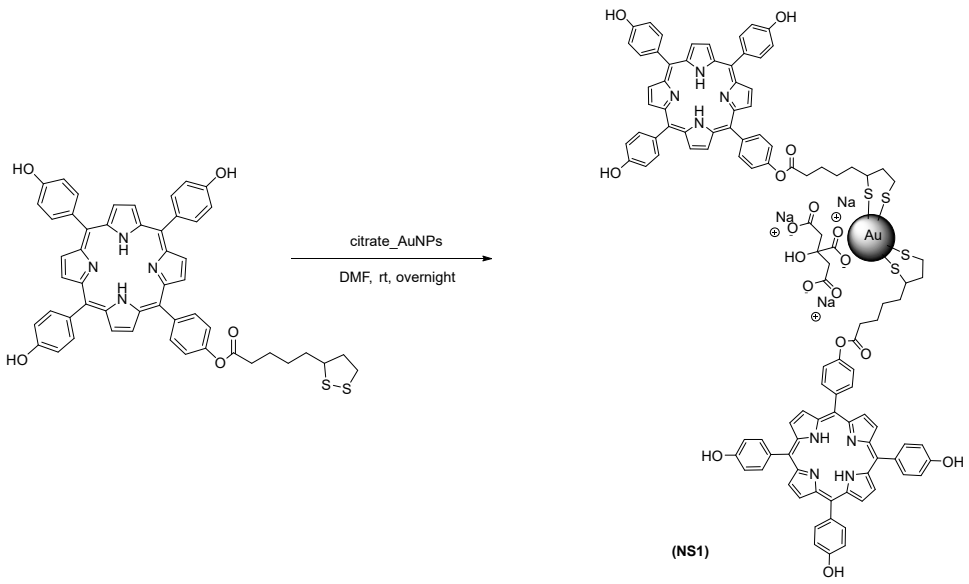

A stock solution of THPP_LA was prepared dissolving 5 mg into 6 mL of DMF (0.0104 mmol, 1.7 mM). From this solution, 3 mL (0. 0052 mmol) were added into a stirring solution of citrate_AuNPs (3 mL). The mixture was stirred overnight at room temperature in the dark. Then, the solution was centrifuged at 9000 rpm for 10 minutes and the solid washed several times with DMSO until the supernatant was cololess. Then it was redispersed into 6 mL of DMSO or H2O with 5% DMSO. For the UV-Vis characterization, the sample (100 µl) was diluted in DMSO (900 µl).

UV-vis (DMSO) : λ (nm) = 424 nm (A = 0,47), 543 nm (A = 0,49).

Conjugation of THPP_LA and MeO-$(PEG)_{750}$-SH on citrate_AuNPs (NS2)

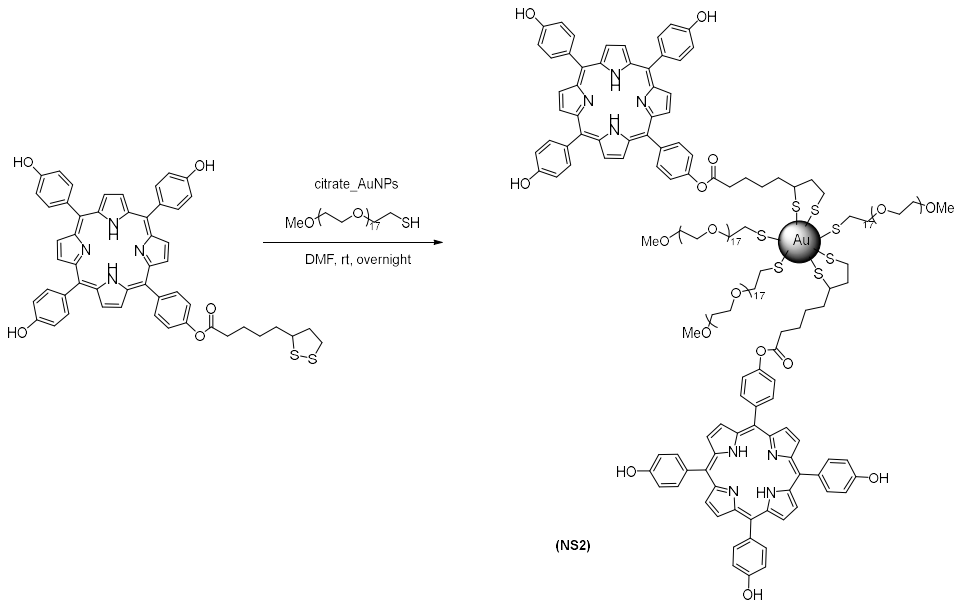

A stock solution of lipoicacid_THPP was prepared dissolving 5 mg into 6 mL of DMF (0.0104 mmol, 1.7 mM). From this solution, 3 mL (0. 0052 mmol) were added into a stirring solution of citrate_AuNPs (3 mL). Then 1 mL of a stock solution of thiol-poly(ethylene glycol)methyl-ether obtained dissolving 16.8 mg in 5 mL of H_2O was added to the solution and the mixture was stirred overnight at room temperature in the dark. Then, the solution was centrifuged at 9000 rpm for 10 minutes and the solid washed several times with DMSO until the supernatant wascolourless . and at the end redispersed into 6 mL of DMSO or H2O with 5% DMSO. For the characterization at the UV-Vis 100 µl of the solution were diluted into 900 µl of DMSO.

UV-vis (DMSO): λ (nm) = 424 nm (A = 0,42), 541 nm (A = 0,49).

Conjugation of triPEG_THPP_LA to citrate_AuNPs (NS3)

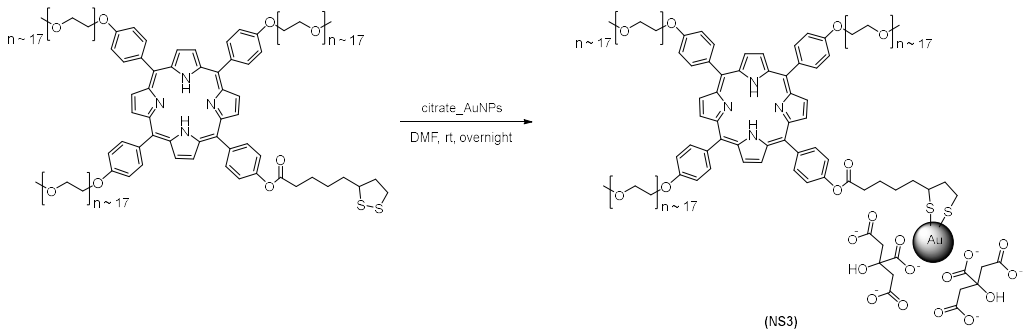

A stock solution of triPEG_THPP_LA was prepared dissolving 39.6 mg (0.01248 mmol) in 6 mL of DMF. 2 mL of this solution were diluted in 1 mL of DMF, then added to citrate_ AuNPs (3 mL) and stirred at room temperature for 2 days.
After removal of the solvent under reduced pressure, dry DMF was added and centrifuged at 10000 rpm for 5 minutes. This procedure was repeated three times, until the supernatant was colourless. Then, it was redispersed in 3mL of DMSO and characterized by UV-vis (100 µl of sample in 900 µl of DMSO).

UV-vis (DMSO): λ (nm) = 425 nm (A = 0,36), 535 nm (A = 0,47).

Conjugation of P5_b on citrate_AuNPs (NS4)

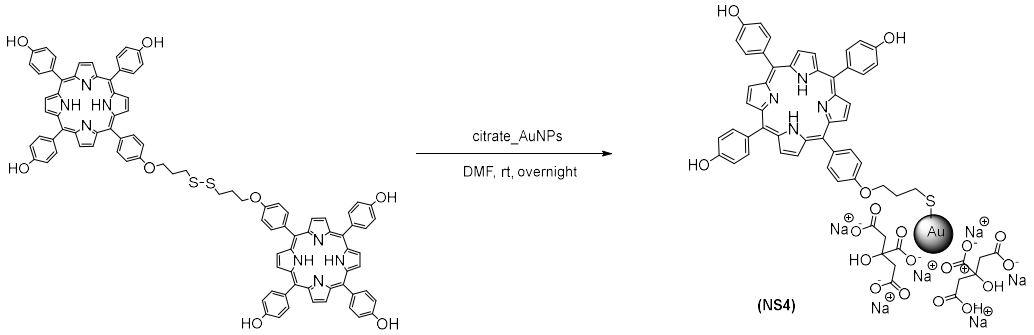

A stock solution of P5_b was prepared dissolving 5 mg into 6 mL of DMF (0.004 mmol, 0,6 mM). From this solution, 3 mL (0.0052 mmol) were added into a stirring solution of citrate_AuNPs (3 mL). Then, the solution was centrifugated at 9000 rpm for 10 minutes and washed several times with DMSO until the supernatant was encolour and at the end redispersed into 6 mL of DMSO. For the characterization at the UV, 100 µl of the sample were diluted into 900 µl of DMSO.

UV-vis (DMSO): λ (nm) = 425 nm (A = 0,47), 530 nm (A = 0,49).

Conjugation of PpIX to bPEI_AuNPs (NS5)

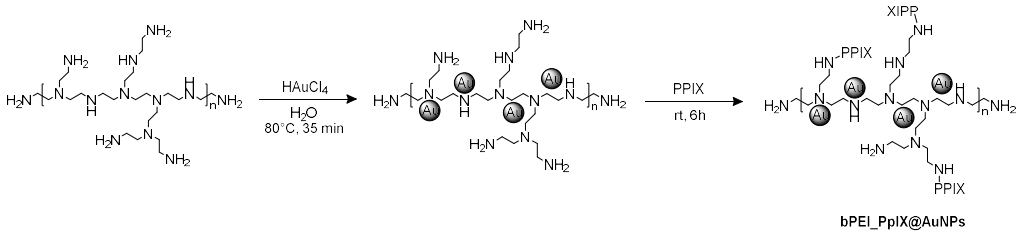

Prior to use, the glassware and magnetic stir bar were thoroughly cleaned with freshly prepared aqua regia, rinsed with ultrapure water, and then oven-dried. Branched PEI (1.0 mL) was firstly homogenized with $HAuCl_4$ solution (10 mL of 1.215 mM, 0.015 mmol) under vigorous stirring. After incubating at 80 °C for 35.0 min, the solution turned into ruby red; it was then cooled to room temperature. Subsequently, Protoporphyrin IX (PpIX, 12 mL of 0.1 mM solution in DMF) was added to the PEI_AuNPs solution, and the mixture was stirred under room temperature for 5.30 h to obtain the nanocomposite of PEI_ PpIX@AuNPs. Finally, the mixture was centrifuged at 15000 rpm for 20 min; after removal of the supernatant the resulting precipitate was redispersed in 1mL of DMSO and characterized at the UV-vis.

UV-vis (DMSO): λ (nm) = 407 nm (A = 0,48), 547 nm (A = 0,58).

2.3.5 Synthesis of liposomes as drug delivery systems

Materials and methods

All the materials were purchased from the Laboratory for Targeted Drug Delivery & Personalized Medicine Technologies in the department of Chemical engineering at the Technion, the Israel Institute of Technology, in Haifa, in Israel, where this work was performed. All the lipids were purchased by Avanti polar lipids and the extrusion process was performed using a LIPEX 10 mL Thermobarrel Extruder Package by Evonik that includes an extruder, an high pressure line, a replacement O-ring kit, heating lines, 100nm polyester drain discs (100/pk, diameter 25 mm), an 100nm pore size polycarbonate filters (100/pk). The membranes used were Nuclepore, Tracks-Etch Membrane 0.2 µm and 0.4 µm with a diameter of 25 mm and were purchased from Whatman. For dialysis process, were used Spectra/Por molecularporous membrane tubing with MWCO: 12-14 kD. Sephadex G-50c was purchased by Sigma Aldrich and activated previously overnight in double distilled water (DDW). For each sample, size distribution, stability, mean diameter and charge were determined at room temperature by multi-angle (173°, 13°) dynamic light scattering using Zetasizer Pro by Malvern, United Kingdom.

POPC 16:0 18:1 = 1-palmitoyl-2-oleoyl-sn-glycero-3-phosphocholine
DSPE-PEG-2000 = 1,2-distearoyl-sn-glycero-3-phosphoethanolamine-N-[(polyethylene glycol)

General protocol for the synthesis of 200nm liposomes through thin film layer method

POPC lipid (31.5 mg, 0.15 mmol, 55%), cholesterol (11.6 mg, 0,03 mmol, 40%) and DSPE-PEG-2000 (10.46 mg, 0,00375 mmol, 5%) were mixed into 3 mL of chloroform until they are completely dissolved. Then, the solvent was removed under progressive reduced pressure (at 200 mbar for 5 minutes, at 100 mbar for 3 minutes and at 2 mbar for 20 minutes) to create a thin film at the bottom of the flask. The film was kept under vacuum overnight in a desiccator. The next day it was hydrated with 3 mL of the solution containing what has to be encapsulated into liposomes for 1h under rotation in a water bath at a temperature above the melting temperature of the lipid (~ 50 °C). The milky solution was then extruded with pore size membranes of 0.4 µm and 0.2 µm successively and the extrusion process was repeated for 5-15 times depending on the compound that is included into liposomes. Finally, each sample was characterized by size and Zeta potential determination and purified by centrifuge, dialysis or sephadex column (see result and discussion).

2.4 References

(1) Chithrani, D. B.; Dunne, M.; Stewart, J.; Allen, C.; Jaffray, D. A. Cellular Uptake and Transport of Gold Nanoparticles Incorporated in a Liposomal Carrier. *Nanomedicine Nanotechnol. Biol. Med.* **2010**, *6* (1), 161–169. https://doi.org/10.1016/j.nano.2009.04.009.

(2) Nahire, R.; Hossain, R.; Patel, R.; Paul, S.; Meghnani, V.; Ambre, A. H.; Gange, K. N.; Katti, K. S.; Leclerc, E.; Srivastava, D. K.; Sarkar, K.; Mallik, S. PH-Triggered Echogenicity and Contents Release from Liposomes. *Mol. Pharm.* **2014**, *11* (11), 4059–4068. https://doi.org/10.1021/mp500186a.

(3) Dicheva, B. M.; ten Hagen, T. L. M.; Schipper, D.; Seynhaeve, A. L. B.; van Rhoon, G. C.; Eggermont, A. M. M.; Koning, G. A. Targeted and Heat-Triggered Doxorubicin Delivery to Tumors by Dual Targeted Cationic Thermosensitive Liposomes. *J. Controlled Release* **2014**, *195*, 37–48. https://doi.org/10.1016/j.jconrel.2014.07.058.

(4) Sarkar, N. R.; Rosendahl, T.; Krueger, A. B.; Banerjee, A. L.; Benton, K.; Mallik, S.; Srivastava, D. K. "Uncorking" of Liposomes by Matrix Metalloproteinase-9. *Chem Commun* **2005**, No. 8, 999–1001. https://doi.org/10.1039/B416827E.

(5) Leung, S. J.; Romanowski, M. Light-Activated Content Release from Liposomes. *Theranostics* **2012**, *2* (10), 1020–1036. https://doi.org/10.7150/thno.4847.

(6) Deng, W.; Chen, W.; Clement, S.; Guller, A.; Zhao, Z.; Engel, A.; Goldys, E. M. Controlled Gene and Drug Release from a Liposomal Delivery Platform Triggered by X-Ray Radiation. *Nat. Commun.* **2018**, *9* (1), 2713. https://doi.org/10.1038/s41467-018-05118-3.

(7) Kanehara et al. - 2008 - Gold(0) Porphyrins on Gold Nanoparticles.Pdf.

(8) Uchida et al. - 2016 - Investigation of Enantioselective Membrane Permeab.Pdf.

(9) Li, Z.; Gentry, Z.; Murphy, B.; VanNieuwenhze, M. S. Scalable Synthesis of Orthogonally Protected β-Methyllanthionines by Indium(III)-Mediated Ring Opening of Aziridines. *Org. Lett.* **2019**, *21* (7), 2200–2203. https://doi.org/10.1021/acs.orglett.9b00125.

(10) Zheng, M.; Li, Z.; Huang, X. Ethylene Glycol Monolayer Protected Nanoparticles: Synthesis, Characterization, and Interactions with Biological Molecules †. *Langmuir* **2004**, *20* (10), 4226–4235. https://doi.org/10.1021/la035981i.

(11) Zhao, P.; Li, N.; Astruc, D. State of the Art in Gold Nanoparticle Synthesis. *Coord. Chem. Rev.* **2013**, *257* (3–4), 638–665. https://doi.org/10.1016/j.ccr.2012.09.002.

(12) Sun, X.; Dong, S.; Wang, E. High-Yield Synthesis of Large Single-Crystalline Gold Nanoplates through a Polyamine Process. *Langmuir* **2005**, *21* (10), 4710–4712. https://doi.org/10.1021/la047267m.

(13) Kim, K.; Lee, H. B.; Lee, J. W.; Park, H. K.; Shin, K. S. Self-Assembly of Poly(Ethylenimine)-Capped Au Nanoparticles at a Toluene−Water Interface for Efficient Surface-Enhanced Raman Scattering. *Langmuir* **2008**, *24* (14), 7178–7183. https://doi.org/10.1021/la800733x.

(14) Haiss, W.; Thanh, N. T. K.; Aveyard, J.; Fernig, D. G. Determination of Size and Concentration of Gold Nanoparticles from UV−Vis Spectra. *Anal. Chem.* **2007**, *79* (11), 4215–4221. https://doi.org/10.1021/ac0702084.

(15) Turkevich, J.; Stevenson, P. C.; Hillier, J. A Study of the Nucleation and Growth Processes in the Synthesis of Colloidal Gold. *Discuss. Faraday Soc.* **1951**, *11*, 55. https://doi.org/10.1039/df9511100055.

(16) Ji, X.; Song, X.; Li, J.; Bai, Y.; Yang, W.; Peng, X. Size Control of Gold Nanocrystals in Citrate Reduction: The Third Role of Citrate. *J. Am. Chem. Soc.* **2007**, *129* (45), 13939–13948. https://doi.org/10.1021/ja074447k.

(17) Subara, D.; Jaswir, I. Gold Nanoparticles: Synthesis and Application for Halal Authentication in Meat and Meat Products. *Int. J. Adv. Sci. Eng. Inf. Technol.* **2018**, *8* (4–2), 1633–1641.

(18) Kimling, J.; Maier, M.; Okenve, B.; Kotaidis, V.; Ballot, H.; Plech, A. Turkevich Method for Gold Nanoparticle Synthesis Revisited. *J. Phys. Chem. B* **2006**, *110* (32), 15700–15707. https://doi.org/10/c72ftp.

(19) Mocanu, A.; Cernica, I.; Tomoaia, G.; Bobos, L.-D.; Horovitz, O.; Tomoaia-Cotisel, M. Self-Assembly Characteristics of Gold Nanoparticles in the Presence of Cysteine. *Colloids Surf. Physicochem. Eng. Asp.* **2009**, *338* (1–3), 93–101. https://doi.org/10.1016/j.colsurfa.2008.12.041.

(20) Calavia, P. G.; Martin, M. J.; Chambrier, I.; Cook, M. J.; Russell, D. A. Towards Optimisation of Surface Enhanced Photodynamic Therapy of Breast Cancer Cells Using Gold Nanoparticle–Photosensitiser Conjugates. *Photochem. Photobiol. Sci.* **2018**, *17* (3), 266–270. https://doi.org/10.1039/c7pp00307b.

(21) Imahori, H.; Norieda, H.; Nishimura, Y.; Yamazaki, I.; Higuchi, K.; Kato, N.; Motohiro, T.; Yamada, H.; Tamaki, K.; Arimura, M.; Sakata, Y. Chain Length Effect on the Structure and Photoelectrochemical Properties of Self-Assembled Monolayers of Porphyrins on Gold Electrodes. *J. Phys. Chem. B* **2000**, *104* (6), 1253–1260. https://doi.org/10.1021/jp992768f.

(22) Hiroto, S.; Miyake, Y.; Shinokubo, H. Synthesis and Functionalization of Porphyrins through Organometallic Methodologies. *Chem. Rev.* **2017**, *117* (4), 2910–3043. https://doi.org/10.1021/acs.chemrev.6b00427.

(23) Canitez, F. K.; Yavuz, M. S.; Ozturk, R. One-Pot Synthesis of Gold Nanoparticles Using Tetradentate Porphyrins. *J. Nanoparticle Res.* **2011**, *13* (12), 7219–7228. https://doi.org/10.1007/s11051-011-0636-0.

(24) Kamber, B.; Hartmann, A.; Eisler, K.; Riniker, B.; Rink, H.; Sieber, P.; Rittel, W. The Synthesis of Cystine Peptides by Iodine Oxidation of S-Trityl-Cysteine and S-Acetamidomethyl-Cysteine Peptides. *Helv. Chim. Acta* **1980**, *63* (4), 899–915. https://doi.org/10.1002/hlca.19800630418.

(25) School of Environmental and Biological Engineering, Nanjing University of Science and Technology, Nanjing 210094, P. R. China; Gu, S. Functionalized Polyethyleneimine-Gold Nanoparticles-Porphyrin Nanocomposite for Electrochemical Glucose Biosensing. *Int. J. Electrochem. Sci.* **2017**, 5092–5103. https://doi.org/10.20964/2017.06.85.

(26) Liu, X.; Atwater, M.; Wang, J.; Huo, Q. Extinction Coefficient of Gold Nanoparticles with Different Sizes and Different Capping Ligands. *Colloids Surf. B Biointerfaces* **2007**, *58* (1), 3–7. https://doi.org/10.1016/j.colsurfb.2006.08.005.

(27) Shum, P.; Kim, J.-M.; Thompson, D. H. Phototriggering of Liposomal Drug Delivery Systems. *Adv. Drug Deliv. Rev.* **2001**, *53* (3), 273–284. https://doi.org/10.1016/S0169-409X(01)00232-0.

(28) Contini, C.; Hindley, J. W.; Macdonald, T. J.; Barritt, J. D.; Ces, O.; Quirke, N. Size Dependency of Gold Nanoparticles Interacting with Model Membranes. *Commun. Chem.* **2020**, *3* (1), 130. https://doi.org/10.1038/s42004-020-00377-y.

(29) Tada, D. B.; Baptista, M. S. Photosensitizing Nanoparticles and the Modulation of ROS Generation. *Front. Chem.* **2015**, *3*. https://doi.org/10.3389/fchem.2015.00033.

(30) Penon, O.; Marín, M. J.; Russell, D. A.; Pérez-García, L. Water Soluble, Multifunctional Antibody-Porphyrin Gold Nanoparticles for Targeted Photodynamic Therapy. *J. Colloid Interface Sci.* **2017**, *496*, 100–110. https://doi.org/10.1016/j.jcis.2017.02.006.

(31) Yaraki, M. T.; Hu, F.; Rezaei, S. D.; Liu, B.; Tan, Y. N. Metal-Enhancement Study of Dual Functional Photosensitizers with Aggregation-Induced Emission and Singlet Oxygen Generation. *Nanoscale Adv.* **2020**, *2* (7), 2859–2869. https://doi.org/10.1039/D0NA00182A.

Chapter 3

Study RNAi Delivery System Ability for the Therapeutic Silencing of KRAS in Lung Cancer

(Study performed during my stage at TECHNION, Haifa Israel)

3.1 Introduction

Cancer is a genetic disease that is caused by specific mutations to that genes that regulate some functions of cells, especially how they grow and divide. Genes carry the instructions to make proteins, that are one of the most important building blocks of the cells. Certain gene changes (gene's mutations) can increase the production of a protein causing cells to evade normal growth controls becoming cancerous. The greatest cause of cancer-related mortality in both men and women is lung cancer that can be divided into two primary categories: small-cell lung cancer (SCLC) and non-small-cell lung cancer (NSCLC). Only around 15% of lung cancers are SCLC while the majority of lung cancers are NSCLC. Their names derive from the appearance of their cells under a microscope: compared to NSCLC cells, SCLC cells are small and spherical. The main distinction is in how aggressive they are: SCLC tends to be more rapid in its spread to other body areas than NSCLC. In *figure 3.1* is reported the histogram of the mutations that cause NSCLC, with 29% of these mutations coming from the KRAS gene (divided in non-G12C (17%) and G12C (12%)).

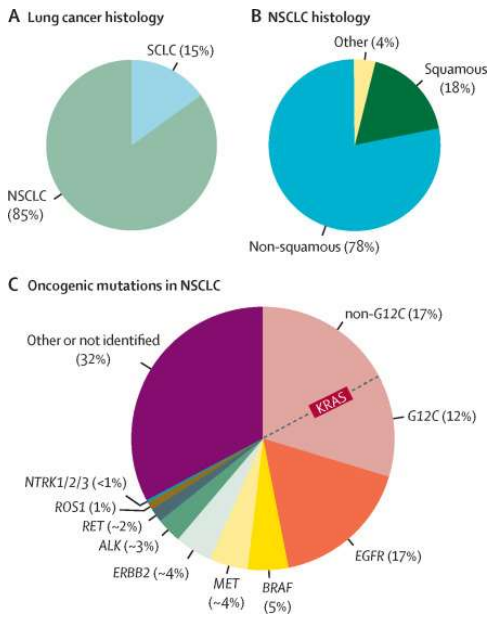

Figure 3.1: Lung cancers are classified into SCLC or NSCLC (A), which are subdivided into squamous and non-squamous histology (B). (C) The frequencies of common oncogenic driver mutations in NSCLC. *Taken by ref.*[1] *Copyright © 2021 Elsevier Ltd. All rights reserved.*

KRAS is an oncogene, a gene that, when mutates, promote the growth of the cells uncontrollably, causing cancer. KRAS mutations have been discovered in a number of human cancers, including 15% of patients with NSCLC. About 50 years ago, KRAS was first discovered by some researchers that were studying viruses that cause uncontrollable cell growth on tissue culture plate and KRAS is nowadays regarded as one of the “master switches” that control cell division in human cells. If it mutates, this switch can become permanently active in the “on” position, leading to the growth of cancer cells uncontrollably. The KRAS proto-oncogene is still considered as the single most elusive cancer target. Despite the wide variety of all cancers, about one-third of them have mutational activation of the RAS GTPases (HRAS, NRAS, and KRAS). Even though many efforts have been made to create pharmaceutical inhibitors of the mutations of KRAS that cause cancers, KRAS is still commonly recognized as "undruggable." The lack of a successful targeting of KRAS brought some scientists to investigate whether RNAi has therapeutic function for drug development. RNA interference (RNAi) is one of the technologies generally known as RNA silencing, that employ small RNA sequences as guides for specific silencing. RNAi was firstly discovered in *C. elegans* and identified as sequence-specific mRNA degradation driven by long double-stranded RNA (dsRNA).[2] Interestingly, the phrase "RNA interference" came about after it was shown that the insertion of a double-stranded RNA (dsRNA) caused quick and precise destruction of target mRNA. Although the use of RNAi in the clinic is highly attractive as a therapeutic approach, several challenges must be overcome to successfully introduce RNAi-based therapies into the clinical settings. Some of these include developing strategies for evaluating systemic biodistribution and subcellular localization, avoiding unfavorable off-target effects and ensuring effective and safe systemic administration. The introduction of an RNA construct that is complementary to an mRNA sequence led to a revolution thanks to gene knockdown bringing to the inhibition of gene’s expression and a reduction in the accumulation of the resulting protein. Even more amazing, siRNA provided a way for researchers to intentionally silence the genes that produce the disease-causing proteins. Moreover, the comprehension of thousands of previously unidentified genes' connections and roles was made easier using siRNA. *Figure 3.2* describes the mechanism by which RNAi prevents the translation of mRNA into protein.

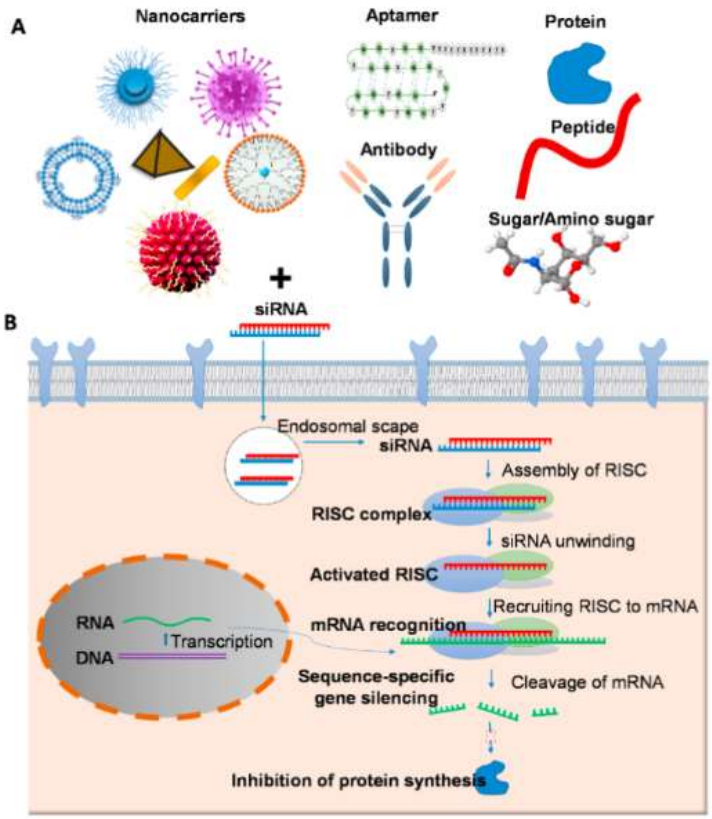

Figure 3.2: Mechanism of silencing of RNAi in cells. *Taken by ref.[3] Copyright © 2021 Elsevier B.V. All rights reserved.*

Briefly, the Dicer recognizes double-stranded RNA (dsRNA) and cleaves it into tiny fragments 21–23 base pairs in length. The dsRNA has sequences able to form a sense (passenger) strand and an antisense (guide) strand with the target mRNA and the dsRNA binds to a protein complex called RNA-induced silencing complex (RISC). A cleavage enzyme in RISC (argonaute 2) destroys the target mRNA when dsRNA, also known as siRNA, is injected, blocking translation. Compared to conventional therapies like small molecules and protein-based drugs, therapies utilizing RNA interference technology offer a number of benefits. Firstly, unlike small molecules and protein-based therapies, which respectively target both extracellular and intracellular organelles as well as extracellular alone, siRNA therapy's targets can be found anywhere and may even include "undruggable" targets. Secondly, protein-based treatments and siRNA have extraordinarily good selectivity while small molecules not. And last, unlike protein-based therapies, siRNA and small molecules are simple to synthesize. Even while siRNA-based therapy has advantages over small molecules, using both in combination therapy to treat the same disease can have

more powerful therapeutic results. Such combination therapy can act through a variety of mechanisms including i) the overcoming of multidrug resistance by downregulating multi-drug resistant genes to enhance the intracellular concentration of the drug, ii) increasing synergistic apoptotic effect through attacking multiple pathways that increase the apoptosis rates, and iii) reducing toxicity of small molecules by inducing a synergistic effect with siRNA thereby decreasing the side effects through lower doses of small molecules. Despite showing promise in vitro, siRNA has a lot of drawbacks in vivo, such as its elimination, immune destruction, instability, toxicity, and off-target effects. Therefore, in order to maximize its stability and effectiveness, siRNA must first be altered to tolerate the internal biological environment. SiRNA can be modified adding moieties to it, incorporating it into polymers, forming conjugates, and even altering its structure. The activity of siRNA can be improved even more through its encapsulation in nano-carriers like liposomes, which safeguards these molecules in vivo. These strategies are used for one specific reason: to help the siRNA to find its target and successfully silence the relevant gene. These substances have important targets in several deadly diseases, whose treatment would change the course of millions of lives. The aforementioned factors must be considered in the design of potential siRNA therapies in order to effectively silence genes and reach their specific targets.

SiRNA has undergone numerous successful chemical alterations to improve its characteristics, such as increase its half-life, improve its blood stability, tune the body ’s immunity and reduce off-targets effects. These changes brought to a more effective siRNA called stealth siRNA. In a previous study was evaluated a delivery platform for long dsRNA based on lipid-modified polyethylenimine (lmPEI) for efficient systemic silencing of GLRaV-3 (grapevine leafroll associated virus) in grapevines.[4] They assessed the ability to use RNAi for treating viral infections in grapevines and demonstrated that dsRNAlmPEI particles synthesis is rapid and scalable, bringing to stable particles in ambient conditions. In this study was combined cryogenic transmission electronic microscopy (CryoTEM) and Fast Fourier Transform (FFT) analysis. KRAS that is rich of aromatic rings can absorbs the electrons fired from CryoTEM to give black dots while the polymer is white. From this images was calculated, through FFT analysis, the inter-fiber spacing (7 nm from one center to another) and was designed the dsRNA-lmPEI molecular mechanics model, as shown in *figure 3.3*.

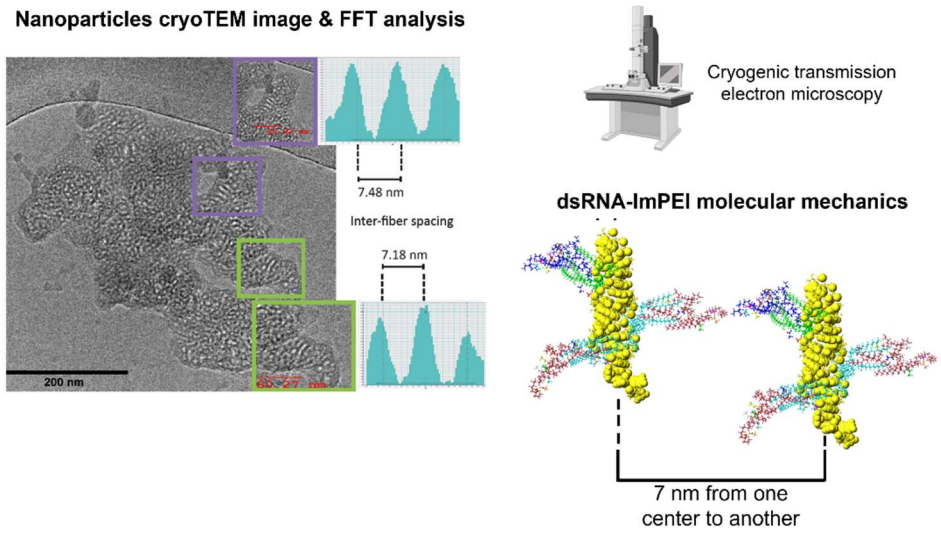

Figure 3.3: CryoTEM image and dsRNA-lmPEI molecular mechanics. *Taken from ref.* [4] *Copyright © 2021 Wiley-VCH GmbH.*

From this previous study, is possible to understand how the lmPEI can arrange around the dsRNA and design a new system able to complex a new RNA sequence, KRAS, and deliver it selectively into lung cancer cells.

3.2 Results and discussion

3.2.1 Introduction

Lipid modified polyethyleneimine (lmPEI) complex KRAS siRNA is composed by five components each of them having a specific role. In *figure 3.4* is reported the structure of all these components and how they can arrange and be opportunely functionalized in the system.

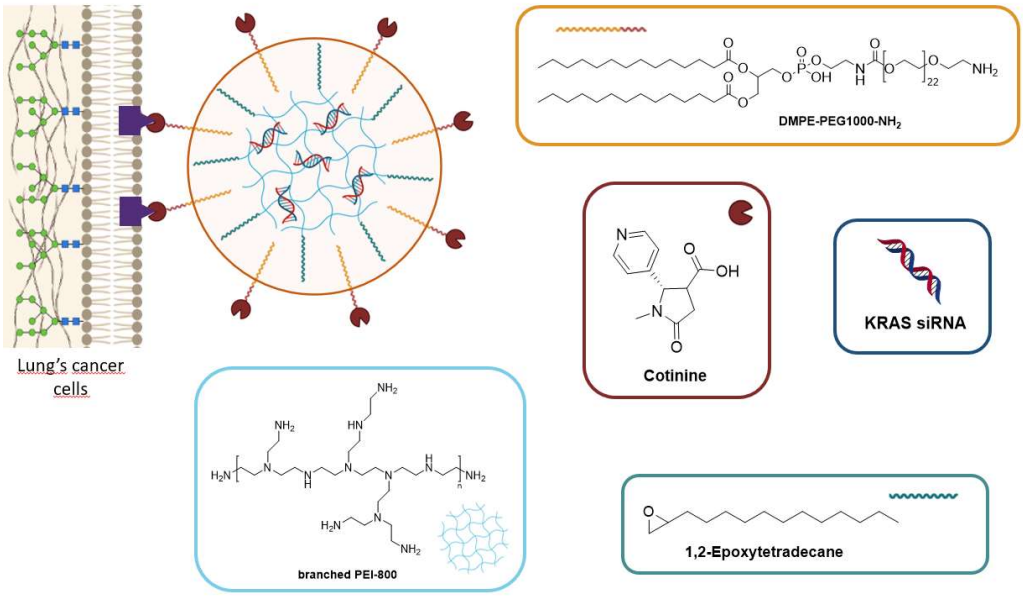

Figure 3.4: Design of the drug delivery system with all its components.

Since KRAS siRNA is negatively charged, the main goal is to induce electrostatic interactions creating a complex of KRAS with a carrier that is positively charged, PEI. Another important part is played by the addition of PEG, a large synthetic hydrophilic polymer, to the liposomal surface that reduces nonspecific interactions between liposomes and cells. PEGylation also decreases the binding of hydrophobic serum proteins that can potentiate consumption of liposomes by phagocytes of the

reticuloendothelial system (RE). In other words, PEGylation creates a "stealth" nanoparticle, which in comparison with its unPEGylated counterpart, has a prolonged circulation time, an increased bioavailability, and a greater potential for tumor targeting. PEG used is a DMPE-PEG_{1000}, a polymer with amine terminal end and composed by 22 polyethylenic repeating units and two lipophilic chains each with 14 carbon atoms. Firstly, DMPE-PEG1000 was covalently bounded with cotinine, an alkaloid with a structure similar to nicotine that is supposed to concentrate mainly in lungs acting as targeting molecule (*figure 3.5*). Furthermore, Cotinine presents a carboxylic acid functionality that easily allows its chemical modification.

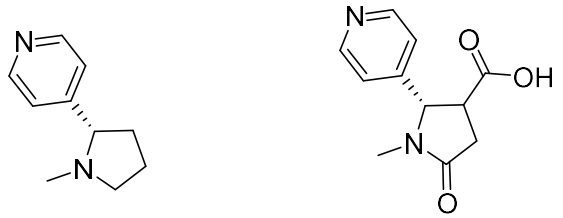

Figure 3.5: Chemical structures of Nicotine and Cotinine.

3.2.2 Synthesis of lmPEI complex KRAS siRNA

Synthesis of DMPE-PEG_{1000}-Cotinine is reported in *scheme 3.1*. Firstly, Cotinine was firstly activated with N,N'-disuccinimidyl carbonate (DSC) and triethylamine (TEA) in DMF at room temperature overnight. Then, a defect of DMPE-PEG_{1000} was added, stirred at room temperature in a mixture of DMF and $CHCl_3$ (3:1) for one hour, monitored by TLC and after chromatographic purification the product was isolated in a yield of 52%. DMPE-PEG_{1000}-Cotinine was then store in a mixture of methanol chloroform (50:50) and keep at -20 degrees.

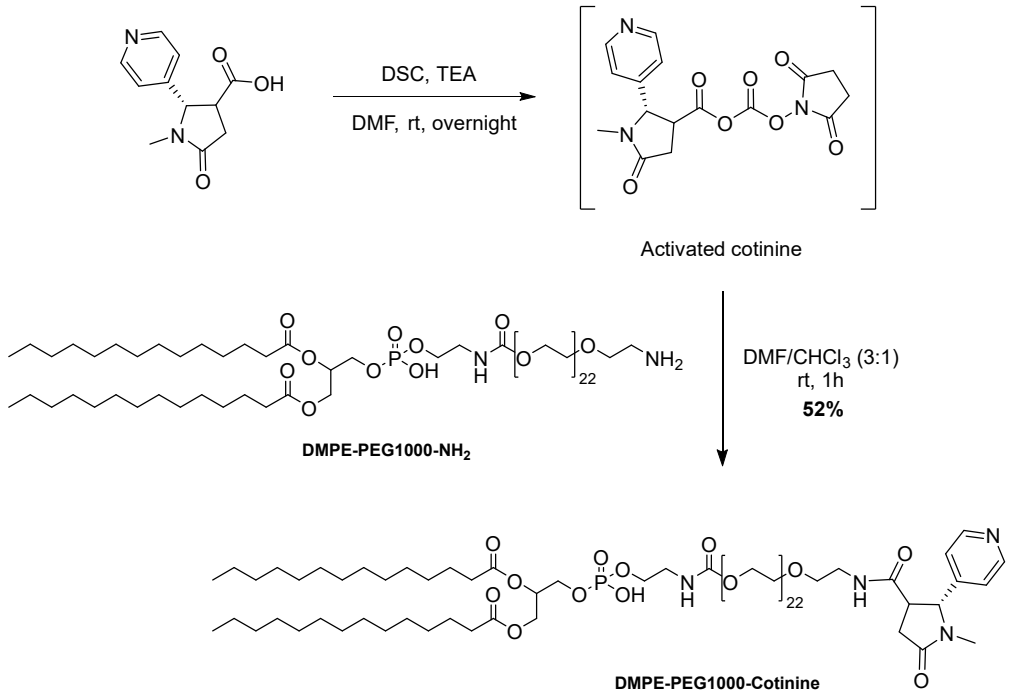

Scheme 3.1: Synthesis of DMPE-PEG_{1000}-Cotinine.

In order to create an interaction between the hydrophobic tails of DMPE-PEG_{1000}-Cotinine and PEI, hydrophobic tails were introduced in the PEI giving lipid modified PEI (lmPEI) that was synthesized as reported in *scheme 3.2*. bPEI was reacted with 1,2-Epoxytetradecane in a 3:1 (epoxide tail:PEI head group) molar ratio and refluxed for 4 hours in absolute ethanol, monitored by TLC until disappearance of free epoxide using Cerium molybdate as stain, stored in 50 ml falcons and used for the complexation reaction without any purification.

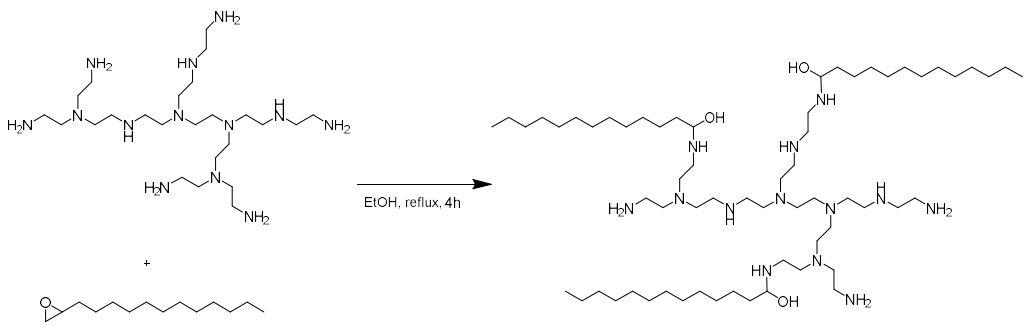

Scheme 3.2: Synthesis of lipid modified Bpei (lmPEI).

The product was characterized with ^{1}HNMR spectra in $CDCl_3$ (*figure 3.6*). ^{1}H NMR revealed a broad multiplet at δ= 2.55 ppm corresponding to the protons of the repeating units of the PEI and two singlet at δ= 1.18 ppm and δ= 0.76 ppm that confirms the presence of around three chains of the epoxide on the polymer.

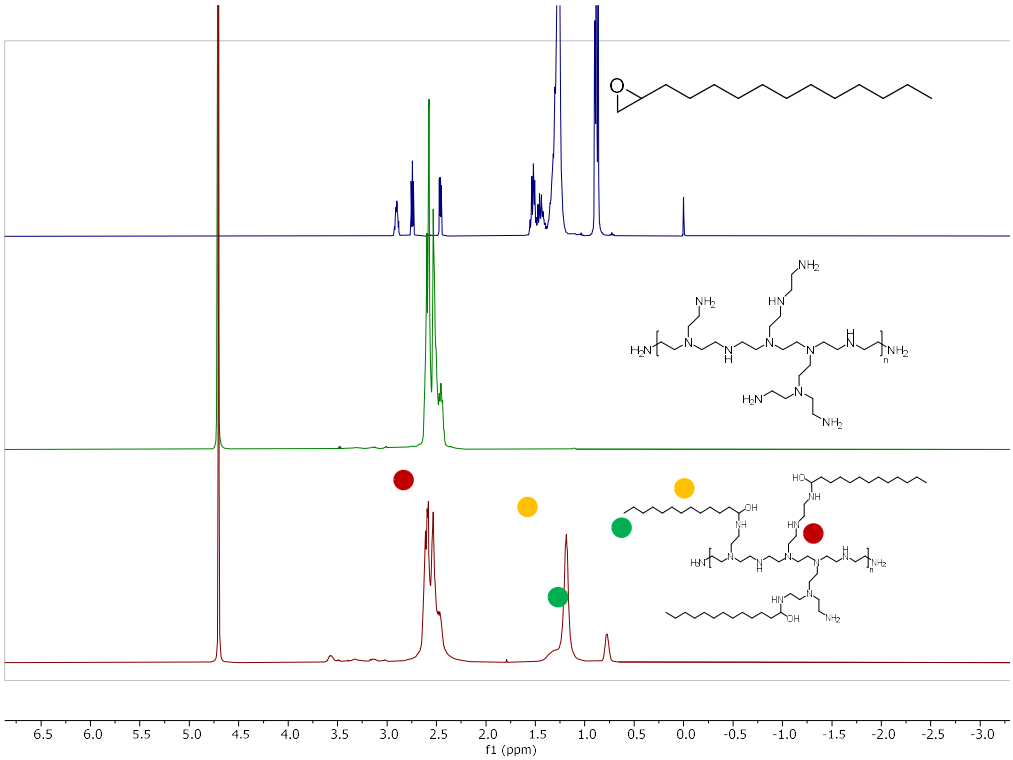

Figure 3.6: ^{1}H NMR ($CDCl_3$) of 1,2-Epoxytetradecane (*top*), Bpei (*middle*) and lmPEI (*bottom*).

Then, KRAS was complexed with lmPEI and DSPE-PEG_{1000}-Cotinine under acidic conditions (pH= 6) to establish electrostatic interactions between the negatively charged KRAS siRNA and cationic lmPEI, to formulate KRAS–lmPEI particles. To be effective, the KRAS-lmPEI particle must bind, protect, and release the KRAS at the target site. Since binding and release rely on lmPEI electrostatic affinity to KRAS, they can be controlled through the N:P ratio. In our study, the N:P ratio is defined as the molar ratio between positively charged amine groups present in lmPEI and negatively charged phosphate groups present on the KRAS. To determine this ratio, a constant weight of KRAS siRNA was converted to its equivalent mole phosphate groups and lmPEI was accordingly conjugated in order to reach the desired mole of protonated amines. In previous experiments conducted with a similar delivery system for a dsRNA to target GLRaV-3's ability to replicate and assemble, was

observed that, increasing the N:P ratio, the particle's surface charge elevated while below an N:P ratio of 2 (i.e., 0.01 and 0.1), particles were not formed, indicating insufficient lmPEI to bind dsRNA.

To achieve a desired N:P ratio, a constant amount of KRAS was converted to its equivalent phosphate mole considering its length and double strand structure (21 bp KRAS). Next, amine moles were calculated according to a desired N:P ratio and lmPEI amount was calculated from physical properties such as molecular weight and number of amine groups in a repeating unit. For example, 36 mg of dsRNA are equal to ≈0.0001 mole of negatively charged phosphate groups. To reach N:P ratio of 2:1, ≈0.0002 mole of amine groups, is needed. For this delivery system were evaluated different N:P ratio and % of DMPE-PEG_{1000}-Cotinine to guarantee the more polydisperse nanoparticles with a zeta potential near to zero. N:P ratio and % of DMPE-PEG_{1000}-Cotinine tested were respectively 1, 2, 5, 10, 20 and 2.5%, 5% and 10% and all the complexes were characterized by the average size, polydispersity index and zeta potential. In all the complexation reactions, the synthesis of KRAS-lmPEI nanoparticles (*top*) and the complexation reaction in practice (*bottom*) were performed as described in *scheme 3.3*:

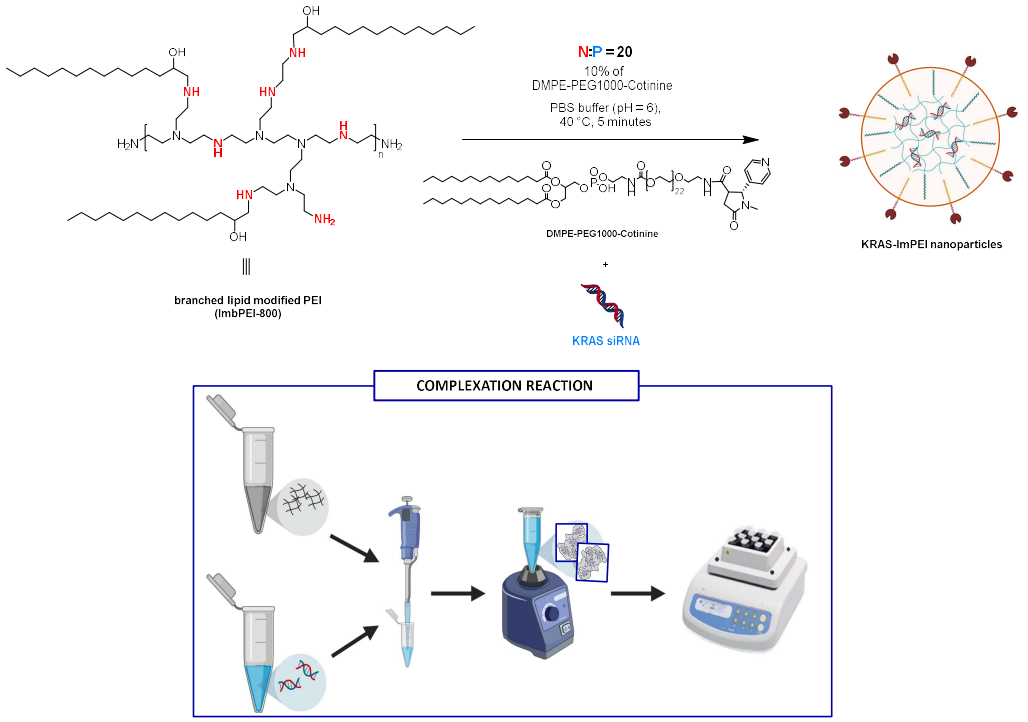

Scheme 3.3: Complexation reaction of KRAS-lmPEI nanoparticles.

Briefly, RNA primary solution is prepared diluting the stock solution in acetic PBS buffer (pH=6) to obtain the desired concentration calculated on the N:P ratio. Then, in a different Eppendorf, DMPE-PEG_{1000}-Cotinine and lmPEI are mixed and both the solutions were heated at 40°C for 5 minutes. Finally, the DMPE-PEG_{1000}-Cotinine + lmPEI is added under vortex to the RNA solution and incubated in a baby shaker at 1000 rpm, at a temperature of 40 °C for 20 minutes and characterized by DLS, Zeta potential and electrophoresis gel. The best results were obtained with a N:P ratio of 20 and 10% of DMPE-PEG_{1000}-Cotinine that formed nanoparticles with an average size of 403.8 nm, a polydispersity index of 0.4 and a zeta potential of 37.1 ± 4.67 mV as shown in *figure 3.7*.

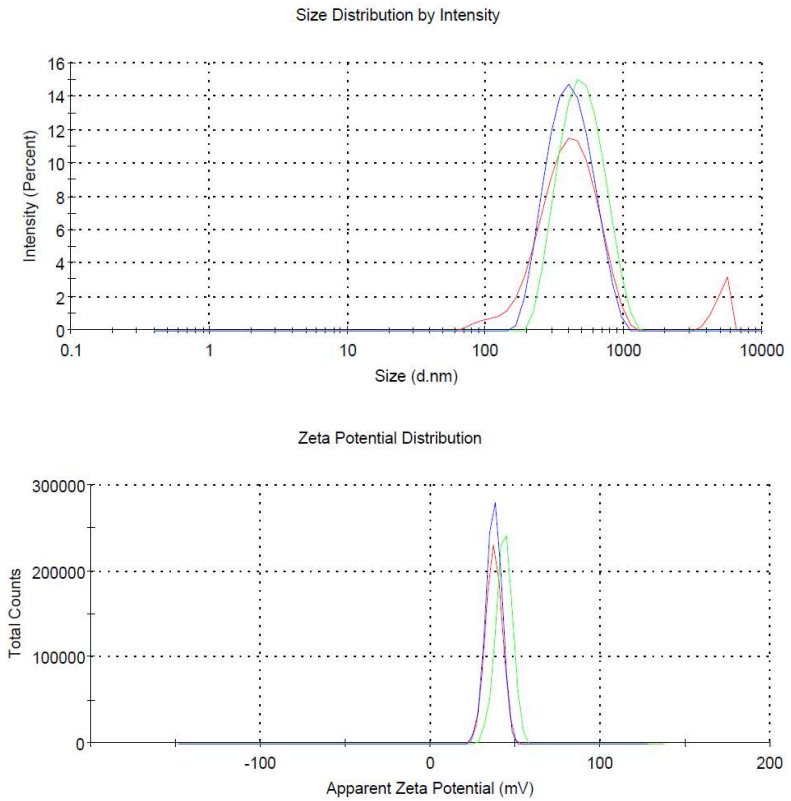

Figure 3.7: DLS (top) and Zeta potential (bottom) of KRAS-lmPEI nanoparticles.

To have a direct confirmation that the KRAS was incapsulated into the nanoparticles, electrophoresis Gel analysis and the Heparin release assay were performed. Gel electrophoresis is made of agarose or polyacrylamide and is a laboratory method used to separate mixtures of DNA, RNA, or proteins according

to the molecular size. In gel electrophoresis, the molecules that need to be separated are pushed by an electrical field through a gel that contains small pores. The molecules travel through the pores in the gel at a speed that is inversely related to their lengths. This means that a small DNA molecule will travel a greater distance through the gel than will a larger DNA molecule. After the electrophoresis is complete, the molecules in the gel can be stained to make them visible. DNA may be visualized using ethidium bromide which, when intercalated into DNA, fluoresce under ultraviolet light. As previously mentioned, gel electrophoresis involves an electrical field; in particular, this field is applied such that one end of the gel has a positive charge and the other end has a negative charge. Because DNA and RNA are negatively charged molecules, they will be pulled toward the positively charged end of the gel. Finally, after the DNA, RNA, or protein molecules have been separated using gel electrophoresis, bands representing molecules of different sizes can be detected. Heparin is a strong negatively charged molecule that can compete with RNA for electrostatic interactions, thus releasing it from particles. The solution was incubated with diluted Heparin for another 20 min at 37 °C in order to release KRAS from particles. Gel electrophoresis can be prepared as follow:

Firstly, the appropriate mass of agarose is weighted into an Erlenmeyer flask. Agarose gels are prepared using a w/v percentage solution. The concentration of agarose in a gel will depend on the sizes of the DNA fragments to be separated, with most gels ranging between 0.5%-2%. The volume of the buffer should not be greater than 1/3 of the capacity of the flask. Then, a running buffer is added to the agarose-containing flask, mixed and melted by heating in a microwave. At 30 s intervals, the flask is removed and the contents is swirled to mix well. Then ethidium bromide (EtBr) is added to a concentration of 0.5 µg/ml and the agarose is allowed to cool either on the benchtop or by incubation in a 65 °C water bath and the gel is placed into the casting apparatus. An appropriate comb is placed into the gel mold to create the wells and the molten agarose is poured into the gel mold. At the end, the comb is removed and the gel is placed in the gel box or alternatively, the gel can also be wrapped in plastic wrap and stored at 4 °C until use. In the wells of the gel is put: (i) Ladder: Ladder is a solution with known DNA sizes used to determine the size of an unknown DNA sample. The DNA ladder usually contains regularly spaced sized samples which when run on an agarose gel looks like a "ladder", (ii) Naked KRAS: free KRAS to see his behavior and retention time on the gel as itself, (iii) the Complex: to see if the KRAS is completely shielded from the nanoparticles and (iv) the Complex + Heparin: to release the KRAS from the

complex. Then, a voltage of 100 V is applied for 35 min and then the separation process is evaluated under a ultraviolet light. In *figure 3.8* is reported the gel under UV light that confirm that when the KRAS is complexed by the nanoparticles it is shielded by them becoming invisible in the gel, while when the complex is treated with heparin, it returned to be visible. From gel electrophoresis and heparin assay, can be stated that the KRAS is present inside the nanoparticles.

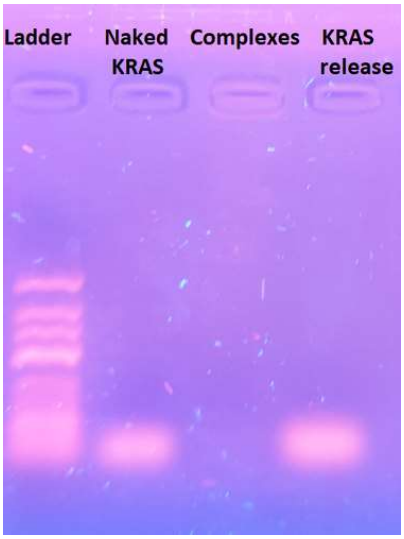

Figure 3.8: Gel electrophoresis and Heparin assay of KRAS-lmPEI nanoparticles.

After the synthesis and characterization of KRAS-lmPEI nanoparticles, a cell viability assay was carried out. Cell viability is defined as the number of healthy cells in a sample and the proliferation of cells is a vital indicator to understand the mechanisms of certain genes, proteins and pathways as cell survival or death after exposing to toxic agents. In this experiment, the goal is to test the toxicity of our formulation for A549 cells in a matrix of percentage of treatment and incubation time. Since this is a preliminary trial, a single incubation time of two hours and different percentages of treatment are chosen. In *figure 3.9* is reported the cell viability experiment using one plate of 96, with each column representing a different treatment (a total of 9 treatments) and each treatment contains 6 repetitions. Each treatment with KRAS was carried out in the presence of lipofectamine reagent that is used to increase the transfection efficiency of siRNA into in vitro cell cultures by lipofection. In a 96-well plate, 7000 cells were seeded per well in a total volume of 200 µl. Then, the plate was incubated for 24

hours to let the cells grow and the next day, different treatment were prepared according to relevant protocols and conditions:

96-well plate	1	2	3	4	5	6	7	8	9	10	11	12
A	PBS	----------	----------	----------	----------	----------	----------	----------	----------	----------	----------	----------
B	|	Medium Only	Untreated Cells	Naked siRNA	siRNA + Lipof.	0.5% v/v KRAS Comp.	1% v/v KRAS Comp.	5% v/v KRAS Comp.	10% v/v KRAS Comp.	20% v/v KRAS Comp.	|	|
C	|										|	|
D	|									|	|
E	|									|	|
F	|									|	|
G	|									|	|
H	----------	----------	----------	----------	----------	----------	----------	----------	----------	----------	----------	PBS

Figure 3.9: Nine treatment with six repetitions each on A549 cells.

As detailed explained in the supporting information, the 9 treatments were respectively: (1) medium only to evaluate how the medium can influence the viability of the cells, (2) untreated cells where is studied how cells proliferate without the treatment, (3) naked KRAS to evaluate the viability of the cells without the use of the delivery system, (4) KRAS + Lipofectamine to have the highest percentage of transfection of KRAS into the cells (5), (6), (7), (8), (9) to study the viability of the cells with different percentage of nanoparticles and determine the less amount of treatment that has an effect on proliferation. Each treatment was incubated for 24 hours and then was treated with Presto Blue reagent (PB, *figure 3.10*) that works as a cell viability indicator by using the reducing power of living cells to quantitatively measure the proliferation of cells.

Figure 3.10: Presto Blue reagent in its oxidized (left) and reduced (right) form.

In other words, the amount of fluorescence of Presto Blue is proportional to the number of living cancerous cells. Consequently, the fluorescence of Presto Blue is inversely proportional to the efficiency of the delivery system. Firstly, was conducted an optimization study on the incubation time of PB on the treatments, on the wavelength of excitation of PB and on the initial number of cells . The incubation time tested were t=0 minutes, 5 minutes, 10 minutes and 15 minutes while the excitation wavelength were 535 nm and 560 nm and the initial number of cells was 2000, 4000, 6000, 8000 and 10000. After the optimization of Presto

Blue experiment, the best conditions to conduct the following viability studies were: 7000 cells to seed, 5 minutes of incubation time of PB and 560 nm of wavelength of excitation of PB. After an incubation time of PB of 5 minutes, the fluorescence of the 96 wells plate was measured. From *figure 3.11*, can be easily concluded that the more efficient percentage of the treatment was 10% and 20% but, in the case of 20% treatment, since cells changed their conformation, was concluded that at this percentage the treatment is supposed to be toxic for cells.

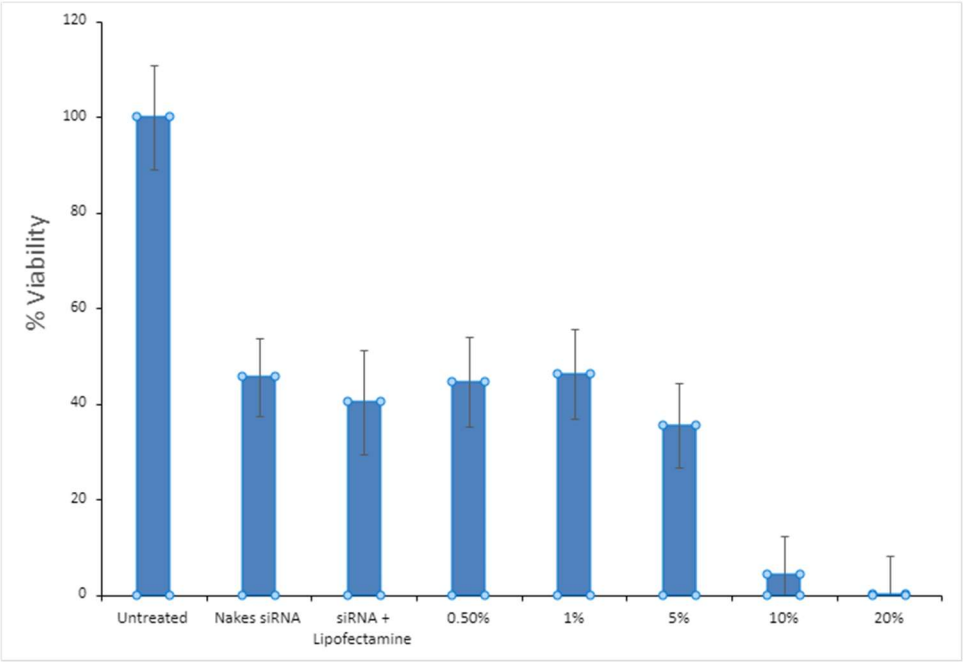

Figure 3.11: % of viability of the cells with the average of 6 repetitions for the 9 treatments

3.3 Experimental Section

Materials and methods

All the materials were purchased from the Laboratory for Targeted Drug Delivery & Personalized Medicine Technologies in the department of Chemical engineering at the Technion, the Israel Institute of Technology, in Haifa, in Israel. Branched Polyethylenimine (Mw = 800 g mol−1) was purchased by Sigma–Aldrich–Merck while 1,2-Epoxytetradecane by Tokyo chemical industry co. For each sample, size distribution, stability, mean diameter and charge were determined at room temperature by multi-angle (173°, 13°) dynamic light scattering using Zetasizer Pro by Malvern, United Kingdom. All cell lines were maintained in 5% CO_2/95% air at 37°C. Lung (A549, human and KP1.9, mice cells) were obtained from the ATCC and maintained in RPMI 1640 supplemented with 10% FBS and 0.1% gentamicin sulfate (GeminiBioproducts). The A549-Luciferase cell line was made following stable transduction with lentivirus carrying the luciferase gene (the lentiviral vector was kindly provided by Craig Logsdon's lab).
Cell lines were routinely tested to confirm the absence of Mycoplasma, and all in vitro experiments were conducted with 60% to 80% confluent cultures. All cells were reverse-transfected with RNAi- Max reagent (Invitrogen) using siRNA molecules (Sigma) at a final concentration of 10 to 20 nmol/L. Media were changed 4 hours following transfections to minimize toxicity. Heparin sodium salt (0.14 m) from porcine intestinal mucosa was purchased by Sigma–Aldrich while for Gel electrophoresis analysis, 2% gel agarose in TAE (X1) with Ethidium Bromide was purchased by Hy-Labs. Cryogenic transmission electron microscopy (cryo-TEM) imaging was performed by Technion Center for Electron Microscopy of Soft Matter (TCEMSM) on a Thermo-Fisher Talos F200C, FEG-equipped high resolution-TEM, operated at 200 kV. Specimens were transferred into a Gatan 626.6 cryoholder and equilibrated below −170 °C. Micrographs were recorded by a Thermo–Fisher Falcon III direct detector camera, at a 4k × 4k resolution. Specimens were examined at TEM nanoprobe mode using volta phase plates for contrast enhancement. Imaging was performed at a low dose mode of work to minimize the exposure of the imaged area to electrons. Images were acquired using the TEM imaging and acquisition (TIA) software. Inter-fiber spacing was deduced by performing radial integration on Fast Fourier Trasformation (FFT) of the relevant obtained images. Integration was done using FIJI software plugin by Paul Baggethun, 2009 version. PrestoBlue™ Cell

Viability Reagent, Lipofectamine® RNAiMAX Reagent and Gibco™ Opti-MEM medium for viability test were purchased by Termofischer Scientific.

FDDW = filtered double distilled water

3.3.1 Synthesis of branched lipid modified polyethyleneimine (blmPEI)

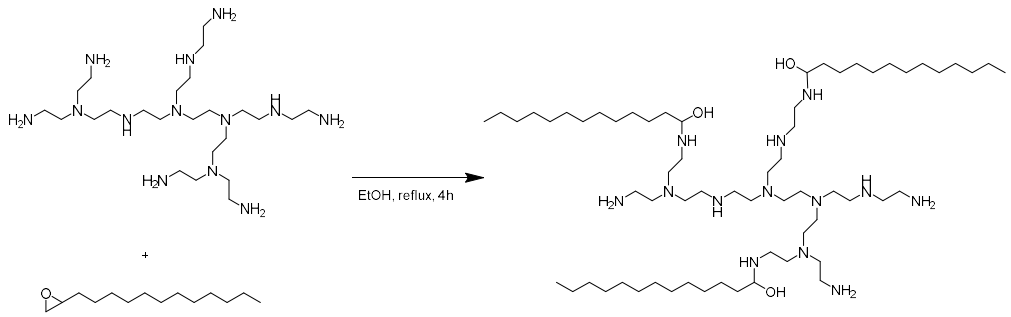

In an 500 ml Erlenmeyer flask, bPEI-800 (2.12 g, 0.00265 mmol) was dissolved in ethanol (150 ml) and heated at 90 °C under stirring. Then, 1,2 Epoxytetradecane (3 eq, 2 ml, 0,0079 mmol) was added and the reaction was refluxed for 4 hours and monitored with thin layer chromatography using chloroform-heptane (7:3) as eluent and Cerium molybdate as stain.
The crude was use for the complexation with KRAS without further purifications and stocked in 50 ml falcons.

^{1}H NMR (400 MHz, D_2O): δ(ppm)= 3.69 – 2.06 (m, 148H), 1.57 – 0.91 (m, 66H), 0.78 (br. s, 9H).

3.3.2 Synthesis of blmPEI-Cotinine

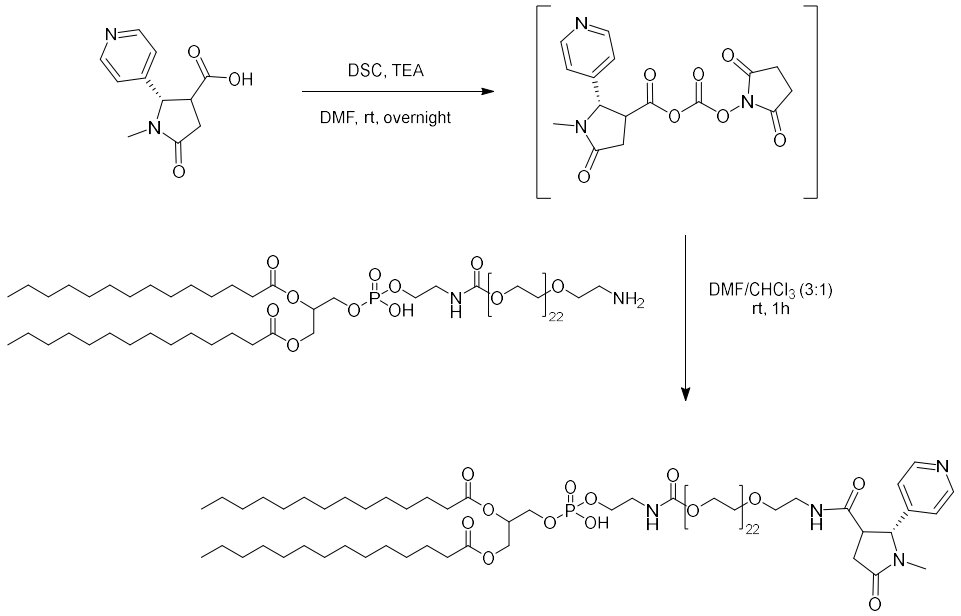

In a two neck round bottom flask, 1 eq of trans-4-cotininecarboxylic acid (250 mg, 1.14 mmol), 1.1 eq. of DSC (1.25 mmol) and 3 eq. of triethylamine (3.42 mmol, 465 µl) were added in dilute solution of DMF (~20ml) and inert (nitrogen gas) at 25 degrees for overnight. When the reaction was over, to 3 ml from the solution reaction DMPE-PEG1000-NH_2 (MW = 1692, 100 mg, 0,06 mmol) and chloroform (1 ml) for better dissolving were added. The reaction ended after an hour the DMF was evaporate by adding heptane. The crude was purified by a flash chromatography silica gel, gradient of $CHCl_3$/MeOH/NH_4OH as eluent. Then, the fractions with the product were evaporated and the crude was washed with diethyl ether, stirred and centrifugated and the supernatant was dried under reduced pressure to obtain the product in a yield of 52% (MW=1894, 58.5 mg). The final product (DMPE-PEG_{1000}-COTININE) was dissolved in methanol/chloroform (50:50), kept at -20 degrees and used without any characterization for the complexation reaction.

3.3.3 Synthesis of KRAS lmPEI nanoparticles

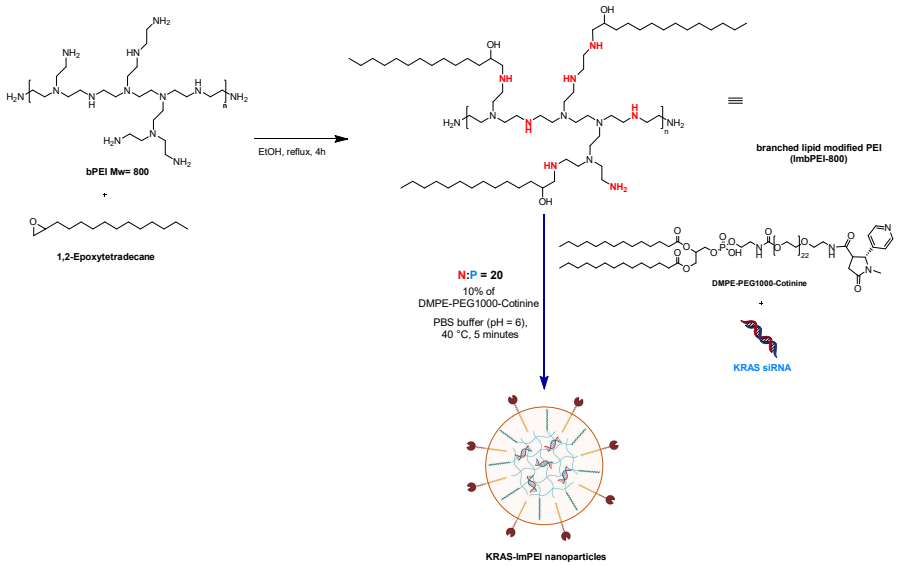

2 ul of stock RNA (KRAS) were put in a water bath at 48 degrees to defrost it slowly, then was diluted into PBS acetic buffer (pH=6, 442 ul) to obtain 444 ul of diluted RNA at a concentration of 45 ng/ul. Out of this volume, 50 ul of the complex itself were taken and 5 ul for additional dilution for "free RNA" in the gel. First, evaporate 195 ul of x10 diluted DMPE-PEG_{1000}-Cotinine for 30 min using the heating block then add 15 ul of lmPEI and 375 ul of pure ethanol into the evaporated eppendorf. Then, the complexation is performed adding, in a 15 mL Falcon, 2.5 mL of acetic PBS buffer (pH=6) and then 250 µl of RNA. Then the lipid solution + polymer and RNA were heated in the acid buffer to 40 degrees for 5 minutes in the Baby shaker and 250 ul lmPEI were added at once and while swirling quickly on top of Vortex. The solution was placed in the incubator in a baby shaker with 1000 rpm, at a temperature of 40 degrees for 20 minutes and characterized by DLS, Zeta potential and electrophoresis gel. The complexes was diluted 100 times in DDW that has been filtered through a 0.22 spinner (FDDW) and analysed by DLS diluting 18 ul of product into 1782 ul of FDDW, where 1000 ul were used for Zeta test and 600 ul for Size test.

DLS (FDDW): average size (nm) = 403.8, PdI = 0.400. Zeta potential (mV) = 33.3
Gel Electrophoresis: see results and discussion.

3.3.4 In Vitro Test – Viability Test

In a 96-well plate, each column represents a different treatment (a total of 9 treatments) and each treatment contains 6 repetitions.

96-well plate	1	2	3	4	5	6	7	8	9	10	11	12
A	PBS	----------	----------	----------	----------	----------	----------	----------	----------	----------	----------	----------
B	|	Medium Only	Untreated Cells	Naked siRNA	siRNA + Lipof.	0.5% v/v KRAS Comp.	1% v/v KRAS Comp.	5% v/v KRAS Comp.	10% v/v KRAS Comp.	20% v/v KRAS Comp.	|	|
C	|										|	|
D	|									|	|
E	|									|	|
F	|									|	|
G	|									|	|
H	----------	----------	----------	----------	----------	----------	----------	----------	----------	----------	----------	PBS

In a 96-well plate, 7000 cells were seeded per well in a total volume of 200 µl. Then, the plate was incubated for 24 hours to let the cells grow and the next day, different treatment were prepared according to relevant protocols and conditions:

- Medium only without any treatment
- Untreated cells in medium
- Naked siRNA. 2 µl of KRAS sequence were mixed into 198 ul of medium -> 2.7 µl of the previous dilution into 997.3 µl of medium. This treatment was used to compare the naked RNA weight per well to the one in the positive control (lipofectamine + siRNA).
- Lipofectamine + siRNA. 1 µl siRNA were diluted into 9 µl Opti-MEM. 2.7 µl of the previous dilution into 7.3 µl of medium.Follow the relevant protocol and add 10 ul of lipo-siRNA complexes into 90 ul Opti-MEM medium.
- 0.5% treatment: add 5 µl of siRNA-lmPEI complexes into 995 µl medium.
- 1% treatment: add 10 µl of siRNA-lmPEI complexes into 990 µl medium.
- 5% treatment: add 50 µl of siRNA-lmPEI complexes into 950 µl medium.
- 10% treatment: add 100 µl of siRNA-lmPEI complexes into 900 µl medium.
- 20% treatment: add 200 µl of siRNA-lmPEI complexes into 800 µl medium.

At this point the medium was removed from the cells and replaced with 100 µl of medium + treatment according to the different lines and the cells were left in the incubation for two hours. Then, the treatment was taken out and the cells were rinsed twice with the help of a clean medium being careful not to detach the cells. 200 µl of a clean medium were added and left in the incubator for an additional 24 hours and after the removal of 100 µl from each well an appropriate amount of

Presto Blue was added (calculation is needed). and incubated for 5 minutes. Finalli, 100 µl from the medium + PBS were transfer to a black plate and fluorescence was measured in a plate reader at wavelengths of 560/590 nm

3.4 References

(1) Thai, A. A.; Solomon, B. J.; Sequist, L. V.; Gainor, J. F.; Heist, R. S. Lung Cancer. *The Lancet* **2021**, *398* (10299), 535–554. https://doi.org/10.1016/S0140-6736(21)00312-3.

(2) Fire, A.; Xu, S.; Montgomery, M. K.; Kostas, S. A.; Driver, S. E.; Mello, C. C. Potent and Specific Genetic Interference by Double-Stranded RNA In. **1998**, *391*, 6.

(3) Alshaer, W.; Zureigat, H.; Al Karaki, A.; Al-Kadash, A.; Gharaibeh, L.; Hatmal, M. M.; Aljabali, A. A. A.; Awidi, A. SiRNA: Mechanism of Action, Challenges, and Therapeutic Approaches. *Eur. J. Pharmacol.* **2021**, *905*, 174178. https://doi.org/10.1016/j.ejphar.2021.174178.

(4) Avital, A.; Muzika, N. S.; Persky, Z.; Bar, G.; Michaeli, Y.; Fridman, Y.; Karny, A.; Shklover, J.; Shainsky, J.; Savaldi-Goldstein, S.; Weissman, H.; Shoseyov, O.; Schroeder, A. Foliar Delivery of SiRNA Particles for Treating Viral Infections in Agricultural Grapevines. *Adv. Funct. Mater.* **2021**, *31* (44), 2101003. https://doi.org/10.1002/adfm.202101003.

Conclusions

During my PhD thesis, novel hybrid nanosystems were synthesized for application in nanomedicine, with particular attention to the treatments of deep-seated tumours. To this purpose it was planned to prepare nanosystems able to deliver photodynamic therapy (PDT) induced by highly penetrating X-Ray irradiation. The idea was to conjugate a photosensitizer (PS), in particular porphyrins, to AuNP, a metal with Z high value and thus able to efficiently adsorb X-ray energy. Considering the high affinity of sulfur for AuNPs, different thiolated linkers were prepared to conjugate the porphyrins to the nanoparticles following two different approaches: a) preparation of AuNPs conveniently functionalized to react with porphyrins b) synthesis of porphyrins functionalized with thiol-ending chains for conjugation to AuNPs. The second approach resulted to be the method of choice. A very important feature required for biological application is that the nanosystem is well dispersed in aqueous media. This can be achieved by using water soluble AuNPs or even improved introducing water soluble chains on the PS.
Moreover, during the five months spent at Technion, it was started the study to encapsulate the nanosystems into liposomes to facilitate the achievement of the tumor and the cellular uptake.
My PhD research work could be briefly summarized in the following points:

1) *synthesis of water dispersed AuNPs*
   20-30 nm citrate_AuNPs nanoparticles were synthetized following the Turkevich method and characterized by UV-Vis spectroscopy and Dinamic light scattering (DLS).
2) *synthesis of functionalized porphyrins*
   The tetra(4-hydroxyphenyl) porphyrin (THPP) was monoalkylated with thiolated linkers of different chain length. To increase the water solubility, PEG chains were bound to the free position of the porphyrin. Each compound was purified and characterized by UV-Vis and NMR spectroscopies.
3) *conjugation to AuNPs*
   A solution of the monoalkylated THPP in DMSO was mixed with aqueous citrate_AuNPs solution, purified through centrifugation and characterized by UV-Vis spectroscopy.
   In the case of PEGylated porphyrin, it was dissolved in water.
4) *a different systems*

Using the same approach, PpIX was connected to PEI_AuNPs, which were synthetized heating PEI with $HAuCl_4$ at 80°C for 30 minutes. In this case, the interaction was based on ionic bonds.

5) *Study on the singlet oxygen production*
   For all the conjugates, their ability to produce singlet oxygen ($^1O_2$) was tested using ADPA that, in the presence of $^1O_2$ produce an endoperoxide. It is possible to evaluate the amount of $^1O_2$ produced observing the decrease of the UV-Vis absorption of ADPA at λ = 378 nm, since the endoperoxide doesn't show any absorption at that wavelength.
   The measures were first performed using visible light and then preliminary experiments were carried out under X-ray irradiation, obtaining encouraging results.
6) *synthesis of liposomes and inclusion experiments*
   During my stage period at TECHNION (Haifa, Israel) liposomes were obtained using the thin film layer method. The characterization by DLS evidenced that their dimension was about 200 nm, suitable to include our nanosystems. Indeed, not only simple porphyrin or AuNPs were separately included but also the nanosystem.

A different topic was faced during my stage at Technion (Israel)

Study RNAi Delivery System Ability for the Therapeutic Silencing of KRAS in Lung Cancer

At the Technion was developed another drug delivery system able to complex siRNA (siKRAS), to go selectively into lung cancer cells and to silencing the KRAS mutated using the siRNA interference (RNAi) technology. This drug delivery system was composed by epoxide, bPEI, cotinine, KRAS and DMSPE-PEG_{2000}-NH_2 that was characterized by DLS, zeta potential and gel electrophoresis. Some in vitro study were performed following the viability test with Presto Blue reagent on A549 cells and showed that with 10% of the treatment the viability of lung cancer cells was close to zero, confirming the efficiency of the drug delivery system.